

Bi metallates as conversion-alloying anodes for Na-ion batteries

Anders Brennhagen



Dissertation for the degree of Philosophiae Doctor

Nanostructures and Functional Materials

Department of Chemistry and
Centre for Materials science and Nanotechnology

Faculty of Mathematics and Natural Sciences
University of Oslo

© Anders Brennhagen, 2024

*Series of dissertations submitted to the
Faculty of Mathematics and Natural Sciences, University of Oslo
No. 2730*

ISSN 1501-7710

All rights reserved. No part of this publication may be
reproduced or transmitted, in any form or by any means, without permission.

Cover: UiO.

Print production: Graphic center, University of Oslo.

Some say: "When life gives you lemons, make lemonade."

I say: "When life gives you lemons, open them up and stick them in an X-ray machine."

Preface

I am incredibly lucky and grateful for being alive. Think of all the specific chemical reactions that had to occur over millions of years just to create the simplest lifeforms. Then the many more million years, chemical reactions and seemingly random events, like an asteroid killing the dinosaurs, that made it possible for humans to come into existence. Considering this, it is close to 0% probability that my mum and dad would meet and create me. I am very grateful that they did and that they provided me a safe and good childhood together with my two siblings Håkon and Ingrid, where I had the possibility to develop and pursue my interests.

I am grateful, excited and slightly terrified for living in a world where humans have explored and understood nature to such a great depth and developed technology that enable us to do incredible things. In my lifetime, we might colonise Mars and become the first known interplanetary species, but we might also destroy most of the foundation for life, as we know it. Humans have taken over the planet and induced drastic changes to the climate and nature much faster than any other species before us. Continuing the way we have done the last years will have devastating consequences, but we still have the possibility to change course and manage our planet in a better way.

All PhD theses, up until now, are written by real humans living in a real world where external events could affect the work. Unless artificial intelligence completely takes over our lives, this will also be the case in the future. I started my PhD fellowship in September 2019, and it only took half a year until our everyday lives were drastically changed due to Covid19. This included limited access to the labs during the beginning of my experimental work, thus significantly affecting the planned PhD work. However, the lack of possibilities for conducting experiments and social interactions provided a lot of time to read literature, which resulted in two review articles (Paper 1–2), which I choose to include in this thesis.

Until February 2022, I was still quite optimistic that the world was going to be able to peacefully collaborate to solve the climate crisis, end hunger and create a good planet for all its inhabitants. We had managed to handle the Covid-pandemic reasonably well, and could use that momentum to collectively reduce CO₂ emissions and transition from fossil fuels into renewable energy. This optimism was greatly reduced due to the war in Ukraine and very recently (October 2023) the escalation of the conflict between Israel and Palestine. If we can't agree that we should stop killing each other, how can we agree on anything else?

I am very grateful that I live in peace in Norway, where I have the possibility to choose my own career path and study natural sciences simply because it is interesting. I would thank my four initial supervisors Helmer Fjellvåg, Anja O. Sjøstad, David S. Wragg and Ponniah Vajeeston for writing and getting the Nanoname project granted (NFR project number: 287480) so that I had the financial support to conduct this PhD work. Together with one year of funding from the Department of Chemistry for teaching duties, and six weeks of Covid related extension, this has enabled me to do what I love for more than four years.

I would especially like to thank my main supervisor Helmer, your passion and interest for detailed and complicated chemical problems is truly inspiring. You have helped to increase the quality of scientific discussions in my PhD work greatly. Anja, thank you for

your valuable insight into synthesis of materials and your advice in structuring and finalising my thesis. David, you have taught me almost everything I know about XRD and PDF and I am grateful for all our beamtime experiments together. Vajeeston, I am grateful for your theoretical insight and modelling work in the beginning of the project. I would like to thank Carmen Cavallo as my fifth supervisor. You came in like a whirlwind in the beginning of the project and kick-started my PhD work. Your driving force and supervision in the lab was essential for my progress the first two years. I would also like to thank the Norwegian industry for understanding that batteries are awesome, thus creating many job opportunities within the field, even though that led to three of my supervisors partially or fully left UiO in the middle of the project.

There are also many other current and previous employees at NAFUMA that have been important for my scientific and personal progress during my PhD work. Alexey Y. Kopusov, I truly appreciate our almost daily discussions regarding my research work and other battery related topics. You have also been a great contributor to the beamtime experiments and the articles attached to this thesis. Jonas Sottmann, thank you first of all for the previous work you did on Bi metallates during your PhD, so that I did not have to investigate these complicated systems blindly. I also thank you for our occasional discussions and your contribution to Paper 2. I would like to thank Heesoo Park for your contributions to the theoretical aspects of Paper 1. Amalie Skurtveit, thank you both for the scientific contributions for Paper 1 and Paper 5 and for our scientific (and non-scientific) discussions. You are a great colleague and I hope to continue working with you in the future. I am grateful for having had the opportunity to supervise Casper Skautvedt, Abilash K. Thiagarajan and Shad I. A. Khan during their Master theses, which was very inspiring. I especially thank Casper for your work on BiFeO_3 and contributions to Paper 4. I would like to thank Erlend T. North for your help with collecting and processing large amounts of beamtime data and your assistance in programming. From the numerous synchrotron experiments at ESRF that was conducted during this PhD work I thank Dragos Stoian, Kenneth Marshall and Wouter van Beek from BM31 and Stefano Checchia, Marco Di Michel and Gavin B. M. Vaughan from ID15. I would also like to thank Anuj Pokle for performing the TEM measurements presented in this thesis, and Salah Bra Amedi for assisting in the syntheses of $\text{Bi}_4\text{Ti}_3\text{O}_{12}$ and BiFeO_3 .

Doing a PhD is very exciting, but can be both scientifically and mentally challenging. Therefore, I am very grateful for being a part of a research group with so many nice and smart people that have been a great support. Among them, I would like to mention Amalie, Casper, Erlend, Linn, Frida, Mathilde, Rasmus, Halvor, Julie, Ina, Alexandra, Andrew, Yani, Eline, Johnny and Veronica. There is always a door I can knock on when I want to discuss something scientifically, need a hug or just want to take a break. Finally, I would like to thank my fiancé Birgitte. Thank you for always being there and for letting me spend my life with you.

Abstract

Fundamental insight into the behaviour of electrode materials during (de)sodiation is important for the development of Na-ion batteries (NIBs). In order to design and conduct reliable mechanistic studies of the active materials it is important to understand the influence of other factors: electrolyte, binder, electrode thickness, preparation procedures and measurement protocols. When performing *operando* measurements, combining electrochemistry and structural characterisation, the complexity increases. Obtaining reliable electrochemistry in *operando* cells, avoiding beam damage and finding an acceptable compromise between electrochemical performance and quality of structural data are some of the main issues. This thesis include some initial results and reflections regarding these challenges, before presenting in-depth mechanistic studies on Bi metallates as anode materials for NIBs.

The main part of this thesis reveals new insight into the cycling and degradation mechanisms during (de)sodiation of Bi metallates, which follow a combined conversion-alloying mechanism. We have performed electrochemical characterisation on four different Bi metallates: BiFeO₃, Bi₂MoO₆, Bi₄Ti₃O₁₂ and Bi₂Al₆O₁₂. The measurements showed some clear similarities between the materials where an irreversible conversion reaction occur during the 1st sodiation, forming Bi particles embedded in a Na–M–O matrix (M = Al, Ti, Fe, Mo). Bi further reversibly alloys with Na through a two-step alloying reaction: Bi \rightleftharpoons NaBi \rightleftharpoons Na₃Bi. The materials showed promising rate capabilities as the performance was almost unchanged when increasing the current density from 0.1 to 1 A g⁻¹, and *operando* X-ray diffraction (XRD) of BiFeO₃ confirmed that the main cycling mechanism was the same at these two current densities. One downside is that all the tested Bi metallates showed poor cycling stability, where most of the capacity was lost after 20 cycles. This finding triggered an interest in unravelling the degradation mechanisms of these materials in addition to the general cycling mechanism.

Bi₂MoO₆ and BiFeO₃ were selected for detailed mechanistic cycling studies through *ex situ* and *operando* X-ray scattering and absorption characterisation. An *operando* measurement combining X-ray total scattering and X-ray absorption spectroscopy (XAS) revealed significant new insight into the cycling mechanism of Bi₂MoO₆ for the first 1.5 (de)sodiation cycles. XRD documented the well-known irreversible conversion reaction forming Bi nanoparticles that subsequently reversibly alloy with Na⁺ to NaBi and cubic Na₃Bi (c-Na₃Bi). Pair distribution function (PDF) analysis supported these results, but also showed that the closest Bi–Bi bonds in Bi metal are broken long after the longer Bi–Bi interactions disappear during sodiation. PDF indicated that the local structure in Bi metal changed towards the end of desodiation as a result of oxidation of metallic Bi. This was further proved by X-ray absorption near edge spectroscopy (XANES), which showed a positive oxidation state for Bi at the end of desodiation, and extended X-ray absorption fine structure (EXAFS) showing clear Bi–O bonds.

Operando XRD monitoring more than 20 (de)sodiation cycles combined with *ex situ* XAS measurements showed that the crystallite sizes of the alloying particles increased as a function of cycle number together with a decrease in the number of the Bi–O bonds in the desodiated state. These results enabled us to understand that the Bi–O bonds are at the interface between the Bi-metal particles and the Na–Mo–O matrix. When the alloying

particles grow during cycling, probably due to coalescence, the surface-to-volume ratio decreases, thus explaining the disappearance of the Bi–O bonds. This deactivation of the oxidation of Bi metal was also observed for BiFeO₃ and is considered as the first region of capacity degradation in Bi metallates. The second region is the deactivation of the Bi \rightleftharpoons NaBi reaction and the third a partial deactivation of the NaBi \rightleftharpoons Na₃Bi reaction. This capacity degradation led to only partial cycling between NaBi \rightleftharpoons Na₃Bi after 20 cycles in the tested Bi metallates, where a significant amount of inactive Na₃Bi showed that the system is locked in the sodiated state.

One surprising difference between BiFeO₃ and Bi₂MoO₆ was that BiFeO₃ formed hexagonal Na₃Bi (h-Na₃Bi) in addition to c-Na₃Bi, already during the first two cycles. Bi₂MoO₆, on the other hand, formed only c-Na₃Bi until cycle ~10 where the increased size of the alloying particles led to formation of small amounts of h-Na₃Bi. We have not fully rationalised the different behaviour between the two materials, but it could indicate that the alloying particles formed in BiFeO₃ are slightly larger compared to those formed in Bi₂MoO₆. There also seemed to be a transformation from c-Na₃Bi into h-Na₃Bi during sodiation, as c-Na₃Bi formed first, which could indicate a Na-deficiency in the c-Na₃Bi phase.

The Na–M–O (M = Al, Ti, Fe, Mo, other transition metals) matrix surrounding the alloying particles are considered a determining factor for the cycling stability, but it is challenging to study. In theory, a stable matrix that can prevent coalescence of the alloying particles could lead to good cycling stability. However, through *operando* and *ex situ* XAS for Bi₂MoO₆ and BiFeO₃ we showed that the matrixes undergo significant changes during cycling. In the Na–Mo–O matrix, Mo⁶⁺ does not change oxidation state, but changes coordination from octahedral in the sodiated state to tetrahedral in the desodiated state. For BiFeO₃ both the oxidation state and coordination changes slightly for Fe³⁺, adapting similar features as Fe₃O₄. By reducing the upper cut-off voltage from 2.00 to 0.70 V during galvanostatic cycling we improved the cycling stability for the materials significantly, probably because of reduced changes in the matrixes.

Norsk sammendrag

Grunnleggende forståelse av de kjemiske endringene i elektrodematerialer under (de)natriering er et viktig bidrag for utviklingen av Na-ionebatterier (NIBer). For å oppnå dette er viktig å først forstå hvordan andre faktorer enn det aktive materialet påvirker elektrokjemien. Elektrolytt, bindemiddel, elektrodetykkelse og prosedyrer for elektrodereparering er noen av parameterne som kan påvirke resultatene fra elektrokjemiske målinger. I *operando* målinger, som kombinerer elektrokjemi og strukturell karakterisering, er det enda flere faktorer som fører til økt kompleksitet. Det å oppnå pålitelig elektrokjemi i *operando* celler, unngå at prøven blir skadet av røntgenstrålene og finne et akseptabelt kompromiss mellom elektrokjemisk ytelse og god kvalitet på de strukturelle målingene er noen av hovedproblemene. Denne avhandlingen inneholder resultater og refleksjoner rundt disse aspektene før den presenterer dybdestudier rundt (de)natrieringsmekanismene til Bi-metallater som anodematerialer for NIBer.

Hoveddelen av denne avhandlingen bidrar til ny innsikt om syklings- og degraderingsmekanismene til Bi-metallater som anodematerialer i NIBer. Vi har testet de elektrokjemiske egenskapene til fire forskjellige Bi-metallater som alle følger en reaksjonsmekanisme som kombinerer konvertering og legering: BiFeO_3 , Bi_2MoO_6 , $\text{Bi}_4\text{Ti}_3\text{O}_{12}$ and $\text{Bi}_2\text{Al}_6\text{O}_{12}$. Målingene viser klare likheter mellom de fire materialene der de først gjennomgår en irreversibel konverteringsreaksjon under første natriering der det dannes nanopartikler av Bi omringet av en Na-M-O matriks (M = Al, Ti, Fe, Mo). Videre gjennomgår Bi en legeringsreaksjon gjennom to steg: $\text{Bi} \rightleftharpoons \text{NaBi} \rightleftharpoons \text{Na}_3\text{Bi}$. Bi-metallatene viste gode egenskaper når vi økte strømtettheten fra 0.1 A g^{-1} til 1 A g^{-1} , og *operando* røntgendiffraksjon (XRD) viste at BiFeO_3 hadde samme syklingsmekanisme med de to strømtetthetene. En ulempe med disse materialene er at de hadde dårlig syklingsstabilitet hvor mesteparten av kapasiteten hadde forsvunnet etter 20 sykluser. Derimot, skapte dette en perfekt mulighet for å studere degraderingsmekanismene som førte til den raske nedgangen i kapasitet, i tillegg til den generelle syklingsmekanismen.

Vi valgte Bi_2MoO_6 og BiFeO_3 for detaljerte mekanistiske studier gjennom *ex situ* og *operando* røntgenspredning og -absorpsjon karakterisering. En *operando* måling som kombinerte XRD, partidistribusjonsfunksjon (PDF) analyse og røntgenabsorpsjonsspektroskopi (XAS) ga ny innsikt i syklingsmekanismen til Bi_2MoO_6 under de første 1.5 (de)natrieringssyklusene. XRD viste den forventede syklingsmekanismen med irreversibel konvertering og legering av Bi som dannet NaBi og kubisk Na_3Bi (c- Na_3Bi). PDF støttet disse resultatene, men viste også at de korteste Bi-Bi bindingene i Bi-metall ble brutt betydelig senere enn de andre Bi-Bi bindingene under natriering. Dataene indikerte også at den lokale strukturen i Bi-metall endret seg mot slutten av denatriering som et resultat av oksidasjon av Bi. Dette ble videre bevist av XAS som viste et positivt oksidasjonstall for Bi og Bi-O bindinger ved slutten av denatrieringen.

Operando XRD over mer enn 20 (de)natrieringssykluser av Bi_2MoO_6 kombinert med *ex situ* XAS viste at krystallittstørrelsen til legeringspartiklene økte som en funksjon av syklusnummer sammen med reduksjon av antall Bi-O bindinger i denatriert tilstand. Fra disse resultatene tolket vi at Bi-O bindingene var på grenseflaten mellom Bi-

metallpartiklene og Na–Mo–O matriksen. Når legeringspartiklene vokser under gjentagende (de)natriering minker forholdet mellom overflate og volum, og derfor forsvinner også Bi–O bindingene. Denne prosessen ble også observert for BiFeO₃ og ble ansett som det første stadiet av kapasitetsdegraderingen. Det andre stadiet er deaktiveringen av Bi \rightleftharpoons NaBi reaksjonen og det tredje er en delvis deaktivering av Na \rightleftharpoons Na₃Bi. Denne degraderingen fører til en veldig begrenset kapasitet som kommer fra en ufullstendig reaksjon mellom NaBi \rightleftharpoons Na₃Bi, hvor systemet er delvis låst i natriert tilstand. En overraskende forskjell mellom BiFeO₃ og Bi₂MoO₆ var at BiFeO₃ dannet heksagonal Na₃Bi (h-Na₃Bi) i tillegg til c-Na₃Bi allerede under første natriering. Vi klarer ikke å forklare dette resultatet fullt ut, men det kan bety at legeringspartiklene som ble dannet i BiFeO₃ er litt større enn de som ble dannet i Bi₂MoO₆. Det ser også ut til å være en glidende overgang fra c-Na₃Bi til h-Na₃Bi under natriering som kan tyde på et underskudd av Na⁺ i c-Na₃Bi.

Na–M–O matriksen som omringer legeringspartiklene er ansett som en viktig faktor for syklingsstabiliteten, men den er utfordrende å studere. I teorien, burde en stabil matriks som kan hindre koalesens av legeringspartiklene føre til god syklingsstabilitet. For Bi₂MoO₆ og BiFeO₃ viste vi at dette ikke er tilfellet da *operando* og *ex situ* XAS viste at matriksene endrer seg betydelig under (de)natriering. I Na–Mo–O matriksen endret ikke Mo⁶⁺ oksidasjonstall, men koordinasjonen rundt Mo⁶⁺ endrer seg fra forvrengt oktaedrisk i natriert tilstand til tetraedrisk i denatriert tilstand. I BiFeO₃ endret både oksidasjonstallet og koordinasjonen til Fe³⁺ seg litt. Ved å redusere den øvre grensen i spenningsvinduet fra 2.00 til 0.70 V under galvanostatisk sykling klarte vi å forbedre syklingstabiliteten betraktelig, trolig på grunn av mindre strukturelle endringer i matriksene.

List of papers

Paper 1 (mini review): Benefits and Development Challenges for Conversion-Alloying Anode Materials in Na-Ion Batteries

A. Skurtveit, A. Brennhagen, H. Park, C. Cavallo, and A. Y. Kozosov, *Frontiers in Energy Research*, **2022**, 10, 897755.

Paper 2 (review): Understanding the (de)sodiation mechanisms in Na-based batteries through Operando X-ray methods

A. Brennhagen, C. Cavallo, D. Wragg, J. Sottmann, A. Kozosov, and H. Fjellvåg, *Batteries & Supercaps*, **2021**, 4(7), 1039-1063.

Paper 3: Operando XRD studies on Bi₂MoO₆ as anode material for Na-ion batteries

A. Brennhagen, C. Cavallo, D. S. Wragg, P. Vajeeston, A. O. Sjøstad, A. Y. Kozosov, and H. Fjellvåg, *Nanotechnology*, **2022**, 33(18), 185402.

This article has a corrigendum:

A. Brennhagen, C. Cavallo, D. S. Wragg, P. Vajeeston, A. O. Sjøstad, A. Y. Kozosov, and H. Fjellvåg, "Corrigendum: Operando XRD studies on Bi₂MoO₆ as anode material for Na-ion batteries (2022 Nanotechnology 33 185402)," *Nanotechnology*, **2022**, 33(35), 359501.

Paper 4: Unravelling the (de)sodiation mechanisms of BiFeO₃ at a high rate with operando XRD

A. Brennhagen, C. Skautvedt, C. Cavallo, D. S. Wragg, A. Y. Kozosov, A. O. Sjøstad, and H. Fjellvåg, accepted by *ACS Applied Materials & Interfaces*

Paper 5: Combined operando PDF and XAS revealing the (de)sodiation mechanism of Bi₂MoO₆

A. Brennhagen, A. Skurtveit, D. S. Wragg, C. Cavallo, A. O. Sjøstad, A. Y. Kozosov, and H. Fjellvåg, manuscript in preparation

Abbreviations

BSE	Backscattered electrons
CAM	Conversion-alloying material
CE	Coulombic efficiency
CMC	Carboxymethylcellulose sodium salt
CNT	Carbon nanotubes
CT	Computed tomography
CV	Cyclic voltammetry
DEC	Diethyl carbonate
DFT	Density functional theory
DMC	Dimethyl carbonate
EC	Ethylene carbonate
ECP-N	N-doped Ketjen black
ESRF	European Synchrotron Radiation Facility
EXAFS	Extended X-ray absorption fine structure
FCC	Face-centred cubic
FEC	Fluoroethylene carbonate
FT	Fourier transform
GC	Galvanostatic cycling
KIB	K-ion battery
LIB	Li-ion battery
MD	Molecular dynamics
NAFUMA	Nanostructures and functional materials
NASICON	Na super ionic conductor
NFR	Norges Forskningsråd (The Research Council of Norway)
NG	N-doped graphene
NIB	Na-ion battery
NMP	N-methyl-2-pyrrolidone
NORTEM	The Norwegian Centre for Transmission Electron Microscopy
NSG	N- and S-doped graphene
OCV	Open circuit voltage
PAA	Polyacrylic acid
PANI	Polyaniline
PC	Propylene carbonate
PPMS	Physical property measurement system

PTFE	Polytetrafluoroethylene
PVDF	Polyvinylidene fluoride
RECX	Resource Centre for X-ray Diffraction and Scattering
rGO	Reduced graphene oxide
SAD	Selected area diffraction
SAXS	Small angle X-ray scattering
SE	Secondary electrons
SEI	Solid electrolyte interface
SEM	Scanning electron microscopy
SNBL	Swiss-Norwegian beamlines
STEM	Scanning transmission electron microscopy
TEM	Transmission electron microscopy
TM	Transition metal
TSCT	Total scattering computed tomography
UN	United Nations
XANES	X-ray absorption near edge spectroscopy
XAS	X-ray absorption spectroscopy
XPS	X-ray photoelectron spectroscopy
XRD	X-ray diffraction

Table of Contents

Preface	v
Abstract	vii
Norsk sammendrag.....	ix
List of papers.....	xi
Abbreviations.....	xiii
1. Introduction.....	1
1.1 Motivation.....	1
1.2 Objectives.....	5
1.3 How the papers and results in this thesis address the objectives	5
2. Na-ion batteries.....	7
2.1 Electrochemical principles and battery properties	7
2.1.1 Faraday's law and theoretical capacity.....	7
2.1.2 Cell voltage and energy density	8
2.1.3 Electrochemical processes.....	9
2.1.4 Na-ion storage mechanisms	9
2.2 Review of Na-ion battery materials	11
2.2.1 Cathode materials	11
2.2.2 Anode materials	14
2.2.3 Conductive additives and binders	16
2.2.4 Electrolytes	16
3. Methods and experimental details.....	19
3.1 Electrochemical characterisation	19
3.1.1 Cyclic voltammetry (CV).....	19
3.1.2 Galvanostatic cycling (GC)	19
3.1.3 Cycling at different rates	19
3.2 Structural and morphological characterisation	20
3.2.1 X-ray diffraction (XRD) and pair distribution function (PDF)	20
3.2.2 X-ray absorption spectroscopy (XAS)	24
3.2.3 Scanning electron microscopy (SEM).....	26
3.2.4 Transmission electron microscopy (TEM)	27
3.3 <i>Operando</i> X-ray characterisation	27
3.4 Experimental details.....	28
3.4.1 Chemicals.....	28
3.4.2 Synthesis.....	29

3.4.3	Electrode preparation and cell assembly.....	29
3.4.4	Characterisation	30
4.	Results.....	33
4.1	Benchmarking and experimental challenges.....	33
4.1.1	Parameters affecting electrochemical performance	33
4.1.2	Lessons learned from <i>operando</i> X-ray characterisation and TEM.....	39
4.2	Cycling and degradation mechanisms of Bi metallates.....	45
4.2.1	(De)sodiation mechanisms of Bi ₂ MoO ₆ (Paper 3 and 5).....	45
4.2.2	High-rate cycling and capacity degradation of BiFeO ₃ (Paper 4).....	49
4.2.3	Electrochemical performance of different Bi metallates	51
5.	Summarising discussion	55
5.1	3-step capacity degradation	55
5.2	The effect of the Na–M–O matrix.....	57
5.3	Formation of c-Na ₃ Bi and h-Na ₃ Bi.....	62
5.4	Bi metallates in LIBs vs NIBs.....	65
6.	Concluding remarks and outlook.....	71
7.	References	75

1. Introduction

1.1 Motivation

One of the top priorities for human kind is to achieve the United Nations (UN) sustainable development goals [2]. The goals targeting affordable and clean energy for the world's population (goal 7) and mitigating climate change (goal 13) are related to a massive increase in the use of renewable energy sources and electrification of transport vehicles [2–4]. This, together with the ever-increasing production and usage of smaller electrical devices (cell phones, laptops, remote controls, etc.), leads to a large demand for rechargeable batteries and other energy storage solutions. Li-ion batteries (LIBs) are currently the leading battery technology, but questions regarding abundance, ethics and price of critical elements have led to a wide search for alternative rechargeable battery technologies [5]. Other ion batteries (Na, K, Mg, Ca and Al) [6–9], redox flow [10, 11], metal-air [12, 13], and metal-S batteries [14] are therefore hot research topics.

With the pressing need for energy storage in different applications, several of these battery chemistries will be commercially realised in the future. LIBs will probably still dominate the market for applications where energy density is critical, but the other battery technologies could be promising alternatives for applications where cost, safety and availability of elements are more important. Na, Mg, K, Ca and Al are suggested as alternative metal-ion batteries, and their abundance in the earth's crust is more than three orders of magnitude higher than Li (Figure 1.1, Table 1.1). All of them, except Al, are also much more abundant in seawater, especially Na as it is almost five orders of magnitude more abundant than Li (Table 1.1). The abundance of Ni and Co, which are used in most commercial LIBs, are also low and the main reservoirs are geographically limited [5]. In addition there are ethical challenges regarding the extraction of these elements, especially for Co mining in Congo, which is linked to corruption and child labour [15]. The low availability of Ni, Co and Li could become problematic in the future, with the massive growth in the battery market. Therefore, the lower cost and better accessibilities of materials for the other battery chemistries can become a determining factor.

Mg^{2+} , Ca^{2+} and Al^{3+} are multivalent and can transfer more than one electron per ion, which in theory could lead to comparable or higher energy densities than LIBs. However, the high charge densities of the ions make them challenging to insert and extract reversibly from the active electrode materials, thus limiting the experimental capacity. Na-ion batteries (NIBs) and K-ion batteries (KIBs) have monovalent charge carriers, like LIBs. Hence, it is easier to transfer the knowledge obtained from research on LIBs to NIBs and KIBs compared to other battery systems. The higher mass of Na and K compared to Li, implies that NIBs and KIBs in general have lower energy densities than LIBs. However, because of the high abundance and availability of Na and K, there will likely be a place for these technologies in the future, especially in applications where energy density is less critical. For example, within stationary storage for stabilising the electricity grid or off grid solutions.



Figure 1.1: Representation of the periodic table where the relative sizes of the elemental symbols represents their abundance in the earth's crust. Reprinted with permission from [16]. Copyright 2011 American Chemical Society.

Table 1.1: Abundance of selected elements in the earth's crust and in seawater.

Element	Abundance in earth's crust (mg kg ⁻¹) [17]	Abundance in seawater (mg L ⁻¹) [18]
Li	20	0.18
Na	2.36×10 ⁴	1.08×10 ⁴
K	2.09×10 ⁴	3.99×10 ²
Mg	2.33×10 ⁴	1.29×10 ³
Ca	4.15×10 ⁴	4.12×10 ²
Al	8.23×10 ⁴	2×10 ⁻³
Fe	5.63×10 ⁴	2×10 ⁻³
Mn	9.50×10 ²	2×10 ⁻⁴
Ni	84	5.6×10 ⁻³
Co	25	2×10 ⁻⁵
Bi	8.5×10 ⁻³	2×10 ⁻⁵

NIBs, which are the focus of this thesis, are more promising than KIBs because of the lower mass and smaller ionic radii of Na⁺ compared to K⁺, leading to higher gravimetric and volumetric energy density. They are on the verge of entering the battery market as a big contender, and several large battery manufacturers are heavily investing in the commercialisation of NIBs [19, 20]. The search for new active anode materials is an

important step in this development. Hard carbons are currently the state-of-the art, but shows limited specific capacities up to around 300 mAh g⁻¹ [21, 22].

In order to increase the capacity of the anode there have been several studies on active materials that follow alloying or conversion reactions rather than the conventional intercalation mechanism. These materials can accommodate several Na⁺ ions per formula unit and can therefore, exhibit significantly higher capacities [23]. For example, red P can obtain specific capacities above 2000 mAh g⁻¹ by alloying with Na to form Na₃P [24], and NiP₃ as a conversion material shows capacities above 1000 mAh g⁻¹ [25]. However, materials following these mechanisms undergo large structural changes and volume expansion during sodiation that in general lead to poor cycling stability. In addition, conversion materials tend to have a high working potential (~1 V vs Na/Na⁺) and large voltage hysteresis limiting the useful energy density.

Combined conversion-alloying materials (CAMs) are a group of anode materials that have the potential to combine high capacity and good cycling stability (Paper 1). This is because they form nanosized alloying particles inside a stabilising matrix during the first sodiation [26, 27]. The matrix surrounding the alloying particles should mitigate problems linked to volume expansion and lead to improved cycling stability. For example, Sb₂O₃ and Sb₂S₅ have shown stable capacities at 800–900 mAh g⁻¹, thus surpassing the performance of Sb metal [28, 29]. In addition, the network of electronically conductive alloying particles dispersed in the ionically conductive matrix makes these materials promising for fast cycling [30–32].

There are many possible CAMs, and in general they are little studied and not well understood, compared to other types of anode materials for NIBs (Paper 1–2). Reliable studies of the cycling mechanisms of battery materials are challenging, as they are dependent on *operando* measurements in specialised cells that allows for structural characterisation while maintaining proper electrochemical performance. Several types of *operando* measurements rely on large-scale facilities (synchrotron and neutron sources), which limits the possibilities for measurements (Paper 2). Mechanistic studies of CAMs during cycling is particularly challenging due to the complexity of phase transformations (conversion, alloying and occasionally intercalation) and phase separation (alloying particles inside the matrix). In addition, the formed phases are often nanocrystalline or amorphous, thus limiting the information that can be extracted from X-ray diffraction (XRD), which is the most commonly used *operando* technique. Therefore, other techniques like X-ray absorption spectroscopy (XAS), which could be further divided into X-ray absorption near edge spectroscopy (XANES) and extended X-ray absorption fine structure (EXAFS), and pair distribution function (PDF) analysis are needed for fully understanding these materials (Paper 2).

Bi metallates are a group of CAMs that have shown some promise as anode materials for NIBs. Bi₂(MoO₄)₃ and BiVO₄ reached stable capacities of ~350 mAh g⁻¹ for 100 cycles with an applied current density of 0.15 A g⁻¹ [33], which is significantly better than a corresponding study on Bi metal [34]. The high atomic mass of Bi (208.98 g mol⁻¹) makes the specific capacity of Bi metallates limited, compared to other CAMs. This combined with the limited abundance of Bi (Table 1.1) it is unlikely that Bi metallates will find their way into commercial NIBs, but fundamental understanding of their cycling mechanism

could be transferable to more promising CAMs. Therefore, detailed mechanistic studies of this group of materials will have value for the battery community. The high X-ray scattering of Bi provides strong signals in the X-ray measurements, which make them slightly easier study than other CAMs.

There are only a few good *operando* studies on Bi metallates as anode materials for NIBs [33, 35] and LIBs [36–38] that provides reliable information regarding their cycling mechanisms. A combined *operando* XRD/XANES study on $\text{Bi}_2(\text{MoO}_4)_3$ and BiVO_4 showed that the general cycling mechanism was an irreversible conversion reaction forming Bi nanoparticles embedded in a Na–M–O matrix (M = Al, Ti, V, Fe, Mo, other transition metals) [33]. The Bi particles further reversibly alloys with Na in two steps forming NaBi and cubic Na_3Bi (c- Na_3Bi). The formation of c- Na_3Bi , instead of the thermodynamically stable hexagonal Na_3Bi (h- Na_3Bi), can be explained by the nanosized Na_xBi alloys [34]. The XRD data did not show any diffraction peaks of the amorphous Na–M–O matrixes, but the XANES data for Mo showed that Mo^{6+} was slightly reduced during sodiation. Therefore, it was suggested that the matrix consisted of Na_2MoO_4 that upon sodiation transformed into Na_3MoO_4 [33].

An *operando* XAS study (including XANES and EXAFS) on BiFeO_3 showed the same general cycling mechanism as for BiVO_4 and $\text{Bi}_2(\text{MoO}_4)_3$, but also indicated that Bi was further oxidised to a positive average oxidation state during desodiation [35]. In addition, some redox activity of Fe was observed, and by linear combination fitting it was estimated that ~15% had been reduced to metallic Fe, while the rest was suggested to be in some sort of Fe–O phase. BiVO_4 for LIBs have been thoroughly investigated by *operando* total scattering computed tomography (TSCT), which provided spatially resolved XRD and PDF data throughout the whole electrode [36]. The high quality averaged PDF from this study revealed a small reversible shift in the closest V–O bond from the Na–V–O matrix that had not been previously observed [36], indicating some structural changes in the matrix. It has been suggested that Bi_2MoO_6 forms a matrix of Mo and $\text{Na}_2\text{O}/\text{Li}_2\text{O}$ in the sodiated/lithiated state and MoO_3 and Bi_2O_3 in the desodiated/delithiated state [39–43]. However, there are limited proof of these suggestions and the amorphous and dynamic nature of the matrix makes it difficult to accurately describe.

Bi metallates show in general limited cycling stability as anode materials for NIBs, but complex nanostructuring and carbon additives can in some cases stabilise the capacity [31, 33, 35, 39, 44–46]. Despite the obvious challenges with the cycling stability, none of these studies describe degradation mechanisms in depth. The stability of the matrix during electrochemical cycling and its interactions with the alloying particles are likely crucial aspects of the capacity degradation. Our understanding of these materials are limited and systematic studies are needed to more accurately design Bi metallates (and other CAMs) with both high capacity and good cycling stability.

1.2 Objectives

The main objective in this thesis is to obtain fundamental understanding of the cycling and degradation mechanisms of Bi metallates as anode materials for NIBs. There are several aspects that are not well documented in literature, which we aim to address:

- Determine the limiting chemical parameters for the electrochemical performance of Bi metallates as anode materials in NIBs, with focus on capacity degradation.
- Evaluate whether the (de)sodiation mechanism of Bi metallates always follow the two step alloying reaction of $\text{Bi} \rightleftharpoons \text{NaBi} \rightleftharpoons \text{Na}_3\text{Bi}$, both at high and low (de)sodiation rates. This include:
 - o Nucleation and growth of c- Na_3Bi vs h- Na_3Bi .
 - o Effect of particle size of the constituent Bi-based phases.
- Investigate possible conversion back to the pristine material.
- Obtain atomistic insight into the Na-M-O matrix, and understand its changes during cycling and its impact on the cycling stability.
- Investigate the role of electrode preparation, choice of electrolyte, coin cell assembly and testing procedures for the electrochemical performance.

To reach these objectives we selected the following work strategy:

- Review literature on state-of-the-art Bi metallates and other CAM systems, as well as on potential *operando* techniques suited for NIB materials that could reveal critical information on cycling and degradation mechanisms.
- Screen different Bi metallates by utilising different synthesis procedures to investigate similarities and differences, with regards to Bi/M ratio, different M and particle morphology.
- Select two systems for detailed mechanistic studies and apply *operando* XRD/PDF and XAS at different (de)sodiation rates combined with *ex situ* measurements.

1.3 How the papers and results in this thesis address the objectives

The two review articles, three research papers and additional results attached at the end of this dissertation contain important aspects that together provide a larger unity with new insights into the (de)sodiation mechanisms of Bi metallates. Each of these parts address the objectives of this PhD work in different ways.

Paper 1 (mini review) introduces the concept of CAMs as anode materials for NIBs and includes a detailed literature study that is complementary to Section 2.2. It highlights their promising high-rate capabilities and the possibility of finding a good compromise between cycling stability and high capacity. The paper presents and discuss challenges of studying the cycling mechanisms of CAMs and their promise for fast charging applications due to the formation of a bi-continuous network of alloying particles embedded in a Na-X matrix ($X = \text{O}, \text{S}, \text{Se}, \text{Te}, \text{P}$, oxometallates). The paper introduces the discussion regarding the effect of the matrix on the electrochemical performance of CAMs, which is continued in Section 5.2.

Paper 2 (review) summarises most of the recent work on *operando* X-ray characterisation for Na-ion battery materials. Given the complex cycling mechanisms of Bi metallates, it was important to search in literature for techniques that could be used to provide new insight into these systems. There were a limited amount of studies on CAMs in general and very few on Bi metallates, showing that deep understanding of these materials is missing. However, the wide range of *operando* X-ray studies of other materials provided an overview of relevant techniques. Based on this study and the availability of the techniques we chose XRD, PDF and XAS as the main characterisation methods for the experimental work in this thesis (Paper 3–5). Paper 2 also discuss several topics that are revisited in this thesis: Na-ion storage mechanisms (Section 2.1.4), *ex situ vs operando* characterisation (Section 3.3), scattering from Na metal and beam damage (Section 4.1.2).

Paper 3 is the first of two dedicated in-depth studies of the cycling and degradation mechanism of Bi_2MoO_6 . The second study is presented in Paper 5 (see below). Paper 3 describes a full cycle life study of Bi_2MoO_6 with *operando* XRD providing insight into the general cycling and degradation mechanisms. It indicated that particle growth of the Na_xBi alloys is the main reason for the capacity decay between cycle 10 and 20, where the system locks itself in the sodiated state. The paper also explores the formation and dissolution of the SEI layer through *ex situ* SEM and discusses its effect on the capacity decay. Additionally, several attempts to improve the cycling stability by changing synthesis parameters and ball milling were performed.

In Paper 4 studies of BiFeO_3 at high and low current densities with *operando* XRD were conducted in order to investigate potential differences in the cycling mechanisms at different rates. This study also focuses on the degradation mechanisms through *operando* XRD over the course of 27 (de)sodiation cycles and compare the results to those obtained for Bi_2MoO_6 in Paper 3. *Ex situ* XAS at different stages of cycling was used to support the results obtained from XRD and to provide additional information of the local coordination and oxidation state of Bi in the alloying particles and Fe in the Na–Fe–O matrix. Finally, changes in the cycling stability when reducing the voltage range of the galvanostatic cycling (GC) are explored.

Paper 5 presents a complex *operando* study combining XRD/PDF and XAS (both XANES and EXAFS) over the course of 1.5 (de)sodiation cycles to further investigate the cycling mechanism of Bi_2MoO_6 . This measurement provided detailed insight into the (de)sodiation mechanisms of Bi_2MoO_6 including information of the alloying particles, the matrix and their interactions during cycling. The results were validated by *ex situ* measurements of samples extracted at different potentials. In addition, *ex situ* measurements of samples from later stages of cycling (cycle 5-20) further elucidated the degradation mechanisms, including growth of the alloying particles.

In addition to the papers, this thesis includes results from electrochemical studies of BiFeO_3 , Bi_2MoO_6 , $\text{Bi}_2\text{Al}_6\text{O}_{12}$ and $\text{Bi}_2\text{Ti}_2\text{O}_7$ at low and high current densities, to obtain a broader overview of the performance of Bi metallates in general. We also present results from testing of different electrolytes, binders and solvents to evaluate their effect on the cycling performance. In order to decide whether the factors had a significant impact or not, we evaluated the general uncertainties in the measurements.

2. Na-ion batteries

2.1 Electrochemical principles and battery properties

In this chapter, we briefly describe some basic concepts that are relevant for the work in this thesis and focus more on the practical aspects of the theory. It also includes an overview of different types of battery components for NIBs. The general working mechanisms and more detailed theory of different battery types are presented elsewhere together with a comprehensive review of battery materials [47].

2.1.1 Faraday's law and theoretical capacity

One of the most commonly studied characteristics for battery materials is the specific capacity, usually reported as gravimetric capacity (mAh g^{-1}). It is also possible to report volumetric capacity (mAh cm^{-3}) or areal capacity (mAh cm^{-2}). When screening for possible new active materials for battery electrodes it is good to estimate the theoretical capacity (Q_T) and later compare it to the measured experimental capacity. The theoretical capacity is calculated by Faraday's 1st law of electrolysis (Equation 1).

$$Q_T = \frac{nF}{M} \quad \text{Equation 1}$$

Here Q_T is the theoretical capacity, n is the number of electrons transferred per formula unit of active material, M is the molar mass of the active material and F is the Faraday constant ($96485 \text{ C mol}^{-1} = 26\,801 \text{ mAh g}^{-1}$).

This seems like an easy and unambiguous way of calculating the theoretical capacity of battery materials, but it can be misleading in some cases. One potential problem is selecting the mass of the active material in the charged or discharged state. In LIBs, it is most common to calculate the theoretical capacity based on the discharged state assuming a full cell configuration. Meaning that anode materials use the mass of the delithiated phase while cathodes use the mass of the lithiated phase. For example, LiFePO_4 ($M = 157.76 \text{ g mol}^{-1}$) will have a theoretical capacity of 170 mAh g^{-1} , assuming a transfer of all the Li ions, and graphite ($M = 12.01 \text{ g mol}^{-1}$), assuming a transfer of 1 Li per 6 C atoms, will have $Q_T = 372 \text{ mAh g}^{-1}$.

This convention works well for most materials, but becomes problematic when assessing metallic Li as the active anode material. Theoretical capacity of completely "delithiated" Li would be infinite. Therefore, it is more common to report the capacity for "lithiated" Li, which is 3860 mAh g^{-1} . This becomes misleading when comparing to the theoretical capacity of Si, which is 4200 mAh g^{-1} , when using the mass of delithiated Si and assuming alloying with 4.4 Li⁺ per Si atom. A more proper comparison would in this case be to use the mass of $\text{Li}_{4.4}\text{Si}$ in the calculation, resulting in a theoretical capacity of 2010 mAh g^{-1} .

Another challenge with theoretical capacity occurs for materials with unknown cycling mechanisms. In these cases, it is extra important to describe the assumptions made in the calculations. For example, the theoretical capacity of LiCoO_2 could be reported as either 274 mAh g^{-1} (if all Li is extracted) or 137 mAh g^{-1} (if only half of the Li is extracted), where the latter is much closer to the experimental reversible capacity. An example that is more relevant for this thesis is Bi_2MoO_6 for NIBs, where it is uncertain to what degree Mo

participates in the redox reactions (if it forms Mo metal, Na_2MoO_4 , Na_3MoO_4 or something else) and uncertain if Bi transforms back to Bi_2O_3 , Bi_2MoO_6 or Bi during desodiation. In this case, it is possible to present many different theoretical capacities, which could be confusing and misleading if the assumptions are not properly reported.

When comparing experimental and theoretical capacity, it is important to remember that reactions other than (de)sodiation of the active material occur in the cell and contributes to the capacity. Formation of SEI, (de)sodiation of the conductive additive, and decomposition of electrolyte are some examples of side reactions that could influence the measured capacity. When calculating the specific capacity based solely on the mass of the active material, it can often exceed the theoretical capacity due to the side reactions that are not accounted for. The determination of the mass of the active material could also include significant uncertainties, which influences the measured result. These factors are important to be aware of when reporting specific capacities to avoid misleading conclusions.

2.1.2 Cell voltage and energy density

The chemical potential between the cathode and the anode is often referred to as the cell voltage. The theoretical open circuit voltage (V_{oc}) of a battery can be calculated from the Gibbs free energy of the redox reactions according to (Equation 2):

$$V_{oc} = -\frac{\Delta G}{nF} \quad \text{Equation 2}$$

Here G is the Gibbs free energy (J/mol), n is the number of transferred electrons and F is the Faraday constant (96485 C mol^{-1}).

The voltage multiplied with capacity gives the energy of the battery, which is the property that determines the amount of work it can perform. Hence both the difference in working potential between the electrodes and their specific capacities are important and not just each of them separately. When testing electrode materials that are meant to be promising for practical applications it is, therefore, important to have a high working voltage ($>3 \text{ V vs Na/Na}^+$) for the cathode and low working voltage for the anode ($<1 \text{ V vs Na/Na}^+$). Reactions between 1–3 V are difficult to utilise in practical applications because the voltage of the full cell would be so low that the specific capacity would have to be very high to obtain a competitive energy density.

Calculating the energy density is mostly relevant when evaluating full cells, and in this case, it is also important to describe the assumptions for the calculations. The energy densities could be very different if they are calculated based on the mass of the active materials, the mass of the electrodes, the mass of the battery cell or the mass of the whole battery pack. In this thesis, we report only electrochemical measurements on anode materials in half cells and, therefore, it is not sensible to report the energy densities as it will depend on which cathode it would be coupled with.

2.1.3 Electrochemical processes

There are several processes occurring in a battery apart from the (de)sodiation reactions of the active materials that affects the electrochemical measurements. Solid electrolyte interface (SEI) and cathode electrolyte interface (CEI) are layers that form from decomposition of the electrolyte on the surface of the anode and cathode, respectively [48, 49]. Ideally the formation of these should be avoided or they should work as stable passivation layers after the first cycle. The formation, composition and stability of SEI and CEI depends on the electrolyte, additives, active materials and cycling procedures. In general these layers are difficult to study and understand even though they seem to be crucial for the performance and cycling stability of the batteries. Especially for NIBs the SEI is not much studied, but in general it is seemingly more difficult to form a stable SEI layer because of the higher solubility of Na salts in the most common electrolyte solvents [50]. The highly reactive environment inside batteries could also lead to corrosion of the cell casings or current collectors [51].

All chemical reactions have activation barriers or kinetic limitations that needs to be overcome for the reaction to occur. This is expressed by overpotential in batteries and is the origin of voltage hysteresis in cycling curves, which should be as small as possible to have the highest possible energy efficiency. There are many components and processes that occur simultaneously during (de)sodiation that affects the overpotential in batteries. It is, therefore, difficult to assess the exact role of each process.

Examples of overpotentials are ohmic (internal resistance), activation (charge transfer) and concentration (diffusion) overpotentials [52]. The overpotentials increase when increasing the current density of the measurements, but this increase is not necessarily identical for different reactions. This could lead to changes in the cycling mechanisms of battery materials as more kinetically favoured phase transformations could occur instead of the thermodynamically predicted pathways. Changes in cycling mechanism during cycling at higher rates has been shown for common battery materials as graphite [53], and LiFePO_4 [54–56]. In the case of graphite the overpotential for the intercalation reaction becomes too large at high current densities so that Li plating occurs instead of intercalation between the graphene layers [53].

2.1.4 Na-ion storage mechanisms

There are four main storage mechanisms for Na^+ ions in NIBs: insertion, intercalation, conversion and alloying (Paper 2). Intercalation could be defined as a type of insertion and the terms are sometimes used interchangeably. To avoid confusion, we here define the insertion mechanism as the process where Na^+ ions are inserted into channels in a 3D-network structure (Figure 2.1a), while intercalation is restricted to layered compounds (Figure 2.1b). Intercalation/insertion does not drastically change the atomic structure of the materials, apart from some expansions and small shifts in the layers or the network. These materials can accommodate few Na^+ ions in the structure (usually <1 per formula unit) and, therefore, have limited capacity, but the moderate structural changes could lead to good cycling stability.

Materials that follow alloying (Figure 2.1c) or conversion reactions (Figure 2.1d) can accommodate several Na^+ ions per formula unit and could, therefore, have significantly

higher capacities (Paper 2). The conversion reaction occurs as the cation (usually a multivalent metal) in the pristine material is reduced into its metallic state while Na^+ ions take its place and bind to the anion. The average working voltage of conversion reactions are generally quite high compared to other anode materials, but too low to be interesting as cathodes. They often struggle with a large voltage hysteresis, making them inefficient as battery materials.

In alloying reactions, the alloying element obtains a negative oxidation state as it alloys with several Na^+ ions. The reaction potentials are reasonably low (~ 0.5 V), which together with the high capacity make them promising as anode materials for batteries requiring high energy density. The large structural changes that both conversion and alloying type materials undergo during cycling, make the cycling stability of these materials challenging. The volume expansion, which often leads to particle cracking, is considered as the most detrimental process [57–59].

Combined conversion-alloying materials (CAMs) are a group of anode materials that could provide a good compromise between cycling stability and high capacity. Their cycling mechanism can in most cases be described as an irreversible conversion reaction where metal particles, which further reversibly alloy with Na^+ , are formed inside a stabilising matrix (Figure 2.1e). More details regarding CAMs are described in Paper 1.

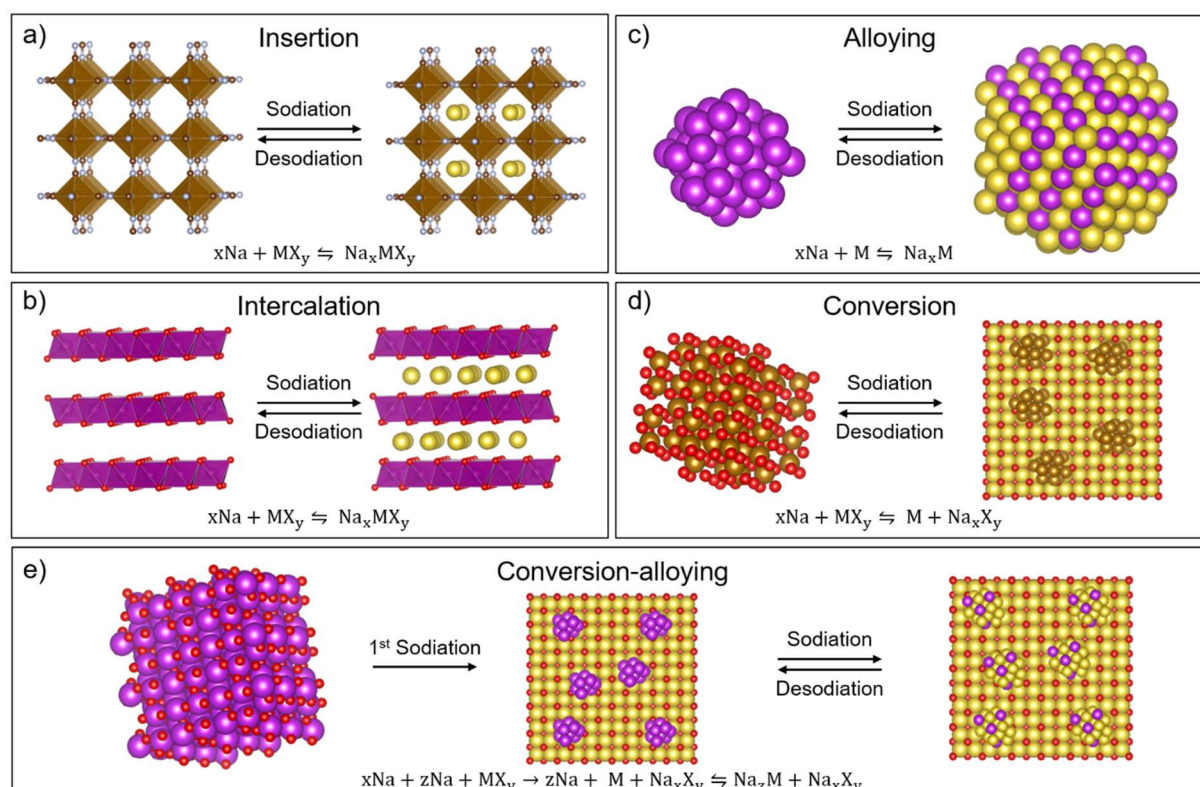


Figure 2.1: Graphical illustration of the main types of cycling mechanisms for active materials in NIB electrodes including general reaction equations. a) Insertion, b) intercalation, c) alloying, d) conversion and e) combined conversion-alloying. M represents a metallic element, which for the intercalation/insertion and conversion reactions often is a transition metal. For alloying and conversion-alloying reactions M mainly represents elements from group 14–15 in the periodic table. X represents electronegative elements (halides and chalcogenides) or polyanions (PO_4^{-3} , SO_4^{-2} , VO_4^{-3} , MoO_4^{-2} , CN^- , etc.). Vesta was used for creating the structural models [60, 61].

2.2 Review of Na-ion battery materials

There has been an increasing interest in Na-ion battery research the last years that has led to the discovery of many candidates for active materials. The main research focus has been on cathode materials that, similar to LIB-cathodes, mostly follow an intercalation or insertion type of mechanism. For anode materials there are several examples of intercalation, insertion, alloying, conversion and combination of these reaction mechanisms. This chapter shortly reviews some of the main groups of active materials for NIBs and include some examples of the performance of selected materials. It is not meant as a comprehensive review as that is found elsewhere [62–64], and more details of the cycling mechanisms revealed by *operando* X-ray techniques are presented in Paper 2. The chapter also briefly describes common binders, carbon additives and electrolytes, and presents their influence on the cycling performance of NIBs.

2.2.1 Cathode materials

Layered transition metal oxides (NaMO_2 , where M is one or more 3d transition metals) is seemingly the most studied group of active materials for cathodes in NIBs [65](Paper 2). They usually arrange in crystal structures where MO_6 octahedra form layers with Na ions intercalated in between. Naming and classification of layered battery materials generally follow the system introduced by Delmas *et al.* [66]. This system uses O (octahedron), P (trigonal prism) or T (tetrahedron) to represent the polyhedron surrounding the Na ion followed by a number indicating the stacking sequence.

The most common phases for pristine layered cathode materials are the O3 phase with stacking order ABCABC of the oxygen layers [67–77] and P2 with stacking order ABBA [78–94]. Both of these materials are in the hexagonal crystal system where O3 has the space group of $R\bar{3}m$ and P2 has $P6_3/mmc$. The O3 phase often transforms into a P3 phase ($R\bar{3}m$ or $R3m$) during charging [67, 72, 76, 77], while the P2 phase often transforms into an O2 phase ($P6_3mc$) [62, 83].

The phases with these notations are widely accepted and unambiguously used in the scientific community, but there seems to be some different methodology for naming distorted versions of these phases (Table 2.1). Monoclinic distortions of O3 (C2/m) and P3 phases (C2/m) are most often denoted O'3 and P'3, with the apostrophe between the letter and the number [67, 72, 95–97]. If the starting material is a hexagonal O3 phase and transforms into a second hexagonal O3 phase (same space group, but different lattice parameters) in the same cycling campaign it is often denoted O3' (with the apostrophe behind the number) [68, 76, 98]. If a third hexagonal phase is observed it can be denoted O3'' [67]. There are also examples of a similar notation for the distorted phases using O'3 for the first, O''3 for the second and O'''3 for the third [96, 97].

Distorted P2 phases are often reported in the orthorhombic crystal system (not monoclinic) and P'2 is generally used to denote the orthorhombic distortion with space group $Cmcm$ [79, 92, 95]. However, monoclinic distorted P2 (C2/c) has also been reported and denoted P'2 [84], and there are examples of P2' being used for the orthorhombic distortion [80, 85, 89]. These different naming schemes lead to confusion regarding the placement of the apostrophe(s), and how to denote the different distortions.

Table 2.1: Overview of reported crystal systems, space groups, stacking order and descriptions of layered NaMO₂ oxides named after Delmas' notation.

Type of phase	Crystal system	Space group	Stacking order, description	References
O3	Hexagonal/trigonal	R $\bar{3}$ m	ABCABC	[67–77]
O'3	Monoclinic	C2/m	Monoclinic distortion of O3	[67, 72, 95–97]
O''3	Monoclinic			[96, 97]
O'''3	Monoclinic			[96, 97]
O''''3	Monoclinic			[96, 97]
O3'	Hexagonal		“Another O3 type” [76]	[68, 76, 98]
O3'	Monoclinic			[77, 99]
O3''	Hexagonal			[67]
O2	Hexagonal	P6 ₃ mc	ABAC	[83]
O1	Hexagonal/trigonal	P $\bar{3}$ 1m	ABAB	[69, 95, 100, 101]
P3	Hexagonal/trigonal	R3m	ABBCCA	[67, 76]
P3	Hexagonal/trigonal	R $\bar{3}$ m	ABBCCA	[72, 76, 77]
P3	Monoclinic	C2/m		[101]
P'3	Monoclinic	C2/m		[76, 95, 98]
P''3	Monoclinic			[96, 97]
P'''3	Monoclinic			[97]
P3'	Monoclinic			[77, 99]
P3''	Hexagonal			[77]
P2	Hexagonal	P6 ₃ /mmc	ABBA	[78–94]
P2	Orthorhombic	Pnma		[102]
P'2	Orthorhombic	Cmcm		[79, 92, 95]
P'2	Monoclinic	C2/c		[84]
P2'	Orthorhombic	Cmcm		[80, 85, 89]
P1	Monoclinic	C2/m	Single layered (AAA)	[100]
OP4	Hexagonal	P $\bar{6}$ m2	ABBACAACBCCB	[82, 84]
Z			Intergrowth between P2, O2 and OP4	[92, 103]
T1/T2				[93]

Other reported phases are O1 with ABAB stacking (hexagonal, $P\bar{3}1m$) [69, 95, 100, 101], P1 with AAA stacking (monoclinic, $C2/m$) [100] and the mixed OP4 phase with ABBACAACBCCB stacking (hexagonal, $P\bar{6}m2$) [82, 84]. In addition, a so-called “Z” phase has been reported in several articles [92, 103]. Sometimes it is only described as an unknown phase while other times it has been described as an intergrowth between the P2 and O2 phases where OP4 is an ordered intermediate in the Z-phase region, as illustrated in Figure 2.2 [103].

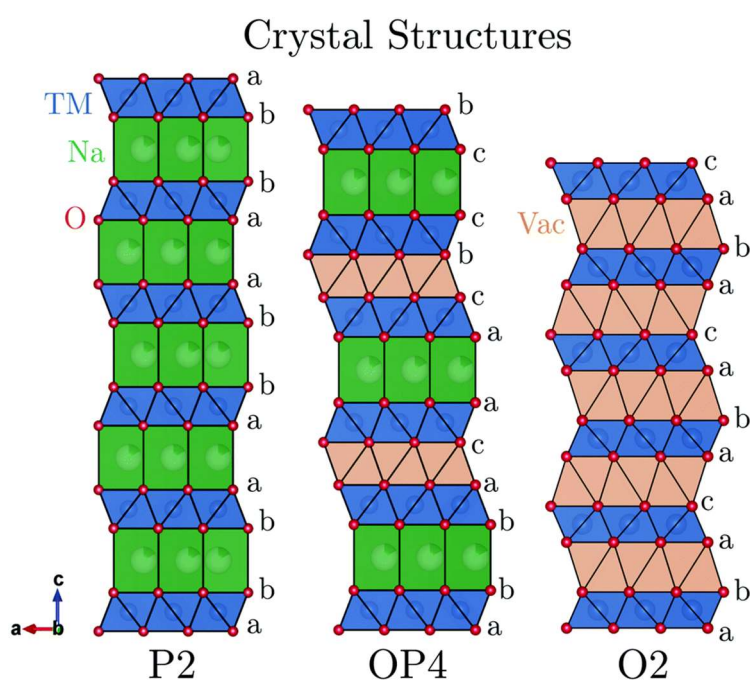


Figure 2.2: Illustration of the layered P2, OP4 and O2 phases. Typical phase transformation upon desodiation. Reproduced from [103] with permission from the Royal Society of Chemistry.

Layered oxides of V, Cr, Fe, Mn, Co and Ni have been widely studied as cathode materials for NIBs [65, 104, 105] (Paper 2). Of these materials, Fe, Mn, Co and Ni seem to be the most promising, but each of the oxides using only one of the transition elements have some severe drawbacks. P2- Na_xMnO_2 shows high initial capacities around 180 mAh g^{-1} with an average working potential vs Na/Na^+ at $\sim 3 \text{ V}$, but struggles with cycling stability [84]. O3- NaNiO_2 shows significantly lower specific capacity of $\sim 120 \text{ mAh g}^{-1}$ and limited cycling stability, but has an average voltage higher than 3 V [96, 97]. O3- Na_xCoO_2 shows quite stable capacities around 140 mAh g^{-1} for a least 30 cycles, with an average voltage of 2.96 V [106], but due to the high cost and ethical concerns regarding Co it is not considered a viable option in commercial NIBs. O3- NaFeO_2 has a very stable redox potential around 3.3 V and shows an initial specific capacity of $\sim 100 \text{ mAh g}^{-1}$ that gradually decrease to 75 mAh g^{-1} after 30 cycles [107].

By combining two or more transition metals in the same layered oxide, the properties can be tuned to reach the desired compromise between energy density, cycling stability and cost [105]. O3- $\text{NaFe}_{1/2}\text{Co}_{1/2}\text{O}_2$ is a good example as it shows higher capacity and better cycling stability than both O3- NaFeO_2 and O3- NaCoO_2 , reaching $160\text{--}140 \text{ mAh g}^{-1}$ over the first 50 cycles and an average potential of 3.14 V vs Na/Na^+ [106]. Another promising

material is O3-NaNi_{1/2}Mn_{1/2}O₂ showing stable capacities around 140 mAh g⁻¹ with an average voltage of ~3 V and excellent rate capabilities [108]. The properties can vary a lot between oxides synthesised in the O3 type or the Na-deficient P2 type. For example, O3 type Na_xFe_{1/2}Mn_{1/2}O₂ (x = 1) delivers reversible capacities of 100–110 mAh g⁻¹ while the P2 type (x = 2/3) delivers up to 190 mAh g⁻¹ [109].

Another promising group of cathode materials for NIBs is polyanionic frameworks, which includes phosphates, fluorophosphates and sulphates. They are often composed of XO₄ (X = P, S) tetrahedra or trigonal XO₃, and MO₆ octahedra [110, 111]. Fluorine might also substitute the oxyanions (phosphates and sulphates) to increase the voltage of the materials. NaFePO₄, Na₂Fe₂(SO₄)₃ and Na super ionic conductor (NASICON) materials (*e.g.* Na₃V₂(PO₄)₃) are some of the most promising cathode materials in this group. NaFePO₄ with maricite structure has shown an initial specific capacity of 142 mAh g⁻¹ and a capacity retention of 95% after 200 cycles [112]. This is significantly better than the olivine structured NaFePO₄ which only obtained a capacity of 125 mAh g⁻¹ and slightly worse cycling stability [113]. The NaFePO₄ materials have an average voltage of ~3 V.

Na₂Fe₂(SO₄)₃ is one of the more promising sulphates for NIBs. In a composite with graphene oxide it showed capacities around 100 mAh g⁻¹, stable for hundreds of cycles and an average voltage of ~3.8 V [114]. A typical NASICON-type structure, Na₃V₂(PO₄)₃, consists of VO₆ octahedra and PO₄ tetrahedra sharing corners. The structure has several channels for fast intercalation of Na⁺ [63]. Na₃V₂(PO₄)₃ shows a specific capacity slightly above 100 mAh g⁻¹ and a stable voltage plateau at 3.4 V. It also shows good cycle life and excellent rate capabilities where it can maintain a capacity above 100 mAh g⁻¹ even at the high current density of 2 A g⁻¹ [115]. Substitution of V with other metals (*e.g.* Al, Fe, Mn or Co) [116-119] or introducing F⁻ into the structure [120, 121] could improve and tune the performance of NASICONs. Prussian blue analogues (PBAs), with general formula Na_xM_A[M_B(CN)₆]_y·zH₂O (M_{A, B} = transition metals, x = 4y - 2, y ≤ 1), are also promising cathode materials for Na-ion batteries showing capacities up to 170 mAh g⁻¹ and average voltages at ~3 V [122]. The PBA structure can be described as face-centred cubic with M_A as packing spheres, M_B(CN)₆ filling the octahedral voids and Na intercalating into (and out of) the tetrahedral voids through large 3D channels.

2.2.2 Anode materials

For anode materials, Na titanates are a group of polyanionic frameworks that show very good cycling stability, but lower specific capacity compared to other anodes. Na₂Ti₆O₁₃ nanorods have shown capacities of ~170 mAh g⁻¹ at 0.1 A g⁻¹ and ~110 mAh g⁻¹ after 2800 cycles at 1 A g⁻¹ with an average voltage of ~0.5 V [123].

Carbon materials are the most commonly used anode materials for NIBs and can roughly be divided into graphite, hard and soft carbons [124]. Graphite shows very poor performance in NIBs compared to LIBs when using conventional carbonate-based electrolytes. However, by using diglyme-based electrolytes it is possible to obtain a reasonable amount of intercalation of solvated Na ions, with an average potential slightly above 0.5 V vs Na/Na⁺. Studies have shown stable capacities of ~150 mAh g⁻¹ with a current density of 0.1 A g⁻¹ and capacities above 100 mAh g⁻¹ for 2500 cycles at 0.5 A g⁻¹ [125, 126]. Hard carbons have lower working potentials (0.1–0.2 V vs Na/Na⁺) and higher

capacities up to $\sim 300 \text{ mAh g}^{-1}$, compared to graphite [21, 22]. Soft carbons have also shown capacities at $\sim 300 \text{ mAh g}^{-1}$, with average voltages of $\sim 0.5 \text{ V}$ [127, 128]. Both hard and soft carbons are amorphous and are produced from various types of organic matter. Their natural abundance, sustainability and low cost are advantageous for these carbon materials [63].

Materials following alloying type reactions have the highest theoretical capacities (up to 2596 mAh g^{-1} for red P to Na_3P) among the active materials for NIBs, as several Na^+ can alloy with one alloying atom [129]. However, they are known to have poor cycling stability due to large volume expansions leading to cracks and particle degradation. The alloying materials are mostly found in group 14 and 15 in the periodic table and include Si, P, Sn, Sb, Bi, Ge and combinations of these. Si is a very promising alloying material for LIBs, but does not show the same performance in NIBs. With nanostructuring, Si has shown stable experimental capacities slightly above 400 mAh g^{-1} with a current density of 50 mA g^{-1} in NIBs [130]. Despite the higher mass of Sn and Sb they actually provide higher and more stable specific capacities than Si, reaching more than 600 mAh g^{-1} over at least 100 cycles [131, 132]. Even heavy Bi-based anodes show similar performance as Si with capacities close to 400 mAh g^{-1} for 2000 cycles at a current density of 0.4 A g^{-1} [133]. Red phosphorus can obtain experimental capacities above 2000 mAh g^{-1} during initial cycles, and with the correct morphology, it can reach stable cycling at 2.6 A g^{-1} with capacities close to 1000 mAh g^{-1} for >600 cycles [24]. These alloying anodes obtain average voltages between $0.2\text{--}0.6 \text{ V}$ [129].

A conversion reaction includes drastic structural changes often leading to limited reversibility and cycle life for anode materials. In return, the capacity is often far greater than that of intercalation compounds, but usually lower than for alloying materials [134]. NiP_3 is a conversion material that shows stable specific capacities above 1000 mAh g^{-1} for approximately 15 cycles before the capacity rapidly declines [25]. MoS_2 (in different types of carbon composites) is one of the most studied conversion materials for NIBs and shows stable capacities between $400\text{--}600 \text{ mAh g}^{-1}$ for at least 100 cycles [135]. A possibly more promising sulphide is VS_2 showing specific capacities of $\sim 700 \text{ mAh g}^{-1}$ for 100 cycles when measured with a specific current of 0.1 A g^{-1} [136]. Amorphous $\text{Fe}_2\text{O}_3/\text{graphene}$ composite has achieved reasonably stable capacities around 400 mAh g^{-1} for at least 50 cycles [137]. The average voltages of the conversion anodes are quite high $\sim 1 \text{ V vs Na/Na}^+$, making them challenging to use in full cells with regards to energy density [40].

Combined conversion-alloying materials (CAMs) can provide a good compromise between high capacity and good cycling stability [26](Paper 1). Sb-based oxides, sulphides and selenides, in different kinds of carbon composites, have shown good performance through reversible conversion and alloying reactions. A $\text{Sb}_2\text{O}_3/\text{C}$ composite reached very high initial capacities above 1200 mAh g^{-1} and maintained 900 mAh g^{-1} after 100 cycles at 50 mA g^{-1} [28]. Sb_2S_5 (in graphene foam) also showed better performance than the pure Sb metal with stable capacities around 800 mAh g^{-1} for more than 300 cycles [29]. $\text{Sb}_2\text{Se}_3/\text{rGO}$ shows stable capacities around 650 mAh g^{-1} for more than 50 cycles at a current density of 0.1 A g^{-1} [138]. However, the conversion reaction has limited reversibility and the high voltages of $1\text{--}3 \text{ V vs Na/Na}^+$ make the conversion reaction difficult to utilise in a real battery. Therefore, several materials are developed with an irreversible initial conversion reaction that forms a stabilising amorphous matrix around

the alloying particles (Paper 1). This methodology has been successfully shown for $\text{Bi}_2(\text{MoO}_4)_3$ and BiVO_4 , where they obtained stable capacities around 350 mAh g^{-1} at 0.15 A g^{-1} for 100 cycles, and capacities above 200 mAh g^{-1} after 1000 cycles at 0.3 A g^{-1} [33]. Since it is mainly the alloying reaction that is active, the average working potentials for these materials are $\sim 0.5 \text{ V vs Na/Na}^+$.

2.2.3 Conductive additives and binders

Battery electrodes need good electronic conductivity. Therefore, conductive additives are usually mixed together with the active material in the electrodes. In most cases, the additive is a type of carbon, where carbon black (*e.g.* Super P), reduced graphene oxide (rGO) and carbon nanotubes (CNT) are among the most common examples [139, 140]. They might either be added during the synthesis of the active material, thus making a composite and/or added during the mixing of the electrode slurry. There are several examples of active materials that have gained improved performance as composites, especially for alloying and conversion materials [23, 140]. For example, an $\text{Sb}_2\text{S}_3/\text{rGO}$ composite showed stable capacities at $\sim 650 \text{ mAh g}^{-1}$ for 100 cycles while the capacity of pure Sb_2S_3 dropped to $\sim 250 \text{ mAh g}^{-1}$ after 10 cycles [141]. Even though it is very common to use different carbon additives in the slurry preparation there seems to be no systematic reviews discussing their effect on the cycling performance of active materials for NIBs.

In order to ensure good adhesion between the electrode components and to the current collector a binder is added to the slurry. Polyvinylidene fluoride (PVDF), carboxymethyl cellulose (CMC), polyacrylic acid (PAA), Na alginate and polytetrafluoroethylene (PTFE) are among the most common binders [142]. These have different solubility in different solvents, thus to a large degree dictate which solvent to use in the slurry mixing. For example, CMC is soluble in H_2O while PVDF depend on the more toxic and volatile *N*-methyl-2-pyrrolidone (NMP) as a solvent. Several studies have shown that binders could have a huge influence on the cycling performance of certain materials and determine whether a material is almost dead or work fantastically [143–147]. However, because of the large spread in studies, it is difficult to find common trends regarding which binders in general work best for certain types of materials [142].

2.2.4 Electrolytes

The most common electrolytes used in NIB research are mimicked from the LIB electrolytes. NaPF_6 and NaClO_4 salts dissolved in carbonate solvents like ethylene carbonate (EC), propylene carbonate (PC), dimethyl carbonate (DMC), diethyl carbonate (DEC) or mixtures of these are the most common electrolytes in NIBs [142]. It has been shown that the electrolyte could have a huge impact of the performance and cycling stability of electrode materials [148, 149]. However, determining which electrolytes in general work best for NIBs has proven to be difficult [142]. Therefore, it seems to be necessary to screen different electrolytes when testing a new material in order to optimise its performance.

Several electrolyte additives have shown to improve the performance of NIBs, where fluoroethylene carbonate (FEC) is the most common. FEC has been shown to generally

lead to lower coulombic efficiency (CE) for the first cycle, but also increase the cycling stability drastically, probably because of the formation of a thicker and stronger SEI layer [142].

Ionic liquids are possible alternatives to the conventional carbonate-based electrolytes, which could lead to improved performance and safety [150]. They often consist of bis(fluorosulfonic)amide ($\text{N}(\text{SO}_2\text{F}_2)^-$, FSA⁻) as the anionic species in combination with different cations like N-methyl-N-propylpyrrolidinium ($\text{C}_3\text{C}_1\text{pyrr}^+$), 1-ethyl-3-methylimidazolium ($\text{C}_2\text{C}_1\text{im}^+$) and trimethylhexylammonium (TMHA⁺) [150].

Solid state electrolytes for NIBs are popular research topics, due to the potential for designing batteries with higher energy densities and increased safety [151, 152]. The main groups of solid state electrolytes are inorganic ceramics, organic polymers and hybrid electrolytes. Among the inorganic solid state electrolytes, NASICON is considered to be one of the most promising groups. A common example of a NASICON electrolyte is $\text{Na}_3\text{Zr}_2\text{Si}_2\text{O}_{12}$, which has shown an ionic conductivity of $6.7 \times 10^{-4} \text{ S cm}^{-1}$ at room temperature [153]. By doping $\text{Na}_3\text{Zr}_2\text{Si}_2\text{O}_{12}$ with Mg and Ni the room temperature conductivity have been shown to exceed $2 \times 10^{-3} \text{ S cm}^{-1}$ [154].

P2 type layered oxides have also been investigated as solid state electrolytes where $\text{Na}_2\text{Zn}_2\text{TeO}_6$ and $\text{Na}_2\text{Mg}_2\text{TeO}_6$ have shown conductivities of 10^{-4} – $10^{-3} \text{ S cm}^{-1}$, which could be further increased by Ga-doping [155–157]. Sulfide-based electrolytes, such as Na_3PS_4 [158] and Na_3SbS_4 [159] also show promise as solid state electrolytes with conductivities of $\sim 10^{-4}$ – $10^{-3} \text{ S cm}^{-1}$. Organic polymers are more flexible and less brittle than inorganic ceramics, which could be beneficial as electrolyte in NIBs [151]. Gel polymer electrolytes consist of liquid electrolyte incorporated inside a polymer matrix, and are on the borderline between solid and liquid electrolytes. They could reach conductivities of $\sim 6 \times 10^{-3} \text{ S cm}^{-1}$ [160, 161], which is significantly higher than most solvent free polymer electrolytes showing conductivities between 10^{-9} – $10^{-6} \text{ S cm}^{-1}$ [151]. In hybrid electrolytes, it is possible to combine the advantages of inorganic and organic solid state electrolytes to reach high performance and stability [162, 163].

The choice of electrolyte, binder, solvent, additives and mixing procedures could have a large impact of the measured performance of the active material. It is therefore difficult to directly compare materials that have been tested in different ways and are at different levels of optimisation.

3. Methods and experimental details

3.1 Electrochemical characterisation

The work leading to this thesis included a significant amount of electrochemical characterisation, where cyclic voltammetry (CV) and galvanostatic cycling (GC) were the main techniques. This chapter provides a brief description of these techniques and some perspectives regarding cycling at different rates.

3.1.1 Cyclic voltammetry (CV)

CV measurements are performed by applying a constant change in voltage, defined as the sweep rate, while measuring the resulting current response [164]. This methodology allows for determination of which potentials must be reached to initiate an electrochemical reaction and provides information of the reaction kinetics. Broad CV peaks are often indicative of slow reaction kinetics as the change in potential occurs faster than the reaction, while sharp peaks indicate fast kinetics. The broadness of the peaks will also vary with the applied sweep rate, and extra information regarding the kinetics and reversibility of the reactions can be obtained by observing changes in the peaks as a function of cycling rate.

3.1.2 Galvanostatic cycling (GC)

GC is the most straightforward technique to measure the performance of battery materials. It is performed by applying a constant current while measuring the change in voltage. The measured capacity of the material is obtained by multiplying the applied current with the time of sodiation or desodiation. The electrochemical reactions occurring in the cell during cycling are represented by voltage plateaus in the (de)sodiation curves, and by studying these it is possible to determine the capacity contributions from different reactions.

Another way of representing the results from GC measurements is by plotting the first derivative of the (de)sodiation curves, thus creating dQ/dV graphs. These graphs present the amount of transferred electrical charge (Q) per voltage step, thus transforming the plateaus in the (de)sodiation curves to peaks in the dQ/dV plot, similar to those obtained from CV measurements. The dQ/dV plots differ from the cyclic voltammograms since the GC measurements are conducted by applying a constant current, while CV measurements utilise a constant change in voltage [165]. This generally results in broader peaks from the CV measurements compared to dQ/dV . If the GC and CV measurements would be performed infinitely slow, the cyclic voltammogram should look identical to the dQ/dV plot. dQ/dV data that are directly calculated from the (de)sodiation curves are often very noisy, and might need to be smoothed or rebinned in order to provide meaningful graphs.

3.1.3 Cycling at different rates

Many battery materials struggle with handling high cycling rates and often experience irreversible damage when being cycled too fast. One common example is graphite, which

is prone to Li plating and dendrite growth when cycled at too high currents [53]. Thermodynamically, Li⁺ should intercalate into graphite, but at high current densities, the overpotential for the intercalation reaction increase more than that for Li plating, thus favouring the latter reaction. This is an example that the cycling mechanisms of battery materials can change drastically when changing the applied current because of the competition between thermodynamics and kinetics. Batteries used in real-life applications often experience irregular cycling on a daily basis with different current densities. Therefore, it is important to test different current densities for new materials and assess changes in the cycling mechanism in order to predict possible degradation mechanisms at elevated cycling rates.

3.2 Structural and morphological characterisation

In this thesis, X-ray diffraction (XRD) and X-ray absorption (XAS) were the main characterisation techniques for obtaining structural information of the studied materials. XRD provided information of the atomic arrangements while XAS provided element specific information regarding oxidation state and local structure. Scanning electron microscopy (SEM) and transmission electron microscopy (TEM) were used to study the morphology and particle sizes of the samples.

3.2.1 X-ray diffraction (XRD) and pair distribution function (PDF)

XRD is one of the most commonly used characterisation techniques as it can quickly identify the crystalline phases in a material. The measurements are performed by irradiating the sample with a monochromatic X-ray beam and measuring the scattered signal at a range of angles. The obtained diffraction pattern contains peaks at specific angles where the beam is exiting the material with constructive interference. These angles can be calculated by Bragg's law (Equation 3).

$$2d\sin\theta = n\lambda \quad \text{Equation 3}$$

Here d is the distance between the defined atomic planes, θ is the angle between the atomic planes and the diffracted X-rays, λ is the wavelength of the X-rays and n is a positive integer.

When measuring the same samples with different X-ray wavelengths the 2θ values of the peaks change. However, by converting the 2θ values into the scattering vector Q (Equation 4), it becomes independent of the wavelength and the Q values will always be the same for the same material.

$$Q = \frac{4\pi}{\lambda} \sin\left(\frac{2\theta}{2}\right) \quad \text{Equation 4}$$

Experimental diffractograms of Bi metal, mixed with 20 wt% carbon black (Super P), and pure Super P are shown in Figure 3.1. The crystalline Bi metal shows clear diffraction peaks, where the peak positions correspond to the distances between the atomic planes in the crystal structure. The peaks' positions and intensities can be used to determine the crystal structure of the material. For amorphous Super P there are only broad bumps in the diffraction pattern as the material lacks long-range order.

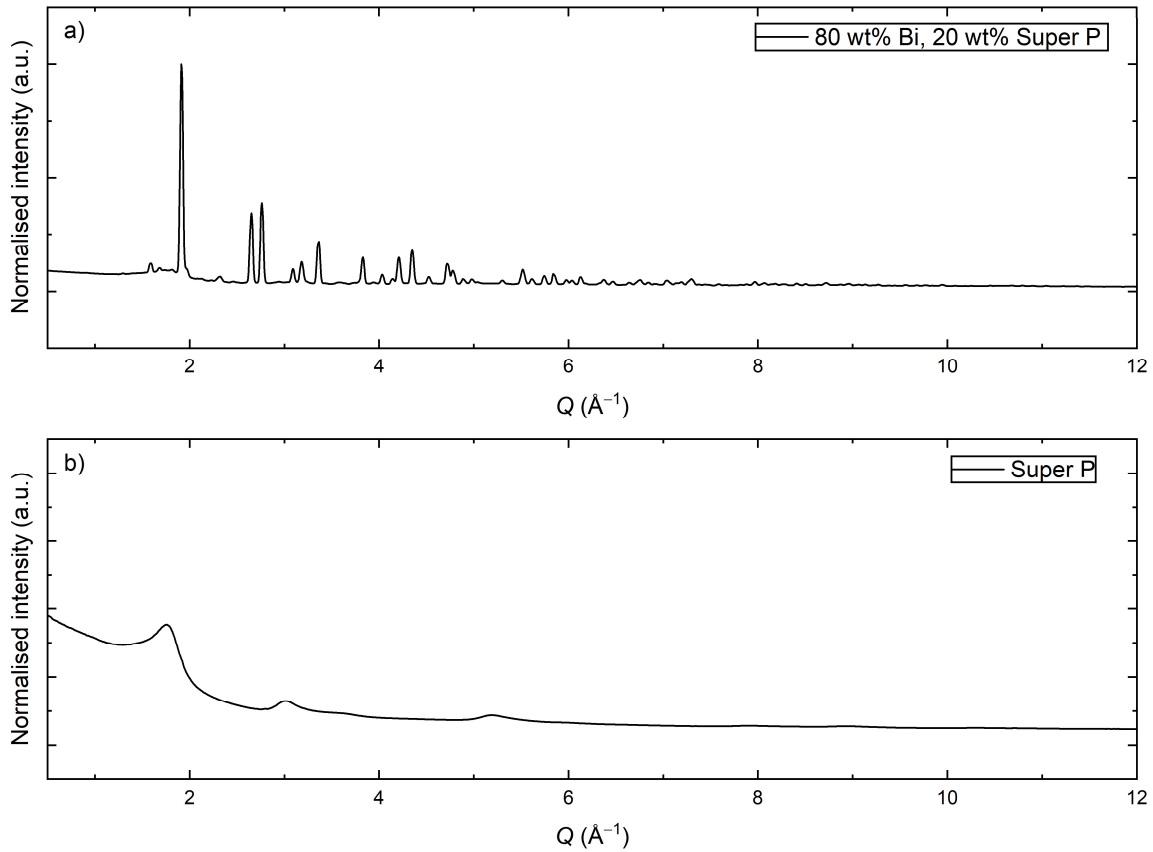


Figure 3.1: Experimental XRD patterns of a) Bi metal mixed with 20 wt% amorphous carbon (Super P) and b) pure Super P. The data are previously unpublished.

The crystallite size of the measured material can be estimated by assessing the broadness of the diffraction peaks. Broader peaks indicate smaller crystallite sizes and sharper peaks larger crystallite sizes. One way of quantitatively estimating the crystallite size is the Scherrer equation (Equation 5).

$$D = \frac{K\lambda}{\beta \cos\theta} \quad \text{Equation 5}$$

D is the estimated diameter of the crystallites, K is the shape factor that is usually taken as 0.89 for spherical particles, λ is the wavelength and β is the full width at half maximum of the peak measured at angle θ .

XRD is a great technique for determining the structure of crystalline materials. However, it is not so useful when the studied material lack long-range order, like amorphous carbon (Super P). PDF can simplified be explained as a Fourier transform of an XRD pattern measured over a wide Q range, which takes into account the total scattering of the material, including both Bragg-scattering and diffuse scattering [166]. PDF provides sensible structural information for both crystalline and amorphous samples.

PDF data from real experiments is usually presented as the reduced pair distribution function $G(r)$. The real atomic pair distribution function, $g(r)$, is not possible to obtain from scattering data due to the phase problem [167]. To calculate $G(r)$ we first estimate

the structure function, $S(Q)$, by normalising the diffraction pattern by the scattering intensities (Equation 6).

$$S(Q) = \frac{I(Q)}{\langle b \rangle^2} \quad \text{Equation 6}$$

Here $\langle b \rangle$ is the compositional average of the scattering amplitudes of the atoms, and $I(Q)$ is the scattering intensity function (i.e. the scattering/diffraction pattern). Then we calculate the reduced scattering function, $F(Q)$, by correcting $S(Q)$ for the decline in scattering power at higher Q values (Equation 7).

$$F(Q) = Q[S(Q) - 1] \quad \text{Equation 7}$$

Finally we perform a Fourier transform of $F(Q)$ to obtain $G(r)$ (Equation 8).

$$G(r) = \frac{2}{\pi} \int_{Q_{\min}}^{Q_{\max}} F(Q) \sin(Qr) dQ \quad \text{Equation 8}$$

The obtained $G(r)$ represents the atomic distances in the measured sample, as exemplified by the experimental PDFs of Bi metal and amorphous carbon, Super P (Figure 3.2). These data show that it is possible to extract information from the local structure of both crystalline and amorphous materials. However, it is important to avoid overinterpreting the data, as not all observed peaks from experimental PDF are real, especially at low r (peaks marked with * in Figure 3.2). The peak resolution in PDF is limited by the Q range and experimental PDFs will usually contain overlapping peaks corresponding to several atomic distances. This is the case for the peak denoted C_{Bi} as it contains significant contribution from the Bi–Bi distances of 4.75 Å in addition to those at 4.55 Å (Figure 3.2a).

An X-ray measurement always contains some background signals from air and the sample holder. In the case of Bi and other heavy elements, it is sometimes necessary to dilute the sample with a low scattering material (in this case Super P) in order to have sufficient X-ray transmission through the sample, leading to extra background. It is important to subtract as much as possible of the contribution from these background signals, in order to obtain a clean PDF of the measured material. However, it is near impossible to remove all background contributions, and you might run into the risk of subtracting too much, which could affect the signal of the material of interest. The problems with background subtraction combined with instrumental limitations and data processing lead to “artificial” noise peaks and limited peak resolution, which is important to be aware of during data analysis.

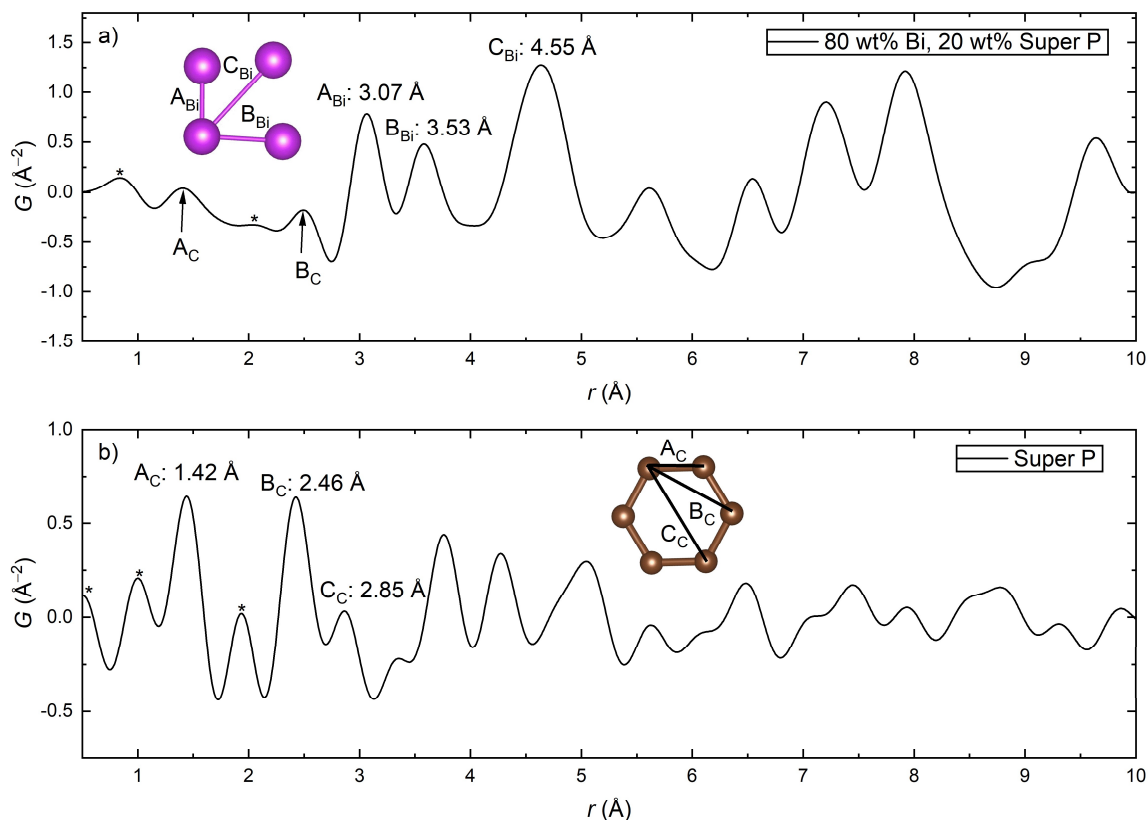


Figure 3.2: Experimental PDFs of a) Bi metal mixed with 20 wt% amorphous carbon (Super P) and b) pure Super P. The three closest Bi–Bi bonds in Bi metal are marked in the figure as A_{Bi} , B_{Bi} and C_{Bi} . The three closest C–C bonds in a six-ring extracted from the crystal structure of graphite are marked in the figure as A_{C} , B_{C} and C_{C} . The written values of the atomic distances are the theoretical values extracted from the crystal structures, and does not necessarily match perfectly with the experimental peak positions. Unidentified peaks that probably are a result of non-ideal data or data processing and not real atomic distances are marked with *. The data are previously unpublished.

PDF can provide a simple estimate of the average crystallite sizes in the materials, as the PDF signal decays at higher r as a function of domain (crystallite) size. This is illustrated by the PDFs of Bi (Figure 3.3a) and Super P (Figure 3.3b) plotted up to 200 Å. The signal of the amorphous Super P approaches 0 at ~ 20 Å as the material has no long-range order at higher r , while the signals of the crystalline Bi decays at a much higher r value. For most real powdered samples this decay is due to imperfect order over very long range, thus being related to the crystallite size. However, even for perfectly crystalline materials the PDF signal will approach 0 at high r values (>200 Å) because of instrumental limitations.

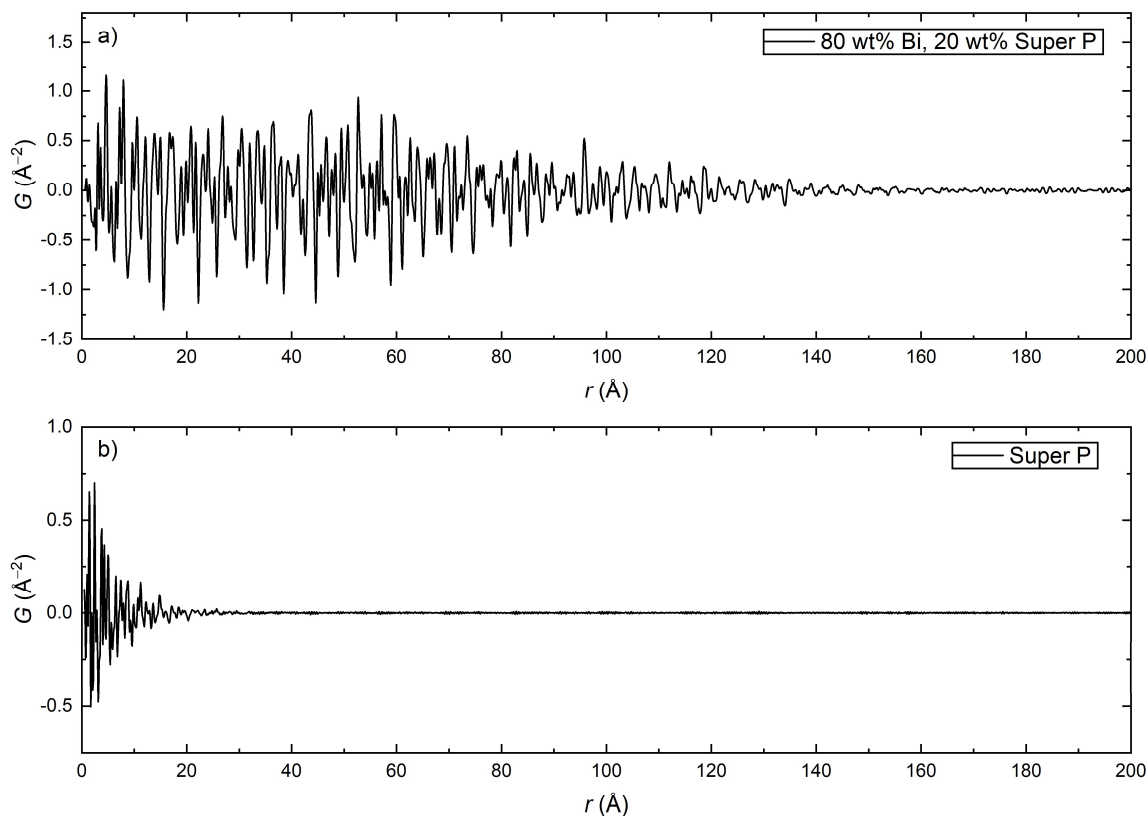


Figure 3.3: Experimental PDFs of a) Bi metal mixed with 20 wt% amorphous carbon (Super P) and b) pure Super P, plotted up to $r = 200$ Å. The data are previously unpublished.

3.2.2 X-ray absorption spectroscopy (XAS)

XAS can provide information regarding the local structure and oxidation state of specific elements in a material [168]. It is based on irradiating the sample with X-rays scanned over a range of energies and measure the absorption. Binding energies of core electrons in atoms ranges from 0.1 keV to 100 keV, and it is typically the excitations of these electrons that are studied in XAS. The X-ray absorbance abruptly increases when the X-rays reach the sufficient energy to excite inner electrons in the sample, which gives rise to the absorption edge. By studying the edge positions and comparing with literature, we can determine which species we have in the sample. The X-ray absorption through a sample is given by Equation 9.

$$\mu t = \ln\left(\frac{I_0}{I_1}\right) \quad \text{Equation 9}$$

Here μ is the absorption coefficient, t is the thickness of the sample, I_0 is the intensity of the incoming X-ray beam and I_1 is the intensity of the transmitted X-ray beam.

By measuring an absorption edge with a small step size in energy, it is possible to obtain detailed information of the local structure and oxidation state of the element. This type of study can be divided into X-ray absorption near edge spectroscopy (XANES) and extended X-ray absorption fine structure (EXAFS). XANES focus on a short energy range close to (and including) the absorption edge, while EXAFS focus on the region at ~ 50 to >600 eV

above the absorption edge (Figure 3.4). In order to properly compare the XAS data between samples with different absorption coefficients and thicknesses it is common to normalise the data to the edge step so that the pre-edge line approaches 0 and the post-edge line approach 1 (Figure 3.4).

XANES provide information regarding the oxidation state of the measured element as the edge position changes slightly as a function of oxidation state. There are several different ways of determining the edge position. The procedure used in this thesis was to use the curve of the first derivative of the XAS data and extract the peak position of the peak corresponding to the absorption edge. Other features in the XANES region, like the pre-edge, provide information about the element's site symmetry and electronic structure (Figure 3.4b).

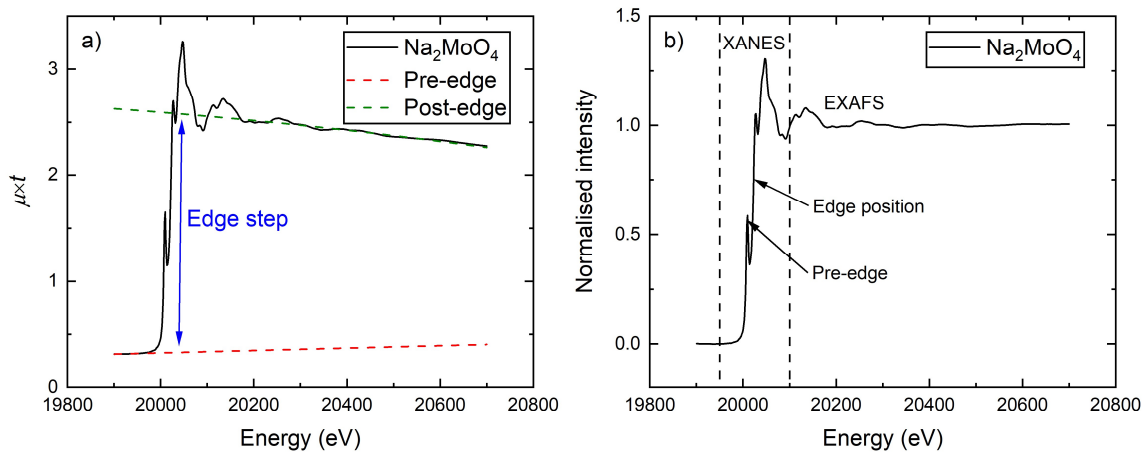


Figure 3.4: Experimental XAS data collect in transmission mode of a crystalline Na_2MoO_4 reference diluted in 20 wt% amorphous carbon (Super P) to allow sufficient X-ray transmission. a) Measured absorption through the sample presented as the absorption coefficient (μ) multiplied with the thickness of the sample (t) as a function of energy, including the edge step, pre- and post-edge lines used for normalisation. b) Normalised XAS graph indicating the XANES and EXAFS regions, the pre-edge and the edge position. The data are previously unpublished.

The EXAFS region provides information of the short range order around the absorbing element in terms of type, number and distribution of neighbouring atoms. The information comes from photoelectrons excited from the central atom that interacts with the neighbouring atoms and scatters back. These photoelectron interactions lead to constructive or destructive interference, and thereby creating the oscillatory part in the EXAFS region. An EXAFS spectrum in k space is analysed as the normalised absorption coefficient (χ), which is calculated from Equation 10.

$$\chi = \frac{\mu - \mu_0}{\Delta\mu} \quad \text{Equation 10}$$

Where μ is the measured absorption, μ_0 is the fitted background curve and $\Delta\mu$ is an estimation of the edge step. The photoelectron wave vector k is related to the photon energy E (Equation 11).

$$k = \sqrt{\frac{2m_e(E - E_0)}{h^2}} \quad \text{Equation 11}$$

Here m_e is the electron rest mass (9.11×10^{-31} kg), E_0 is the binding energy of the photoelectron and h is the Planck constant.

Because of the rapid dampening of the oscillatory signals in EXAFS, it is common to multiply χ with k , k^2 or k^3 in order to enhance the features at high k . The work presented in this thesis generally used k^2 (Figure 3.5a). By performing a Fourier transform (FT) of the k -weighted $\chi(k)$ into $\chi(R)$ it is possible to obtain a graph where the peaks are related to the atomic distances in the local environment around the central atom (Figure 3.5b). The R values for these peaks are not directly the real atomic distances (r), as obtained from PDF, but are typically shifted with 0.2–0.5 Å. This is why we use capital R and not r when discussing the FT EXAFS data in this thesis. By fitting the FT EXAFS curves it is possible to estimate the real r values.

Similarly to PDF there are some peaks that does not directly correlate to atomic distances (marked with * in Figure 3.5b). Some of them are due to limited data quality or data processing, but there are also several signals from non-single-scattering events, which complicates the analysis. This, together with the rapid dampening of the signal at higher R , makes it challenging to extract reliable data from outside the first coordination shell. Especially for samples containing several elements that lead to overlapping bond distances, like Na_2MoO_4 (Figure 3.5b).

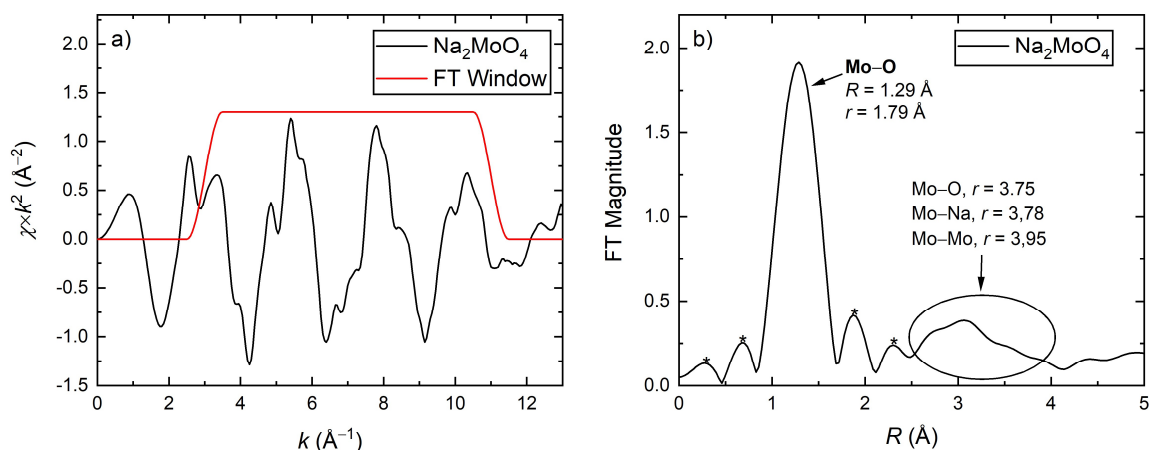


Figure 3.5: Experimental EXAFS data of Na_2MoO_4 mixed with 20 wt% amorphous carbon (Super P). a) $\chi(k)$ multiplied with k^2 to enhance features at high k values. The red curve marks the window used for the Fourier transform (FT) into R space. b) FT EXAFS showing peaks related to the atomic distances in Na_2MoO_4 , with Mo as the central atom. Capital R denote the values from the FT EXAFS, while r denote the theoretical bond lengths extracted from the crystal structure. * marks the peaks that does not correspond to atomic distances. The data are previously unpublished.

3.2.3 Scanning electron microscopy (SEM)

SEM provides images that can be used to study micro- and nanostructures in a material. An electron beam is scanned over the sample and the images are usually constructed by detecting the backscattered electrons (BSEs) or secondary electrons (SEs) that are ejected from the sample. BSEs are emitted from the sample due to elastic scattering of the incoming electrons when interacting with the atoms in the material. They have significantly higher energy than SEs, thus providing information from deeper in the sample. SEs are valence electrons emitted from inelastic collisions with the incoming

electron beam. They usually have an energy of <50 eV and are only detectable from the surface. Therefore, SEs are used to study the topography of the surface. SEs generated deeper than ~10 nm in the sample get absorbed, due to the limited energy, before they reach the detector.

3.2.4 Transmission electron microscopy (TEM)

A transmission electron microscope (TEM) can be operated with either a parallel beam irradiating an area of the sample or a focused beam that is scanned over the sample aiming at one point at a time, thus called scanning transmission electron microscopy (STEM) [169]. The STEM technique is similar to SEM, but mainly detects the transmitted signals induced by the electron beam. TEM can be used either to obtain a direct image of the sample, by displaying the image plane on the viewing screen or to study the diffraction of the sample in the back focal plane (Figure 3.6). The diffraction pattern provides information regarding the crystal structure, similar to XRD, while the direct image provides details of the particle morphology. With a well-prepared sample (thin and crystalline) and a good enough instrument, it is possible to obtain atomic resolution of the images.

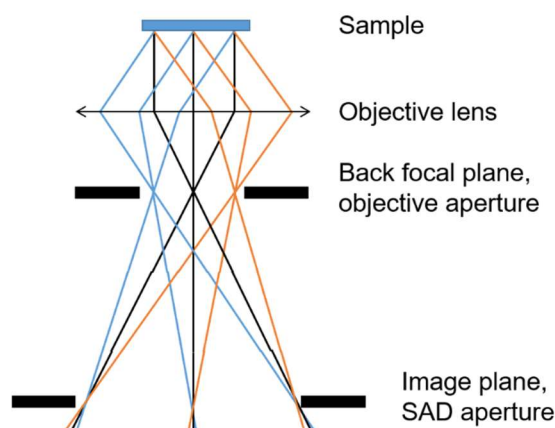


Figure 3.6: A simplified diagram of the electron beam transmitted through the sample in TEM with a parallel beam, marking the objective lens, the back focal plane with the objective aperture where a diffraction pattern is formed and the image plane with the selected area diffraction (SAD) aperture.

3.3 *Operando* X-ray characterisation

In order to fully understand the chemical processes occurring inside a battery during cycling it is essential to utilise *operando* characterisation (Paper 2). In an *operando* measurement, the studied battery should operate as close as possible to the real life use. However, with most techniques it is not possible to place an unmodified commercial battery cell into an X-ray beam and obtain detailed information of the atomic structure and morphology of the active materials in the electrodes. Therefore, modifications to the experiments are always made to obtain an acceptable compromise between realistic battery performance and data quality of the structural measurements.

In most cases, specialised *operando* cells with X-ray transparent windows are needed, and several designs have been developed and used (Paper 2). These cells might struggle to

obtain the same reliable performance as coin cells, and the background signals from the cell components reduce the quality of the X-ray signals. In addition, it is important with a decent time resolution of the X-ray measurements in order to determine when and how the chemical reactions progress in the battery during cycling. Reasonably powerful synchrotron radiation is often necessary for acquiring data of high quality with acceptable time resolution. However, it is important to not use too powerful X-ray radiation as that can induce beam damage and alternate the chemistry in the cell.

Despite these challenges, *operando* measurements are in general superior to *ex situ* experiments, where the material is extracted from the cell. When performing *ex situ* measurements, there is a risk that the sample reacts during sample preparation and no longer represents the real system (Paper 2). This can lead to misleading or wrong conclusions. It is also time consuming to prepare a sufficient amount of *ex situ* samples to obtain satisfactory insight into the cycling mechanism, as several samples per (de)sodiation cycle is needed. Another advantage of *operando* characterisation is that the same sample is studied through the whole measurement. Therefore, all measurement points are directly comparable to each other with regards to intensity of the measured signal, after correcting for possible changes in intensities of the incoming beam. When comparing different *ex situ* samples, it is difficult to trust small changes in intensities as the samples may have different packing densities and may have been extracted from different regions of the electrodes, which could affect the results.

However, *ex situ* samples generally lead to stronger X-ray signals with fewer background components and it is easier to interpret and trust the data, given that the sample has not reacted. Therefore, it is favourable to include *ex situ* measurements to support the observations in the *operando* data. The combination of *ex situ* and *operando* measurements is especially important for techniques like PDF and EXAFS where it could be difficult to separate the signal of your active material from other contributions.

3.4 Experimental details

Most of the experimental details for this thesis are presented in Papers 3–5. This chapter presents additional details for results that are included in this thesis and are complementary to what was presented in the papers. The procedures for preparation of electrode sheets and cell assembly are described in general terms. For detailed overview of all the samples and procedures, see the data archive for the Nanoname project at dataverse.no [170].

3.4.1 Chemicals

$\text{Bi}_2\text{Al}_6\text{O}_{12}\times\text{xH}_2\text{O}$ (99.9%), Bi_2O_3 (99.8%), NaClO_4 (98%), titanium(IV)butoxide (97%), Na-metal blocks, citric acid (99.5%), carboxymethylcellulose sodium salt (CMC, Sigma-Aldrich), dimethyl carbonate (DMC, 99%), N-methyl-2-pyrrolidone (NMP, 99.5%), ethylene carbonate (EC, 99%), diethyl carbonate (DEC, 99%), propylene carbonate (PC, 99.7%), fluoroethylene carbonate (FEC, 99%) were purchased from Sigma Aldrich. Super P was bought from Timical, Kynar polyvinylidene fluoride (PVDF) from Arkema, $\text{Na}_2\text{Fe}[\text{Fe}(\text{CN})_6]\times 2\text{H}_2\text{O}$ (Fennac) from Altris, BiVO_4 (99.9%) from Alfa Aesar, HNO_3 (69%)

from VWR, double-sided dendritic Cu foil (99.9%, 10 μm thick) from Schlenk and NaPF_6 from Fluorochem. Distilled H_2O (Resistivity $>1 \text{ M}\Omega \text{ cm}^{-1}$) was produced in the home lab facility at UiO.

Na, DMC, DEC, EC, PC, FEC, NaClO_4 , NaPF_6 and Fennac were stored in an Ar-filled glovebox (M-Braun). The H_2O and O_2 levels in the glovebox were usually $<0.1 \text{ ppm}$, but occasionally the levels were unintentionally elevated due to maintenance or user errors. This was probably the case during preparation of Electrolyte 2 and could explain its poor performance (Section 4.1.1). NMP was stored in a chemical cabinet with a protective cap. All chemicals were used as purchased without any further purification or treatments, unless specified in the following sections.

3.4.2 Synthesis

The synthesis procedures of Bi_2MoO_6 and BiFeO_3 are presented in Paper 3 and Paper 4, respectively. Commercial BiVO_4 was mixed with Super P in a 7:3 ratio and ball milled for 2 h in a Pulverisette P7 premium line ball mill. $\text{Bi}_4\text{Ti}_3\text{O}_{12}$ was synthesised by mixing 4.35 g (12.8 mmol) titanium(IV)butoxide with 150 g citric acid and heating the mixture in a beaker on a hotplate set to $300 \text{ }^\circ\text{C}$ with a magnetic stirrer until the citric acid melted. Then 2.98 g (8.5 mmol) of Bi_2O_3 were dissolved in 20 mL of concentrated HNO_3 , which was added to the solution dropwise. Following this, the solution was transferred to a shallow ceramic container. The solution was kept under stirring and heating at $200 \text{ }^\circ\text{C}$ until the mixture became a very viscous liquid. Then it was transferred to a heating cabinet set to $180 \text{ }^\circ\text{C}$ and dried overnight in the ceramic container, which was covered by Al foil with small holes. The sample was then calcined at $400 \text{ }^\circ\text{C}$ for 12 hours the following day.

3.4.3 Electrode preparation and cell assembly

Slurries of Bi metallates were prepared by mixing 80 wt% of active material with 10 wt% binder and 10 wt% Super P together with 1–3 mL of solvent. The total dry mass of the slurries was in the range of 0.1–1.0 g. Two different binder-solvent systems were used: PVDF-NMP and CMC- H_2O . The slurries were mixed in a Thinky mixer (ARE 250) with a procedure consisting of a mixing step of 3–5 min at a speed of 2000 rpm followed by a defoaming step of 1.5–2.0 min at 750 rpm. This mixing procedure was repeated if necessary to obtain a homogenous slurry.

The slurries were coated onto dendritic Cu foil with a coating height of 50–1000 μm and was further dried overnight in air. 15 mm discs were cut from the electrode sheets the following day before drying in a Büchi oven at $60\text{--}80 \text{ }^\circ\text{C}$ in dynamic vacuum for 3–6 h. After cooling to room temperature, the electrodes were transferred to the glovebox for coin cell assembly. Electrode preparation of Fennac-based cathodes was performed in a similar manner, except for an active material:carbon:binder ratio of 85:15:10, coating on carbon-coated Al foil and drying in Büchi oven at $140 \text{ }^\circ\text{C}$ overnight.

The electrolytes used in this thesis were prepared and stored inside the glovebox. All electrolytes were prepared by mixing NaPF_6 or NaClO_4 into 1:1 mixtures of EC:DMC, EC:DEC or simply in PC. The EC had to be heated on a hotplate at $50 \text{ }^\circ\text{C}$ to melt before

mixing with DMC or DEC. 5 vol% of FEC was added to each electrolyte and all electrolytes had a salt concentration of 1 M.

Coin cells (CR2032, stainless steel, 304, Pi-Kem) and *operando* cells were assembled in either half-cell configuration with metallic Na as the counter electrode or in full cells with Fennac as cathode. The Na electrodes were prepared by cutting Na chunks into smaller pieces, which were rolled flat and stamped into 14 mm discs. The discs were then brushed on each side with a toothbrush (medium, First Price) to ensure a fresh surface. The half cells were assembled with the Na electrode in the anode casing, followed by separator (Whatman GE, 16–18 mm in diameter), wetted with 80 μl of electrolyte and the Bi-metallate electrode. In coin cells a spacer, a spring wafer and the cathode casing was added before it was closed and sealed using an automatic coin cell crimper (Hohsen). Full cells were assembled in the same way, except that the Bi-metallate electrode was placed in the anode casing and the Fennac electrode was placed in the cathode casing. We used two different *operando* cells in this study named “piston cell” (Figure 3.7a) [171] and “Swagelok cell” (Figure 3.7b) [172]. The piston cell had glassy carbon windows attached with silver paste and the Swagelok cell used Kapton windows glued with epoxy.

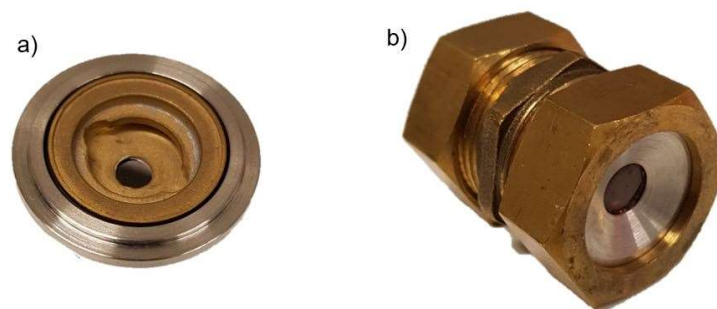


Figure 3.7: Images of *operando* cells used in this thesis. a) Piston cell and b) Swagelok cell.

3.4.4 Characterisation

Galvanostatic cycling (GC) measurements were performed with several different battery cyclers: MPG2 (Biologic), SP150 (Biologic), CT-4008T-5V10mA-164 (Neware, named Neware1), MIHW-200-160CH (Neware, named Neware2) and Battsmall (Astrol). The measurements were performed with a voltage range of 0.01–2.00 V, except when stated otherwise in the text, and current densities of 0.1 or 1 A g⁻¹. Some measurements included an initial 12 h rest to let the open circuit voltage (OCV) stabilise before cycling.

Operando XRD measurements of Bi-based electrodes were performed at the ID15A beamline at the European Synchrotron Radiation Facility (ESRF). The wavelength of the beam was 0.1425 Å, the beam size was 125×150 μm and we used a Pilatus CdTe 2M detector from DECTRIS. The piston cell used for this measurement was assembled in the home lab at UiO 1 week before the first measurements and transferred to the ESRF in Grenoble in a sealed coffee bag. The cell did not work during an initial electrochemical test, probably due to leakage of electrolyte. Therefore, we opened the cell inside a glovebox in Grenoble added more electrolyte and transferred it back to the beamline before the measurements. In the first *operando* measurement the beam was focused on a single point of the cell, leading to beam damage that inhibited the electrochemistry in that

point. The following measurement was performed by mapping a larger area with grid scans of 32×40 steps (1280 pixels) with increments of 0.1 mm horizontally and 0.05 mm vertically. Each grid scan took ~8 min and scanned a total rectangular area of 3.2×2 mm.

The combined *operando* XRD/XAS measurements presented in this thesis were performed at beamline BM31, which is a part of the Swiss-Norwegian Beamlines (SNBL) at ESRF. We used a DEXELA detector and monochromatic radiation with a wavelength of 0.3396 Å for the XRD measurements. The visualisation of the 2D diffraction data was done in FIEWER. The XAS measurements of the Bi L3 edge and Mo K edge were performed in transmission mode with ion chamber detectors in the energy range of 13.3–13.6 keV for the Bi edge and 19.9–20.2 keV for the Mo edge. A step size of 0.3 eV was used together with a 200 ms exposure resulting in a scan time of 3 min and 20 s per edge.

Electrodes used for preparation of *ex situ* samples for TEM measurements were cycled at 0.1 A g⁻¹ between 0.01–2.00 V until the desired stage of cycling before disassembly with a coin cell disassembling tool (Hoshen) inside the glovebox. The electrodes were carefully extracted from the disassembled batteries, cleaned with 0.5 mL DEC per electrode and dried for 1 h inside the glovebox. Following this, the electrode material was scraped from the Cu foil, ground carefully in a mortar and sprinkled onto a Cu grid with holey carbon. The samples were exposed to air for <5 min during transfer to the TEM. Pristine Bi₂MoO₆ powder was directly sprinkled onto the Cu grid before measurement. The TEM experiments were conducted at The Norwegian Centre for Transmission Electron Microscopy (NORTEM) with the Titan Themis microscope (FEI Company) in STEM mode. The images were collected with an acceleration voltage of 300 kV and a dark field detector (DF4).

4. Results

4.1 Benchmarking and experimental challenges

From the experimental work leading up to this dissertation, there were many interesting results that did not fit into the papers. Among these are benchmarking studies that were important for designing the final experiments. The most relevant of these results are presented in this chapter, which contains a discussion regarding how different parameters affect the electrochemical performance and experimental challenges that had to be solved or avoided. The experimental challenges include electrochemistry in *operando* cells, strong scattering effects from Na counter electrode and beam damage. Most of the results presented here are previously unpublished and contribute to a better understanding of the experimental choices and results presented in Paper 3–5 and later in this thesis.

4.1.1 Parameters affecting electrochemical performance

Throughout the work leading up to this thesis, a large amount of coin cells were assembled and tested, providing useful information of which factors had a significant impact on the electrochemical performance of the Bi metallates. Before assessing the effect of changing certain parameters, it is important to have an estimate of the natural spread in the measurements due to human error and non-controllable parameters. One of the known uncertainties comes from weighing of the electrodes as the scale has an intrinsic uncertainty of ± 0.1 mg, which in practice could be even higher when weighing inside the glovebox. In order to determine the standard deviation of our measurements, we analysed the performance of 120 coin cells that should have been identical (Figure 4.1 and Table 4.1).

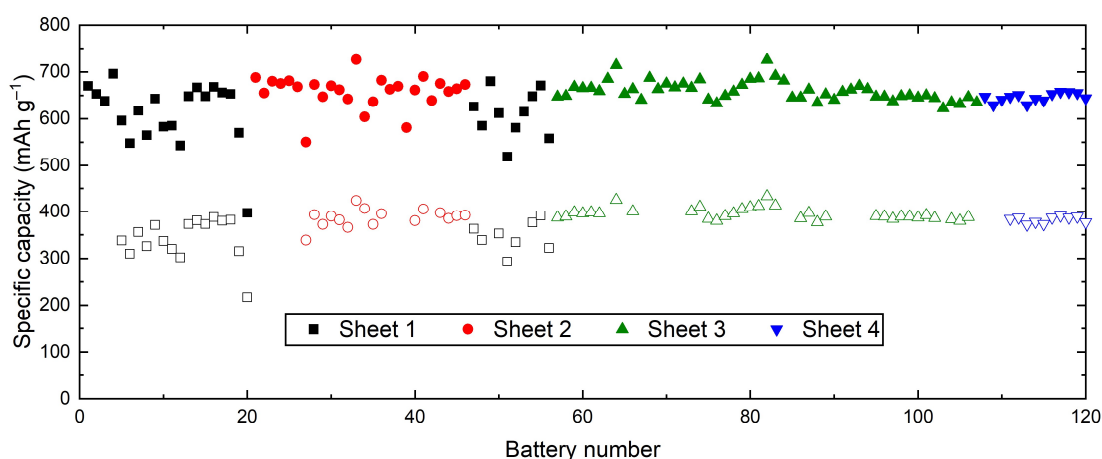


Figure 4.1: Specific capacities from the 1st (filled symbols) and 2nd sodiation (empty symbols) obtained from GC measurements of 120 coin cells that were supposed to be identical, visualising the uncertainties in the measurements. The Bi₂MoO₆-based electrodes in the batteries were extracted from four electrode sheets that were prepared using the same procedures.

The 120 coin cells were selected from four electrode sheets, with Bi₂MoO₆ as active material from two batches synthesised with the same procedure. Sheet 1 and 2 contained Bi₂MoO₆ from the first synthesis batch and Sheet 3 and 4 from the second batch. The

procedures for electrode preparation, coin cell assembly and electrochemical measurements were the same for all the selected coin cells. Cells with an initial OCV lower than 2 V was removed from the selection as outliers, since the low initial OCV indicated an error in the cell assembly. For simplicity, only the specific capacities of the 1st and 2nd sodiation were evaluated. The average values for the specific capacities and the standard deviation were calculated for each of the electrode sheets and for all the coin cells in total (Table 4.1).

Table 4.1: Average specific capacities for the 1st and 2nd sodiation of batteries with Bi₂MoO₆ electrodes that were supposed to be identical, with calculated sample standard deviation (STDEV.S) and percentages (STDEV.S/average). Numbers are provided for each of the four electrode sheets and for all the batteries in total.

Electrode sheet	Name in lab journal	Sodiation no.	Average (mAh g ⁻¹)	Standard deviation (mAh g ⁻¹)	Percent (%)
Sheet 1	AB_T_080	1 st	611	62	10
		2 nd	343	40	12
Sheet 2	AB_T_094	1 st	658	35	5
		2 nd	387	19	5
Sheet 3	AB_T_102	1 st	659	21	3
		2 nd	395	13	3
Sheet 4	AB_T_108	1 st	646	10	1
		2 nd	383	7	2
Average of all coin cells		1 st	645	42	7
		2 nd	377	32	9

There were some small variations between the different electrode sheets, but in total the uncertainties were slightly below 10%. This means that a changing parameter needs to induce a reproducible difference larger than 10% in the specific capacity to count as a significant effect. One interesting observation is that the standard deviation for the assembled batteries seems to decrease with time, showing that increased experience in electrode preparation and cell assembly could lead to more reliable experiments (Figure 4.1).

During the experiments, we noticed a significant difference between two batches of the same type of electrolyte (1 M NaPF₆ in PC +5% FEC). One of the batches showed worse performance (named Electrolyte 2) than the other batch, which behaved normally (Electrolyte 1). Electrolyte 2 had probably reacted with moisture. It showed similar performance as Electrolyte 1 in coin cells cycled at 0.1 A g⁻¹ with only slightly lower capacity (Figure 4.2a, b and d). However, the overpotentials for the redox reactions (visible in the (de)sodiation curves) were significantly higher for Electrolyte 2. At increased current densities (1 A g⁻¹) the overpotentials became so large that the capacity was massively reduced (Figure 4.2a, c and e). This shows the importance of always testing the electrolyte properly after preparation to ensure it leads the targeted performance.

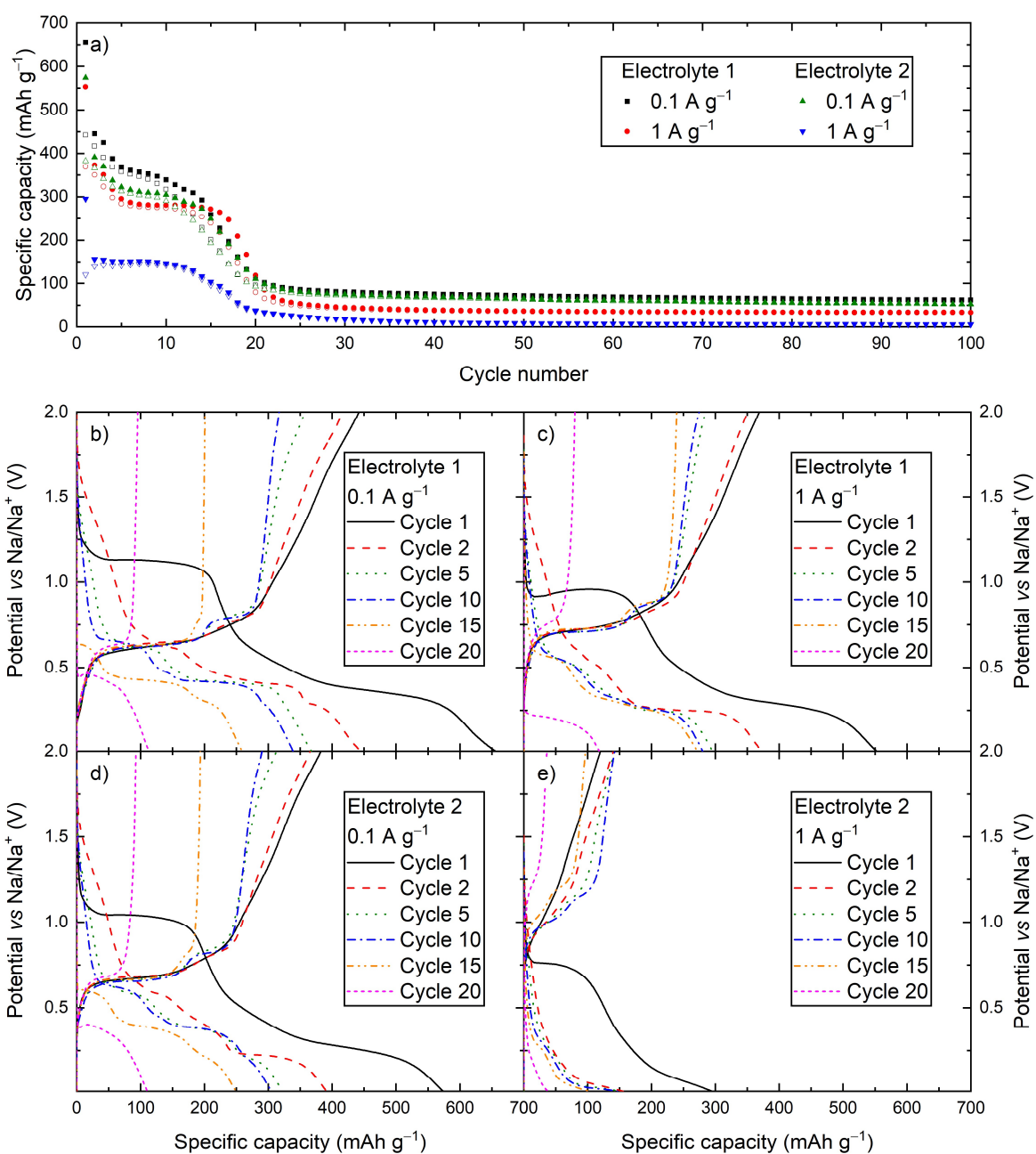


Figure 4.2: GC measurements of Bi_2MoO_6 with two different batches of electrolyte: Electrolyte 1 (good) and Electrolyte 2 (bad). a) Specific capacity per cycle plot from measurements of the two electrolytes at 0.1 A g^{-1} and 1 A g^{-1} , filled symbols correspond to sodiation and empty symbols correspond to desodiation. b), c), d) and e) selected (de)sodiation curves from the measurements. Details are provided in the legends.

In an attempt to improve the electrochemical performance of the Bi metallates, we changed several parameters and evaluated their effect. These parameters include type of electrolyte, amount of electrolyte, type of binder, thickness of electrode, synthesis conditions for Bi_2MoO_6 , cycling rate, resting step and voltage range (Table 4.2).

Different electrolyte compositions have shown a significant effect on the performance of certain battery materials [142]. In order to determine whether or not replacing the electrolyte could improve the performance of Bi metallates, we tested 6 different

electrolytes with our reference system: BiVO₄:C anodes based on commercial BiVO₄ that was ball milled with Super P. Two different salts, NaClO₄ and NaPF₆, and 3 different combinations of solvents, EC:DMC, EC:DEC and PC, were tested. All electrolytes had a salt concentration of 1 M and 5 vol% of FEC as an additive.

The statistics in this dataset is limited (2–5 coin cells per electrolyte system), which would mean that the difference in performance should be significantly larger than our estimated uncertainty of ~10% to be trustworthy. There were some small differences in performance between the different electrolytes, but also between batteries tested with the same electrolytes. One representative measurement from each electrode are shown in Figure 4.3 and the differences are too small to be deemed significant. The set of electrolytes tested here are similar in nature, as they are all based on carbonated solvents, while other electrolytes (*e.g.* ionic liquids or glyme based) could potentially show a significant difference.

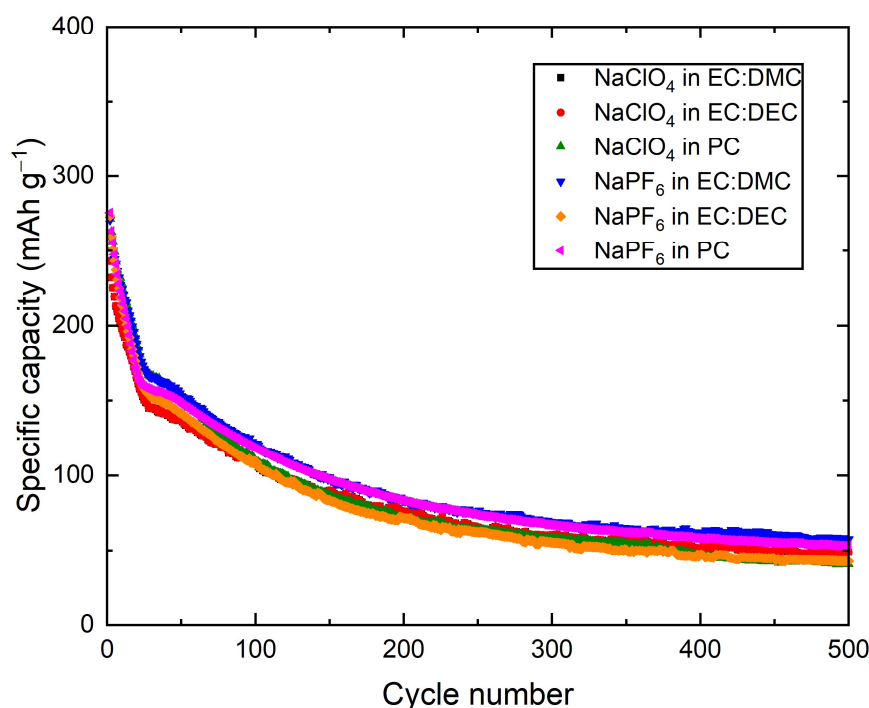


Figure 4.3: Capacity per cycle plot from testing of different electrolytes with BiVO₄:C anodes cycled in half cells vs Na metal with a voltage range of 0.01–2.00 V and a current density of 0.1 A g⁻¹.

Changing the cycling conditions of the coin cells had a significant impact on the materials' behaviour. The well-known effect of loss in performance including increased overpotential when increasing the current density is present also for Bi metallates, even though the effect is smaller than for most materials (Figure 4.4a and Section 4.2.3). A larger effect was observed when changing the cut-off voltage and thereby removing certain reactions from the cycling scheme (Paper 4 and Paper 5). Removing the NaBi \rightleftharpoons Na₃Bi reaction by increasing the lower cut-off voltage to 0.50 V increased the cycling stability slightly, but limited the capacity to such a degree the overall performance was worse than at normal cycling conditions (Figure 4.4a, d and e).

On the other hand, reducing the upper cut-off voltage to 0.70 V, thus avoiding the $\text{Bi} \rightleftharpoons \text{NaBi}$ reaction and isolating the $\text{NaBi} \rightleftharpoons \text{Na}_3\text{Bi}$ reaction, led to a drastic improvement of the cycling stability. The reduced cut-off voltage limited the reversible capacity to $\sim 200 \text{ mAh g}^{-1}$, but the increased cycling stability lead to improved overall performance after 20 cycles compared to normal cycling between 0.01–2.00 V (Figure 4.4a and b). At 1 A g^{-1} the isolated $\text{NaBi} \rightleftharpoons \text{Na}_3\text{Bi}$ reaction (cycling between 0.01–0.80 V) maintained the capacity even better than the measurement at 0.1 A g^{-1} (Figure 4.4a and c). The same effect was observed for BiFeO_3 (Paper 4), and it is natural to think that this could be a common feature for Bi-based materials in general.

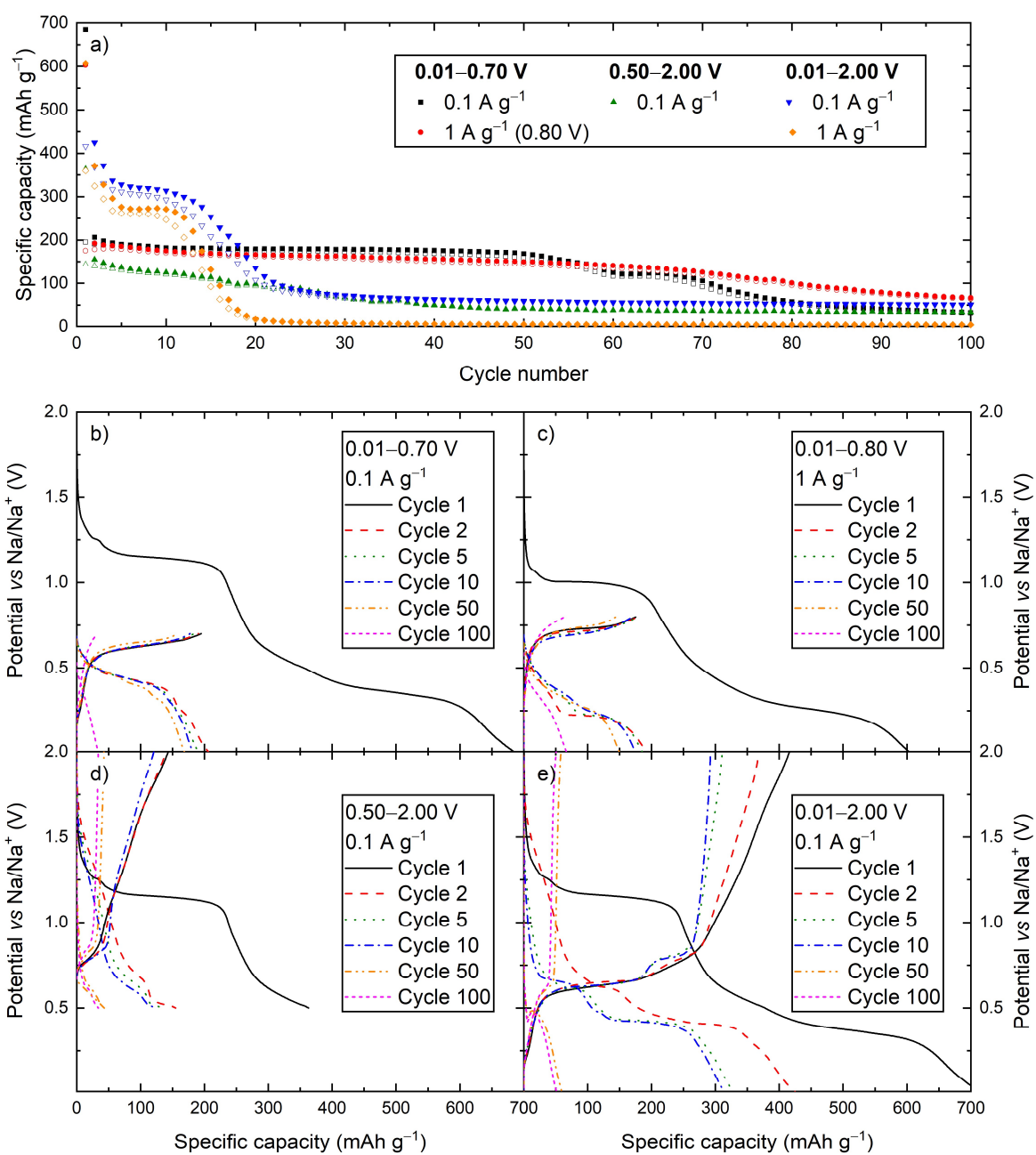


Figure 4.4: a) Capacity per cycle plots and b-e) (de)sodiation curves derived from GC measurements of Bi_2MoO_6 at different cycling conditions (specified in the legends). Retrieved from Paper 5.

The difference in performance between measurements at 0.1 and 1 A g⁻¹ for Bi₂MoO₆ was minimal. However, when increasing the current density even more, to 5 A g⁻¹, the specific capacities of the material were much lower (~100 mAh g⁻¹ at 2nd sodiation) as the upper limit of what the battery could handle was reached. The effect of resting the coin cells for 12 h, in order to let the OCV stabilise, before starting the GC measurements had no significant effect on the measured specific capacity: the difference between the average of the capacities of the two data sets were less than 1%.

Using CMC as binder and H₂O as solvent instead of PVDF and NMP in the electrode fabrication could possibly have a significant effect on the electrochemical performance. The batteries with CMC/H₂O in the active electrodes showed on average 18% higher specific capacity for the 2nd sodiation compared to electrodes with PVDF/NMP. However, this is based on comparison of only two batteries per binder system and a larger dataset with better statistics would be needed to prove this.

Increasing the thickness of the electrode could in principle reduce the measured specific capacity significantly, as it will be more difficult to utilise all the active material in thicker electrodes. In this study, we have tested electrodes that have been coated with wet thicknesses between 50–1000 μm (resulting in active mass loading per electrode of 0.6–13.3 mg). Within this range of thicknesses and active masses, there were no clear significant changes in performance, meaning that Bi metallates (at least Bi₂MoO₆) is not very sensitive to scaling up the electrode thickness. The thickest electrodes showed some indications of reduced performance, particularly at higher rates, but the statistics are not sufficient to draw any clear conclusions. If we would continue to increase the thickness of the electrodes to the extreme, we would of course reach a point where the performance would decrease.

When comparing the specific capacities measured from the electrodes with the lowest mass loadings, it was possible to find differences larger than the 10% limit we set earlier. However, the intrinsic uncertainty of at least ±0.1 mg for weighing the electrodes have a much larger impact on the uncertainty of the specific capacity obtained from thinner electrodes: for an electrode with 0.6 mg of active material the weighing uncertainty in itself is 17%. Therefore, the specific capacities for the thinnest electrodes are not accurate.

Varying the amount of electrolyte between 80–120 μL did not have any significant effect on the performance (Paper 3), but going to very low amounts is expected to induce some problems for the electrochemistry. Varying the time (15 min to 24 h) and temperature (160–200 °C) for the solvothermal synthesis of Bi₂MoO₆, did have some impact on both the crystal structure and electrochemistry (Paper 3). However, it did not show any drastic change in the overall performance. In summary, it was only the reduction of the upper cut-off voltage and isolation of the NaBi ⇌ Na₃Bi that provided a significant improvement of the performance of the Bi metallates.

Table 4.2: List over changing parameters throughout the study and comments regarding their effect on the electrochemical performance of Bi metallates.

Parameter	Conclusion
Different electrolytes	No significant effect (except for bad batch).
Binder (CMC/H ₂ O vs PVDF/NMP)	Possible effect, but limited data.
12 h rest for coin cell before measurement	No significant effect.
Wet thickness of electrode	Possible effect, but limited data.
Amount of electrolyte	No significant effect (Paper 3).
Synthesis conditions (time and temperature) for Bi ₂ MoO ₆	Small change, but not significant for overall performance (Paper 3).
Cycling rate	No significant effect on capacity from 0.1 to 1 A g ⁻¹ , but increase in overpotential. Significantly reduced capacity at 5 A g ⁻¹ .
Different cut-off voltages	Cycling between 0.01–0.70 V provides significantly better cycling stability.

4.1.2 Lessons learned from *operando* X-ray characterisation and TEM

There are several experimental challenges that could occur during *operando* X-ray measurements: obtaining reliable electrochemistry in *operando* cells, strong X-ray scattering from the Na-metal counter electrode and beam damage (Paper 2). This section presents our experiences with these challenges from the experimental work leading to this thesis, in addition to observed beam damage during TEM measurements.

In the present PhD work, two different *operando* cells were employed: piston cell [171] and Swagelok cell [172] (Figure 3.7 in Section 3.4.4). The piston cell has conductive glassy carbon windows that are glued to the cell parts with silver paste to ensure electronic conductivity. It was difficult to create a good seal with the silver paste and there were several cases of cells visibly leaking electrolyte. However, for the materials tested in this thesis most of the cells showed sensible electrochemistry, regardless of leaking electrolyte, indicating that this was not a major problem.

The largest problem encountered with the piston cells was that we did not obtain reliable electrochemistry for cathode materials, as the cells usually did not manage to reach a voltage higher than ~3 V during the first charge. Despite several experiments assessing the electrochemical contribution from air exposure, stack pressure, silver paste and glassy carbon, we were not able to find the root of this problem and solve it. Therefore, all presented data from piston cells are from measurements in half cells cycled to a maximum voltage of 2.00 V vs Na/Na⁺.

Swagelok cells with Kapton windows (glued with epoxy) worked fine for cathode materials and was significantly less prone to electrolyte leakage. These cells were used in several successful *operando* XRD and XAS measurements for some time, for example the measurements presented in Figure 4.5. However, after extensive use, the flexibility of the

Kapton windows led to a lack of pressure in the cell followed by inactivity in the region of the cell covered by the X-ray windows. This meant that the electrochemistry in ~70% of the cell worked fine, while the area that was measured with X-rays was inactive. Hence, no changes in the diffraction pattern was observed. Because of these issues with the Swagelok cells, we mostly used the piston cells and focused on half-cell measurements of anode materials.

Another challenge that was encountered during *operando* measurements was strong scattering effects from the Na-metal counter electrode, which created problems for both XRD and XAS data. When Na metal was cut from a block and flattened by rolling just once the resulting electrode consisted of large crystalline domains. These domains resulted in strong Bragg spots in the 2D XRD data, instead of rings that are typical for powders. In the worst cases, the X-ray scattering from the Na electrode was so strong that it acted as a secondary X-ray source, meaning that some of the Bragg spots from Na created their own set of diffraction rings centred around themselves (Figure 4.5a).

This effect did not only disturb the diffraction data, but also had an impact on the absorption measurements. *Operando* XAS measurements of the Bi L3 edge during (de)sodiation of Bi_2MoO_6 showed clear peaks in the XANES spectra that shifted in energy between each scan (Figure 4.5b). These shifting peaks made it impossible to extract reliable data from the EXAFS region of the spectra, and made the XANES data challenging to analyse. One way to avoid these problems is to use a full-cell configuration with a powder-based cathode, thus removing the Na-metal electrode (Figure 4.5c). Another strategy is to flatten and fold the Na metal many times (>10) to make it more polycrystalline, thus removing the strongest Bragg spots. This last procedure was chosen for the *operando* measurements presented in Paper 3–5.

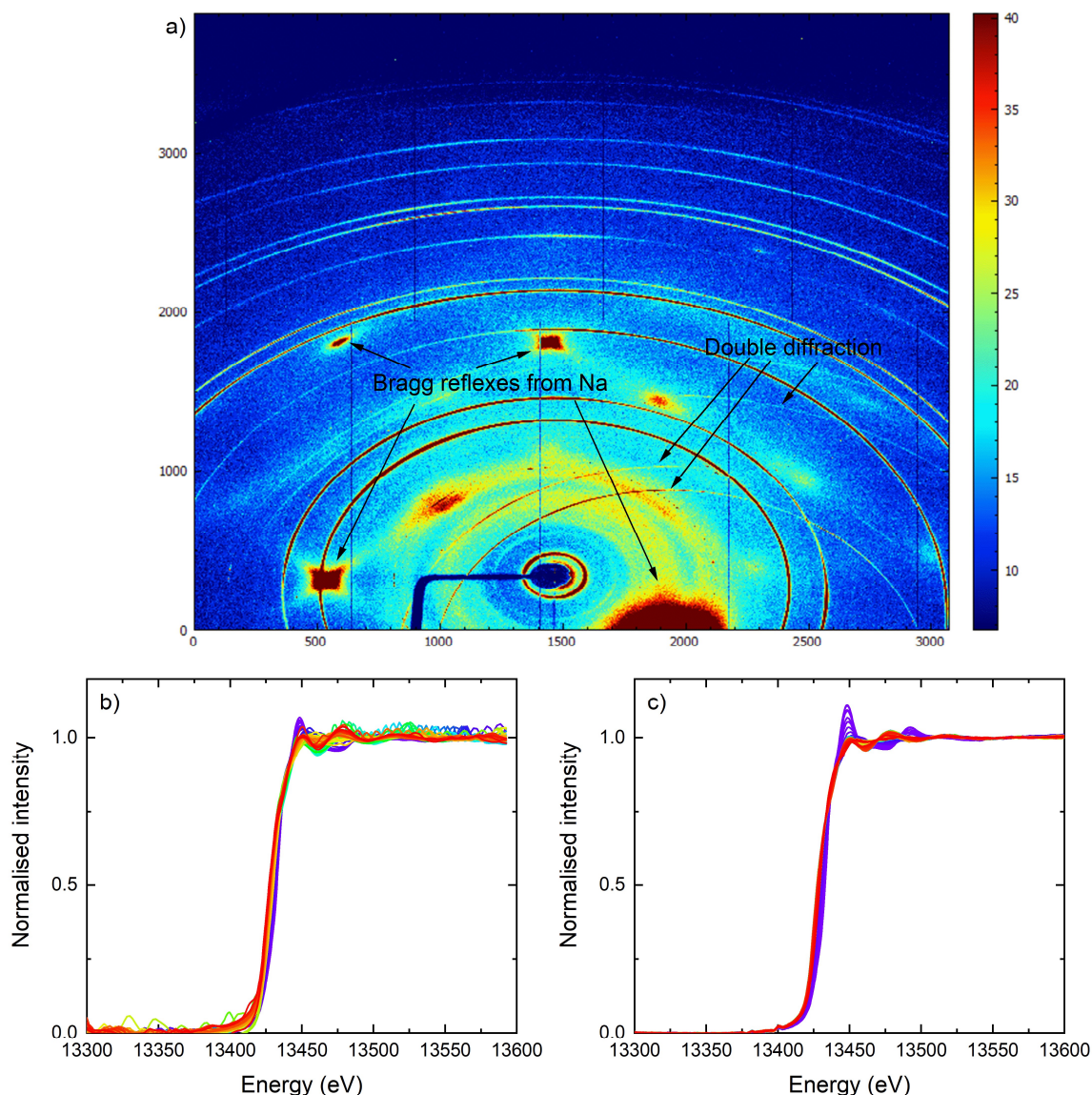


Figure 4.5: Data from combined *operando* XRD/XAS measurements, illustrating the problem with strong X-ray scattering from the Na counter electrode. a) 2D image of a diffraction pattern showing strong Bragg reflexes from Na, where the strongest reflex acts as a secondary source creating extra diffraction rings centred on itself. b) *Operando* XANES of the Bi L3 edge measured on a Bi_2MoO_6 -based electrode in half cell configuration vs Na metal, showing irregular peaks above and below the absorption edge that are moving during the measurement. c) *Operando* XANES on the Bi L3 edge on Bi_2MoO_6 -based electrode in full cell configuration vs Fennac as cathode.

An issue of beam damage was encountered at the ID15A beamline at ESRF, where the X-ray beam altered the electrochemistry in an *operando* XRD/PDF measurement on Bi metal. The beamline had recently gone through an upgrade leading to a very intense beam with a flux of $\sim 10^{14}$ photons/s/mm². In the initial *operando* experiment, the sample was kept stationary and the measurement was performed in a single point of the *operando* cell. Even though the data showed sensible chemical changes during the first sodiation, the observed phase transformations quickly deviated from the electrochemistry (Figure 4.6a–b). This indicated that the electrochemistry of the measured area did not behave

properly, even though the rest of the cell worked fine according to the (de)sodiation curves (Figure 4.6b).

This observation, led us to moving the cell in a grid scan of 32×40 steps (1280 pixels) with increments of 0.1 mm horizontally and 0.05 mm vertically. With this strategy, each measured point did not receive too much beam exposure and we could collect data from almost the whole part of the cell that was covered with glassy carbon windows. This measurement tactic worked successfully, and by averaging the XRD data from all the pixels, we obtained a sensible *operando* XRD data set that followed the electrochemistry (Figure 4.6c–d). The electrochemistry in the cell became noisy towards the end of the measurement, due to the failed initial tests and possibly leakage of electrolyte.

This measurement provided XRD data in all the pixels of the scanned area, allowing us to locate the alloying particles and observe how they changed during cycling. By selecting the main peak of h-Na₃Bi as a region of interest in the XRD patterns and plotting the intensity of this peak from all the pixels of the grid scans, we obtained maps of the whole scanned area showing the distribution of h-Na₃Bi in the electrode (Figure 4.6e–f). In the first full grid scan (scan no. 2) there were some h-Na₃Bi present as a result of the initial electrochemical cycling tests (Figure 4.6e), but at full sodiation (scan no. 15) the alloying particles contained significantly more h-Na₃Bi (Figure 4.6f). These maps also showed areas with almost no intensity in the XRD signals, proving that the distribution of the active material in the electrode was not homogeneous.

The results from the measurements at ID15A showed that beam damage could be a big problem when using a very intense X-ray beam. The exact reason why the electrochemistry failed in the measured area when aiming at one single point was not confirmed, but damage to the electrolyte in the irradiated area is one possible explanation [173]. In the *operando* measurements performed at BM31, we did not notice any problems with beam damage, even when the beam was aimed at one single point of the cell. The explanation for this is that BM31 has a much less intense beam (flux of $\sim 10^{10}$ photons/s/mm²), thus limiting the possibilities for beam damage.

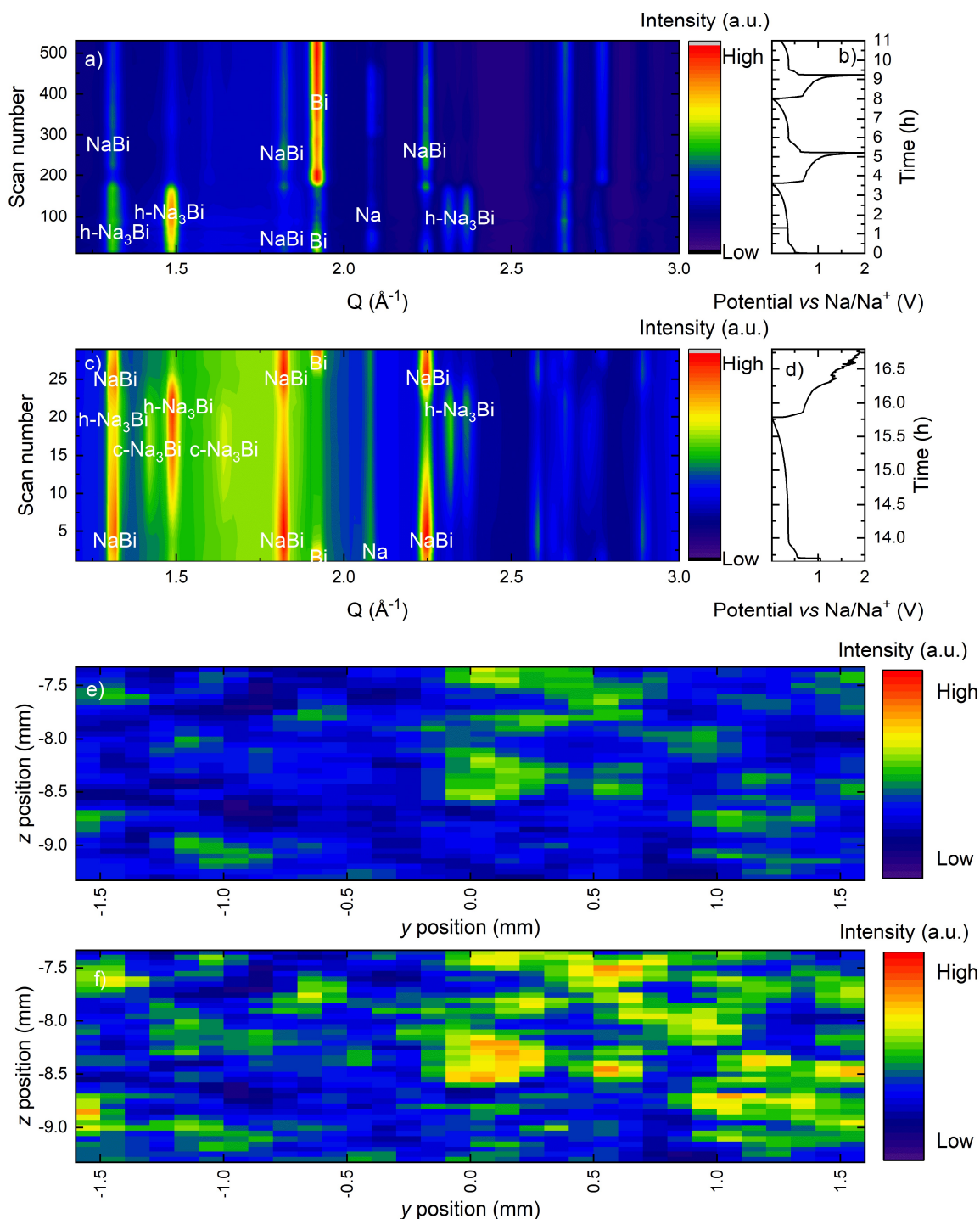


Figure 4.6: Operando XRD on a Bi-based electrode measured at (a–b) one point in the cell vs (c–d) average of grid scans. Full grid scans showing the intensities of the main $h\text{-Na}_3\text{Bi}$ peak in each pixel at e) scan no. 2 and f) scan no. 15.

Another example of beam damage, this time from an electron beam, was observed during TEM measurements. The idea behind the TEM experiments was to accurately measure the size of the Na_xBi particles embedded in a Na-Mo-O matrix as a result of (de)sodiation of Bi_2MoO_6 . However, the beam damage and air sensitivity of the cycled samples made these

results less trustworthy than the estimations from XRD/PDF. The TEM results were, therefore, omitted from the papers.

The clearest example of electron-beam damage was observed during imaging of pristine Bi_2MoO_6 powder. When studying the nanoplatelets of Bi_2MoO_6 , we observed formation of Bi particles from the platelets after only a few seconds, as a result of the reducing electron beam. These particles coalesce into larger particles during exposure of only a few minutes (Figure 4.7). This showed that even for the pristine material it was difficult to obtain reliable TEM images at high magnification.

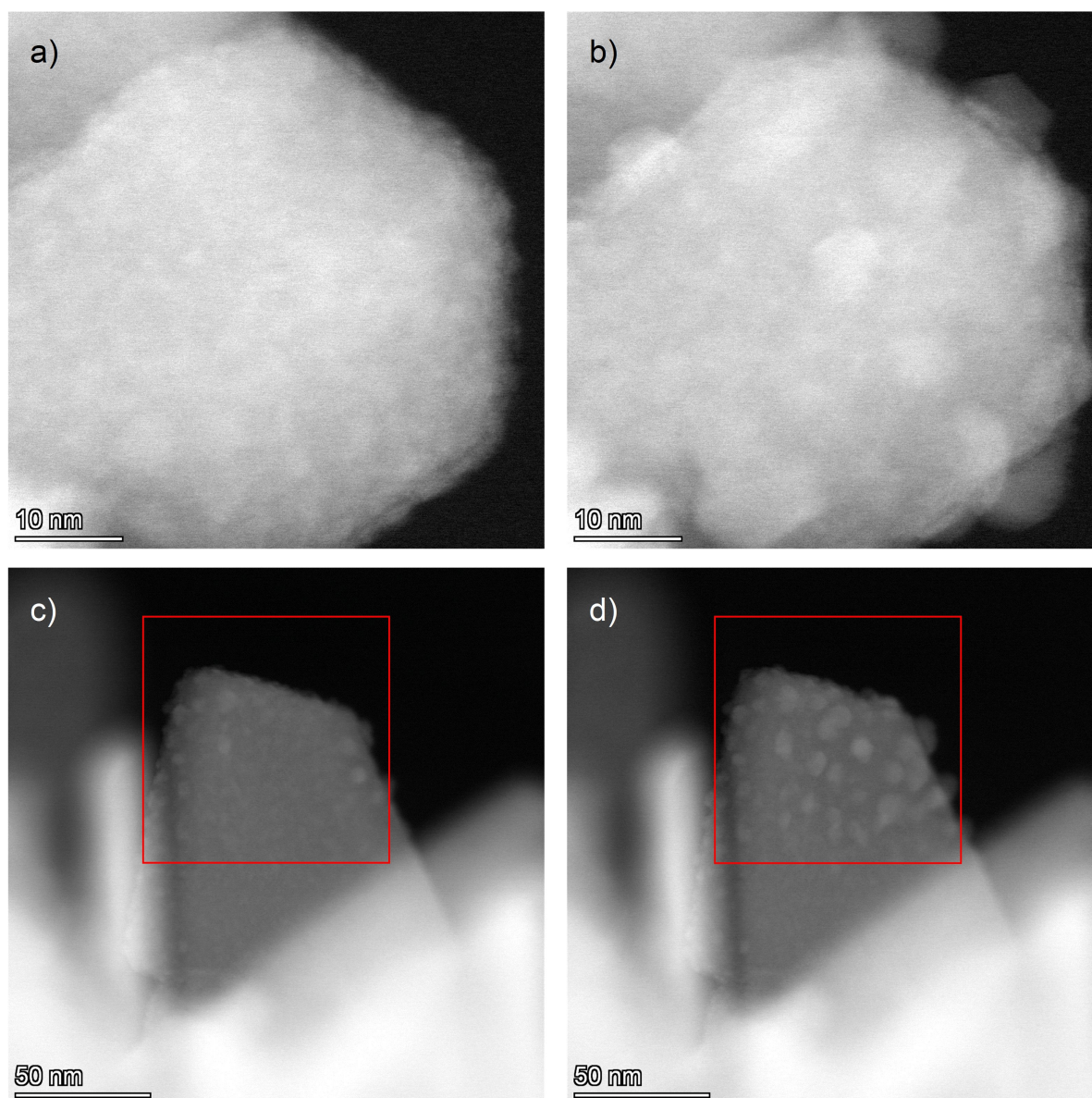


Figure 4.7: TEM images illustrating beam damage induced by the electron beam at 300 kV in STEM mode on a pristine Bi_2MoO_6 sample. Images with a field of view of 50 nm: a) first image captured after zooming in and focusing on the area of interest and b) image captured after exposure of 2.5 min. c) and d) images at lower magnification showing the beam damage after 4 min exposure of the area marked with the red boxes.

Fully sodiated samples should be less prone to reduction from the electron beam since Bi is already reduced. However, due to the air sensitivity of the Na_3Bi phases and limited

possibilities for inert transfer of the samples to the TEM we did not attempt to measure these sodiated samples. Instead, we measured desodiated samples containing Bi metal inside the Na–Mo–O matrix. Like for pristine Bi_2MoO_6 , the Bi particles in these samples quickly coalesced at high magnification due to the electron beam. This made it impossible to accurately determine the size of the Bi particles as they were estimated to be significantly smaller than 10 nm during the first cycles, based on XRD/PDF data. The only clear result we obtained from these TEM experiments (apart from beam induced changes) was that we actually formed nanosized alloying particles inside a matrix, which has been previously shown for similar materials [36].

4.2 Cycling and degradation mechanisms of Bi metallates

This chapter summarises the results from Paper 3–5 and discuss them briefly in context of literature and additional results from electrochemical measurements of Bi metallates. First, we present the main findings for the Bi_2MoO_6 and BiFeO_3 system, before comparing them with other tested Bi metallates. More thorough discussions regarding central topics of this thesis are provided in Chapter 5.

4.2.1 (De)sodiation mechanisms of Bi_2MoO_6 (Paper 3 and 5)

Bi_2MoO_6 has been previously investigated as an anode material for NIBs as a composite with N- and S-doped graphene (NSG) [39]. The study showed a specific capacity of $\sim 900 \text{ mAh g}^{-1}$ in the first sodiation, which quickly dropped to $\sim 300 \text{ mAh g}^{-1}$ after 10 cycles and maintained $\sim 250 \text{ mAh g}^{-1}$ after 50 cycles. These are higher capacities than what we obtained for Bi_2MoO_6 , where the initial sodiation capacity of $\sim 650 \text{ mAh g}^{-1}$ was reduced to $< 100 \text{ mAh g}^{-1}$ after 20 cycles (Paper 3). It is difficult to know if this difference in performance was due to the composite fabrication with doped graphene, different cycling conditions, different electrode preparation procedures, different electrolytes or a combination of these. Nevertheless, it is clear that the cycling stability is an unsolved issue for this material.

The study on $\text{Bi}_2\text{MoO}_6/\text{NSG}$ did not provide any insight into the cycling and degradation mechanism of the material, apart from hypotheses based on the (de)sodiation curves [39]. Therefore, most of our initial expectations for the cycling mechanism of Bi_2MoO_6 were based on previous *operando* XRD/XAS studies on $\text{Bi}_2(\text{MoO}_4)_3$ [33]. The structural formula of $\text{Bi}_2(\text{MoO}_4)_3$ is a bit misleading as it indicates that the structure consist of tetrahedral MoO_4^{2-} anions, while in reality the polyhedra around Mo is much more complicated. The structure consist of 3 different Mo sites where each of them are linked to 6 oxygen, all with different bond lengths, and the polyhedra could be described as distorted octahedra similar to those in Bi_2MoO_6 . As an example, the Mo–O distances for one of the sites in $\text{Bi}_2(\text{MoO}_4)_3$ are 1.72, 1.73, 1.86, 1.89, 2.13 and 2.62 Å. Therefore, it might have been better to use the more general formula of $\text{Bi}_2\text{Mo}_3\text{O}_{12}$. However, to be consistent with the cited literature, we will continue using $\text{Bi}_2(\text{MoO}_4)_3$ to describe this structure in this thesis.

Operando XRD on Bi_2MoO_6 showed that the main cycling mechanism was as expected, where an irreversible conversion reaction occurred during the first sodiation forming Bi nanoparticles embedded in a Na–Mo–O matrix (Paper 3). The Bi particles further goes

through a two-step reversible alloying reaction: $\text{Bi} \rightleftharpoons \text{NaBi} \rightleftharpoons \text{c-Na}_3\text{Bi}$ (Figure 4.8). The Na–Mo–O matrix was invisible in the XRD patterns due to its amorphous nature and the weak X-ray scattering of Na, Mo and O compared to Bi. Screening for possible Na–Mo–O phases in “The Materials Project” showed that they were electronic insulators [174], indicating that the matrix formed in Bi_2MoO_6 is likely an insulator as well.

In order to study the cycling mechanism in more detail we performed a combined *operando* PDF/XAS measurement over the course of 1.5 (de)sodiation cycles on Bi_2MoO_6 (Paper 5). The XAS data from the Mo K edge showed that Mo^{6+} did not change oxidation state and did not contribute to the capacity throughout the whole cycling regime. However, the local structure around Mo^{6+} changes from close to octahedral coordination in the sodiated state (possibly similar to Na_4MoO_5) to tetrahedral coordination in the desodiated state (similar to Na_2MoO_4). This transformation occurs at ~ 0.7 V during desodiation, which could explain why the cycling stability increased drastically when cycling with 0.7 V as the upper cut-off voltage, since the matrix is more stable below this voltage. These changes in the matrix are different from what was shown for $\text{Bi}_2(\text{MoO}_4)_3$, where there was a small change in oxidation state of Mo and no observed change in coordination [33]. This topic will be discussed in more detail in Section 5.2. XANES data of the Bi L3 edge from the *operando* measurement showed that the oxidation state of Bi changed as expected from +3 in Bi_2MoO_6 to a clearly negative oxidation state during sodiation. Due the lack of reliable Bi^{3-} references, we cannot confirm that the oxidation state reach exactly -3 , but it is likely very close.

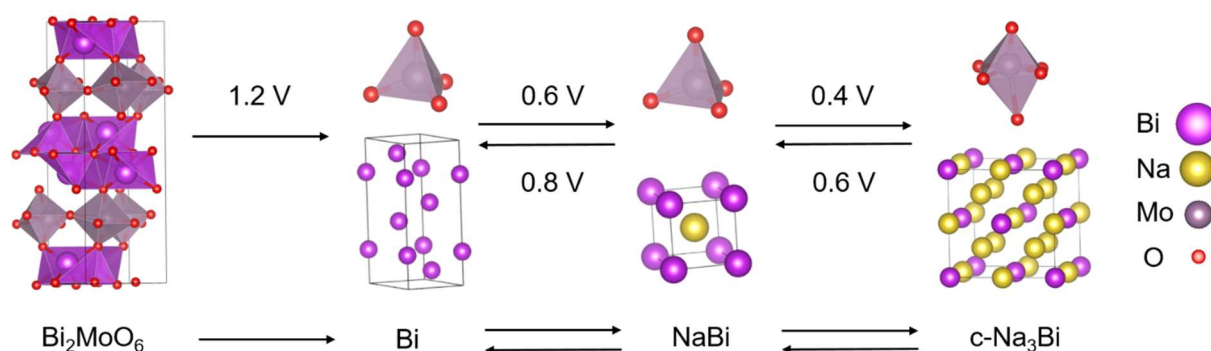


Figure 4.8: Graphical illustration of the cycling mechanism where Bi_2MoO_6 irreversibly converts into Bi, which further reversibly alloys to NaBi and c- Na_3Bi , in a Na–Mo–O matrix with tetrahedrally coordinated Mo^{6+} , which further reversibly shifts into distorted octahedral coordination. Adapted from Paper 5.

During desodiation, the edge position of Bi surpassed that of the Bi-metal reference showing that Bi obtains a positive oxidation state at the end of desodiation, likely between +1 and +2. This was surprising, as the XRD data did not show any diffraction peaks other than Bi metal and that a positive oxidation state of Bi had not been observed for $\text{Bi}_2(\text{MoO}_4)_3$ and BiVO_4 after the first cycle [33]. The FT EXAFS at full desodiation showed the presence of the expected double peak corresponding to Bi metal between 2–3.3 Å, but also a clear peak corresponding to Bi–O bonds between 1–2 Å (Paper 5). Bi–O bonds at the interface between Bi-metal nanoparticles and the Na–Mo–O matrix is a likely explanation for this observation.

These Bi–O bonds were not directly visible in *operando* PDF, but an indication of their formation was discovered when studying the intensities of the peaks at ~ 3 Å and ~ 3.5 Å. The closest Bi–Bi bonds in Bi metal are theoretically 3.07 Å in length and the second shortest Bi–Bi distances are 3.53 Å. In Bi₂O₃, the five closest Bi–Bi distances are in the range of 3.46–3.72 Å. The PDF data showed a decrease in the peak at ~ 3 Å and an increase in the peak at ~ 3.5 Å towards the end of desodiation, indicating formation of Bi–O–Bi bonds at the expense of Bi–Bi bonds. Another observation from *operando* PDF was that the closest Bi–Bi bonds were broken significantly later than the other bonds in Bi metal during sodiation (Paper 5).

The *operando* XRD study over the course of 34 (de)sodiation cycles indicated a gradual growth in size of the alloying particles with increasing cycle number, as the diffraction peaks became sharper (Paper 3). This could explain why h-Na₃Bi formed after ~ 10 cycles, as it has been shown to form in larger Bi particles [34]. This growth and its effect on the Na–Mo–O matrix was further studied with *ex situ* XRD/PDF and XAS (Paper 5). Fitting of XRD and PDF data from *ex situ* measurements on desodiated Bi₂MoO₆ samples estimated that the average crystallite size of Bi was 2–3 nm after the 1st cycle and increased to 7–10 nm after the 20th cycle. When studying the XAS data from the corresponding samples it was also clear that the oxidation state of Bi decreased together with the intensity of the Bi–O peak in FT EXAFS as the crystallite sizes of Bi increased. This makes sense as the interface area between the Bi particles and the Na–Mo–O matrix decreases when the Bi particles grow, thus leading to fewer Bi–O bonds.

To strengthen our hypothesis, we estimated the surface-to-volume ratios for Bi particles of different sizes. For simplicity, we assumed cubic particles with primitive packing and an atomic diameter for Bi of 3.1 Å. This showed that a ~ 2 nm Bi particle would have a surface-to-volume ratio of $\sim 2/3$ (Figure 4.9). By assuming that all the surface atoms bind to oxygen and obtain an oxidation state of +3, the average oxidation state of this Bi particle as a whole would be +2. This corresponds well with the estimated crystallite sizes from XRD/PDF and oxidation state from XANES after the 1st desodiation of Bi₂MoO₆ (Paper 5). With the same assumptions a 5 nm large Bi particle should have an average oxidation state of +1 and a 10 nm large particle should have +0.5 (Figure 4.9). This is also reasonable compared to the observed results from Paper 5.

This growth of the Na_xBi particles would necessarily lead to a thicker Na–Mo–O matrix with longer distances between the alloying particles (Figure 4.10). Given the presumed, electronically insulating nature of the matrix it would hinder electron transport, which could be the main factor for capacity degradation. The *operando* XRD measurement over 34 cycles provided some insight into this capacity degradation (Paper 3). The data showed that the diffraction peaks of Bi and partially NaBi disappeared during the capacity decay, indicating that the system locks itself in a partially sodiated state. These degradation reactions will be discussed more in detail in Section 5.1.

A *post-mortem* SEM study at different stages of cycling showed that a thick SEI layer forms on the surface of the Bi₂MoO₆ particles during sodiation and dissolves again during desodiation, somewhere below 0.9 V (Paper 3). This process likely consumes a significant amount of electrolyte, but applying extra electrolyte did not improve the cycling stability. Therefore, the consumption of electrolyte was not the main degradation factor. The

formation and dissolution of the SEI seemingly stopped between cycle 10 and 20, but it was disregarded as a symptom rather than a cause for the capacity degradation.

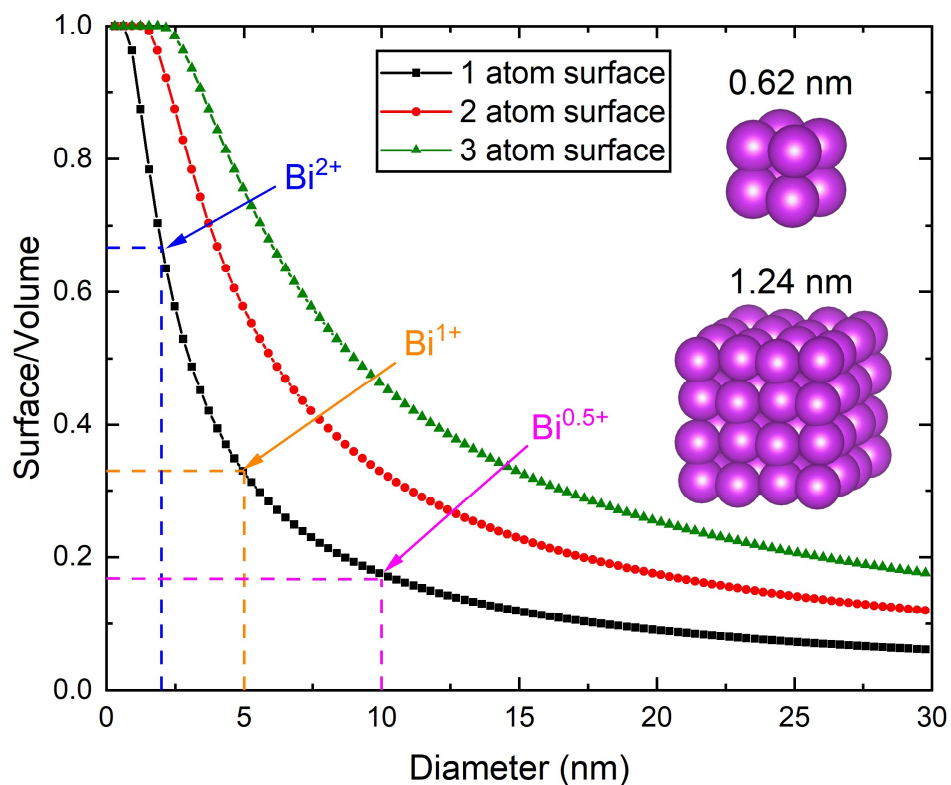


Figure 4.9: Estimation of surface-to-volume ratios of Bi particles assuming cubic particles with primitive packing and an atomic diameter of 3.1 Å. The black curve assumes that only the outermost atoms contributes to the surface bonding, the red assumes a width of two atoms in the surface and the green assumes three atoms. The blue, orange and pink lines and arrows indicate what the diameter of the Bi particles should be for the average oxidation state of Bi to be +2, +1 and +0.5, respectively, assuming that all the surface atoms are Bi³⁺. The cubes on the right side exemplifies two cubes used in the calculation, which was extracted from the crystal structure of Bi by visualisation in Vesta. The data are previously unpublished.

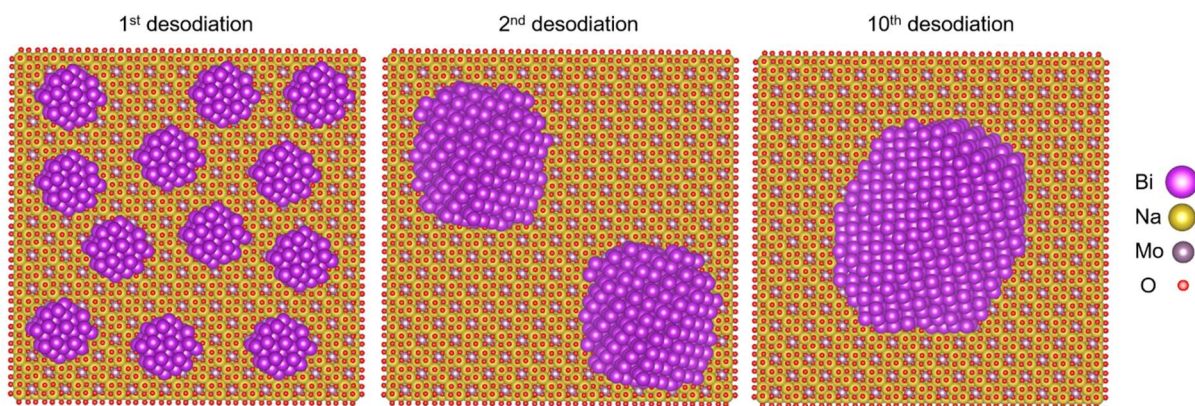


Figure 4.10: Graphical illustration of the growth of the Bi particles in the Na–Mo–O matrix with increasing cycle number. Adapted from Paper 5.

4.2.2 High-rate cycling and capacity degradation of BiFeO₃ (Paper 4)

The electrochemical performance of BiFeO₃ (with ~12 wt% of Bi₂O₃ as impurity) was similar to what has been shown in literature [31, 35], as it showed a specific capacity of ~600 mAh g⁻¹ in the first sodiation that dropped to ~200 mAh g⁻¹ after 20 cycles (Paper 4). BiFeO₃ maintains its performance well during cycling at a high current density (1 A g⁻¹), and to explore potential differences in the cycling mechanism we performed *operando* XRD over the course of 2 cycles at 1 A g⁻¹ (Figure 4.11) and 0.1 A g⁻¹ (Figure 4.12). This showed that the cycling mechanism at the two different cycling rates were the same, and that BiFeO₃ could be fully sodiated to Na₃Bi even at 1 A g⁻¹.

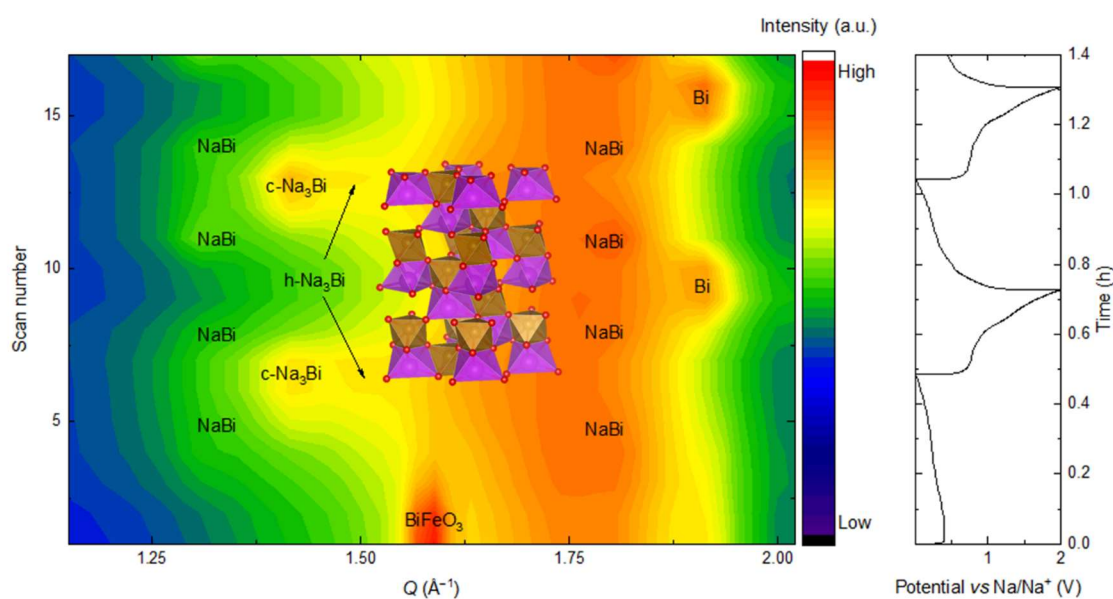


Figure 4.11: Table of content (TOC) graphic from Paper 4 showing *operando* XRD of BiFeO₃, cycled at 1 A g⁻¹ with a voltage range of 0.01–2.00 V, and an illustration of the crystal structure of BiFeO₃ in the middle.

A surprising result from these *operando* measurements was that BiFeO₃ formed both c-Na₃Bi and h-Na₃Bi already during the first sodiation (Figure 4.11 and Figure 4.12), contrary to Bi₂MoO₆ that only formed c-Na₃Bi (Paper 3 and 5). This could indicate that the alloying particles formed in BiFeO₃ are slightly larger than those formed in Bi₂MoO₆, as h-Na₃Bi tend to form in larger NaBi particles [34]. Surface Rietveld refinements helped the tracking of phase transformations during cycling, and revealed that c-Na₃Bi formed prior to h-Na₃Bi (Figure 4.12c). This raised a discussion regarding possible Na deficiency in the c-Na₃Bi structure, where it was speculated that when the full stoichiometry of Na₃Bi is obtained the phase transforms into h-Na₃Bi.

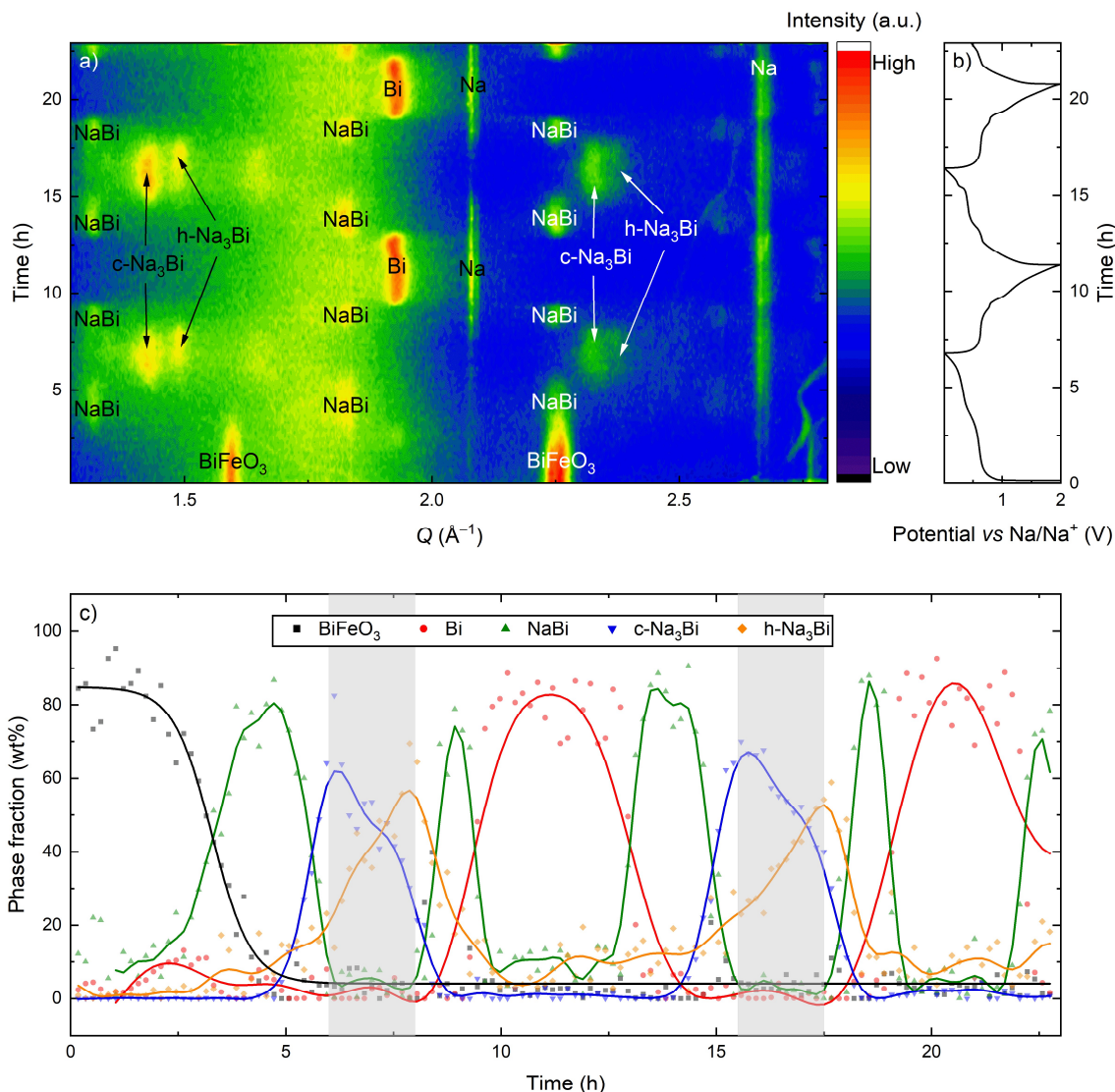


Figure 4.12: Contour plot derived from *operando* XRD measurement of BiFeO_3 over the course of 2 (de)sodiation cycles, b) corresponding (de)sodiation curves measured at 0.1 A g^{-1} between 0.01–2.00 V. c) Phase fractions in wt% retrieved from surface Rietveld refinement of the diffraction data plotted in a), showing the evolution of the Bi-containing phases as a function of time. The grey areas in c) highlight the regions where only the two different phases of Na_3Bi are present. Adapted from Paper 4.

Surface Rietveld refinements of an *operando* XRD measurement of BiFeO_3 at 0.2 A g^{-1} over the course of 27 (de)sodiation cycles provided insight into the capacity degradation (Paper 4). The results from the refinements combined with *ex situ* XAS data of the Bi L3 edge and detailed study of the (de)sodiation curves made it possible to extract three distinct regions of capacity degradation for BiFeO_3 . In region 1, the capacity from the oxidation of Bi metal leading to Bi–O bonds at the interface between the Bi particles and the Na–Fe–O matrix disappears. Region 2 shows the emerging irreversibility of the $\text{Bi} \rightleftharpoons \text{NaBi}$ reaction, while Region 3 corresponds to a partial deactivation of the $\text{NaBi} \rightleftharpoons \text{Na}_3\text{Bi}$ reaction. This means that Na_3Bi was only partially able to dealloy to NaBi and NaBi was not able to form Bi during desodiation. Hence, a significant amount of inactive Na_3Bi is present in the system. These results indicated that the oxidation of Bi metal and the $\text{Bi} \rightleftharpoons$

NaBi reaction were more damaging for the cycling stability than the $\text{NaBi} \rightleftharpoons \text{Na}_3\text{Bi}$ reaction. This initiated the electrochemical tests with a reduced upper cut-off voltage of 0.7 V, thus isolating the cycling of the $\text{NaBi} \rightleftharpoons \text{Na}_3\text{Bi}$ reaction, which showed significantly better cycling stability (Figure 4.13). However, it is difficult to know if it is the isolation of the $\text{NaBi} \rightleftharpoons \text{Na}_3\text{Bi}$ reaction, reduction of structural changes in the matrix or a combination that is the main reason for the improved cycling stability. This will be discussed further in Section 5.1 and 5.2.

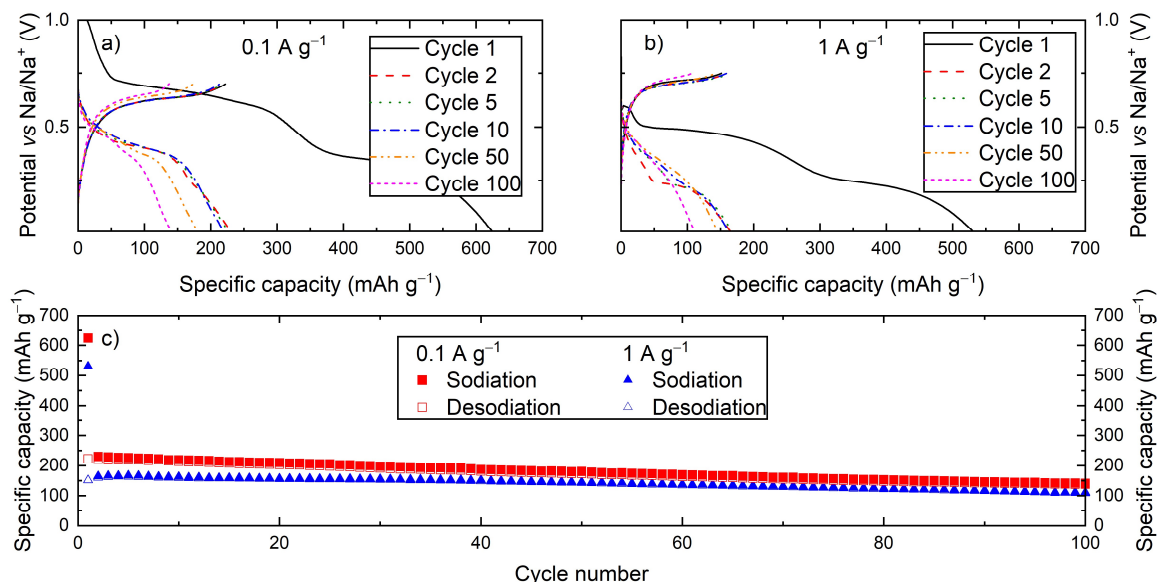


Figure 4.13: GC measurements of BiFeO_3 with a reduced upper cut-off voltage leading to increased cycling stability. Selected (de)sodiation curves obtained from measurements at a) 0.1 A g^{-1} with a voltage range of 0.01–0.70 V and b) 1 A g^{-1} between 0.01–0.75 V. c) Capacity per cycle plot extracted from the measurements in a) and b). Retrieved from Paper 4.

Paper 4 also provides some insights into the Na–Fe–O matrix. Through *ex situ* XANES measurements, it was shown that Fe in the Na–Fe–O matrix is redox active and slightly changes oxidation state and coordination during cycling. The oxidation state of Fe was initially +3 and was slightly reduced during sodiation, but the edge position did not surpass that of the Fe_3O_4 reference, indicating that the average oxidation state was never below +2.67. The observed pre-edge feature indicated that Fe partially transitions from octahedral coordination in BiFeO_3 to tetrahedral coordination in the Na–Fe–O matrix.

4.2.3 Electrochemical performance of different Bi metallates

Several other Bi metallates were evaluated and compared throughout this study. In addition to Bi_2MoO_6 and BiFeO_3 , we here present results from $\text{Bi}_4\text{Ti}_3\text{O}_{12}$ and $\text{Bi}_2\text{Al}_6\text{O}_{12}$. $\text{Bi}_4\text{Ti}_3\text{O}_{12}$ was synthesised as described in Section 3.4.2, while $\text{Bi}_2\text{Al}_6\text{O}_{12}$ was purchased commercially (Table 4.3).

Table 4.3: Overview of Bi metallates presented in this thesis. Including phase fractions obtained from Rietveld refinements for those samples that contained a significant amount of impurities.

Compound	Commercial/synthesised	Phase fractions
Bi ₂ MoO ₆	Synthesised	
BiFeO ₃	Synthesised	12 wt% Bi ₂ O ₃ impurity
Bi ₄ Ti ₃ O ₁₂	Synthesised	67 wt% Bi ₄ Ti ₃ O ₁₂ , 27 wt% Bi ₂ Ti ₂ O ₇ , 8 wt% Bi ₂ O ₃
Bi ₂ Al ₆ O ₁₂	Commercial	

GC measurements of the Bi metallates showed some common characteristics, where all of them undergo an initial irreversible conversion reaction, forming Bi particles embedded in a Na–M–O matrix (Figure 4.14 and Figure 4.15). In the following cycles, they show plateaus in the (de)sodiation curves corresponding to the $\text{Bi} \rightleftharpoons \text{NaBi}$ (~ 0.6 V during sodiation and ~ 0.8 V during desodiation) and $\text{NaBi} \rightleftharpoons \text{Na}_3\text{Bi}$ reactions (~ 0.4 V during sodiation and ~ 0.6 V during desodiation) in the GC measurements at 0.1 A g^{-1} (Figure 4.14a, c, e and g). There is also some capacity contribution above 1 V related to the further oxidation of Bi that, based on the results of BiFeO₃ (Paper 4) and Bi₂MoO₆ (Paper 5), is due to Bi–O bonds at the interface between Bi particles and the Na–M–O matrix. Cycling at the higher rate of 1 A g^{-1} showed that all the samples handle fast cycling reasonably well, maybe except for Bi₂Al₆O₁₂, with only minor losses in capacity (Figure 4.14b, d, f and h). However, there is a significant increase in the overpotential of the reactions because of the increased current density.

The most prominent challenge for these materials is the cycling stability as the majority of the capacity is lost after 20 cycles (Figure 4.15). For example the specific capacities of BiFeO₃ and Bi₂MoO₆, which performed the best of the tested materials, decay from $\sim 450 \text{ mAh g}^{-1}$ in the second cycle to $\sim 150 \text{ mAh g}^{-1}$ in the 20th cycle (Figure 4.15a). During faster cycling (1 A g^{-1}) the capacity decay followed the same trend. The degradation mechanisms leading to this capacity decay will be discussed further in Section 5.1.

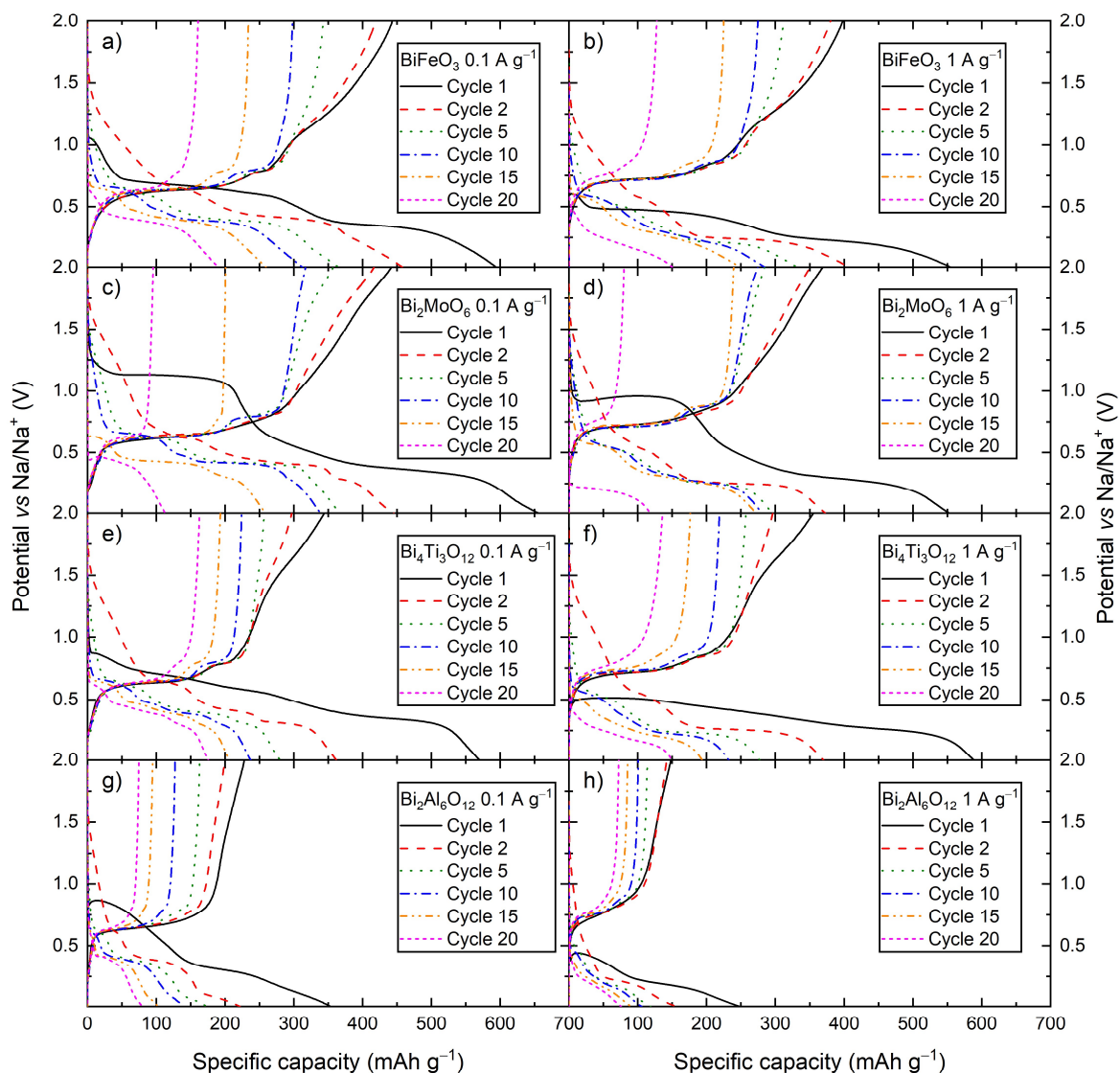


Figure 4.14: (De)sodiation curves obtained from galvanostatic cycling between 0.01–2.00 V with current densities of 0.1 A g⁻¹ (left) and 1 A g⁻¹ (right) for different Bi metallates (specified in the legends). The data are previously unpublished.

In order to understand how much of the capacity that originates from reactions other than $\text{Bi} \rightleftharpoons \text{Na}_3\text{Bi}$ we calculated the specific capacity based on the mass of Bi in each of the electrodes rather than the mass of the Bi metallates (Figure 4.15c and d). When comparing these capacities to the theoretical capacity of Bi it is clear that all the samples, maybe except for Bi₂Al₆O₁₂, have contributions from other reactions. Some of the capacity comes from electrochemical activity of Super P and formation of SEI (Paper 3), but the majority of the extra capacity is due to the reaction above 1 V where Bi–O bonds are formed (Paper 4 and 5).

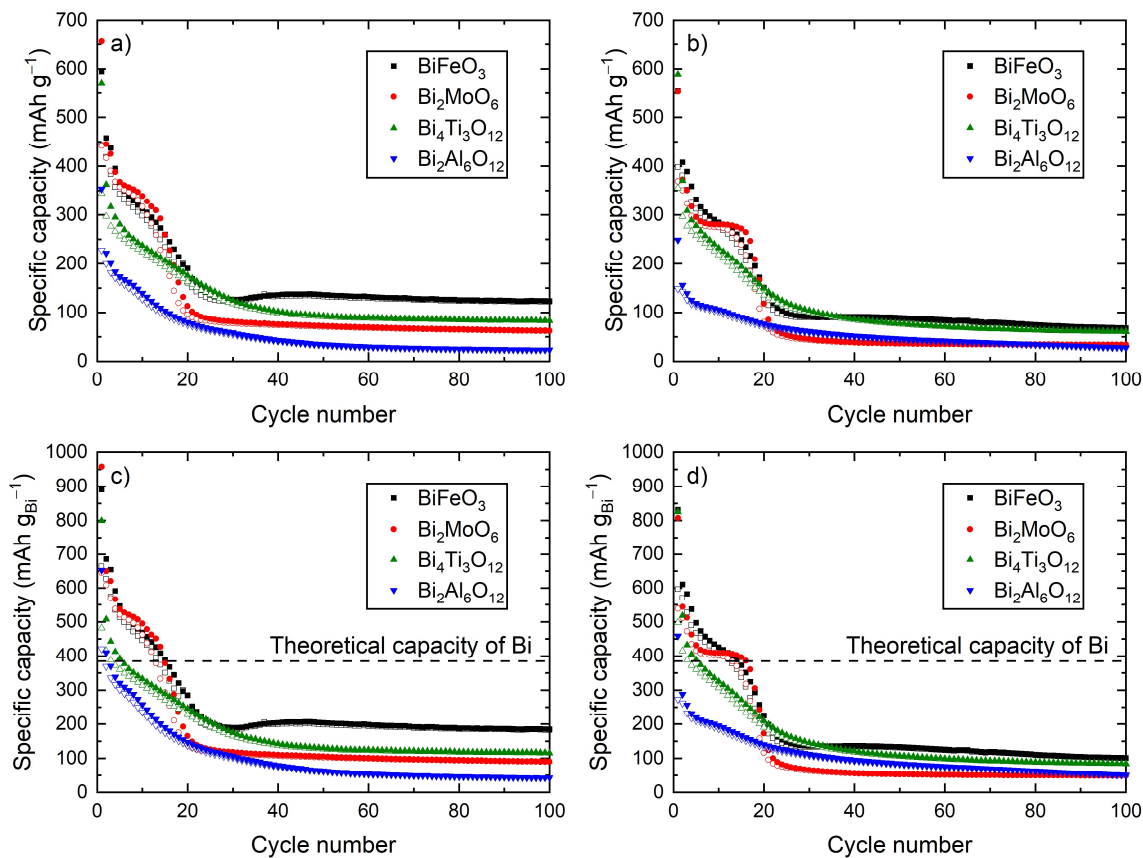


Figure 4.15: Specific capacity per cycle of different Bi metallates obtained from GC measurements between 0.01–2.00 V of different Bi metallates at a) 0.1 A g⁻¹ and b) 1 A g⁻¹. Specific capacity (calculated based on the mass of Bi in each sample) per cycle of different Bi metallates obtained from GC measurements at c) 0.1 A g⁻¹ and d) 1 A g⁻¹. Filled symbols are sodiation capacities and empty symbols are from desodiation. The data are previously unpublished.

5. Summarising discussion

Here we discuss central topics in more detail and in a wider perspective with regards to existing literature on Bi metallates and other CAMs. These topics include: capacity degradation in Bi metallates, changes in Na–M–O matrixes, formation of c-Na₃Bi vs h-Na₃Bi and differences between Bi metallates in NIBs vs LIBs.

5.1 3-step capacity degradation

All the tested Bi metallates in the previous chapter showed a similar capacity decay during the first 20 cycles. For BiFeO₃ and Bi₂MoO₆ we revealed that the degradation can be divided into 3-steps (Paper 4), which could be valid for the other Bi metallates as well:

1. Deactivation of the oxidation reaction of Bi metal that formed Bi–O bonds at the interface between Bi and Na–M–O matrix
2. Irreversibility of the Bi \rightleftharpoons NaBi reaction
3. Partial irreversibility of the NaBi \rightleftharpoons Na₃Bi reaction

These three steps are clearly visible from (de)sodiation curves, capacity per cycle plots, *ex situ* XAS measurements and changes in phase fractions from surface Rietveld refinements of *operando* XRD data for both materials (Figure 5.1). Since the cycling stability of BiFeO₃ is slightly better than for Bi₂MoO₆, these degradation steps occur at higher cycle numbers for BiFeO₃. The first indication for step 1 was the disappearance of the electrochemical signals above 1 V during desodiation and above 0.7 V during sodiation (Figure 5.1c). This was further supported by the XANES data for desodiated samples from cycle 1–10 showing a reduction in the oxidation state of Bi (Figure 5.1e) and the disappearance of the Bi–O peak in the corresponding FT EXAFS data (Figure 5.1f). Step 2 and step 3 were more directly observed from the *operando* XRD data where the Bragg reflections of Bi disappeared from the diffractograms and the intensities of the NaBi peaks were greatly reduced (Figure 5.1a–b), together with the corresponding plateaus in the (de)sodiation curves (Figure 5.1d). After region 3, the system was mainly locked in the sodiated state with large amounts of inactive Na₃Bi, while a small part of the NaBi \rightleftharpoons Na₃Bi reaction remained and contributed to the limited capacity.

The underlying reason for this capacity degradation is likely the coalescence of the alloying particles during cycling, as described in Section 4.2.1. Since step 1 and step 2 of the capacity degradation occurred first it is natural to think that these are the most detrimental. When avoiding these reactions in the electrochemical cycling by decreasing the upper cut-off voltage to 0.7 V the cycling stability increased significantly. This could mean that the coalescence of the Na_xBi particles mainly occurs above 0.7 V as a part of the reactions related to step 1 or step 2. This aspect will be discussed further in Section 5.2 where the effect of the matrix surrounding the alloying particles will be included.

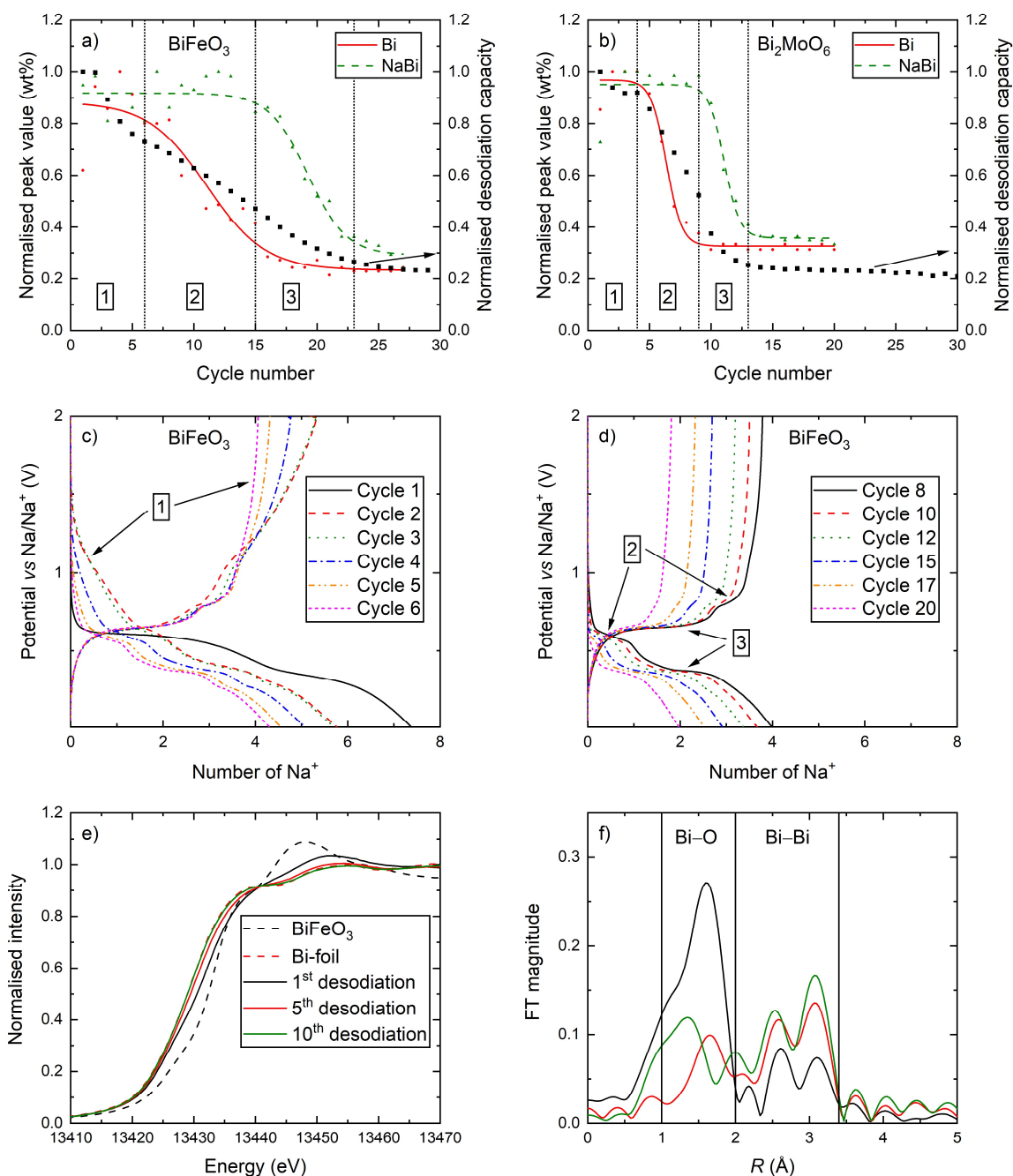


Figure 5.1: Maximum normalised phase fractions for Bi and NaBi vs cycle number extracted from surface Rietveld refinements of *operando* XRD of a) BiFeO₃ for the first 27 (de)sodiation cycles (Paper 4) and corresponding results for b) Bi₂MoO₆ (Paper 3). GC measurement of BiFeO₃ was performed at 0.2 A g⁻¹, while for Bi₂MoO₆ the specific current was 0.1 A g⁻¹. Both measurements had a voltage range of 0.01–2.00 V. c) and d) (de)sodiation curves of BiFeO₃ plotted as potential vs Na/Na⁺ against the calculated number of Na⁺ ions transferred per formula unit obtained from the *operando* measurements shown in a), highlighting the capacity decay in c) cycle 1–6 and d) cycle 8–20. e) XANES spectra of the Bi L3 edge for desodiated BiFeO₃ at different stages of cycling compared to pristine BiFeO₃ and Bi metal as references, f) corresponding FT EXAFS spectra. Adapted from Paper 4.

In both BiFeO_3 and Bi_2MoO_6 , the rate of degradation for step no. 3 seems to be a bit higher than for step no. 2: the maximum peak intensity of the NaBi phase is reduced faster when its decay begins compared to the peak intensities of Bi. There are some uncertainties in the results from the surface Rietveld refinements, because of limited data quality and time resolution in the *operando* XRD measurements. However, the normalised desodiation capacity per cycle graphs also indicate that there is a sudden change in decay rate between step 2 and 3. It is not certain why step 2 and step 3 would decay at different rates, but this could be an interesting topic for future studies. Maybe the change in rate is coincidental and the explanation is simply that the alloying particles continue to grow with cycle number leading to a more rapid capacity decay at later stages of cycling.

The other Bi metallates ($\text{Bi}_4\text{Ti}_3\text{O}_{12}$ and $\text{Bi}_2\text{Al}_6\text{O}_{12}$) that were electrochemically tested in this work were not studied to the same detail. However, their (de)sodiation curves from the figures in Section 4.2.3 show similar features as BiFeO_3 and Bi_2MoO_6 . This indicates that they do follow a similar 3-step capacity degradation.

5.2 The effect of the Na–M–O matrix

The matrixes formed in CAMs and their interactions with the alloying particles are considered to be determining factors for the electrochemical performance of the materials (Paper 1). However, they are difficult to study and are not well understood. From *operando* and *ex situ* XAS studies of Bi metallates it is evident that the structure and behaviour of the matrix vary for different types of non-alloying metals (M), and when varying the ratio between Bi and M.

In Bi_2MoO_6 (2:1 ratio of Bi:Mo), the matrix contains Mo^{6+} that does not change oxidation state during cycling, but the coordination changes from tetrahedral to octahedral according to the change observed for the pre edge in the XANES spectra of the Mo K edge (Figure 5.2a). On the other hand, $\text{Bi}_2(\text{MoO}_4)_3$ (2:3 ratio of Bi:Mo) show a slight change in oxidation state of Mo, as the edge position shifts, but no clear change in coordination (Figure 5.2c) [33]. The measurements of these two compounds are performed with different electrode compositions and preparation procedures, which make direct comparison difficult. However, these results indicate that varying the composition between Bi and Mo does have an influence on the matrix during cycling.

For BiFeO_3 , the electrode composition and preparation procedures are the same as for Bi_2MoO_6 . The differences observed here are, therefore, directly related to the active materials. In BiFeO_3 , Fe seems to change both oxidation state and local coordination as a result of cycling (Figure 5.2b). The change in average oxidation state is small as the edge position does not go below that of Fe_3O_4 . In the study performed by Surendran *et al.*, Fe showed a bigger change in the XANES edge position and hence oxidation state, meaning that Fe in BiFeO_3 could be more reduced during sodiation than what we observed (Figure 5.2d) [35]. This difference is likely due to a combination of smaller particles (~50 nm), thinner electrodes (wet thickness = 130 μm) and lower cycling rates (C/20) that were used in their study [35], as all of these parameters would lower the overpotentials for the reactions allowing more redox on Fe before the cut-off voltage is reached.

Some of the Fe in the Na-Fe-O matrix seems to change coordination from octahedral in BiFeO_3 to tetrahedral during sodiation, similar to the coordination observed for spinel type Fe_3O_4 , as evidenced from the pre-edge feature in the XANES spectra (Figure 5.2b). Additional magnetic measurement with physical property measurement system (PPMS) of sodiated BiFeO_3 samples showed ferromagnetic behaviour, indicating the presence of Fe_3O_4 . However, the amount of ferromagnetic iron in the samples was estimated to be <5% showing that most of the matrix contained other Fe-containing phases, being para- or antiferromagnetic. There are a lot of possible Na-Fe-O phases that have been experimentally observed with various Na:Fe ratios, oxidation states and coordinations for Fe-cations (*e.g.* Na_3FeO_3 , Na_5FeO_4 , NaFeO_2 , Na_4FeO_3 and NaFe_2O_3) [174]. In addition, it could be possible to form Na_2O , Fe metal, Fe_2O_3 and Fe_3O_4 . This plethora of possible structures for iron may explain why the matrix is amorphous and goes through gradual changes in both oxidation state and coordination, while it also makes it difficult to accurately describe the chemical phase(s) in the matrix.

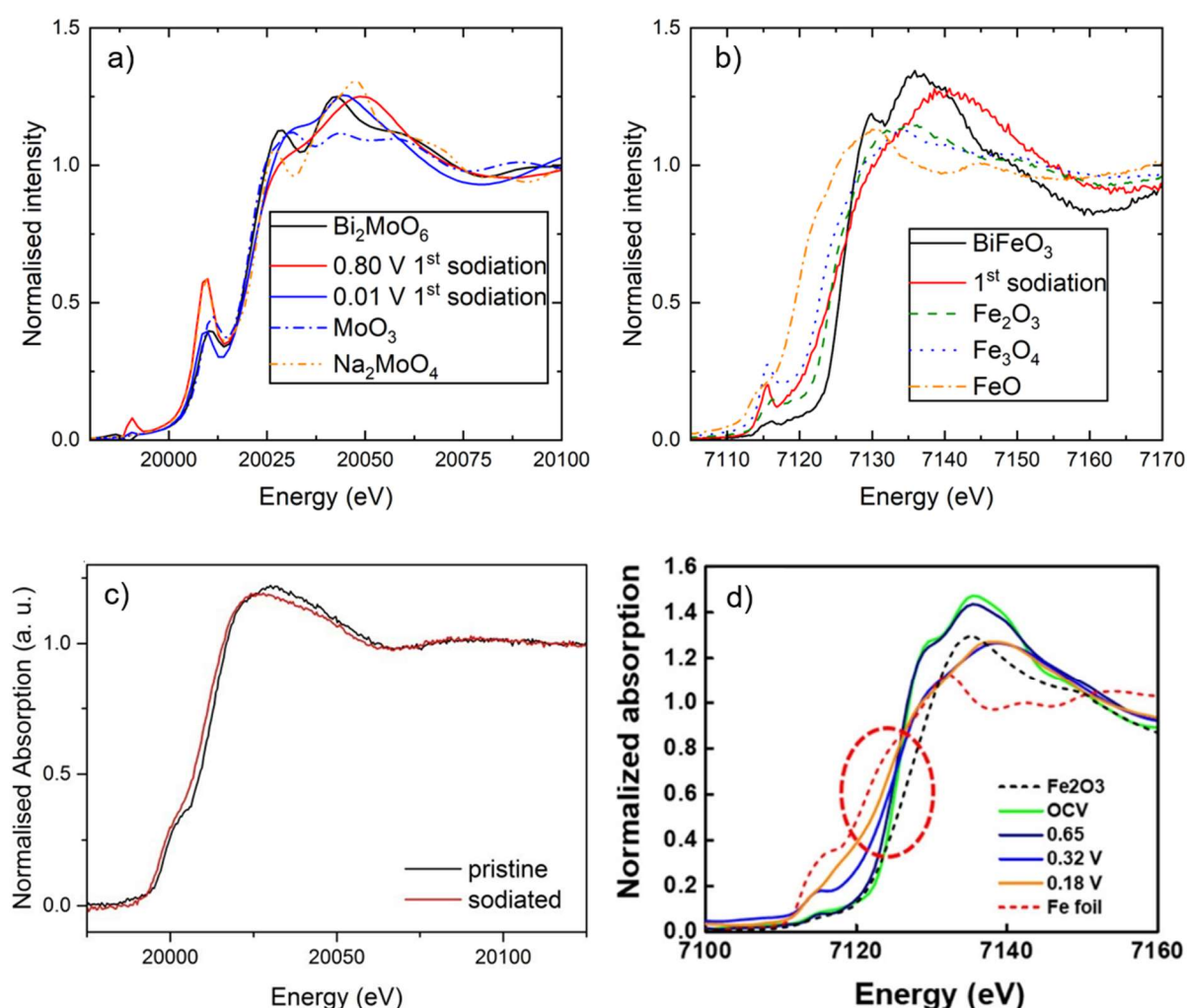


Figure 5.2: *Ex situ* XANES measurements on a) Mo K edge in pristine and sodiated Bi_2MoO_6 (Paper 5) and b) Fe K edge in pristine and sodiated BiFeO_3 (Paper 4). c) Mo K edge for pristine and sodiated state of $\text{Bi}_2(\text{MoO}_4)_3$. Adapted with permission from [33]. Copyright 2017 American Chemical Society. d) *Operando* XANES data of BiFeO_3 . Adapted with permission from [35]. Copyright 2022 American Chemical Society.

There are a few studies of CAMs as anode materials for NIBs providing some insight into the composition and structure of the matrix (Table 5.1 and Paper S1–S2). However, very few of the studies track the structural changes in the matrix during cycling and discuss how it influences the cycling stability. In addition, the various particle sizes, carbon composites, electrode fabrication procedures and measurement protocols obfuscate the effect of the matrix. Therefore, it is difficult to make a systematic analysis of chemical and structural parameters that influence the overall conversion-alloying process, and thereby determine the optimal characteristics of the matrix. Still it is clear that certain features are beneficial. A matrix that is stable, in the sense that it can prevent coalescence of the alloying particles, will likely lead to good cycling stability for Bi metallates and other CAMs. The matrix will obviously not be completely rigid as it will change due to the volume expansion of the alloying particles. However, the structural and chemical changes should be as small as possible and include a minimal amount of bond breaking to prevent the alloying particles to move and coalesce inside the matrix. It is also important to investigate within which voltage windows the matrix is stable and what type of alloying reactions it can accommodate.

One clear indication that a stable matrix provides good cycling stability is the GC measurement of Bi_2MoO_6 with an upper cut-off voltage of 0.7 V, which improved the cycling stability drastically (Paper 5): *operando* XAS measurement of the Mo K edge indicated that there was no significant change in the matrix during desodiation below 0.7 V. The reason for the stability of the matrix below 0.7 V is likely because the $\text{Bi} \rightleftharpoons \text{NaBi}$ reaction is avoided, thereby reducing the volume expansion of the alloying particles and the following strain on the matrix. Section 5.1 clearly showed that oxidation of Bi metal and the $\text{Bi} \rightleftharpoons \text{NaBi}$ were the first reactions to become inactive during capacity degradation when cycling to 2.0 V. However, we do not believe the reactions in themselves were the main problem, but the changes they induce in the matrixes. Therefore, finding a matrix that could handle both steps of the alloying reactions, not just $\text{NaBi} \rightleftharpoons \text{Na}_3\text{Bi}$, could lead to a great improvement of Bi metallates.

For BiFeO_3 , the cycling stability also improved significantly with 0.7 V as upper cut-off voltage. Unfortunately, we do not have XAS data of the Fe K edge at intermediate states of sodiation. Therefore, we do not know at which voltages the Na–Fe–O matrix undergoes the main structural changes. The *operando* XAS study of BiFeO_3 performed by Surendran *et al.* managed to better track the changes of Fe, showing that a significant amount of the changes in the matrix occurred below 0.7 V (Figure 5.2d) [33]. The changes might not be exactly the same for BiFeO_3 in our study, but it is likely that there are some structural changes occurring in the matrix below 0.7 V. Nevertheless, the limited cut-off voltage probably reduced the amount of structural changes in the matrix because of less strain from the alloying reactions, thus increasing the cycling stability.

A study on Sb_2Se_3 showed the coalescence of Sb particles during desodiation using *in situ* TEM, indicating that coalescence of particles is also a problem for CAMs based on other alloying elements than Bi [175]. The same study showed that reducing the upper cut off voltage from 2.5 to 1.5 V, thus avoiding the transformation from Na_2Se to Se, improved the cycling stability in a similar fashion as our Bi metallates [175]. This indicates that

finding a voltage window where the matrix is stable and can mitigate coalescence of alloying particles are not just beneficial for Bi metallates, but also for CAMs in general.

Table 5.1: Overview of studies on CAMs for NIBs that provide some insight into the chemical composition and structure of the matrix. The table contains chemical formula of the material, characterisation techniques used to study the matrix and proposed chemical phases in the matrix. The names of the carbon composites are simplified and grouped into carbon nanotubes (CNT), reduced graphene oxide (rGO), graphene, N-doped graphene (NG) or other carbon composites (C).

Material	Techniques	Proposed matrix	Ref.
SnO ₂ /CNT	<i>In situ</i> TEM	Na ₂ O	[176]
SnO ₂	<i>In situ</i> TEM	Na ₂ O	[177]
SnO/CNT	<i>Ex situ</i> TEM	Na ₂ O	[178]
SnS/CNT	<i>Ex situ</i> XRD	Na ₂ S ₅ , HNaS, Na ₂ S ₂	[179]
SnS ₂ /rGO	<i>Ex situ</i> TEM	Na ₂ S	[180]
Sn ₄ P ₃	<i>Ex situ</i> TEM, XRD, XAS	Na _x P	[181]
Sn ₄ P ₃ /rGO	<i>Ex situ</i> TEM, XRD	P ⇌ Na ₃ P	[182]
Sb ₂ O ₃ /rGO	<i>Operando</i> XRD, quasi <i>in situ</i> XPS	Na ₂ O	[183]
Sb ₂ S ₃ /C	<i>In situ</i> TEM, DFT, MD	Na ₂ S	[184]
Sb ₂ Se ₃	<i>In situ</i> TEM	Se ⇌ Na ₂ Se	[175]
Sb ₂ Se ₃	<i>In situ</i> TEM	Na ₂ Se	[185]
Sb ₂ Se ₃ /rGO	<i>Operando</i> XRD, <i>ex situ</i> TEM	Na ₂ Se	[138]
SbVO ₄ /rGO	<i>Operando</i> XRD, <i>ex situ</i> TEM, XPS	Na ₃ VO ₄	[186]
Sb ₂ MoO ₆	<i>Ex situ</i> XRD, XPS, TEM	Na ₂ MoO ₄	[30]
FeSbO ₄	<i>Operando</i> XRD, <i>ex situ</i> XPS, DFT	Fe + Na ₂ O	[187]
MnSb ₂ S ₄ /rGO	<i>Ex situ</i> XRD	Na _x MnS → Na ₂ S + Mn ⇌ MnS	[188]
Bi ₂ S ₃	<i>Operando</i> XRD/XAS	Na ₂ S ₄ ⇌ Na ₂ S	[172]
Bi ₂ S/NG	<i>In situ</i> XRD	Na ₂ S	[189]
Bi ₂ Se ₃ /C	<i>Ex situ</i> XRD, XPS	Na ₂ Se	[190]
Bi ₂ Se ₃ /graphene	<i>Ex situ</i> XRD, TEM	Na ₂ Se	[191]
BiVO ₄ /C	<i>Operando</i> XRD/XAS, DFT	Na ₃ VO ₄ ⇌ Na ₄ VO ₄	[33]
Bi ₂ (MoO ₄) ₃ /C	<i>Operando</i> XRD/XAS, DFT	Na ₂ MoO ₄ ⇌ Na ₃ MoO ₄	[33]
BiFeO ₃	<i>Ex situ</i> XRD	Fe + Na ₂ O	[31]
BiFeO ₃	<i>Operando</i> XAS	Fe(II,III)-O ⇌ Fe + Fe-O + Na ₂ O	[35]

Sottmann *et al.* managed to obtain good cycling stability without reducing the upper cut-off voltage for $\text{Bi}_2(\text{MoO}_4)_3$ and BiVO_4 , through heavy ball milling (24 h) with large amounts of carbon (30 wt%) [33]. Here it is likely that the particle size of the pristine materials obtained from ball milling (crystallite size of ~ 60 nm, estimated from XRD) was so small that the coalescence of Bi did not cause any significant problems. Therefore, the stability of the matrix was not crucial in this case. The same study showed that BiVO_4 and $\text{Bi}_2(\text{MoO}_4)_3$ that went through less ball milling (20 min) had larger particles (crystallite size of ~ 600 nm) and showed comparable cycling stability to Bi_2MoO_6 and BiFeO_3 , thus likely being limited by the changes in the matrixes accompanied by coalescence of the alloying particles [33].

The strategy of nanosizing the particles of the active material and creating carbon composites is a common way of creating high-performing CAMs [26, 58, 192, 193]. However, if CAMs should approach commercialisation it would be important to limit the processing steps and the amount of carbon additives in order to reduce the cost and increase the specific capacity of electrodes. Therefore, it would be valuable to develop CAMs that can obtain good cycling stability without the need for complex nanostructuring and carbon additives. With a stable matrix that prevents coalescence of alloying particles this should be possible, even for materials with primary particle sizes in the micrometre range.

Many Na–M–O materials have poor electronic conductivity [174], but this should not cause any major problems if the pathways for the electrons are shorter than ~ 10 nm, as quantum-mechanical tunnelling can occur between the metallic alloying particles [194]. For all the tested Bi metallates, this condition should be satisfied if there is an even distribution of sufficiently small Na_xBi particles in a Na–M–O matrix. When considering $\text{Bi}_2(\text{MoO}_4)_3$, which is one of the Bi metallates with the lowest Bi loading, and assuming a formation of metallic Bi particles inside a Na_2MoO_4 matrix, the Bi particles will account for 30% of the volume. With this volume fraction, the distances between the alloying particles should be significantly smaller than 10 nm, assuming an even distribution of particles with sizes in the range of 2–10 nm (estimated sizes of Bi particles formed in Bi_2MoO_6 , Section 4.2.1).

It is difficult to find studies that directly assess the conductivities of materials with metal particles inside oxide matrixes, especially for amorphous materials, and how that is related to the electrochemical performance. However, it has been shown that poorly conductive, amorphous FePO_4 thin films up ~ 50 nm are able to achieve decent electrochemical performance in LIBs [195–197]. The performance decreased with increasing thickness, whereas films thicker than 100 nm showed very poor performance. Based on these results it is likely that the electronic conductivity of the matrix in most CAMs will start to affect the electrochemical performance when the distance between the alloying particles will be >10 nm, and will become detrimental at distances >50 nm. Nevertheless, having a matrix with good electronic conductivity could be beneficial as the performance of the active material would be less sensitive to the thickness of the matrix.

A more important property of the matrix is the Na^+ conductivity. Given the amorphous nature of most matrixes in CAMs it is difficult to theoretically predict their ionic conductivity, since most of the theory is based on crystalline systems [152, 198].

However, it is sensible to think that the amorphous matrixes formed in CAMs contain enough Na-ions and vacancies to generally be good ionic conductors. If the matrix would have poor ionic conductivity, we would not expect the good cycling behaviour at higher rates that is generally observed in CAMs [30–32].

5.3 Formation of c-Na₃Bi and h-Na₃Bi.

Even though the sodiated Bi phases are much better understood than the Na–M–O matrixes there are still new things to discover. Most of the prior knowledge of these phases comes from the work of Sottmann *et al.* where they showed that nanocrystalline Bi particles formed c-Na₃Bi, and microcrystalline Bi particles formed h-Na₃Bi upon sodiation [34, 199]. They further showed that Bi₂(MoO₄)₃ and BiVO₄ as CAMs for NIBs formed c-Na₃Bi, because of the nanocrystalline nature of the alloying particles inside the Na–M–O matrix [33]. These results are consistent with what we observed for Bi₂MoO₆ (Paper 3 and 5), but not completely for BiFeO₃ as it formed some h-Na₃Bi (Paper 4).

The studies of Sottmann *et al.* also provided an explanation for why the c-Na₃Bi (ordered FCC structure) phase formed in these systems rather than the thermodynamically stable h-Na₃Bi (Na₃As structure) [34]. Certain relationships in the crystal structures of NaBi (CuAu structure) and c-Na₃Bi are likely to make the transformation between these two phases smoother, because it requires less structural rearrangement and bond breaking compared to the NaBi \rightleftharpoons h-Na₃Bi reaction. In nanocrystalline NaBi particles, this smoother transformation into c-Na₃Bi is the most favourable one, while thermodynamics control the transformation of larger particles leading to h-Na₃Bi. Another possible explanation could be limited volume and pressure due to containment by the matrix. The crystal structure of c-Na₃Bi has a smaller volume (113 Å³ per formula unit) compared to h-Na₃Bi (124 Å³ per formula unit), meaning that in a confined space, or under increased pressure, it could be favourable to form c-Na₃Bi. Since most Bi metallates lead to nanocrystalline Na_xBi particles, they tend to form c-Na₃Bi.

The formation of c-Na₃Bi and h-Na₃Bi occur at different voltages. h-Na₃Bi, as the most thermodynamically stable phase, forms at higher potentials (0.51 V) than c-Na₃Bi (0.38 V) during sodiation (Figure 5.3) [34]. Several other factors could also influence the formation potentials as determined from the dQ/dV graphs, however the comparative study of Sottmann *et al.* showed that there is a clear difference in the voltages for formation of these two phases [34]. For BiVO₄ and Bi₂(MoO₄)₃, the peak potentials in dQ/dV for formation of c-Na₃Bi were in the range of 0.39–0.44 V, showing that the exact potential values may vary [33].

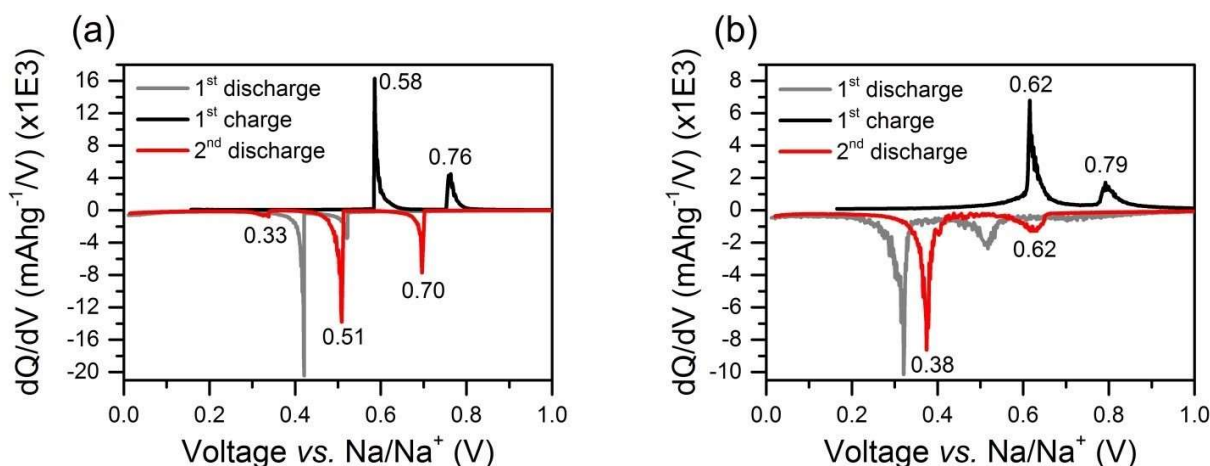


Figure 5.3: dQ/dV plots of a) microcrystalline Bi/C from 20 min ball milling, which forms h- Na_3Bi , and b) nanocrystalline Bi/C from 24 h ball milling, which forms c- Na_3Bi . Reused with permission from [34]. Copyright 2016 American Chemical Society.

From the GC measurements of Bi_2MoO_6 and BiFeO_3 , it is possible to observe the formation of c- Na_3Bi vs h- Na_3Bi by studying the dQ/dV data. The formation potentials during sodiation vary slightly between the different cycles, but there is a clear separation of the peaks corresponding to formation of c- Na_3Bi (0.38–0.45 V) and h- Na_3Bi (0.45–0.51 V, Figure 5.4). *Operando* XRD of Bi_2MoO_6 showed that diffraction peaks of h- Na_3Bi were visible after ~ 10 cycles (Paper 3). This corresponds well with the dQ/dV peak for formation of h- Na_3Bi (~ 0.48 V), which appeared after ~ 8 cycles and gradually replaced the peak for formation of c- Na_3Bi (~ 0.43 V, Figure 5.4a).

Operando XRD data showed that BiFeO_3 formed h- Na_3Bi , in combination with c- Na_3Bi , already during the 1st sodiation (Paper 4). In the dQ/dV graphs, there is a visible bump in the h- Na_3Bi region in cycle 3, which increases in intensity the following cycles (Figure 5.4b). One possible reason for why the peak is not visible for the first two cycles is that the disordered nature of the chemical structures at this stage leads to overlapping peaks and less defined signals. A support to this hypothesis are the shifts in the peaks for both Bi_2MoO_6 and BiFeO_3 as the systems become more ordered during the first cycles (Figure 5.4).

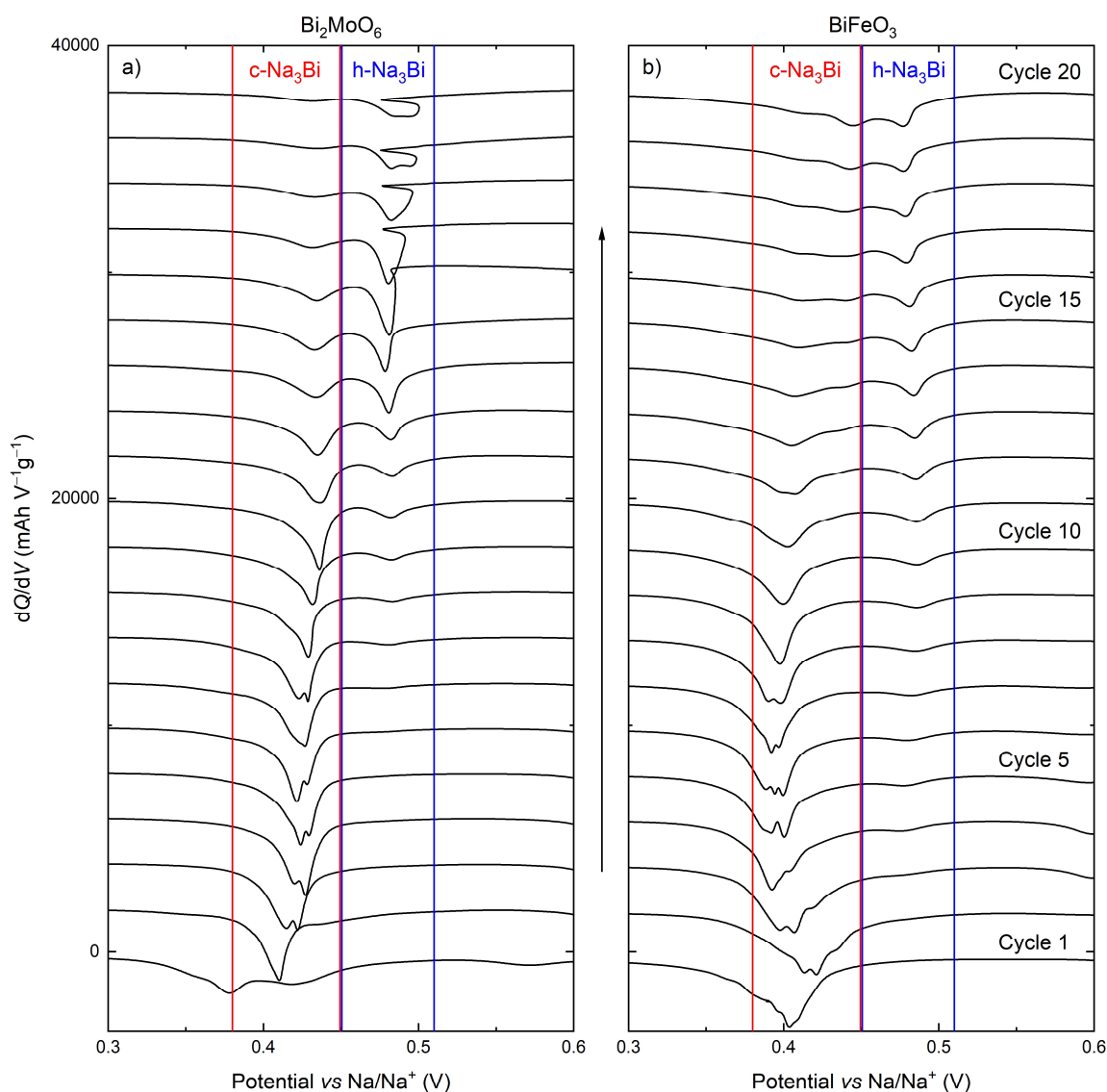


Figure 5.4: dQ/dV plots derived from sodiation curves of GC measurements with a current density of 25 mA g^{-1} and a voltage range of $0.01\text{--}2.00 \text{ V}$ of a) Bi_2MoO_6 and b) BiFeO_3 . The fields between the vertical lines indicate the areas where we expect to observe peaks for the formation of $\text{c-Na}_3\text{Bi}$ (red) and $\text{h-Na}_3\text{Bi}$ (blue) from NaBi . The data are previously unpublished.

One interesting observation is that the peak positions for formation of $\text{c-Na}_3\text{Bi}$ are very similar during the second sodiation for the two systems (0.41 V for Bi_2MoO_6 and 0.42 V for BiFeO_3). In the following cycles, the peaks shift toward higher voltages for Bi_2MoO_6 and lower for BiFeO_3 , reaching 0.43 V (Bi_2MoO_6) and 0.40 V (BiFeO_3) in cycle 10. This could indicate that formation of $\text{c-Na}_3\text{Bi}$ is more thermodynamically favourable in Bi_2MoO_6 than in BiFeO_3 after the second cycle, which partly explains the earlier formation of $\text{h-Na}_3\text{Bi}$ in BiFeO_3 . This difference in formation potential of the $\text{c-Na}_3\text{Bi}$ phases in BiFeO_3 and Bi_2MoO_6 could be an effect of different electrode preparation procedures (electrode thickness, binder and solvent), particle size and morphology. However, it could also be an effect of the different matrixes where the more gradual changes in the Na-Fe-O matrix might not confine the alloying particles as strictly as the Na-Mo-O matrix and, therefore, the stability of the high-pressure $\text{c-Na}_3\text{Bi}$ phase is lower in BiFeO_3 .

The *operando* XRD results of BiFeO₃ for the two first (de)sodiation cycles showed that c-Na₃Bi formed before h-Na₃Bi (Figure 4.12), indicating that c-Na₃Bi transformed into h-Na₃Bi towards the end of sodiation. In Paper 4, we suggested that this could be due to a small sodium deficiency in the c-Na₃Bi phase during formation and that c-Na₃Bi transformed into h-Na₃Bi when the full stoichiometry was obtained. Another explanation could be that Na⁺ at the end of sodiation enters the Na-Fe-O matrix, and not the alloying particles, thus reducing Fe. As discussed in Section 5.3, it is possible that the oxidation state of Fe and the structure of the matrix changes at low potentials. These changes could possibly allow the c-Na₃Bi structure to rearrange and transform into h-Na₃Bi, however, the reasons are not obvious.

The exact reason for the formation of h-Na₃Bi in BiFeO₃ already during the 1st sodiation is not clear. It could possibly be as simple as that BiFeO₃ forms larger NaBi particles than Bi₂MoO₆, during the initial sodiation, hence favouring the thermodynamically stable phase upon alloying. Another explanation could be that the Bi₂O₃ impurities (~12 wt%) in the BiFeO₃ sample is the main cause for formation of h-Na₃Bi. However, the estimated amount of h-Na₃Bi formed in BiFeO₃ from the surface Rietveld refinements in Figure 4.12, is significantly larger than what the Bi₂O₃ impurities can account for. Therefore, at least some of the h-Na₃Bi originates from BiFeO₃.

5.4 Bi metallates in LIBs vs NIBs

This thesis' main focus is on Bi metallates for NIBs, but the results are also relevant for LIBs. Overviews of the electrochemical studies performed on Bi metallates for LIBs and NIBs are provided in Table 5.2 and Table 5.3, respectively. The limited amount of studies along with a wide spread in experimental procedures and results make it very difficult to draw any clear conclusions regarding the relative performance of the different Bi metallates within each of the two battery systems. One difference that can be claimed with some statistical support is that Bi₅Nb₃O₁₅ in general show lower capacities than the rest of the Bi metallates tested for LIBs (Table 5.2).

One thing that is clear from the tables, is that the electrochemical performance of Bi metallates are in general better for LIBs (Table 5.2) than for NIBs (Table 5.3). Two good examples are BiVO₄/C and Bi₂(MoO₄)₃/C composites, that were prepared by ball milling for 20 min, as these have been studied with the same procedures for both LIBs and NIBs. In LIBs, BiVO₄ showed a reversible specific capacity (1st desodiation capacity) of ~570 mAh g⁻¹ [37] and Bi₂(MoO₄)₃ reached ~850 mAh g⁻¹ [38], when cycled between 0.01–2.00 V and a current density of 0.15 A g⁻¹. The corresponding studies in NIBs showed that BiVO₄ obtained a reversible specific capacity of ~350 mAh g⁻¹, while Bi₂(MoO₄)₃ showed ~330 mAh g⁻¹ [33]. Bi₂MoO₆ also show higher reversible capacities in LIBs reaching ~900 mAh g⁻¹ in several studies [40, 43, 200, 201], compared to ~440 mAh g⁻¹ in NIBs as observed in this thesis. This indicates that some redox reactions are utilised in Bi metallates in LIBs that are not present during cycling in NIBs.

Table 5.2: Overview of studies evaluating the electrochemical performance of Bi metallates as anode materials for LIBs. The table shows the name of the compound, approximated specific desodiation capacities from the 1st and 50th cycles, cycling conditions (current density/C-rate and voltage range) and references. Abbreviations for the carbon-based additives in the composites: ECP-N = N-doped Ketjen black, PANI = polyaniline, rGO = reduced graphene oxide, CNT = carbon nanotubes and C = other carbon additives.

Material	Specific desodiation capacities (mAh g ⁻¹)		Cycling conditions	Ref.
	1 st cycle	50 th cycle		
BiVO ₄ /C-20min	570	430	0.15 A g ⁻¹ , 0.01–2.00 V	[37]
	700	480	0.15 A g ⁻¹ , 0.01–2.50 V	
BiVO ₄ /C-20min	850	600	0.15 A g ⁻¹ , 0.01–2.50 V	[36]
BiVO ₄	1180	780	1.1 A g ⁻¹ , 0.01–3.50 V	[202]
Bi ₄ V ₂ O ₁₁	250	90	C/10, 1.0–3.3 V	[203]
Bi ₂ Mn ₄ O ₁₀ /ECP-N	820	580	0.16 A g ⁻¹ , 0.05–3.00 V	[204]
Bi ₂ Mn ₄ O ₁₀ /C	600	570	0.3 A g ⁻¹ , 0.01–3.00 V	[205]
Bi ₂ Mn ₄ O ₁₀	510	220		
Bi ₂ Mn ₄ O ₁₀	850	750	0.2C, 0.01–3.00 V	[206]
Bi ₂ Mn ₄ O ₁₀	600	400	0.16 A g ⁻¹ , 0.05–3.00 V	[207]
BiFeO ₃	750	370	0.56 A g ⁻¹ , 0.5–3.0 V	[208]
BiFeO ₃	750	650	0.1 A g ⁻¹ , 0.001–2.5 V	[209]
Bi ₅ Nb ₃ O ₁₅ /CNT	490	300	0.1 A g ⁻¹ , 0.01–3.00 V	[210]
Bi ₅ Nb ₃ O ₁₅ /C	330	280	0.1 A g ⁻¹ , 0–3 V	[211]
Bi ₅ Nb ₃ O ₁₅	370	300	0.1 A g ⁻¹ , 0–3 V	[212]
BiNbO ₄	160	130	0.1 A g ⁻¹ , 1–3 V	[213]
Bi ₂ (MoO ₄) ₃ /C-20min	980	810	0.15 A g ⁻¹ , 0.01–2.50 V	[38]
	850	350	0.15 A g ⁻¹ , 0.01–2.00 V	
Bi ₂ MoO ₆ /rGO	900	730	0.1 A g ⁻¹ , 0.01–3.00 V	[40]
Bi ₂ MoO ₆ /rGO	450	200	0.1C, 0.2–3.0 V	[41]
Bi ₂ MoO ₆ /C	900	500	0.1 A g ⁻¹ , 0.01–3.00 V	[201]
Bi ₂ MoO ₆ /PANI	760	700	0.1 A g ⁻¹ , 0.01–3.00 V	[43]
Bi ₂ MoO ₆	760	450		
Bi ₂ MoO ₆	900	840	0.05 A g ⁻¹ , 0.01–3.00 V	[200]
Bi ₂ MoO ₆	1100	500	0.5 A g ⁻¹ , 0–3 V	[42]

Table 5.3: Overview of studies evaluating the electrochemical performance of Bi metallates as anode materials for NIBs. The table shows the name of the compound, approximated specific desodiation capacities from the 1st and 50th cycles, cycling conditions (current density/C-rate and voltage range) and references. Abbreviations for the carbon-based additives in the composites: NSG = N- and S-doped graphene, rGO = reduced graphene oxide and C = other carbon additives.

Material	Specific desodiation capacities (mAh g ⁻¹)		Cycling conditions	Ref.
	1 st cycle	50 th cycle		
BiVO ₄ /C-24h	370	350	0.15 A g ⁻¹ , 0.01–2.00 V	[33]
BiVO ₄ /C-20min	350	200		
BiVO ₄ /rGO-5	560	520	0.1 A g ⁻¹ , 0.01–3.00 V	[45]
Black-BiVO ₄ /rGO-400	400	300		
BiVO ₄	630	430	0.1 A g ⁻¹ , 0.01–2.00 V	[44]
BiFeO ₃ /graphene	600	580	0.05 A g ⁻¹ , 0.01–3.00 V	[214]
BiFeO ₃ /pectin	190	120	0.5 A g ⁻¹ , 0.05–2.50 V	[46]
BiFeO ₃	100	60		
BiFeO ₃	500	200	0.1 A g ⁻¹ , 0.01–3.00 V	[31]
BiFeO ₃	550	220	C/20, 0.05–3.00 V	[35]
BiFeO ₃	440	130	0.1 A g ⁻¹ , 0.01–2.00 V	This work
Bi ₂ (MoO ₄) ₃ /C-24h	350	330	0.15 A g ⁻¹ , 0.01–2.00 V	[33]
Bi ₂ (MoO ₄) ₃ /C-20min	330	220		
Bi ₂ MoO ₆ /NSG	600	250	0.2 A g ⁻¹ , 0.01–3.00 V	[39]
Bi ₂ MoO ₆	440	70	0.1 A g ⁻¹ , 0.01–2.00 V	This work
Bi ₄ Ti ₃ O ₁₂	340	90	0.1 A g ⁻¹ , 0.01–2.00 V	This work
Bi ₂ Al ₆ O ₁₂	230	30	0.1 A g ⁻¹ , 0.01–2.00 V	This work

The alloying reactions, $A \rightleftharpoons ABi \rightleftharpoons A_3Bi$ ($A = Li, Na$), should contribute to an equal amount of specific capacity in the two battery systems. Therefore, the extra capacity obtained for LIBs must come from other reactions. One possibility is increased oxidation of Bi metal after dealloying, which was shown to occur for BiFeO₃ and Bi₂MoO₆ in this thesis. This phenomenon was not directly discussed in any of the studies of Bi metallates for LIBs, and the *operando* XANES studies of BiVO₄ and Bi₂(MoO₄)₃ indicated that the final desodiated state was metallic Bi with oxidation state 0 [37, 38]. Therefore, it is more likely that redox activity of the matrix accounts for most of the extra capacity obtained in LIB.

The standard reduction potential of Li⁺ is ~0.3 V lower than for Na⁺, meaning that there is more room for redox reactions at lower potentials in LIBs (compared to NIBs) before

running into the trouble of metal plating. This opens up for the possibility of increased redox activity of the metal (M) in the Na–M–O matrix in LIBs. *Operando* XANES on $\text{Bi}_2(\text{MoO}_4)_3$ showed that Mo was more reduced in LIBs [38] compared to NIBs [33]. The difference in the observed redox activity between LIBs and NIBs was not as large as expected based on the specific capacities from coin cell measurements. This is probably because of issues with the electrochemistry during the *operando* experiment: the measured delithiation capacity of the *operando* experiment was $\sim 550 \text{ mAh g}^{-1}$, compared to $\sim 850 \text{ mAh g}^{-1}$ when cycled in a coin cell [38]. Therefore, the change in oxidation state of Mo is in general expected to be significantly larger than what was shown by the XANES data in the *operando* experiment of $\text{Bi}_2(\text{MoO}_4)_3$ for LIBs [38]. It could be possible that Mo^{6+} is reduced all the way to Mo metal in some of the coin cell measurements of $\text{Bi}_2(\text{MoO}_4)_3$ and Bi_2MoO_6 in LIBs, as is suggested in several studies [38, 39, 41-43, 200], but that still remains to be confirmed. Most of the redox activity of Mo is suggested to occur at potentials $< 0.3 \text{ V vs Li/Li}^+$, which together with the higher reduction potential of Na^+ explain why Mo^{6+} is not reduced to a large degree in NIBs.

The cycling stability of Bi metallates might be better in LIBs compared to NIBs, but it is difficult to draw any clear conclusions from the limited amount of literature. In Section 5.2, we discussed the hypothesis that a stable matrix, which could mitigate coalescence of alloying particles, would be beneficial for the cycling stability. If we continue this train of thought when assessing LIBs it is likely that the cycling stability could be significantly better because the volume expansion of the alloying reactions would be much smaller ($\sim 115 \%$ for $\text{Bi} \rightleftharpoons \text{Li}_3\text{Bi}$ vs $\sim 218\%$ for $\text{Bi} \rightleftharpoons \text{c-Na}_3\text{Bi}$), leading to less strain on the matrix. On the other hand, the increased redox activity of the Na–M–O matrix could lead to a less stable matrix as it will be accompanied by structural changes and bond breaking. However, limiting the voltage range to avoid redox activity of the Na–M–O matrix should mitigate this potential problem.

Another interesting difference is the structure and stability of the Li_xBi and Na_xBi phases. LiBi and NaBi have the same tetragonal crystal structure, apart from the larger unit cell parameters of NaBi , and they have both been observed during cycling of Bi metallates [33, 36–38]. However, there are results suggesting that a transformation directly between $\text{Bi} \rightleftharpoons \text{Li}_3\text{Bi}$, thus skipping the LiBi intermediate, could occur during the first cycle for BiVO_4 [36, 210, 211]. From the data presented in this thesis, there are no signs of such direct transformation from Bi to Na_3Bi occurring for Bi metallates in NIBs. The apparent absence of LiBi in the first cycle could be related to limited time resolution and data quality making it difficult to observe LiBi in the highly disordered system. However, this could also be a potential difference between LIBs and NIBs, which could be explained by the fact that the stability of the ABi phase compared to A_3Bi ($\text{A} = \text{Li, Na, K, Rb, Cs}$) increases with the size of the alkali metal [174].

The most thermodynamically stable Li_3Bi phase has a cubic crystal structure with the same structure type as $\text{c-Na}_3\text{Bi}$. There are theoretical calculations showing that $\text{h-Li}_3\text{Bi}$ has an formation energy of 0.01 eV above the hull [174], but it has so far not been observed experimentally. The difference in size between Bi and the alkali ions could offer an explanation for the relative stability between the cubic and hexagonal polymorphs of A_3Bi . The cubic polymorphs are thermodynamically stable for Li_3Bi and Cs_3Bi , where the

size difference between cation and anion are the largest, while the other A_3Bi phases with more equally sized ions are most stable in a hexagonal crystal structure [174].

As discussed previously it is predicted that the transformation from the tetragonal $LiBi/NaBi$ structure to the cubic Li_3Bi/Na_3Bi structure is smoother compared to formation of the hexagonal phases. In addition, the confined space for the alloying particles inside the $Na-M-O$ matrix formed in Bi metallates could also favour the formation of the cubic phases. Hence there are some factors that could lead to formation of $c-Na_3Bi$, while thermodynamics favour the formation of $h-Na_3Bi$. For Li , all these factors dictates that $c-Li_3Bi$ should form, which could explain why $h-Li_3Bi$ has not observed experimentally. In the Li system it has been experimentally shown that it is possible to synthesise Li_2Bi in a hexagonal crystal structure (P-62c) [215]. Na_2Bi structures have also been predicted to be stable, but only at high pressures, and it has not yet been observed experimentally [216]. The structure of Li_2Bi is very different from both $LiBi$ and $c-Li_3Bi$ and would include large structural rearrangements to form during electrochemical cycling. Therefore, it is not likely that Li_2Bi would be formed during electrochemical lithiation of Bi and the transformation directly between $LiBi$ and $c-Li_3Bi$ is observed instead.

6. Concluding remarks and outlook

The work in this thesis provided new insight into the cycling and degradation mechanisms of Bi metallates by utilising a combination of extensive *ex situ* measurements combined with state-of-the-art *operando* X-ray characterisation: diffraction, PDF and XAS. Electrochemical evaluation of four different Bi metallates (BiFeO_3 , Bi_2MoO_6 , $\text{Bi}_4\text{Ti}_3\text{O}_{12}$ and $\text{Bi}_2\text{Al}_6\text{O}_{12}$), showed that they have similar cycling mechanisms and performance. All the tested Bi metallates maintained their performance well when subjected to a high current density of 1 A g^{-1} , indicating good rate capabilities. By the combination of *operando* XRD and *ex situ* XAS, the general cycling mechanism of Bi metallates (exemplified by Bi_2MoO_6 and BiFeO_3) was confirmed: an irreversible conversion reaction during the first sodiation forms Bi nanoparticles embedded in a Na–M–O matrix, where Bi further reversibly alloys with Na forming Na_3Bi via NaBi as an intermediate phase. *Operando* XRD at 0.1 and 1 A g^{-1} of BiFeO_3 showed that the cycling mechanism was the same at the two different current densities.

It was discovered that Bi obtains a positive oxidation state during desodiation. This is interpreted as a result of Bi–O bonds forming at the interphase between the Bi particles and the Na–M–O matrix on oxidation. This reaction explains some of the discrepancies between the theoretical and experimental capacity for these materials. Other factors contributing to the calculated specific capacities include: sodiation of the carbon additive, SEI formation, weighing uncertainties and for some Bi metallates (for example BiFeO_3) redox activity of the matrix. All these reactions complicate the analysis of electrochemical measurements.

To obtain acceptable control over the tested systems and mitigate misinterpretations of the data, we conducted a series of reference measurements. This included measuring 120 coin cells that were supposed to be identical, where the measured specific capacities of the 1st and 2nd sodiation showed a standard deviation of slightly less than 10%. Further we evaluated how different parameters affected the electrochemical performance, including: electrolyte, binder, electrode thickness, preparation procedures and measurement protocols. The only clear significant difference in cycling behaviour was observed when the upper cut-off voltage was decreased to 0.7 V as this strongly improved the cycling stability. These results does not show that the other parameters are irrelevant for electrochemical performance, but within the limited selection of variables in this study, no clear correlation was found. Testing a broader range of electrolytes and binder systems in a more systematic way, than what was presented in this thesis, will probably discover significant differences.

In order to be able to systematically and quantitatively compare the performance of different Bi metallates (and other battery materials) it is important to know the effect of parameters other than the active material. The electrochemical studies of Bi metallates in literature use different carbon additives, electrolytes, electrode preparation procedures and measurement protocols, making it difficult to systematically compare the studies. Implementing standard testing procedures might be difficult to achieve, but would help immensely when assessing the effect of changing the chemical composition of the Bi metallates. A more realistic target is to ensure that publications must include several electrochemical measurements of the same system with an assessment of the

uncertainties in the reported specific capacities. In addition, it is important to provide accurate experimental details regarding the procedures and assumptions that affect the reported results.

There are clear indications that creating composites between Bi metallates (and other CAMs) and carbon additives (e.g. rGO, CNT) could improve the electrochemistry of the materials drastically. The seemingly improved performance could be explained by increased electronic conductivity of the material due to the carbon composite and the ability of better handling volume expansions of the active material. However, in most studies it is unclear exactly what is due to the composite fabrication and what is due to other factors in the electrochemical characterisation. It is also likely that the composites have to be synthesised in specific ways for the carbon additive to have its desired effect, probably including nanosized particles of the Bi metallates in close contact with the additive throughout the sample. In other words, it is many ways of synthesising poorly performing composites, but since failed attempts are seldom reported one might get the impression that the carbon additives consistently improve all type of materials. Nevertheless, it is likely that properly synthesised composite materials could have significantly better electrochemical performance than the pure Bi metallates. Understanding how to synthesise these composites properly and understanding how they change the cycling mechanisms and improve the performance of the materials may be of great value.

Operando measurements add an extra layer of complexity and challenges as it combines electrochemical and structural measurements. This thesis discuss some of the challenges regarding the effect of beam damage, strong scattering effects from Na-metal counter electrodes and varying electrochemistry in *operando* cells. Scanning the X-ray beam over a larger area of the sample proved successful for reducing the effect of beam damage and preparing the Na electrode by folding the Na metal several times reduced the scattering problem of the counter electrode. The various designs of *operando* cells might lead to differences in electrochemistry that deviates from coin cell data, as experienced in the work leading to this thesis. It is therefore important with proper electrochemical tests of the cells before conducting the *operando* measurements.

The *operando* XRD studies of BiFeO₃ and Bi₂MoO₆ revealed a difference between the two systems in the fully sodiated state where BiFeO₃ formed a combination of h-Na₃Bi and c-Na₃Bi, while Bi₂MoO₆ formed only c-Na₃Bi. There were also differences in the activities of the matrixes, where the Na-Fe-O matrix showed some redox on Fe³⁺, while the Na-Mo-O matrix did not show any change in oxidation state for Mo⁶⁺. However, Mo⁶⁺ changed coordination from distorted octahedral in sodiated samples to tetrahedral in desodiated samples. *Operando* XAS indicated that this change of coordination occurred at ~0.7 V during desodiation. Hence, the matrix could be stable and prevent coalescence of the alloying particles when cycled below this voltage, which could explain why Bi₂MoO₆ showed significantly better cycling stability with an upper cut-off voltage of 0.7 V instead of 2.0 V.

By performing *operando* XRD over the course of >20 cycles we highlighted important aspects of the degradation mechanisms of Bi₂MoO₆ and BiFeO₃, which could be valid for Bi metallates in general. These results, together with *ex situ* XAS measurements of the Bi

L3 edge, showed that both materials undergo a 3-step capacity degradation where each step corresponds to the deactivation of one chemical reaction. The first step was the deactivation of the formation of B–O bonds at the interface between the Bi particles and the Na–M–O matrix. The second step was the deactivation of the $\text{Bi} \rightleftharpoons \text{NaBi}$ reaction, while the third step was an increased irreversibility in the $\text{NaBi} \rightleftharpoons \text{Na}_3\text{Bi}$ reaction. The system was partially locked in the sodiated state as *operando* and *ex situ* XRD indicated a significant amount of inactive Na_3Bi . The measurements also showed a clear increase in average crystallite size of the alloying particles as a function of cycle number, probably caused by coalescence, thus increasing transport distances of the charge carriers and the impedance in the material. This is considered as the main driver for capacity degradation.

We have obtained a lot of new knowledge regarding the cycling and degradation mechanisms of Bi metallates, by performing *operando* XRD over >20 cycles, *operando* XRD at high rate and a combined *operando* PDF/XAS measurement. However, there is still much more to learn about these complex systems. The conclusions concerning the capacity degradation are mainly based on *ex situ* measurements. With *operando* PDF/XAS at later stages of cycling, we could ensure that these results were not affected by measurements of reacted samples and draw more detailed conclusions with greater confidence.

One aspect that should be investigated further is the differences in cycling mechanisms of Bi_2MoO_6 and BiFeO_3 with an upper cut-off voltage of 0.7 V, compared to 2.0 V, to understand why the cycling stability is significantly better with the lower cut-off voltage. Particularly an *operando* XAS measurement of the Mo K edge, to observe possible changes in the Na–Mo–O matrix below 0.7 V, would directly prove if our hypothesis stating that the matrix does not change structure within this voltage range is correct. Combining this with XRD studies revealing potential crystallite growth of the alloying particles for the first 20 cycles with 0.7 V as upper cut-off voltage would also prove if the matrix is able to prevent the coalescence of the alloying particles. Hence, it would show if it is this coalescence that is the determining factor for the cycling stability. Other techniques that could bring us further down the path towards full understanding of the cycling mechanism of Bi metallates are total scattering computed tomography (TSCT) techniques including small angle X-ray scattering computed tomography (SAXS-CT) in *operando* mode. These measurements will enable us to obtain new information regarding changes in particle sizes and inhomogeneities throughout the whole electrode with chemical phase information at both nano and micro scale.

The structure and properties of the matrixes formed in Bi metallates are still not well understood. In order to obtain further understanding it may be sensible to systematically synthesise and study the properties of amorphous and crystalline Na–M–O and M–O phases that are suggested to form upon reduction of the Bi metallates. Furthermore, developing alternative synthesis routes for forming Bi particles embedded in a Na–M–O matrix could potentially solve the problem of the low initial Coulombic efficiency, in addition to increasing our understanding of these systems.

As was shown in this thesis, it is possible to create nanoparticles of Na_xBi embedded inside a Na–M–O matrix with different compositions and sizes by the means of electrochemical (de)sodiation. By varying the cycling rate and voltage windows, we believe that it is

possible to accurately control the sizes of the alloying particles. This would likely also be the case for other CAMs, meaning that electrochemical sodiation (or lithiation) of CAMs could be used as a general synthesis method for creating metallic or semiconducting nanoparticles embedded inside a matrix, hopefully also with a capability to accurately control and tune compositions, particle sizes and properties of the materials. This could potentially be of interest to other fields than battery research, for example, catalysis and electronics.

There are certain similarities and differences between the cycling mechanisms of Bi metallates in LIBs vs NIBs. The main conversion and alloying reactions are similar for Bi metallates in the two battery systems, but the measured specific capacity is in general significantly higher for LIBs. This is explained by the increased redox activity of the matrix, probably due to the more negative reduction potential of Li^+ compared to Na^+ . Both the cubic and hexagonal versions of Na_3Bi could form from Bi metallates in NIBs, while for LIBs only the cubic polymorph (c- Li_3Bi) is formed. The reason why c- Na_3Bi forms instead of the thermodynamically stable h- Na_3Bi is likely because of a smoother phase transformation between NaBi and c- Na_3Bi requiring less structural rearrangements and bond breaking. For Li, both thermodynamics and the structural relations between LiBi and the Li_3Bi polymorphs predict a formation of c- Li_3Bi , which explains why h- Li_3Bi has still not been observed experimentally. It could be interesting to continue studying the conditions for forming the various A_xBi phases, especially with regards to formation of c- Na_3Bi vs h- Na_3Bi . As shown previously, c- Na_3Bi forms from nanosized NaBi particles while h- Na_3Bi forms from microsized particles [34], but the exact crossover point is not known. Therefore, it would be interesting to study sodiation of Bi particles of several different sizes in the range of 1–100 nm to determine when each of the polymorphs form and if they can coexist in the same particle. In that way it could be possible to predict and control the formation of c- Na_3Bi vs h- Na_3Bi .

In order to identify and understand more of the subtle, yet important differences between LIBs and NIBs, with regards to performance and cycling mechanisms of Bi metallates and other CAMs, it is important to perform proper comparative studies with similar experimental procedures. The *operando* XANES and XRD measurements performed by Ruud *et al.* [37, 38] and Sottmann *et al.* [33] on BiVO_4 and $\text{Bi}_2(\text{MoO}_4)_3$ are good examples of studies that can be used to extract some differences between LIBs and NIBs. We need more of these type of *operando* studies for different materials and proper control of both the electrochemistry and the structural measurements.

Bi metallates will most likely not find their way into commercial NIBs or LIBs as anode materials, because of their limited electrochemical performance and the limited abundance of Bi. However, the used methods, ideas and obtained knowledge from this PhD work could be transferred to promising CAMs with better electrochemical performance. Hopefully, this could finally lead to high-performing and abundant CAMs that will be used in commercial NIBs in the future.

7. References

- [1] C. E. Skautvedt, "Syntese og karakterisering av BiFeO₃ som anodemateriale i Na-ionebatterier", Master thesis, University of Oslo, 2022.
- [2] Independent Group of Scientists appointed by the Secretary-General, *Global sustainable Development Report 2023: Times of crisis, times of change: Science for accelerating transformations to sustainable development*, (United Nations, New York, 2023).
- [3] DNV, *Energy Transition Outlook 2023*, DNV, 2023.
- [4] IPCC [Core Writing Team, H. Lee and J. Romero (eds.)], *Climate Change 2023: Synthesis Report. Contribution of Working Groups I, II and III to the Sixth Assessment Report of the Intergovernmental Panel on Climate Change*, IPCC, Geneva, Switzerland, 2023.
- [5] European Commission, *Report on Raw Materials for Battery Applications*, Brussels, 2018.
- [6] K. Chayambuka, G. Mulder, D. L. Danilov, and P. H. Notten, "From li-ion batteries toward Na-ion chemistries: challenges and opportunities," *Advanced energy materials*, **2020**, 10(38), 2001310.
- [7] T. Hosaka, K. Kubota, A. S. Hameed, and S. Komaba, "Research development on K-ion batteries," *Chemical reviews*, **2020**, 120(14), 6358-6466.
- [8] Y. Liang, H. Dong, D. Aurbach, and Y. Yao, "Current status and future directions of multivalent metal-ion batteries," *Nature Energy*, **2020**, 5(9), 646-656.
- [9] L. Stievano, I. de Meazza, J. Bitenc, C. Cavallo, S. Brutti, and M. A. Navarra, "Emerging calcium batteries," *Journal of Power Sources*, **2021**, 482, 228875.
- [10] C. Sun and H. Zhang, "Review of the development of first-generation redox flow batteries: iron-chromium system," *ChemSusChem*, **2022**, 15(1), e202101798.
- [11] K. Lourenssen, J. Williams, F. Ahmadpour, R. Clemmer, and S. Tasnim, "Vanadium redox flow batteries: A comprehensive review," *Journal of Energy Storage*, **2019**, 25, 100844.
- [12] P. Mao, H. Arandiyani, S. S. Mofarah, P. Koshy, C. Pozo-Gonzalo, R. Zheng, Z. Wang, Y. Wang, S. K. Bhargava, and H. Sun, "A comprehensive review of cathode materials for Na-air batteries," *Energy Advances*, **2023**.
- [13] J.-W. Jung, S.-H. Cho, J. S. Nam, and I.-D. Kim, "Current and future cathode materials for non-aqueous Li-air (O₂) battery technology—A focused review," *Energy Storage Materials*, **2020**, 24, 512-528.
- [14] S. H. Chung and A. Manthiram, "Current status and future prospects of metal-sulfur batteries," *Advanced Materials*, **2019**, 31(27), 1901125.
- [15] B. K. Sovacool, "The precarious political economy of cobalt: Balancing prosperity, poverty, and brutality in artisanal and industrial mining in the Democratic Republic of the Congo," *The Extractive Industries and Society*, **2019**, 6(3), 915-939.
- [16] M. J. Winter, "Diffusion cartograms for the display of periodic table data," *Journal of Chemical Education*, **2011**, 88(11), 1507-1510.
- [17] T. Helmenstine. "Abundance of Elements in Earth's Crust - Periodic Table and List." 2018, <https://sciencenotes.org/abundance-of-elements-in-earths-crust-periodic-table-and-list/> (accessed 19.10.2023, 2023).
- [18] T. Helmenstine. "Abundance of Elements in Seawater - Periodic Table and List." 2018, <https://sciencenotes.org/abundance-of-elements-in-earths-oceans-periodic-table-and-list/> (accessed 19.10.2023, 2023).
- [19] Y. Gokhale. "Sodium-ion batteries | Current status of the technology and supply chain." 2023, EVreporter. <https://evreporter.com/sodium-ion-batteries-current-status-of-the-technology-and-supply-chain/> (accessed 19.10.2023, 2023).
- [20] Northvolt. "Northvolt develops state-of-the-art sodium-ion battery validated at 160 Wh/kg." 2023, Northvolt. <https://northvolt.com/articles/northvolt-sodium-ion/> (accessed 21.11.2023, 2023).
- [21] Y. Li, Y. S. Hu, M. M. Titirici, L. Chen, and X. Huang, "Hard carbon microtubes made from renewable cotton as high-performance anode material for sodium-ion batteries," *Advanced energy materials*, **2016**, 6(18), 1600659.

- [22] A. Beda, C. Villevieille, P.-L. Taberna, P. Simon, and C. M. Ghimbeu, "Self-supported binder-free hard carbon electrodes for sodium-ion batteries: insights into their sodium storage mechanisms," *Journal of Materials Chemistry A*, **2020**, 8(11), 5558-5571.
- [23] H. Zhang, I. Hasa, and S. Passerini, "Beyond Insertion for Na-Ion Batteries: Nanostructured Alloying and Conversion Anode Materials," *Advanced Energy Materials*, **2018**, 8(17), 1702582.
- [24] J. Zhou, X. Liu, W. Cai, Y. Zhu, J. Liang, K. Zhang, Y. Lan, Z. Jiang, G. Wang, and Y. Qian, "Wet-Chemical Synthesis of Hollow Red-Phosphorus Nanospheres with Porous Shells as Anodes for High-Performance Lithium-Ion and Sodium-Ion Batteries," *Advanced Materials*, **2017**, 29(29), 1700214.
- [25] J. Fullenwarth, A. Darwiche, A. Soares, B. Donnadieu, and L. Monconduit, "NiP₃: a promising negative electrode for Li- and Na-ion batteries," *Journal of Materials Chemistry A*, **2014**, 2(7), 2050-2059.
- [26] L. Fang, N. Bahlawane, W. Sun, H. Pan, B. B. Xu, M. Yan, and Y. Jiang, "Conversion-alloying anode materials for sodium ion batteries," *Small*, **2021**, 17(37), 2101137.
- [27] L. Wang, J. Światowska, S. Dai, M. Cao, Z. Zhong, Y. Shen, and M. Wang, "Promises and challenges of alloy-type and conversion-type anode materials for sodium-ion batteries," *Materials today energy*, **2019**, 11, 46-60.
- [28] J. Fei, Y. Cui, J. Li, Z. Xu, J. Yang, R. Wang, Y. Cheng, and J. Hang, "A flexible Sb₂O₃/carbon cloth composite as a free-standing high performance anode for sodium ion batteries," *Chemical Communications*, **2017**, 53(98), 13165-13167.
- [29] Y. Lu, N. Zhang, S. Jiang, Y. Zhang, M. Zhou, Z. Tao, L. A. Archer, and J. Chen, "High-Capacity and Ultrafast Na-Ion Storage of a Self-Supported 3D Porous Antimony Persulfide-Graphene Foam Architecture," *Nano Letters*, **2017**, 17(6), 3668-3674.
- [30] X. Lu, Z. Wang, K. Liu, J. Luo, P. Wang, C. Niu, H. Wang, and W. Li, "Hierarchical Sb₂MoO₆ microspheres for high-performance sodium-ion battery anode," *Energy Storage Materials*, **2019**, 17, 101-110.
- [31] L. Durai, B. Moorthy, C. I. Thomas, D. K. Kim, and K. K. Bharathi, "Electrochemical properties of BiFeO₃ nanoparticles: anode material for sodium-ion battery application," *Materials Science in Semiconductor Processing*, **2017**, 68, 165-171.
- [32] M.-K. Kim, S.-H. Yu, A. Jin, J. Kim, I.-H. Ko, K.-S. Lee, J. Mun, and Y.-E. Sung, "Bismuth oxide as a high capacity anode material for sodium-ion batteries," *Chemical Communications*, **2016**, 52(79), 11775-11778.
- [33] J. Sottmann, M. Herrmann, P. Vajeeston, A. Ruud, C. Drathen, H. Emerich, D. S. Wragg, and H. Fjellvåg, "Bismuth Vanadate and Molybdate: Stable Alloying Anodes for Sodium-Ion Batteries," *Chemistry of Materials*, **2017**, 29(7), 2803-2810.
- [34] J. Sottmann, M. Herrmann, P. Vajeeston, Y. Hu, A. Ruud, C. Drathen, H. Emerich, H. Fjellvåg, and D. S. Wragg, "How Crystallite Size Controls the Reaction Path in Nonaqueous Metal Ion Batteries: The Example of Sodium Bismuth Alloying," *Chemistry of Materials*, **2016**, 28(8), 2750-2756.
- [35] A. Surendran, H. Enale, A. Thottungal, A. Sarapulova, M. Knapp, S. Nishanthi, D. Dixon, and A. Bhaskar, "Unveiling the Electrochemical Mechanism of High-Capacity Negative Electrode Model-System BiFeO₃ in Sodium-Ion Batteries: An In Operando XAS Investigation," *ACS applied materials & interfaces*, **2022**, 14(6), 7856-7868.
- [36] J. Sottmann, A. Ruud, Ø. S. Fjellvåg, G. B. M. Vaughan, M. Di Michel, H. Fjellvåg, O. I. Lebedev, P. Vajeeston, and D. S. Wragg, "5D total scattering computed tomography reveals the full reaction mechanism of a bismuth vanadate lithium ion battery anode," *Physical Chemistry Chemical Physics*, **2022**, 24(44), 27075-27085.
- [37] A. Ruud, J. Sottmann, P. Vajeeston, and H. Fjellvåg, "Operando investigations of lithiation and delithiation processes in a BiVO₄ anode material," *Physical Chemistry Chemical Physics*, **2018**, 20(47), 29798-29803.
- [38] A. Ruud, J. Sottmann, P. Vajeeston, and H. Fjellvåg, "Direct observation of reversible conversion and alloying reactions in a Bi₂(MoO₄)₃-based lithium-ion battery anode," *Journal of Materials Chemistry A*, **2019**, 7(30), 17906-17913.

- [39] X. Xu, M. Li, and T. Yu, "Facile Synthesis of Bi₂MoO₆ Nanosheets@Nitrogen and Sulfur Codoped Graphene Composites for Sodium-ion Batteries," *Chemical Research in Chinese Universities*, **2020**, 36(1), 115-119.
- [40] X. Zhai, J. Gao, R. Xue, X. Xu, L. Wang, Q. Tian, and Y. Liu, "Facile synthesis of Bi₂MoO₆/reduced graphene oxide composites as anode materials towards enhanced lithium storage performance," *Journal of colloid and interface science*, **2018**, 518, 242-251.
- [41] M. Shetty, M. Murthy, M. Shastri, M. Sindhusree, H. Nagaswarupa, P. D. Shivaramu, and D. Rangappa, "Hydrothermally synthesized Bi₂MoO₆/Reduced Graphene Oxide composite as anodes for lithium-ion batteries," *Ceramics International*, **2019**, 45(18), 24965-24970.
- [42] S. Yuan, Y. Zhao, W. Chen, C. Wu, X. Wang, L. Zhang, and Q. Wang, "Self-assembled 3D hierarchical porous Bi₂MoO₆ microspheres toward high capacity and ultra-long-life anode material for Li-ion batteries," *ACS Applied Materials & Interfaces*, **2017**, 9(26), 21781-21790.
- [43] Y. Zhang, G. Zhao, P. Ge, T. Wu, L. Li, P. Cai, C. Liu, G. Zou, H. Hou, and X. Ji, "Bi₂MoO₆ microsphere with double-polyaniline layers toward ultrastable lithium energy storage by reinforced structure," *Inorganic chemistry*, **2019**, 58(9), 6410-6421.
- [44] R. Muruganantham and W. R. Liu, "A Venture Synthesis and Fabrication of BiVO₄ as a Highly Stable Anode Material for Na-Ion Batteries," *ChemistrySelect*, **2017**, 2(26), 8187-8195.
- [45] X. Xu, Y. Xu, F. Xu, G. Jiang, J. Jian, H. Yu, E. Zhang, D. Shchukin, S. Kaskel, and H. Wang, "Black BiVO₄: size tailored synthesis, rich oxygen vacancies, and sodium storage performance," *Journal of Materials Chemistry A*, **2020**, 8(4), 1636-1645.
- [46] B. Sun, S. Mao, S. Zhu, G. Zhou, Y. Xia, and Y. Zhao, "Improved rate and cycling performances of electrodes based on BiFeO₃ nanoflakes by compositing with organic pectin for advanced rechargeable Na-ion batteries," *ACS Applied Nano Materials*, **2018**, 1(3), 1291-1299.
- [47] C. Daniel and J. O. Besenhard, *Handbook of Battery Materials* 2nd ed. USA: Wiley-VCH, 2011.
- [48] Y. Chu, Y. Shen, F. Guo, X. Zhao, Q. Dong, Q. Zhang, W. Li, H. Chen, Z. Luo, and L. Chen, "Advanced characterizations of solid electrolyte interphases in lithium-ion batteries," *Electrochemical energy reviews*, **2020**, 3, 187-219.
- [49] Sungjemmenla, V. SK, C. B. Soni, V. Kumar, and Z. W. Seh, "Understanding the Cathode-Electrolyte Interphase in Lithium-Ion Batteries," *Energy Technology*, **2022**, 10(9), 2200421.
- [50] L. A. Ma, A. J. Naylor, L. Nyholm, and R. Younesi, "Strategies for mitigating dissolution of solid electrolyte interphases in sodium-ion batteries," *Angewandte Chemie International Edition*, **2021**, 60(9), 4855-4863.
- [51] F. Sauvage, L. Laffont, J.-M. Tarascon, and E. Baudrin, "Factors affecting the electrochemical reactivity vs. lithium of carbon-free LiFePO₄ thin films," *Journal of Power Sources*, **2008**, 175(1), 495-501.
- [52] D. Linden, T. B. Reddy, *Handbook of Batteries*. New York: McGraw-Hill, 2002.
- [53] D. P. Finegan, A. Quinn, D. S. Wragg, A. M. Colclasure, X. Lu, C. Tan, T. M. Heenan, R. Jervis, D. J. Brett, and S. Das, "Spatial dynamics of lithiation and lithium plating during high-rate operation of graphite electrodes," *Energy & Environmental Science*, **2020**, 13(8), 2570-2584.
- [54] M. Z. Bazant, "Theory of chemical kinetics and charge transfer based on nonequilibrium thermodynamics," *Accounts of chemical research*, **2013**, 46(5), 1144-1160.
- [55] H. Liu, F. C. Strobridge, O. J. Borkiewicz, K. M. Wiaderek, K. W. Chapman, P. J. Chupas, and C. P. Grey, "Capturing metastable structures during high-rate cycling of LiFePO₄ nanoparticle electrodes," *Science*, **2014**, 344(6191), 1252817.
- [56] X. Zhang, M. van Hulzen, D. P. Singh, A. Brownrigg, J. P. Wright, N. H. van Dijk, and M. Wagemaker, "Direct view on the phase evolution in individual LiFePO₄ nanoparticles during Li-ion battery cycling," *Nature Communications*, **2015**, 6(1), 8333.
- [57] M. Lao, Y. Zhang, W. Luo, Q. Yan, W. Sun, and S. X. Dou, "Alloy-based anode materials toward advanced sodium-ion batteries," *Advanced Materials*, **2017**, 29(48), 1700622.

- [58] Z. Zhang, R. Wang, J. Zeng, K. Shi, C. Zhu, and X. Yan, "Size effects in sodium ion batteries," *Advanced Functional Materials*, **2021**, 31(52), 2106047.
- [59] J. Wang, C. Eng, Y.-c. K. Chen-Wiegart, and J. Wang, "Probing three-dimensional sodiation-desodiation equilibrium in sodium-ion batteries by in situ hard X-ray nanotomography," *Nature communications*, **2015**, 6(1), 7496.
- [60] K. Momma and F. Izumi, "VESTA 3 for three-dimensional visualization of crystal, volumetric and morphology data," *Journal of applied crystallography*, **2011**, 44(6), 1272-1276.
- [61] K. Momma and F. Izumi, "VESTA: a three-dimensional visualization system for electronic and structural analysis," *Journal of Applied crystallography*, **2008**, 41(3), 653-658.
- [62] N. Yabuuchi, K. Kubota, M. Dahbi, and S. Komaba, "Research development on sodium-ion batteries," *Chemical reviews*, **2014**, 114(23), 11636-11682.
- [63] S. Mukherjee, S. Bin Mujib, D. Soares, and G. Singh, "Electrode materials for high-performance sodium-ion batteries," *Materials*, **2019**, 12(12), 1952.
- [64] Y. Yu, *Sodium-ion Batteries: Energy Storage Materials and Technologies*. John Wiley & Sons, 2022.
- [65] Q. Liu, Z. Hu, M. Chen, C. Zou, H. Jin, S. Wang, S. L. Chou, and S. X. Dou, "Recent progress of layered transition metal oxide cathodes for sodium-ion batteries," *Small*, **2019**, 15(32), 1805381.
- [66] C. Delmas, C. Fouassier, and P. Hagenmuller, "Structural classification and properties of the layered oxides," *Physica B+ c*, **1980**, 99(1-4), 81-85.
- [67] F. Ding, C. Zhao, D. Zhou, Q. Meng, D. Xiao, Q. Zhang, Y. Niu, Y. Li, X. Rong, Y. Lu, L. Chen, and Y.-S. Hu, "A Novel Ni-rich O3-Na[Ni_{0.60}Fe_{0.25}Mn_{0.15}]O₂ Cathode for Na-ion Batteries," *Energy Storage Materials*, **2020**, 30, 420-430.
- [68] N. Su, Y. Lyu, and B. Guo, "Electrochemical and in-situ X-ray diffraction studies of Na_{1.2}Ni_{0.2}Mn_{0.2}Ru_{0.4}O₂ as a cathode material for sodium-ion batteries," *Electrochemistry Communications*, **2018**, 87, 71-75.
- [69] X. Zhang, K. Jiang, S. Guo, X. Mu, X. Zhang, P. He, M. Han, and H. Zhou, "Exploring a high capacity O3-type cathode for sodium-ion batteries and its structural evolution during an electrochemical process," *Chemical Communications*, **2018**, 54(86), 12167-12170.
- [70] Y. Xiao, P.-F. Wang, Y.-X. Yin, Y.-F. Zhu, Y.-B. Niu, X.-D. Zhang, J. Zhang, X. Yu, X.-D. Guo, B.-H. Zhong, and Y.-G. Guo, "Exposing {010} Active Facets by Multiple-Layer Oriented Stacking Nanosheets for High-Performance Capacitive Sodium-Ion Oxide Cathode," *Advanced Materials*, **2018**, 30(40), 1803765.
- [71] L. Sun, Y. Xie, X.-Z. Liao, H. Wang, G. Tan, Z. Chen, Y. Ren, J. Gim, W. Tang, Y.-S. He, K. Amine, and Z.-F. Ma, "Insight into Ca-Substitution Effects on O3-Type NaNi_{1/3}Fe_{1/3}Mn_{1/3}O₂ Cathode Materials for Sodium-Ion Batteries Application," *Small*, **2018**, 14(21), 1704523.
- [72] B. M. de Boisse, J.-H. Cheng, D. Carlier, M. Guignard, C.-J. Pan, S. Bordere, D. Filimonov, C. Drathen, E. Suard, and B.-J. Hwang, "O3-Na_xMn_{1/3}Fe_{2/3}O₂ as a positive electrode material for Na-ion batteries: structural evolutions and redox mechanisms upon Na⁺(de) intercalation," *Journal of Materials Chemistry A*, **2015**, 3(20), 10976-10989.
- [73] J. Wang, X. He, D. Zhou, F. Schappacher, X. Zhang, H. Liu, M. C. Stan, X. Cao, R. Kloepsch, M. S. Sofy, G. Schumacher, and J. Li, "O3-type Na[Fe_{1/3}Ni_{1/3}Ti_{1/3}]O₂ cathode material for rechargeable sodium ion batteries," *Journal of Materials Chemistry A*, **2016**, 4(9), 3431-3437.
- [74] L. Mu, S. Xu, Y. Li, Y. S. Hu, H. Li, L. Chen, and X. Huang, "Prototype sodium-ion batteries using an air-stable and Co/Ni-free O3-layered metal oxide cathode," *Advanced materials*, **2015**, 27(43), 6928-6933.
- [75] Y. Yu, W. Kong, Q. Li, D. Ning, G. Schuck, G. Schumacher, C. Su, and X. Liu, "Understanding the Multiple Effects of TiO₂ Coating on NaMn_{0.33}Fe_{0.33}Ni_{0.33}O₂ Cathode Material for Na-Ion Batteries," *ACS Applied Energy Materials*, **2020**, 3(1), 933-942.
- [76] K. Kubota, T. Asari, H. Yoshida, N. Yaabuuchi, H. Shiiba, M. Nakayama, and S. Komaba, "Understanding the Structural Evolution and Redox Mechanism of a NaFeO₂-NaCoO₂ Solid

- Solution for Sodium-Ion Batteries," *Advanced Functional Materials*, **2016**, 26(33), 6047-6059.
- [77] P.-F. Wang, H.-R. Yao, X.-Y. Liu, J.-N. Zhang, L. Gu, X.-Q. Yu, Y.-X. Yin, and Y.-G. Guo, "Ti-Substituted $\text{NaNi}_{0.5}\text{Mn}_{0.5-x}\text{Ti}_x\text{O}_2$ Cathodes with Reversible O3-P3 Phase Transition for High-Performance Sodium-Ion Batteries," *Advanced Materials*, **2017**, 29(19), 1700210.
- [78] Y. Xiao, Y.-F. Zhu, H.-R. Yao, P.-F. Wang, X.-D. Zhang, H. Li, X. Yang, L. Gu, Y.-C. Li, T. Wang, Y.-X. Yin, X.-D. Guo, B.-H. Zhong, and Y.-G. Guo, "A Stable Layered Oxide Cathode Material for High-Performance Sodium-Ion Battery," *Advanced Energy Materials*, **2019**, 9(19), 1803978.
- [79] E. Marelli, C. Villevieille, S. Park, N. Hérault, and C. Marino, "Co-Free P2- $\text{Na}_{0.67}\text{Mn}_{0.6}\text{Fe}_{0.25}\text{Al}_{0.15}\text{O}_2$ as Promising Cathode Material for Sodium-Ion Batteries," *ACS Applied Energy Materials*, **2018**, 1(11), 5960-5967.
- [80] Y. Xiao, Y. F. Zhu, W. Xiang, Z. G. Wu, Y. C. Li, J. Lai, S. Li, E. Wang, Z. G. Yang, C. L. Xu, B. H. Zhong, and X. D. Guo, "Deciphering an Abnormal Layered-Tunnel Heterostructure Induced by Chemical Substitution for the Sodium Oxide Cathode," *Angewandte Chemie - International Edition*, **2020**, 59(4), 1491-1495.
- [81] L. Yang, X. Li, X. Ma, S. Xiong, P. Liu, Y. Tang, S. Cheng, Y.-Y. Hu, M. Liu, and H. Chen, "Design of high-performance cathode materials with single-phase pathway for sodium ion batteries: A study on P2- $\text{Na}_x(\text{Li}_y\text{Mn}_{1-y})\text{O}_2$ compounds," *Journal of Power Sources*, **2018**, 381, 171-180.
- [82] D. Goonetilleke, S. Wang, E. Gonzalo, M. Galcerán, D. Saurel, S. J. Day, F. Fauth, T. Rojo, and N. Sharma, "Exploring the rate dependence of phase evolution in P2-type $\text{Na}_{2/3}\text{Mn}_{0.8}\text{Fe}_{0.1}\text{Ti}_{0.1}\text{O}_2$," *Journal of Materials Chemistry A*, **2019**, 7(19), 12115-12125.
- [83] Y. H. Jung, A. S. Christiansen, R. E. Johnsen, P. Norby, and D. K. Kim, "In situ X-ray diffraction studies on structural changes of a P2 layered material during electrochemical desodiation/sodiation," *Advanced Functional Materials*, **2015**, 25(21), 3227-3237.
- [84] A. Kulka, C. Marino, K. Walczak, C. Borca, C. Bolli, P. Novák, and C. Villevieille, "Influence of Na/Mn arrangements and P2/P'2 phase ratio on the electrochemical performance of Na_xMnO_2 cathodes for sodium-ion batteries," *Journal of Materials Chemistry A*, **2020**, 8(12), 6022-6033.
- [85] K. Liu, S. Tan, J. Moon, C. J. Jafta, C. Li, T. Kobayashi, H. Lyu, C. A. Bridges, S. Men, and W. Guo, "Insights into the Enhanced Cycle and Rate Performances of the F-Substituted P2-Type Oxide Cathodes for Sodium-Ion Batteries," *Advanced Energy Materials*, **2020**.
- [86] D. Sehrawat, S. Cheong, A. Rawal, A. M. Glushenkov, H. E. A. Brand, B. Cowie, E. Gonzalo, T. Rojo, P. J. P. Naeyaert, C. D. Ling, M. Avdeev, and N. Sharma, "Investigation of K modified P2 $\text{Na}_{0.7}\text{Mn}_{0.8}\text{Mg}_{0.2}\text{O}_2$ as a cathode material for sodium-ion batteries," *CrystEngComm*, **2019**, 21(1), 172-181.
- [87] Y. Zhu, W. Nie, P. Chen, Y. Zhou, and Y. Xu, "Li-doping stabilized P2- $\text{Li}_{0.2}\text{Na}_{1.0}\text{Mn}_{0.8}\text{O}_2$ sodium ion cathode with oxygen redox activity," *International Journal of Energy Research*, **2020**, 44(4), 3253-3259.
- [88] S. Kjeldgaard, S. Birgisson, A. G. Kielland, and B. B. Iversen, "Operando powder X-ray diffraction study of P2- $\text{Na}_x\text{Ni}_{0.3}\text{Mn}_{0.7}\text{O}_2$ cathode material during electrochemical cycling," *Journal of Applied Crystallography*, **2018**, 51(5), 1304-1310.
- [89] Q. Liu, Z. Hu, M. Chen, C. Zou, H. Jin, S. Wang, Q. Gu, and S. Chou, "P2-type $\text{Na}_{2/3}\text{Ni}_{1/3}\text{Mn}_{2/3}\text{O}_2$ as a cathode material with high-rate and long-life for sodium ion storage," *Journal of Materials Chemistry A*, **2019**, 7(15), 9215-9221.
- [90] N. Sharma, N. Tapia-Ruiz, G. Singh, A. R. Armstrong, J. C. Pramudita, H. E. A. Brand, J. Billaud, P. G. Bruce, and T. Rojo, "Rate Dependent Performance Related to Crystal Structure Evolution of $\text{Na}_{0.67}\text{Mn}_{0.8}\text{Mg}_{0.2}\text{O}_2$ in a Sodium-Ion Battery," *Chemistry of Materials*, **2015**, 27(20), 6976-6986.
- [91] X. Cao, H. Li, Y. Qiao, X. Li, M. Jia, J. Cabana, and H. Zhou, "Stabilizing Reversible Oxygen Redox Chemistry in Layered Oxides for Sodium-Ion Batteries," *Advanced Energy Materials*, **2020**, 1903785.

- [92] E. Talaie, V. Duffort, H. L. Smith, B. Fultz, and L. F. Nazar, "Structure of the high voltage phase of layered P2-Na_{2/3-z}[Mn_{1/2}Fe_{1/2}]O₂ and the positive effect of Ni substitution on its stability," *Energy & Environmental Science*, **2015**, 8(8), 2512-2523.
- [93] H. Ma, H. Su, K. Amine, X. Liu, S. Jaffer, T. Shang, L. Gu, and H. Yu, "Triphase electrode performance adjustment for rechargeable ion batteries," *Nano Energy*, **2018**, 43, 1-10.
- [94] W. Kong, H. Wang, L. Sun, C. Su, and X. Liu, "Understanding the synergic roles of MgO coating on the cycling and rate performance of Na_{0.67}Mn_{0.5}Fe_{0.5}O₂ cathode," *Applied Surface Science*, **2019**, 497, 143814.
- [95] P. F. Wang, H. R. Yao, Y. You, Y. G. Sun, Y. X. Yin, and Y. G. Guo, "Understanding the structural evolution and Na⁺ kinetics in honeycomb-ordered O'3-Na₃Ni₂SbO₆ cathodes," *Nano Research*, **2018**, 11(6), 3258-3271.
- [96] L. Wang, J. Wang, X. Zhang, Y. Ren, P. Zuo, G. Yin, and J. Wang, "Unravelling the origin of irreversible capacity loss in NaNiO₂ for high voltage sodium ion batteries," *Nano Energy*, **2017**, 34, 215-223.
- [97] M. H. Han, E. Gonzalo, M. Casas-Cabanas, and T. Rojo, "Structural evolution and electrochemistry of monoclinic NaNiO₂ upon the first cycling process," *Journal of Power Sources*, **2014**, 258, 266-271.
- [98] X. Chen, S. Hwang, R. Chisnell, Y. Wang, F. Wu, S. Kim, J. W. Lynn, D. Su, and X. Li, "Reversible flat to rippling phase transition in Fe containing layered battery electrode materials," *Advanced Functional Materials*, **2018**, 28(39), 1803896.
- [99] Y. Xie, H. Wang, G. Xu, J. Wang, H. Sheng, Z. Chen, Y. Ren, C. J. Sun, J. Wen, and J. Wang, "In Operando XRD and TXM Study on the Metastable Structure Change of NaNi_{1/3}Fe_{1/3}Mn_{1/3}O₂ under Electrochemical Sodium-Ion Intercalation," *Advanced Energy Materials*, **2016**, 6(24), 1601306.
- [100] C. Heubner, B. Matthey, T. Lein, F. Wolke, T. Liebmann, C. Lämmel, M. Schneider, M. Herrmann, and A. Michaelis, "Insights into the electrochemical Li/Na-exchange in layered LiCoO₂ cathode material," *Energy Storage Materials*, **2020**, 27, 377-386.
- [101] H. Dai, C. Yang, X. Ou, X. Liang, H. Xue, W. Wang, and G. Xu, "Unravelling the electrochemical properties and thermal behavior of NaNi_{2/3}Sb_{1/3}O₂ cathode for sodium-ion batteries by in situ X-ray diffraction investigation," *Electrochimica Acta*, **2017**, 257, 146-154.
- [102] M. Guignard, C. Didier, J. Darriet, P. Bordet, E. Elkaïm, and C. Delmas, "P2-Na_xVO₂ system as electrodes for batteries and electron-correlated materials," *Nature materials*, **2013**, 12(1), 74-80.
- [103] J. W. Somerville, A. Sobkowiak, N. Tapia-Ruiz, J. Billaud, J. G. Lozano, R. A. House, L. C. Gallington, T. Ericsson, L. Häggström, and M. R. Roberts, "Nature of the "Z"-phase in layered Na-ion battery cathodes," *Energy & Environmental Science*, **2019**, 12(7), 2223-2232.
- [104] Y. Zhao, Q. Liu, X. Zhao, D. Mu, G. Tan, L. Li, R. Chen, and F. Wu, "Structure evolution of layered transition metal oxide cathode materials for Na-ion batteries: Issues, mechanism and strategies," *Materials Today*, **2022**, 62, 271-295.
- [105] M. H. Han, E. Gonzalo, G. Singh, and T. Rojo, "A comprehensive review of sodium layered oxides: powerful cathodes for Na-ion batteries," *Energy & Environmental Science*, **2015**, 8(1), 81-102.
- [106] H. Yoshida, N. Yabuuchi, and S. Komaba, "NaFe_{0.5}Co_{0.5}O₂ as high energy and power positive electrode for Na-ion batteries," *Electrochemistry Communications*, **2013**, 34, 60-63.
- [107] N. Yabuuchi, H. Yoshida, and S. Komaba, "Crystal structures and electrode performance of alpha-NaFeO₂ for rechargeable sodium batteries," *Electrochemistry*, **2012**, 80(10), 716-719.
- [108] E. de la Llave, V. Borgel, K.-J. Park, J.-Y. Hwang, Y.-K. Sun, P. Hartmann, F.-F. Chesneau, and D. Aurbach, "Comparison between Na-Ion and Li-Ion cells: understanding the critical role of the cathodes stability and the anodes pretreatment on the cells behavior," *ACS applied materials & interfaces*, **2016**, 8(3), 1867-1875.

- [109] N. Yabuuchi, M. Kajiyama, J. Iwatate, H. Nishikawa, S. Hitomi, R. Okuyama, R. Usui, Y. Yamada, and S. Komaba, "P2-type $\text{Na}_x[\text{Fe}_{1/2}\text{Mn}_{1/2}]\text{O}_2$ made from earth-abundant elements for rechargeable Na batteries," *Nature Materials*, **2012**, 11(6), 512-517.
- [110] B. Senthilkumar, C. Murugesan, L. Sharma, S. Lochab, and P. Barpanda, "An overview of mixed polyanionic cathode materials for sodium-ion batteries," *Small Methods*, **2019**, 3(4), 1800253.
- [111] C. Masquelier and L. Croguennec, "Polyanionic (phosphates, silicates, sulfates) frameworks as electrode materials for rechargeable Li (or Na) batteries," *Chemical Reviews*, **2013**, 113(8), 6552-6591.
- [112] J. Kim, D.-H. Seo, H. Kim, I. Park, J.-K. Yoo, S.-K. Jung, Y.-U. Park, W. A. Goddard III, and K. Kang, "Unexpected discovery of low-cost maricite NaFePO_4 as a high-performance electrode for Na-ion batteries," *Energy & Environmental Science*, **2015**, 8(2), 540-545.
- [113] S.-M. Oh, S.-T. Myung, J. Hassoun, B. Scrosati, and Y.-K. Sun, "Reversible NaFePO_4 electrode for sodium secondary batteries," *Electrochemistry Communications*, **2012**, 22, 149-152.
- [114] M. Chen, D. Cortie, Z. Hu, H. Jin, S. Wang, Q. Gu, W. Hua, E. Wang, W. Lai, L. Chen, S.-L. Chou, X.-L. Wang, and S.-X. Dou, "A Novel Graphene Oxide Wrapped $\text{Na}_2\text{Fe}_2(\text{SO}_4)_3/\text{C}$ Cathode Composite for Long Life and High Energy Density Sodium-Ion Batteries," *Advanced Energy Materials*, **2018**, 8(27), 1800944.
- [115] C. Wang, D. Du, M. Song, Y. Wang, and F. Li, "A High-Power $\text{Na}_3\text{V}_2(\text{PO}_4)_3\text{-Bi}$ Sodium-Ion Full Battery in a Wide Temperature Range," *Advanced Energy Materials*, **2019**, 9(16), 1900022.
- [116] B. Singh, Z. Wang, S. Park, G. S. Gautam, J.-N. Chotard, L. Croguennec, D. Carlier, A. K. Cheetham, C. Masquelier, and P. Canepa, "A chemical map of NaSICON electrode materials for sodium-ion batteries," *Journal of Materials Chemistry A*, **2021**, 9(1), 281-292.
- [117] F. Chen, V. M. Kovrugin, R. David, O. Mentré, F. Fauth, J. N. Chotard, and C. Masquelier, "A NASICON-type positive electrode for Na batteries with high energy density: $\text{Na}_4\text{MnV}(\text{PO}_4)_3$," *Small Methods*, **2019**, 3(4), 1800218.
- [118] F. Lalère, V. Seznec, M. Courty, R. David, J. Chotard, and C. Masquelier, "Improving the energy density of $\text{Na}_3\text{V}_2(\text{PO}_4)_3$ -based positive electrodes through V/Al substitution," *Journal of Materials Chemistry A*, **2015**, 3(31), 16198-16205.
- [119] S. Park, J.-N. Chotard, D. Carlier, I. Moog, M. Courty, M. Duttine, F. Fauth, A. Iadecola, L. Croguennec, and C. Masquelier, "Crystal structures and local environments of NASICON-type $\text{Na}_3\text{FeV}(\text{PO}_4)_3$ and $\text{Na}_4\text{FeV}(\text{PO}_4)_3$ positive electrode materials for Na-ion batteries," *Chemistry of Materials*, **2021**, 33(13), 5355-5367.
- [120] M. Bianchini, F. Fauth, N. Brisset, F. Weill, E. Suard, C. Masquelier, and L. Croguennec, "Comprehensive investigation of the $\text{Na}_3\text{V}_2(\text{PO}_4)_2\text{F}_3\text{-NaV}_2(\text{PO}_4)_2\text{F}_3$ system by operando high resolution synchrotron X-ray diffraction," *Chemistry of Materials*, **2015**, 27(8), 3009-3020.
- [121] L. H. Nguyen, J. Olchowka, S. Belin, P. Sanz Camacho, M. Duttine, A. Iadecola, F. Fauth, D. Carlier, C. Masquelier, and L. Croguennec, "Monitoring the crystal structure and the electrochemical properties of $\text{Na}_3(\text{VO})_2(\text{PO}_4)_2\text{F}$ through Fe^{3+} substitution," *ACS Applied Materials & Interfaces*, **2019**, 11(42), 38808-38818.
- [122] J. Qian, C. Wu, Y. Cao, Z. Ma, Y. Huang, X. Ai, and H. Yang, "Prussian blue cathode materials for sodium-ion batteries and other ion batteries," *Advanced Energy Materials*, **2018**, 8(17), 1702619.
- [123] K. Cao, L. Jiao, W. K. Pang, H. Liu, T. Zhou, Z. Guo, Y. Wang, and H. Yuan, " $\text{Na}_2\text{Ti}_6\text{O}_{13}$ Nanorods with Dominant Large Interlayer Spacing Exposed Facet for High-Performance Na-Ion Batteries," *Small*, **2016**, 12(22), 2991-2997.
- [124] H. Hou, X. Qiu, W. Wei, Y. Zhang, and X. Ji, "Carbon anode materials for advanced sodium-ion batteries," *Advanced energy materials*, **2017**, 7(24), 1602898.
- [125] H. Kim, J. Hong, Y.-U. Park, J. Kim, I. Hwang, and K. Kang, "Sodium Storage Behavior in Natural Graphite using Ether-based Electrolyte Systems," *Advanced Functional Materials*, **2015**, 25(4), 534-541.
- [126] H.-J. Liang, B.-H. Hou, W.-H. Li, Q.-L. Ning, X. Yang, Z.-Y. Gu, X.-J. Nie, G. Wang, and X.-L. Wu, "Staging Na/K-ion de-/intercalation of graphite retrieved from spent Li-ion batteries: in

- operando X-ray diffraction studies and an advanced anode material for Na/K-ion batteries," *Energy & Environmental Science*, **2019**, 12(12), 3575-3584.
- [127] W. Luo, Z. Jian, Z. Xing, W. Wang, C. Bommier, M. M. Lerner, and X. Ji, "Electrochemically expandable soft carbon as anodes for Na-ion batteries," *ACS central science*, **2015**, 1(9), 516-522.
- [128] B. Cao, H. Liu, B. Xu, Y. Lei, X. Chen, and H. Song, "Mesoporous soft carbon as an anode material for sodium ion batteries with superior rate and cycling performance," *Journal of Materials Chemistry A*, **2016**, 4(17), 6472-6478.
- [129] H. Tan, D. Chen, X. Rui, and Y. Yu, "Peering into alloy anodes for sodium-ion batteries: current trends, challenges, and opportunities," *Advanced Functional Materials*, **2019**, 29(14), 1808745.
- [130] L. Zhang, X. Hu, C. Chen, H. Guo, X. Liu, G. Xu, H. Zhong, S. Cheng, P. Wu, and J. Meng, "In operando mechanism analysis on nanocrystalline silicon anode material for reversible and ultrafast sodium storage," *Advanced Materials*, **2017**, 29(5), 1604708.
- [131] M. Fukunishi, N. Yabuuchi, M. Dahbi, J.-Y. Son, Y. Cui, H. Oji, and S. Komaba, "Impact of the Cut-Off Voltage on Cyclability and Passive Interphase of Sn-Polyacrylate Composite Electrodes for Sodium-Ion Batteries," *The Journal of Physical Chemistry C*, **2016**, 120(28), 15017-15026.
- [132] L. Liang, Y. Xu, C. Wang, L. Wen, Y. Fang, Y. Mi, M. Zhou, H. Zhao, and Y. Lei, "Large-scale highly ordered Sb nanorod array anodes with high capacity and rate capability for sodium-ion batteries," *Energy & Environmental Science*, **2015**, 8(10), 2954-2962.
- [133] C. Wang, L. Wang, F. Li, F. Cheng, and J. Chen, "Bulk Bismuth as a High-Capacity and Ultralong Cycle-Life Anode for Sodium-Ion Batteries by Coupling with Glyme-Based Electrolytes," *Advanced Materials*, **2017**, 29(35), 1702212.
- [134] X. Wei, X. Wang, X. Tan, Q. An, and L. Mai, "Nanostructured conversion-type negative electrode materials for low-cost and high-performance sodium-ion batteries," *Advanced Functional Materials*, **2018**, 28(46), 1804458.
- [135] W. Ren, H. Zhang, C. Guan, and C. Cheng, "Ultrathin MoS₂ Nanosheets@Metal Organic Framework-Derived N-Doped Carbon Nanowall Arrays as Sodium Ion Battery Anode with Superior Cycling Life and Rate Capability," *Advanced Functional Materials*, **2017**, 27(32), 1702116.
- [136] J. Zhou, L. Wang, M. Yang, J. Wu, F. Chen, W. Huang, N. Han, H. Ye, F. Zhao, and Y. Li, "Hierarchical VS₂ nanosheet assemblies: a universal host material for the reversible storage of alkali metal ions," *Advanced Materials*, **2017**, 29(35), 1702061.
- [137] D. Li, J. Zhou, X. Chen, and H. Song, "Amorphous Fe₂O₃/graphene composite nanosheets with enhanced electrochemical performance for sodium-ion battery," *ACS Applied Materials & Interfaces*, **2016**, 8(45), 30899-30907.
- [138] X. Ou, C. Yang, X. Xiong, F. Zheng, Q. Pan, C. Jin, M. Liu, and K. Huang, "A new rGO-overcoated Sb₂Se₃ nanorods anode for Na⁺ battery: in Situ X-ray diffraction study on a live sodiation/desodiation process," *Advanced Functional Materials*, **2017**, 27(13), 1606242.
- [139] K.-H. Nam, K. H. Chae, J.-H. Choi, K.-J. Jeon, and C.-M. Park, "Superior carbon black: High-performance anode and conducting additive for rechargeable Li- and Na-ion batteries," *Chemical Engineering Journal*, **2021**, 417, 129242.
- [140] M.-S. Balogun, Y. Luo, W. Qiu, P. Liu, and Y. Tong, "A review of carbon materials and their composites with alloy metals for sodium ion battery anodes," *Carbon*, **2016**, 98, 162-178.
- [141] C. Ma, J. Xu, J. Alvarado, B. Qu, J. Somerville, J. Y. Lee, and Y. S. Meng, "Investigating the energy storage mechanism of SnS₂-rGO composite anode for advanced Na-ion batteries," *Chemistry of Materials*, **2015**, 27(16), 5633-5640.
- [142] C. Bommier and X. Ji, "Electrolytes, SEI formation, and binders: a review of nonelectrode factors for sodium-ion battery anodes," *Small*, **2018**, 14(16), 1703576.
- [143] K. Dai, H. Zhao, Z. Wang, X. Song, V. Battaglia, and G. Liu, "Toward high specific capacity and high cycling stability of pure tin nanoparticles with conductive polymer binder for sodium ion batteries," *Journal of Power Sources*, **2014**, 263, 276-279.

- [144] J. Ming, H. Ming, W.-J. Kwak, C. Shin, J. Zheng, and Y.-K. Sun, "The binder effect on an oxide-based anode in lithium and sodium-ion battery applications: the fastest way to ultrahigh performance," *Chemical Communications*, **2014**, 50(87), 13307-13310.
- [145] V. M. Nagulapati, J. H. Lee, H. S. Kim, J. Oh, I. T. Kim, J. Hur, and S. G. Lee, "Novel hybrid binder mixture tailored to enhance the electrochemical performance of SbTe bi-metallic anode for sodium ion batteries," *Journal of Electroanalytical Chemistry*, **2020**, 865, 114160.
- [146] W. Xiao, Q. Sun, M. N. Banis, B. Wang, W. Li, M. Li, A. Lushington, R. Li, X. Li, and T. K. Sham, "Understanding the Critical Role of Binders in Phosphorus/Carbon Anode for Sodium-Ion Batteries through Unexpected Mechanism," *Advanced Functional Materials*, **2020**, 30(32), 2000060.
- [147] Z. Xu, J. Liu, C. Chen, H. Potapenko, and M. Wu, "Hydrophilic binder interface interactions inducing inadhesion and capacity collapse in sodium-ion battery," *Journal of Power Sources*, **2019**, 427, 62-69.
- [148] A. Ponrouch, E. Marchante, M. Courty, J.-M. Tarascon, and M. R. Palacin, "In search of an optimized electrolyte for Na-ion batteries," *Energy & Environmental Science*, **2012**, 5(9), 8572-8583.
- [149] A. Ponrouch, R. Dedryvère, D. Monti, A. E. Demet, J. M. A. Mba, L. Croguennec, C. Masquelier, P. Johansson, and M. R. Palacín, "Towards high energy density sodium ion batteries through electrolyte optimization," *Energy & Environmental Science*, **2013**, 6(8), 2361-2369.
- [150] R. Hagiwara, K. Matsumoto, J. Hwang, and T. Nohira, "Sodium ion batteries using ionic liquids as electrolytes," *The Chemical Record*, **2019**, 19(4), 758-770.
- [151] Y. Wang, S. Song, C. Xu, N. Hu, J. Molenda, and L. Lu, "Development of solid-state electrolytes for sodium-ion battery—A short review," *Nano Materials Science*, **2019**, 1(2), 91-100.
- [152] T. Famprakis, P. Canepa, J. A. Dawson, M. S. Islam, and C. Masquelier, "Fundamentals of inorganic solid-state electrolytes for batteries," *Nature materials*, **2019**, 18(12), 1278-1291.
- [153] J. B. Goodenough, H.-P. Hong, and J. Kavalas, "Fast Na⁺-ion transport in skeleton structures," *Materials Research Bulletin*, **1976**, 11(2), 203-220.
- [154] M. Samiee, B. Radhakrishnan, Z. Rice, Z. Deng, Y. S. Meng, S. P. Ong, and J. Luo, "Divalent-doped Na₃Zr₂Si₂PO₁₂ sodium superionic conductor: Improving the ionic conductivity via simultaneously optimizing the phase and chemistry of the primary and secondary phases," *Journal of Power Sources*, **2017**, 347, 229-237.
- [155] X. Li, F. Bianchini, J. Wind, C. Pettersen, D. S. Wragg, P. Vajeeston, and H. Fjellvåg, "Insights into crystal structure and diffusion of biphasic Na₂Zn₂TeO₆," *ACS Applied Materials & Interfaces*, **2020**, 12(25), 28188-28198.
- [156] Y. Li, Z. Deng, J. Peng, J. Gu, E. Chen, Y. Yu, J. Wu, X. Li, J. Luo, and Y. Huang, "New P2-type honeycomb-layered sodium-ion conductor: Na₂Mg₂TeO₆," *ACS Applied Materials & Interfaces*, **2018**, 10(18), 15760-15766.
- [157] Y. Li, Z. Deng, J. Peng, E. Chen, Y. Yu, X. Li, J. Luo, Y. Huang, J. Zhu, and C. Fang, "A P2-type layered superionic conductor Ga-doped Na₂Zn₂TeO₆ for all-solid-state sodium-ion batteries," *Chemistry—A European Journal*, **2018**, 24(5), 1057-1061.
- [158] A. Hayashi, K. Noi, A. Sakuda, and M. Tatsumisago, "Superionic glass-ceramic electrolytes for room-temperature rechargeable sodium batteries," *Nature communications*, **2012**, 3(1), 856.
- [159] L. Zhang, D. Zhang, K. Yang, X. Yan, L. Wang, J. Mi, B. Xu, and Y. Li, "Vacancy-contained tetragonal Na₃SbS₄ superionic conductor," *Advanced science*, **2016**, 3(10), 1600089.
- [160] D. Kumar and S. A. Hashmi, "Ionic liquid based sodium ion conducting gel polymer electrolytes," *Solid State Ionics*, **2010**, 181(8), 416-423.
- [161] J. Zheng, Y. Zhao, X. Feng, W. Chen, and Y. Zhao, "Novel safer phosphonate-based gel polymer electrolytes for sodium-ion batteries with excellent cycling performance," *Journal of Materials Chemistry A*, **2018**, 6(15), 6559-6564.

- [162] Z. Zhang, Q. Zhang, C. Ren, F. Luo, Q. Ma, Y.-S. Hu, Z. Zhou, H. Li, X. Huang, and L. Chen, "A ceramic/polymer composite solid electrolyte for sodium batteries," *Journal of Materials Chemistry A*, **2016**, 4(41), 15823-15828.
- [163] Z. Zhang, K. Xu, X. Rong, Y.-S. Hu, H. Li, X. Huang, and L. Chen, "Na_{3.4}Zr_{1.8}Mg_{0.2}Si₂PO₁₂ filled poly (ethylene oxide)/Na (CF₃SO₂)₂N as flexible composite polymer electrolyte for solid-state sodium batteries," *Journal of Power Sources*, **2017**, 372, 270-275.
- [164] P. T. Kissinger and W. R. Heineman, "Cyclic voltammetry," *Journal of chemical education*, **1983**, 60(9), 702.
- [165] M. S. Palagonia, C. Erinmwingbovo, D. Brogioli, and F. La Mantia, "Comparison between cyclic voltammetry and differential charge plots from galvanostatic cycling," *Journal of Electroanalytical Chemistry*, **2019**, 847, 113170.
- [166] T. Egami and S. J. Billinge, *Underneath the Bragg peaks: structural analysis of complex materials*. Newnes, 2012.
- [167] W. Clegg, *X-ray Crystallography*. Oxford University Press, USA, 2015.
- [168] B. K. Teo, *EXAFS: basic principles and data analysis*. Springer Science & Business Media, 2012.
- [169] B. Fultz and J. M. Howe, *Transmission electron microscopy and diffractometry of materials*. Springer Science & Business Media, 2012.
- [170] A. Brennhagen and Nafuma. *Experimental data for the Nanoname project*, DataverseNO, 2023, <https://doi.org/10.18710/ZFADJS>.
- [171] O. A. Drozhzhin, I. V. Tereshchenko, H. Emerich, E. V. Antipov, A. M. Abakumov, and D. Chernyshov, "An electrochemical cell with sapphire windows for operando synchrotron X-ray powder diffraction and spectroscopy studies of high-power and high-voltage electrodes for metal-ion batteries," *Journal of Synchrotron Radiation*, **2018**, 25(2), 468-472.
- [172] J. Sottmann, R. Homs-Regajo, D. S. Wragg, H. Fjellvåg, S. Margadonna, and H. Emerich, "Versatile electrochemical cell for Li/Na-ion batteries and high-throughput setup for combined operando X-ray diffraction and absorption spectroscopy," *Journal of Applied Crystallography*, **2016**, 49(6), 1972-1981.
- [173] C. K. Christensen, M. A. Karlsen, A. Ø. Drejer, B. P. Andersen, C. L. Jakobsen, M. Johansen, D. R. Sørensen, I. Kantor, M. R. V. Jørgensen, and D. B. Ravnsbæk, "Beam damage in operando X-ray diffraction studies of Li-ion batteries," *Journal of Synchrotron Radiation*, **2023**, 30(3).
- [174] A. Jain, S. P. Ong, G. Hautier, W. Chen, W. D. Richards, S. Dacek, S. Cholia, D. Gunter, D. Skinner, and G. Ceder, "Commentary: The Materials Project: A materials genome approach to accelerating materials innovation," *APL materials*, **2013**, 1(1).
- [175] Q. Li, P. Du, Y. Yuan, W. Yao, Z. Ma, B. Guo, Y. Lyu, P. Wang, H. Wang, A. Nie, R. Shahbazian-Yassar, and J. Lu, "Real-Time TEM Study of Nanopore Evolution in Battery Materials and Their Suppression for Enhanced Cycling Performance," *Nano Letters*, **2019**, 19(5), 3074-3082.
- [176] J. Cui, Z.-L. Xu, S. Yao, J. Huang, J.-Q. Huang, S. Abouali, M. A. Garakani, X. Ning, and J.-K. Kim, "Enhanced conversion reaction kinetics in low crystallinity SnO₂/CNT anodes for Na-ion batteries," *Journal of Materials Chemistry A*, **2016**, 4(28), 10964-10973.
- [177] M. Gu, A. Kushima, Y. Shao, J.-G. Zhang, J. Liu, N. D. Browning, J. Li, and C. Wang, "Probing the failure mechanism of SnO₂ nanowires for sodium-ion batteries," *Nano letters*, **2013**, 13(11), 5203-5211.
- [178] M. Chen, D. Chao, J. Liu, J. Yan, B. Zhang, Y. Huang, J. Lin, and Z. X. Shen, "Rapid pseudocapacitive sodium-ion response induced by 2D ultrathin tin monoxide nanoarrays," *Advanced Functional Materials*, **2017**, 27(12), 1606232.
- [179] J. Choi, N. R. Kim, K. Lim, K. Ku, H. J. Yoon, J. G. Kang, K. Kang, P. V. Braun, H. J. Jin, and Y. S. Yun, "Tin Sulfide-Based Nanohybrid for High-Performance Anode of Sodium-Ion Batteries," *Small*, **2017**, 13(30), 1700767.
- [180] Y. Jiang, M. Wei, J. Feng, Y. Ma, and S. Xiong, "Enhancing the cycling stability of Na-ion batteries by bonding SnS₂ ultrafine nanocrystals on amino-functionalized graphene hybrid nanosheets," *Energy & Environmental Science*, **2016**, 9(4), 1430-1438.

- [181] Y. Kim, Y. Kim, A. Choi, S. Woo, D. Mok, N. S. Choi, Y. S. Jung, J. H. Ryu, S. M. Oh, and K. T. Lee, "Tin phosphide as a promising anode material for Na-ion batteries," *Advanced materials*, **2014**, 26(24), 4139-4144.
- [182] Q. Li, Z. Li, Z. Zhang, C. Li, J. Ma, C. Wang, X. Ge, S. Dong, and L. Yin, "Low-Temperature Solution-Based Phosphorization Reaction Route to Sn_4P_3 /Reduced Graphene Oxide Nanohybrids as Anodes for Sodium Ion Batteries," *Advanced Energy Materials*, **2016**, 6(15), 1600376.
- [183] H. Li, K. Qian, X. Qin, D. Liu, R. Shi, A. Ran, C. Han, Y.-B. He, F. Kang, and B. Li, "The different Li/Na ion storage mechanisms of nano Sb_2O_3 anchored on graphene," *Journal of Power Sources*, **2018**, 385, 114-121.
- [184] S. Yao, J. Cui, Z. Lu, Z. L. Xu, L. Qin, J. Huang, Z. Sadighi, F. Ciucci, and J. K. Kim, "Unveiling the unique phase transformation behavior and sodiation kinetics of 1D van der Waals Sb_2S_3 anodes for sodium ion batteries," *Advanced Energy Materials*, **2017**, 7(8), 1602149.
- [185] Y. Wu, W. Luo, P. Gao, C. Zhu, X. Hu, K. Qu, J. Chen, Y. Wang, L. Sun, and L. Mai, "Unveiling the microscopic origin of asymmetric phase transformations in (de) sodiated Sb_2Se_3 with in situ transmission electron microscopy," *Nano Energy*, **2020**, 77, 105299.
- [186] J. Pan, Y. Zhang, L. Li, Z. Cheng, Y. Li, X. Yang, J. Yang, and Y. Qian, "Polyanions Enhance Conversion Reactions for Lithium/Sodium-Ion Batteries: The Case of SbVO_4 Nanoparticles on Reduced Graphene Oxide," *Small Methods*, **2019**, 3(10), 1900231.
- [187] E. Edison, P. K. Gogoi, Y. Zheng, S. Sreejith, S. J. Pennycook, C. T. Lim, and M. Srinivasan, "Electrochemically induced amorphization and unique lithium and sodium storage pathways in FeSbO_4 nanocrystals," *ACS applied materials & interfaces*, **2019**, 11(22), 20082-20090.
- [188] X. Jiao, X. Hu, G. Xi, G. Li, L. Qiu, Y. Zou, and X. Zhang, "Mn Sb_2S_4 nanorods linked with interconnected reduced graphene oxide as high-performance anode for sodium ion batteries," *Electrochimica Acta*, **2021**, 366, 137317.
- [189] C. Lu, Z. Li, L. Yu, L. Zhang, Z. Xia, T. Jiang, W. Yin, S. Dou, Z. Liu, and J. Sun, "Nanostructured Bi_2S_3 encapsulated within three-dimensional N-doped graphene as active and flexible anodes for sodium-ion batteries," *Nano Research*, **2018**, 11, 4614-4626.
- [190] L. Xie, Z. Yang, J. Sun, H. Zhou, X. Chi, H. Chen, A. X. Li, Y. Yao, and S. Chen, " Bi_2Se_3 /C nanocomposite as a new sodium-ion battery anode material," *Nano-Micro Letters*, **2018**, 10, 1-9.
- [191] D. Li, J. Zhou, X. Chen, and H. Song, "Graphene-loaded Bi_2Se_3 : a conversion-alloying-type anode material for ultrafast gravimetric and volumetric Na storage," *ACS applied materials & interfaces*, **2018**, 10(36), 30379-30387.
- [192] S. Dai, L. Wang, Y. Shen, and M. Wang, "Bismuth selenide nanocrystalline array electrodes for high-performance sodium-ion batteries," *Applied Materials Today*, **2020**, 18, 100455.
- [193] S. Wen, J. Zhao, Y. Zhao, T. Xu, and J. Xu, "Reduced graphene oxide (RGO) decorated Sb_2S_3 nanorods as anode material for sodium-ion batteries," *Chemical Physics Letters*, **2019**, 716, 171-176.
- [194] G. Ruschau, S. Yoshikawa, and R. Newnham, "Resistivities of conductive composites," *Journal of applied physics*, **1992**, 72(3), 953-959.
- [195] K. B. Gandrud, A. Pettersen, O. Nilsen, and H. Fjellvåg, "High-performing iron phosphate for enhanced lithium ion solid state batteries as grown by atomic layer deposition," *Journal of Materials Chemistry A*, **2013**, 1(32), 9054-9059.
- [196] K. B. Gandrud, O. Nilsen, and H. Fjellvåg, "Ultra-high power capabilities in amorphous FePO_4 thin films," *Journal of Power Sources*, **2016**, 306, 454-458.
- [197] A. Brennhagen, K. B. Kvamme, K. S. Sverdlilje, and O. Nilsen, "High power iron phosphate cathodes by atomic layer deposition," *Solid State Ionics*, **2020**, 353, 115377.
- [198] A. Chandra, A. Bhatt, and A. Chandra, "Ion conduction in superionic glassy electrolytes: an overview," *Journal of Materials Science & Technology*, **2013**, 29(3), 193-208.
- [199] J. Sottmann, "Synchrotron Based Operando Methods for Characterization of Non-Aqueous Rechargeable Battery Electrode Materials " Ph.D. dissertation, University of Oslo, 2017.

- [200] Y. Zheng, T. Zhou, X. Zhao, W. K. Pang, H. Gao, S. Li, Z. Zhou, H. Liu, and Z. Guo, "Atomic interface engineering and electric-field effect in ultrathin Bi_2MoO_6 nanosheets for superior lithium ion storage," *Advanced Materials*, **2017**, 29(26), 1700396.
- [201] T. Zhang, E. Olsson, M. Choolaei, V. Stolojan, C. Feng, H. Wu, S. Wang, and Q. Cai, "Synthesis and Electrochemical Properties of Bi_2MoO_6 /Carbon Anode for Lithium-Ion Battery Application," *Materials*, **2020**, 13(5), 1132.
- [202] D. P. Dubal, K. Jayaramulu, R. Zboril, R. A. Fischer, and P. Gomez-Romero, "Unveiling BiVO_4 nanorods as a novel anode material for high performance lithium ion capacitors: beyond intercalation strategies," *Journal of Materials Chemistry A*, **2018**, 6(14), 6096-6106.
- [203] S. Lakkepally, Y. Kalegowda, V. Ramarao, E. Hanumantharayappa, and A. Siddaramanna, "Room temperature synthesis of amorphous $\text{Bi}_4\text{V}_2\text{O}_{11}$ as cathode material for Li secondary batteries," *Materials Research Express*, **2018**, 5(11), 115501.
- [204] Z. Jing, C.-f. Xu, Y.-y. Long, and Q.-h. Li, "Preparation and electrochemical performance of nitrogen-doped carbon-coated $\text{Bi}_2\text{Mn}_4\text{O}_{10}$ anode materials for lithium-ion batteries," *Transactions of Nonferrous Metals Society of China*, **2020**, 30(8), 2188-2199.
- [205] Z. Song, H. Zhang, K. Feng, H. Wang, X. Li, and H. Zhang, " $\text{Bi}_2\text{Mn}_4\text{O}_{10}$: a new mullite-type anode material for lithium-ion batteries," *Dalton Transactions*, **2018**, 47(23), 7739-7746.
- [206] C. Cheng, Y. Cheng, and G. Lai, "Micro/nanostructured $\text{Bi}_2\text{Mn}_4\text{O}_{10}$ with hierarchical spindle morphology as a highly efficient anode material for lithium-ion batteries," *Journal of the American Ceramic Society*, **2022**, 105(10), 6086-6095.
- [207] J. Zhan and Y. Long, "Synthesis of $\text{Bi}_2\text{Mn}_4\text{O}_{10}$ nanoparticles and its anode properties for LIB," *Ceramics International*, **2018**, 44(12), 14891-14895.
- [208] H. Xia, F. Yan, M. O. Lai, L. Lu, and W. Song, "Electrochemical properties of BiFeO_3 thin films prepared by pulsed laser deposition," *Functional Materials Letters*, **2009**, 2(04), 163-167.
- [209] N. Oli, J. F. Flórez Gómez, C. C. Zuluaga Gómez, R. K. Katiyar, G. Morell, and R. S. Katiyar, "Revealing Underestimated Performance in the Bismuth Ferrite (BiFeO_3) Anode for High-Capacity and Long-Cycling Lithium-Ion Batteries," *ACS Applied Energy Materials*, **2023**, 6(21), 10853-10861.
- [210] X.-Z. Li, N. Zhang, Y.-R. Wu, Q.-Z. Lai, Y.-R. Zhu, J.-H. Zhang, P. Cui, and T.-F. Yi, "Interconnected $\text{Bi}_5\text{Nb}_3\text{O}_{15}$ @CNTs network as high-performance anode materials of Li-ion battery," *Rare Metals*, **2022**, 41(10), 3401-3411.
- [211] Y. Li, R. Zheng, H. Yu, X. Cheng, H. Zhu, Y. Bai, T. Liu, M. Shui, and J. Shu, "Carbon-coated $\text{Bi}_5\text{Nb}_3\text{O}_{15}$ as anode material in rechargeable batteries for enhanced lithium storage," *Ceramics International*, **2018**, 44(10), 11505-11511.
- [212] Y. Li, R. Zheng, H. Yu, X. Cheng, T. Liu, N. Peng, J. Zhang, M. Shui, and J. Shu, "Fabrication of one-dimensional architecture $\text{Bi}_5\text{Nb}_3\text{O}_{15}$ nanowires by electrospinning for lithium-ion batteries with enhanced electrochemical performance," *Electrochimica Acta*, **2019**, 299.
- [213] G. Tang, H. Zhu, H. Yu, X. Cheng, R. Zheng, T. Liu, J. Zhang, M. Shui, and J. Shu, "Ultra-long BiNbO_4 nanowires with hierarchical architecture exhibiting reversible lithium storage," *Journal of Electroanalytical Chemistry*, **2018**, 823, 245-252.
- [214] X. Ding and Y. Liu, "Hollow bismuth ferrite combined graphene as advanced anode material for sodium-ion batteries," *Progress in Natural Science: Materials International*, **2020**, 30(2), 153-159.
- [215] V. Pavlyuk, M. Sozanskyi, G. Dmytriv, S. Indris, and H. Ehrenberg, "Amendment of the Li-Bi Phase Diagram Crystal and Electronic Structure of Li_2Bi ," *Journal of Phase Equilibria and Diffusion*, **2015**, 36, 544-553.
- [216] X. Cheng, R. Li, D. Li, Y. Li, and X.-Q. Chen, "Stable compositions and structures in the Na-Bi system," *Physical Chemistry Chemical Physics*, **2015**, 17(10), 6933-6947.

Paper 1 – Mini review

Benefits and Development Challenges for Conversion-Alloying Anode Materials in Na-Ion Batteries

A. Skurtveit, A. Brennhagen, H. Park, C. Cavallo, and A. Y. Kozlov

Frontiers in Energy Research, **2022**, 10, 897755.



Benefits and Development Challenges for Conversion-Alloying Anode Materials in Na-Ion Batteries

Amalie Skurtveit^{1*†}, Anders Brennhagen¹, Heesoo Park¹, Carmen Cavallo¹ and Alexey Y. Koposov^{1,2*}

¹Centre for Material Science and Nanotechnology, Department of Chemistry, University of Oslo, Oslo, Norway, ²Department of Battery Technology, Institute for Energy Technology (IFE), Kjeller, Norway

OPEN ACCESS

Edited by:

Nuria Tapia-Ruiz,
Lancaster University, United Kingdom

Reviewed by:

Brij Kishore,
University of Birmingham,
United Kingdom

*Correspondence:

Amalie Skurtveit
amalie.skurtveit@kjemi.uio.no
Alexey Y. Koposov
alexey.koposov@kjemi.uio.no

[†]These authors share first authorship

Specialty section:

This article was submitted to
Electrochemical Energy Conversion
and Storage,
a section of the journal
Frontiers in Energy Research

Received: 16 March 2022

Accepted: 06 April 2022

Published: 25 April 2022

Citation:

Skurtveit A, Brennhagen A, Park H,
Cavallo C and Koposov AY (2022)
Benefits and Development Challenges
for Conversion-Alloying Anode
Materials in Na-Ion Batteries.
Front. Energy Res. 10:897755.
doi: 10.3389/fenrg.2022.897755

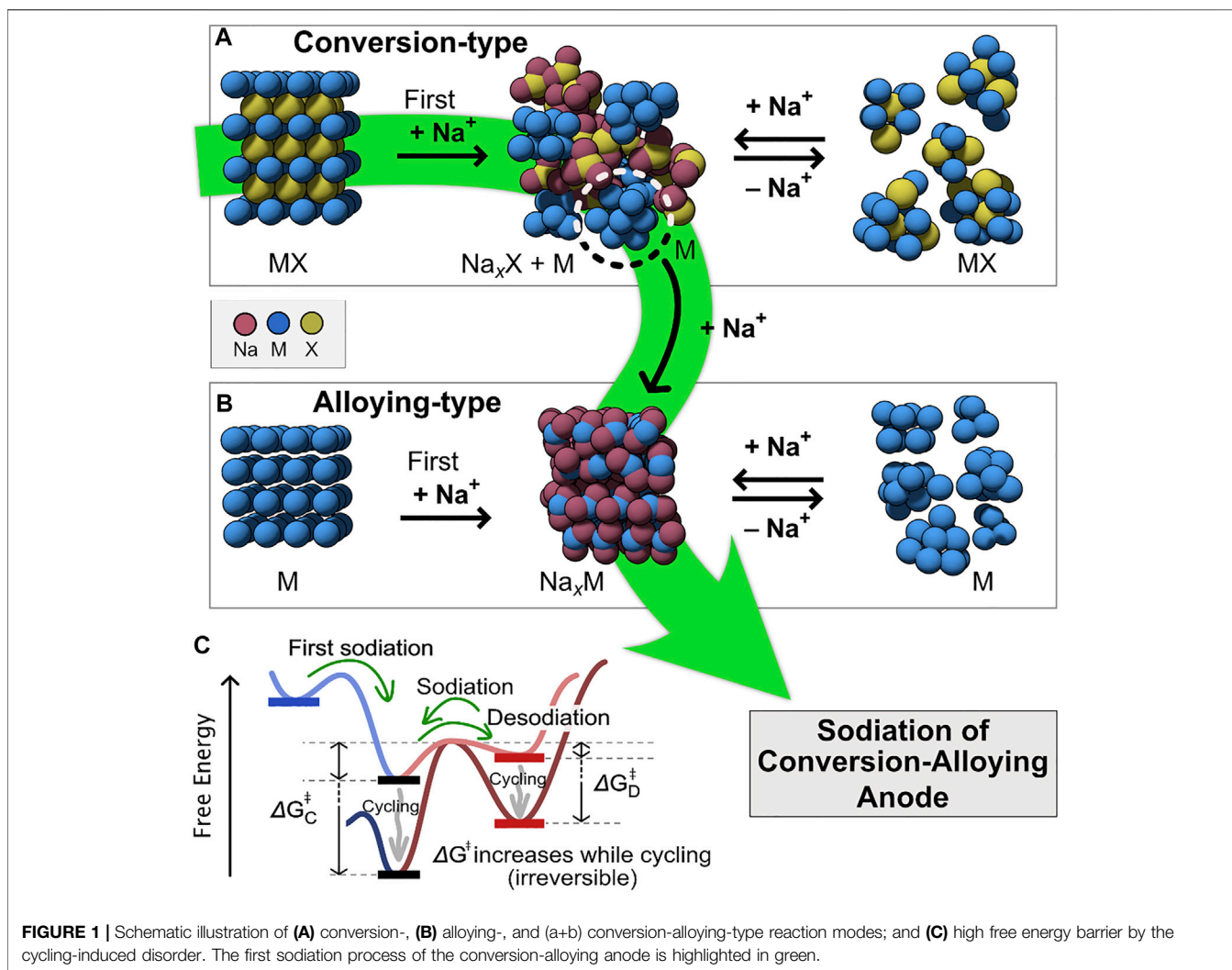
Over the past decade, Na-ion batteries (NIBs) have gained a substantial interest within the research community and relevant industry. NIBs are now emerging as a cost-effective and sustainable alternative to modern Li-ion batteries (LIBs). Similar to the parent LIB technology, NIB requires a new set of materials, which can boost battery capacity without sacrificing cycling stability, rate capabilities, and other performance targets. In NIB chemistry, anodes have received less attention compared to cathode chemistry, leaving hard carbon as a primary anode material, although its intercalation/adsorption mechanism limits the allowed number of Na-ions. Promising alternative groups of anodes are materials that undergo the combined conversion and alloying reactions (i.e., conversion-alloying anodes), due to the beneficial high theoretical capacity and good cycling stability. The conversion reaction in conversion-alloying anodes can be either reversible or irreversible, each possessing its advantages. However, the complexity of their operating mechanism(s) severely impedes their development. The present mini-review provides a survey of the recent developments of conversion-alloying-type anode materials for Na-ion batteries discussed in the context of their operation mechanism(s). Considering the chemical complexity of the conversion-alloying materials, the suggestions and guidance on characterization are provided along with theoretical considerations.

Keywords: sodium-ion batteries, conversion-alloying anodes, operando x-ray methods, (de)sodiation mechanism, *in situ* TEM, specific capacity, Na-ion batteries

INTRODUCTION

Na-ion batteries (NIBs) represent a cost-effective and sustainable alternative to Li-ion batteries (LIBs), promising for application in large-scale stationary energy storage systems (Vaalma et al., 2018; Hasa et al., 2021). While operating under the same rocking-chair principle as LIBs, the conventional anode materials used for LIBs, graphite and Si, are not suited for the use in NIBs (Moriwake et al., 2017; Zhang et al., 2017). Studies of hard carbon materials (most common anode material) are still in progress, but additional research efforts are focused on the other anode materials that follow different operating mechanisms, such as alloying and conversion (Wu et al., 2018; Usiskin et al., 2021; Zheng et al., 2021).

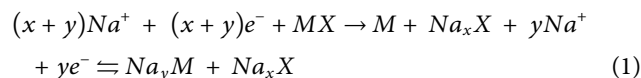
Conversion-based anode materials (**Figure 1A**) are mainly composed of transition metal oxides, sulfides, selenides, and phosphides, while elements from groups 14 and 15 (Si, Ge, Sn, P, Sb, Bi, or binary alloys of these, e.g., BiSb, etc.) represent the most common alloying-based anode materials (**Figure 1B**)



(Zhang H. et al., 2018). Both the alloying- and the conversion-based materials exhibit high theoretical capacities ranging between 300–2000 mA h g⁻¹ (Wang L. et al., 2019). However, as the chemical bonding structure and morphology constantly are altered during the (de)sodiation process (Figures 1A,B), both the conversion- and alloying-type anodes suffer from large volume expansion/contraction (Yao et al., 2017; Chen et al., 2019). This often leads to poor cycling stability (Tan et al., 2019; Wang L. et al., 2019; Fang et al., 2021; Villevieille, 2022). Moreover, before the (de)sodiation process reaches the final state, the varying intermediate alloy compositions are formed as crystalline (Figure 1C), of which metastability is determined within the energy of 70 meV/atom above the convex hull (ground state) (Sun et al., 2016). In addition, the mechanical stress by extensive volume variation limits the electronic contact and causes the electrode pulverization in the pure conversion and alloying process. Consequently, their thermodynamic change, which is caused by the kinetic factor after cycling, increases the free energy barrier and results in performance loss (Hudak et al., 2014; Huang et al., 2020).

Conversion-alloying materials (CAMs) offer a new strategy paving the diversity of available compounds for an innovative

anode material (Wang L. et al., 2019; Fang et al., 2021). CAMs can potentially deliver high specific capacities without the structural degradation mentioned above. Additionally, CAMs can also offer a reduction of the average working potential compared to pure conversion anodes and therefore increase the energy density in a full cell. CAMs combine the conversion and alloying mechanisms (Figure 1, Eq. 1).



The conversion reaction in these materials can be either reversible or irreversible. A reversible conversion reaction provides significantly higher capacities but suffers from the same problems as pure conversion reactions. Therefore, most studies on CAMs are with an irreversible conversion reaction and these will be the focus of this review. The initial irreversible conversion reaction results in the formation of electrochemically active nanoparticles dispersed within a matrix comprised of Na_nX (X = O, S, Se, Te, P, oxometallates). The formed active nanoparticles or clusters then participate in the reaction with

Na-ions through a reversible alloying mechanism. The formed matrix is capable of conducting Na-ions, and together with the active nanoparticles, which have high electronic conductivity, they secure a bi-continuous network beneficial for the electron- and Na⁺-transport that translates into enhanced performance at high cycling rates (Kim et al., 2016; Durai et al., 2017; Lu et al., 2019). The beneficial role of entropy stabilization can be expected in enhancing the cycling performance of the anode during the redox phenomena (Wang Q. et al., 2019; Ghigna et al., 2020). The Na_nX matrix can accommodate the volumetric changes occurring during cycling and provide a physical separation between formed nanoparticles/clusters essentially prohibiting agglomeration/electrochemical sintering of active components as well as particle pulverization. A good compromise between high capacity and cycling stability makes CAMs promising for implementation in next-generation NIBs.

CONVERSION-ALLOYING MATERIALS

CAMs must include an element that should be capable of alloying with Na-ions in its pure form. Therefore, CAMs for NIBs are based on elements from groups 14 or 15 (e.g., Ge, Sn, Sb, or Bi). CAMs require one or more elements that can participate in the conversion reaction, resulting in two classes: binary or ternary. Binary materials, primarily represented by Ge-, Sn-, Sb-, and Bi-based oxides, chalcogenides, and phosphides are the most investigated CAMs (Gu et al., 2013; Sottmann et al., 2016b; Li et al., 2019; Li C. C. et al., 2020; Wu et al., 2020; Shi et al., 2021). The oxides generally adopt a non-layered structure, while the chalcogenides tend to form layered structures due to the increased polarization of the electron cloud of the anions (Tan et al., 2019). In addition to the conversion and alloying reaction, the layered CAMs also include intercalation in the reaction mechanism. The performance of binary CAMs have been extensively reviewed elsewhere (Zhang H. et al., 2018; Fang et al., 2021).

Compared to binary CAMs, ternary materials are significantly less studied, however, several examples based on Bi- and Sb-based oxometallates of transition metals (BiFeO₃, Bi₂(MoO₄)₃, BiVO₄, Sb₂MoO₆, SbVO₄, Bi₂MoO₆) were reported (Durai et al., 2017; Sottmann et al., 2017; Lu et al., 2019; Pan et al., 2019; Brennhagen et al., 2022; Surendran et al., 2022). The choice of the second cation (Fe, Mo, V, etc.) is driven by the ability of the element to form a stable matrix without affecting gravimetric capacity. The large number of transition metals introduces the possibility to produce a variety of ternary CAMs.

The work reported by Sottmann *et al.*, illustrates the benefits of CAMs by comparing three Bi-based anodes: Bi-metal, BiVO₄, and Bi₂(MoO₄)₃ (Sottmann et al., 2016a; Sottmann et al., 2017). Bi-metal had a high initial capacity (~500 mAh g⁻¹), rapidly decaying after 100 cycles to ~300 mAh g⁻¹. BiVO₄ and Bi₂(MoO₄)₃ showed stable capacities of ~350 mAh g⁻¹ during the first 100 cycles. Sb₂MoO₆ exhibited stable capacities of ~600 mAh g⁻¹ for 100 cycles when cycled at 200 mA g⁻¹, and 450 mAh g⁻¹ for 450 cycles at 2 A g⁻¹. It also showed great rate capabilities maintaining the capacity of ~400 mAh g⁻¹ cycled at

5 A g⁻¹, without any signs of significant degradation (Lu et al., 2019). However, recent studies on Sb₂MoO₆ have not been able to reproduce such incredible performances (Yang et al., 2019; Wu and Wang, 2020). Such discrepancies make the comparison between active materials difficult, not only because of the complexity of batteries in general, but also because of the number of choices for selecting other components of the electrodes. This can undermine materials' development because the materials themselves may have variations in chemical composition and different morphological features, surface chemistry, (nano)particle's sizes, and surface coatings that can substantially alter the electrochemical performance. The testing procedures of the materials (potential window, current density, temperature, *etc.*) are also different between studies, complicating the comparison of "equal" materials even more.

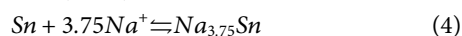
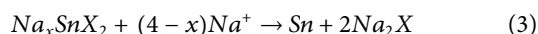
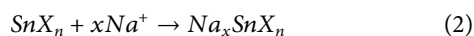
Nanostructuring techniques can generally improve the performance of CAMs, often applied in combination with carbon-based additives/coatings (Sottmann et al., 2016b; Sottmann et al., 2017; Wen et al., 2019; Dai et al., 2020), which is driven by the electrical conductivity. Many CAMs in their pristine state do not have high electronic conductivity, nor has the matrix formed through the conversion process. Creating nanosized CAMs mitigates the consequences of the volume change during the (de)sodiation processes and enhances their activity towards the conversion and alloying reaction (Poizot et al., 2000; Xu et al., 2016; Fang et al., 2019). This leads to a considerable reduction of the diffusion distance of Na-ions in the solid phase, which is beneficial for cycling stability and rate capability (Fang et al., 2021).

THE (DE)SODIATION MECHANISM

The rational design of CAMs is practically impossible without understanding the operating mechanism of CAMs. However, CAMs typically undergo a set of complex structural and chemical transformations during cycling (Fang et al., 2021). That often involves transformation through or into amorphous phases, which complicates the characterization of the materials. The "standard set" of electrochemical characterization techniques can aid in the overall understanding of the conversion-alloying mechanism, but other characterization techniques are also required. Due to complexity of the operating mechanism (i.e., formation of new phases, amorphization, *etc.*), *post mortem* and *ex situ* characterization techniques do not reveal the full scope of the reaction mechanisms. Additionally, air sensitivity and general instability of the materials after sodiation or metastable intermediates also represent a significant issue with *ex situ* characterization (Gao et al., 2018). Techniques such as *operando* X-ray diffraction (XRD), *operando* X-ray absorption spectroscopy (XAS), and *in situ* transmission electron microscopy (TEM) have emerged as suitable characterization techniques providing information complementary to the *post mortem* techniques. Worth mentioning that data-driven guidance is also considered as powerful tool to acquire in-

depth understanding of reaction processes and metastable intermediates (Bai et al., 2018). Mechanistic insights into the conversion-alloying reaction can be obtained by monitoring changes in both crystalline and amorphous phases, oxidation states of active elements, and local structure during (de)sodiation combined with structural modeling (Shadike et al., 2018; Cui et al., 2021a; Brennhagen et al., 2021).

For example, by applying *operando* XRD and *in situ* TEM it has been shown that layered Sn-chalcogenides (SnS_2 and SnSe_2) generally undergo through an intercalation step in addition to the conversion and alloying reactions (Eqs 2–4, respectively) (Shi et al., 2019; Liu et al., 2020; Zhang et al., 2020). *In situ* TEM have also been used to study other binary CAMs, and examples include Sb_2Se_3 , Sb_2S_3 , $\text{Sb}_2\text{Te}_3/\text{C}$ Bi_2Te_3 , SnO_2 , and $\text{Sb}_2\text{Se}_3/\text{rGO}$ (Gu et al., 2013; Ou et al., 2017; Yang et al., 2017; Yao et al., 2017; Wu et al., 2020; Cui et al., 2021b).



Upon sodiation of SnX_n ($X = \text{S}, \text{Se}$), the intercalation of Na-ions 1) occur in the voltage range of $\sim 2.5\text{--}1.1$ V vs. Na/Na^+ , followed by the conversion reaction 2) in the range $1.1\text{--}0.6$ V vs. Na/Na^+ , and the 1st cycle is finalized by the alloying reaction 3) in the $0.6\text{--}0.1$ V region vs. Na/Na^+ . Often, *in situ* TEM can be complementary to *operando* XRD, and *vice versa* (Ou et al., 2017).

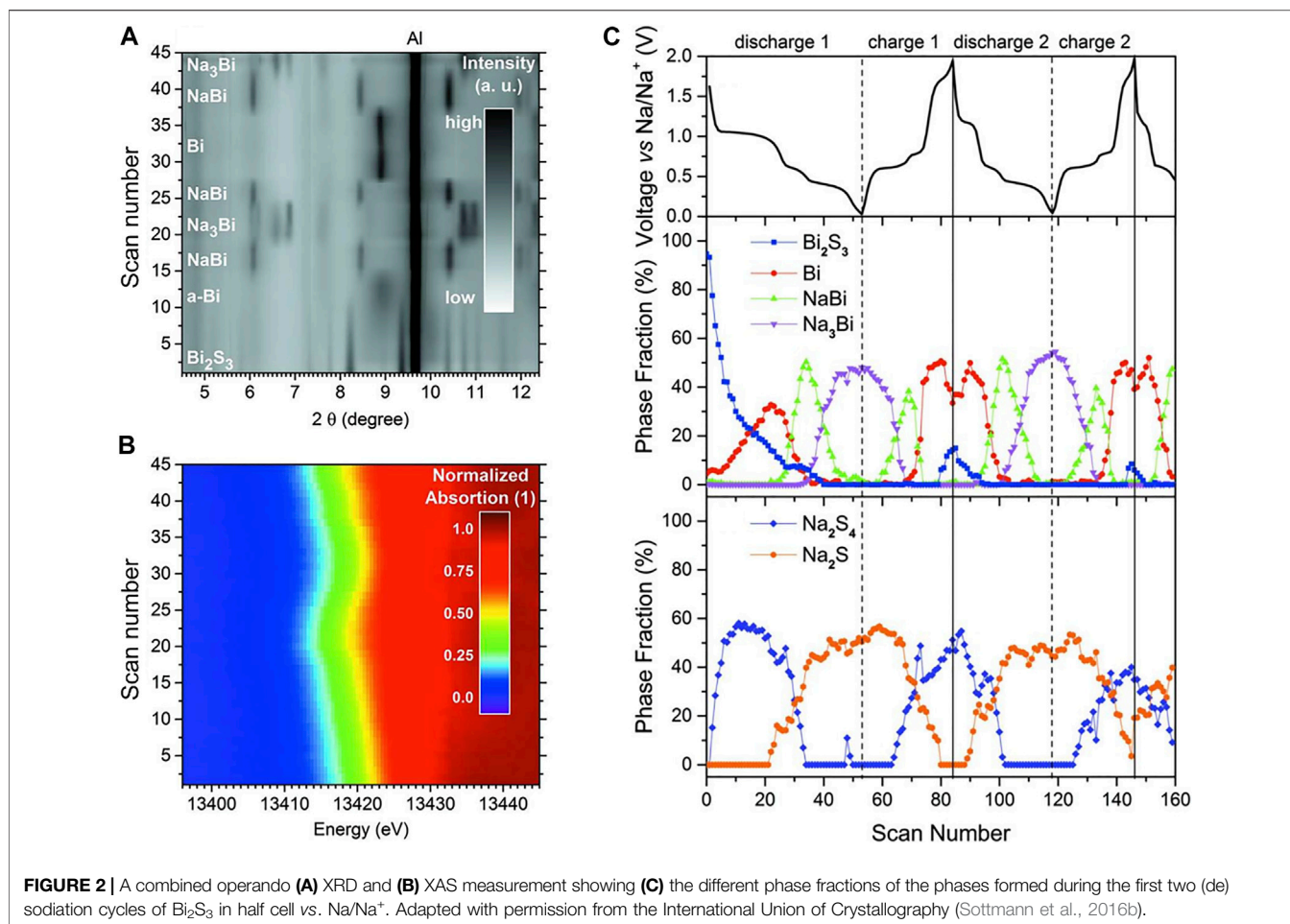
Operando XRD (due to its availability) is the most common characterization technique for assessment of the operation mechanism of CAMs (Brennhagen et al., 2021). *Operando* XRD has been used to elucidate the conversion and alloying reactions for binary CAM anodes (e.g., SnS_2 , Bi_2S_3 , Sb_2S_3 , $\text{Sb}_2\text{O}_3/\text{Sb}$, $\text{Sb}_2\text{O}_3/\text{rGO}$, $\text{Sb}_2\text{S}_3/\text{FeS}_2$, and $\text{Sb}_2\text{Se}_3/\text{rGO}$) (Sottmann et al., 2016b; Ou et al., 2017; Li et al., 2018; Ma et al., 2018; Shi et al., 2019; Cao et al., 2020). In many cases, (ternary CAMs) the matrix formed through the conversion is amorphous (Durai et al., 2017; Lu et al., 2019; Pan et al., 2019; Brennhagen et al., 2022), which calls for other characterization techniques to obtain an understanding of the operation mechanism. *Pair distribution function* (PDF) analysis is among such techniques allowing elucidating amorphous phases formed during (de)sodiation. However, to the best of our knowledge, no *operando* PDF has been performed on CAMs, while bulk Sb and Sn metal (a pure alloying anode) has been studied using *operando* PDF, showing that these relatively simple alloying reactions also contains amorphous intermediates (Allan et al., 2016; Stratford et al., 2017). This also means that we have more to learn from the alloying reactions in CAMs, even though the cycling mechanisms might seem quite clear when only using *operando* XRD.

Another useful *operando* technique, which is used to monitor specific elements in CAMs is *operando* XAS, where X-ray energies are scanned across the absorption edges of the target elements. This technique has been utilized to gain information on changes in oxidation states and local structures during cycling for Bi_2O_3 , Bi_2S_3 , BiVO_4 , $\text{Bi}_2(\text{MoO}_4)_3$, SnO_2 , and BiFeO_3 (Kim et al., 2016; Sottmann et al., 2016b; Sottmann et al., 2017; Dixon et al., 2019; Surendran et al., 2022). In the case of Bi_2S_3 , a measurement

combining *operando* XRD and XAS was used to reveal important aspects of the cycling mechanism (Figure 2) (Sottmann et al., 2016b). During the first sodiation, the irreversible conversion reaction forms amorphous Bi (wide and diffuse peak, Figure 2A) which further goes through a two-step alloying reaction into crystalline NaBi and Na_3Bi . A sharper peak for the Bi phase was observed after the first desodiation, indicating higher degree of crystallinity. The changes in the oxidation states of Bi are also linked to the edge shift in the XANES data (Figure 2B), showing that the oxidation state varies from Bi^{3+} in Bi_2S_3 to Bi^{3-} in Na_3Bi . The study further shows that the Na_xS matrix is not stable because it cycles between Na_2S_4 and Na_2S (Figure 2C). The conversion reaction is partially reversible because some Bi_2S_3 is retrieved at the end of the desodiation (Figure 2C), which is beneficial for specific capacity, but not practical for cycling stability (the second cycle demonstrates diminished formation of Bi_2S_3). Similar instabilities in the matrixes of some ternary CAMs, such as Bi_2MoO_6 and BiFeO_3 , were observed (Brennhagen et al., 2022; Surendran et al., 2022). However, detailed studies on the behavior of the matrixes linked to the electrochemical performance are difficult to perform due to the complexity of the cycling mechanisms and species formed. As a result, such studies are limited and not always conclusive. This illustrates the importance of analysis of the matrix materials when working and designing CAMs.

DISCUSSION

There are clear indications that CAMs have significantly better cycling stability than the pure conversion or alloying materials, while still possessing higher capacities than intercalation materials. Variety of chemical compositions makes it possible to meet the desired compromise of high capacity, good cycling stability, cost, and environmental friendliness. There is a large playground for evaluation of alloying elements with transition metals to produce ternary CAMs. Until present, only a few examples have been explored and there are more to discover in the future. Although the main general cycling mechanism is relatively well understood, the details of the mechanisms have only recently begun to unravel. The stability of the matrix is crucial to maintaining cycling stability and therefore deserves more research efforts. Meanwhile, the non-equilibrium phase of the nanoparticles formed through conversion is also relevant for materials design because co-existing phases (matrix) often exhibit and maintain extreme non-stoichiometry (Yao et al., 2017). There have been high-throughput search reports, along with the accelerated discovery efforts of promising anodes. However, due to the complicated electrochemical reaction with co-existing metastable phases in CAMs, the most high-throughput investigations of anodes have focused yet on single-phase mode within the limited length scale (Ong et al., 2011; Kirklin et al., 2013; Zhang X. et al., 2018; Zhang et al., 2019). This complexity makes CAMs challenging to study and develop. While CAM anodes emerge, it is critical to understand and classify the metastability of intermediate



compounds for elements in the active anode's (de)sodiation reactions to provide data-driven guidance.

One of the biggest challenges with CAMs in full cells is the irreversible capacity loss during the first sodiation due to the irreversible conversion reaction. This demands that the cathode or electrolyte should supply more reaction Na-ions for the first discharge and could lead to a significant amount of dead mass for the subsequent cycles. This problem could be solved by presodiation. Even though this complicates the battery production, it could be viable due to the high capacity, good cycling stability, and rate performance that CAMs could potentially deliver. In addition, the design and optimization of the active element/matrix combination can also assist in mitigation of this complex challenge.

Estimation of the theoretical capacity of CAMs represents a challenge and requires a detailed understanding of the cycling mechanism, which involves multiple chemical and electrochemical transformations. Calculation of the theoretical capacity for CAMs is done by either assuming a fully reversible conversion and alloying reactions or assuming that only the alloying reaction contributes to the capacity. However, for several materials described above partially reversible conversion reactions and/or some electrochemical reactions in the matrix are commonly encountered, which complicate the

estimation of theoretical capacities. Such uncertainty, before determination of the operating mechanism makes it difficult to assess which reactions should be included in the calculated theoretical capacities. The 1-st cycle irreversible capacity (from the irreversible conversion reaction) combined with the SEI formation increases the gap between theoretical and measured specific capacity. It can still be useful to compare the theoretical capacity of certain stages of the reactions to the specific capacities of the corresponding plateaus in the (de)sodiation curves to improve the understanding of the reaction mechanisms.

Considering the abovementioned complication, it is very important to provide all the necessary details of the study and do comparative studies to get a clearer picture of the actual performance of the material as was emphasized in a few recent publications (Li J. et al., 2020; Stephan, 2021; Sun, 2021). The experimental uncertainties add to the complexity of the problem for assessment of the specific vs. theoretical capacities of CAMs. That includes proper consideration of other components of the electrodes, potentially uneven distribution of active material on the electrode sheet, proper statistics of the results, and accurate measurement of the mass of the active material. The latter can deliver an error of $\geq 10\%$ to the calculated specific capacity when performed at the laboratory scale (Brennhagen et al., 2022). In addition, specific current densities rather than C-rates should be preferably reported when working with

these materials, as a determination of the C-rate requires an accurate estimation of the theoretical capacity.

In conclusion, CAMs, while yet underexplored and poorly understood deliver a large potential for the future of NIBs, however, their challenges and operating mechanisms have to be properly examined. That requires not only synthetic efforts, but also careful consideration of the electrochemical characterization techniques as well as development and selection of the *operando* tools.

AUTHOR CONTRIBUTIONS

AS: conceptualization, main writing, reviewing, and editing, literature study. AB: conceptualization, writing, reviewing, and

editing. HP: conceptualization, writing, reviewing, editing, and visualization. CC: conceptualization, writing, reviewing, and editing. AK: conceptualization, writing, reviewing, and editing.

FUNDING

This work was performed within MoZEEs, a Norwegian Centre for Environment-friendly Energy Research (FME), co-sponsored by the Research Council of Norway (project number 257653) and 40 partners from research, industry and public sector. The Research Council of Norway is also acknowledged through the project NanoName (number 287480). The PhD fellowship for AS was provided by the Department of Chemistry of University of Oslo.

REFERENCES

- Allan, P. K., Griffin, J. M., Darwiche, A., Borkiewicz, O. J., Wiaderek, K. M., Chapman, K. W., et al. (2016). Tracking Sodium-Antimonide Phase Transformations in Sodium-Ion Anodes: Insights from Operando Pair Distribution Function Analysis and Solid-State NMR Spectroscopy. *J. Am. Chem. Soc.* 138 (7), 2352–2365. doi:10.1021/jacs.5b13273
- Bai, Q., Yang, L., Chen, H., and Mo, Y. (2018). Computational Studies of Electrode Materials in Sodium-Ion Batteries. *Adv. Energ. Mater.* 8 (17), 1702998. doi:10.1002/aenm.201702998
- Brennhagen, A., Cavallo, C., Wrapp, D. S., Sottmann, J., Kopolov, A. Y., and Fjellvåg, H. (2021). Understanding the (De)Sodiation Mechanisms in Na-Based Batteries through Operando X-Ray Methods. *Batteries & Supercaps* 4 (7), 1039–1063. doi:10.1002/batt.202000294
- Brennhagen, A., Cavallo, C., Wrapp, D. S., Vajeeston, P., Sjästad, A. O., Kopolov, A. Y., et al. (2022). Operando XRD Studies on Bi₂MoO₆ as Anode Material for Na-Ion Batteries. *Nanotechnology* 33 (18), 185402. doi:10.1088/1361-6528/ac4eb5
- Cao, L., Gao, X., Zhang, B., Ou, X., Zhang, J., and Luo, W.-B. (2020). Bimetallic Sulfide Sb₂S₃@FeS₂ Hollow Nanorods as High-Performance Anode Materials for Sodium-Ion Batteries. *ACS Nano* 14 (3), 3610–3620. doi:10.1021/acsnano.0c00020
- Chen, W., Zhang, X., Mi, L., Liu, C., Zhang, J., Cui, S., et al. (2019). High-Performance Flexible Freestanding Anode with Hierarchical 3D Carbon-Networks/F27S8/Graphene for Applicable Sodium-Ion Batteries. *Adv. Mater.* 31 (8), 1806664. doi:10.1002/adma.201806664
- Cui, J., Zheng, H., and He, K. (2021a). *In Situ* TEM Study on Conversion-Type Electrodes for Rechargeable Ion Batteries. *Adv. Mater.* 33 (6), 2000699. doi:10.1002/adma.202000699
- Cui, J., Zheng, H., Zhang, Z., Hwang, S., Yang, X.-Q., and He, K. (2021b). Origin of Anomalous High-Rate Na-Ion Electrochemistry in Layered Bismuth telluride Anodes. *Matter* 4 (4), 1335–1351. doi:10.1016/j.matt.2021.01.005
- Dai, S., Wang, L., Shen, Y., and Wang, M. (2020). Bismuth Selenide Nanocrystalline Array Electrodes for High-Performance Sodium-Ion Batteries. *Appl. Mater. Today* 18, 100455. doi:10.1016/j.apmt.2019.100455
- Dixon, D., Ávila, M., Ehrenberg, H., and Bhaskar, A. (2019). Difference in Electrochemical Mechanism of SnO₂ Conversion in Lithium-Ion and Sodium-Ion Batteries: Combined in Operando and *Ex Situ* XAS Investigations. *ACS Omega* 4 (6), 9731–9738. doi:10.1021/acsomega.9b00563
- Durai, L., Moorthy, B., Issac Thomas, C., Kyung Kim, D., and Kamala Bharathi, K. (2017). Electrochemical Properties of BiFeO₃ Nanoparticles: Anode Material for Sodium-Ion Battery Application. *Mater. Sci. Semiconductor Process.* 68, 165–171. doi:10.1016/j.mssp.2017.06.003
- Fang, L., Bahlawane, N., Sun, W., Pan, H., Xu, B. B., Yan, M., et al. (2021). Conversion-Alloying Anode Materials for Sodium Ion Batteries. *Small* 17 (37), 2101137. doi:10.1002/smll.202101137
- Fang, Y., Yu, X.-Y., and Lou, X. W. (2019). Nanostructured Electrode Materials for Advanced Sodium-Ion Batteries. *Matter* 1 (1), 90–114. doi:10.1016/j.matt.2019.05.007
- Gao, H., Ma, W., Yang, W., Wang, J., Niu, J., Luo, F., et al. (2018). Sodium Storage Mechanisms of Bismuth in Sodium Ion Batteries: An Operando X-ray Diffraction Study. *J. Power Sourc.* 379, 1–9. doi:10.1016/j.jpowsour.2018.01.017
- Ghigna, P., Airolidi, L., Fracchia, M., Callegari, D., Anselmi-Tamburini, U., D'Angelo, P., et al. (2020). Lithiation Mechanism in High-Entropy Oxides as Anode Materials for Li-Ion Batteries: An Operando XAS Study. *ACS Appl. Mater. Inter.* 12 (45), 50344–50354. doi:10.1021/acsmi.0c13161
- Gu, M., Kushima, A., Shao, Y., Zhang, J.-G., Liu, J., Browning, N. D., et al. (2013). Probing the Failure Mechanism of SnO₂ Nanowires for Sodium-Ion Batteries. *Nano Lett.* 13 (11), 5203–5211. doi:10.1021/nl402633n
- Hasa, I., Mariyappan, S., Saurel, D., Adelhelm, P., Kopolov, A. Y., Masquelier, C., et al. (2021). Challenges of Today for Na-Based Batteries of the Future: From Materials to Cell Metrics. *J. Power Sourc.* 482, 228872. doi:10.1016/j.jpowsour.2020.228872
- Huang, Y.-X., Wu, F., and Chen, R.-J. (2020). Thermodynamic Analysis and Kinetic Optimization of High-Energy Batteries Based on Multi-Electron Reactions. *Natl. Sci. Rev.* 7 (8), 1367–1386. doi:10.1093/nsr/nwaa075
- Hudak, N. S., Davis, L. E., and Nagasubramanian, G. (2014). Cycling-Induced Changes in the Entropy Profiles of Lithium Cobalt Oxide Electrodes. *J. Electrochem. Soc.* 162 (3), A315–A321. doi:10.1149/2.0071503jes
- Kim, M.-K., Yu, S.-H., Jin, A., Kim, J., Ko, I.-H., Lee, K.-S., et al. (2016). Bismuth Oxide as a High Capacity Anode Material for Sodium-Ion Batteries. *Chem. Commun.* 52 (79), 11775–11778. doi:10.1039/C6CC06712C
- Kirklín, S., Meredig, B., and Wolverton, C. (2013). High-Throughput Computational Screening of New Li-Ion Battery Anode Materials. *Adv. Energ. Mater.* 3 (2), 252–262. doi:10.1002/aenm.201200593
- Li, C. C., Wang, B., Chen, D., Gan, L.-Y., Feng, Y., Zhang, Y., et al. (2020a). Topotactic Transformation Synthesis of 2D Ultrathin GeS₂ Nanosheets toward High-Rate and High-Energy-Density Sodium-Ion Half/Full Batteries. *ACS Nano* 14 (1), 531–540. doi:10.1021/acsnano.9b06855
- Li, H., Qian, K., Qin, X., Liu, D., Shi, R., Ran, A., et al. (2018). The Different Li/Na Ion Storage Mechanisms of Nano Sb₂O₃ Anchored on Graphene. *J. Power Sourc.* 385, 114–121. doi:10.1016/j.jpowsour.2018.03.031
- Li, J., Arbizzani, C., Kjelstrup, S., Xiao, J., Xia, Y.-y., Yu, Y., et al. (2020b). Good Practice Guide for Papers on Batteries for the Journal of Power Sources. *J. Power Sourc.* 452, 227824. doi:10.1016/j.jpowsour.2020.227824
- Li, W., Li, X., Liao, J., Zhao, B., Zhang, L., Liu, Y., et al. (2019). Structural Design of Ge-Based Anodes with Chemical Bonding for High-Performance Na-Ion Batteries. *Energ. Storage Mater.* 20, 380–387. doi:10.1016/j.ensm.2019.04.034
- Liu, Z., Daali, A., Xu, G.-L., Zhuang, M., Zuo, X., Sun, C.-J., et al. (2020). Highly Reversible Sodiation/Desodiation from a Carbon-Sandwiched SnS₂ Nanosheet Anode for Sodium Ion Batteries. *Nano Lett.* 20 (5), 3844–3851. doi:10.1021/acsnanolett.0c00964
- Lu, X., Wang, Z., Liu, K., Luo, J., Wang, P., Niu, C., et al. (2019). Hierarchical Sb₂MoO₆ Microspheres for High-Performance Sodium-Ion Battery Anode. *Energ. Storage Mater.* 17, 101–110. doi:10.1016/j.ensm.2018.11.021
- Ma, W., Wang, J., Gao, H., Niu, J., Luo, F., Peng, Z., et al. (2018). A Mesoporous Antimony-Based Nanocomposite for Advanced Sodium Ion Batteries. *Energ. Storage Mater.* 13, 247–256. doi:10.1016/j.ensm.2018.01.016

- Moriwake, H., Kuwabara, A., Fisher, C. A. J., and Ikuhara, Y. (2017). Why Is Sodium-Intercalated Graphite Unstable? *RSC Adv.* 7 (58), 36550–36554. doi:10.1039/C7RA06777A
- Ong, S. P., Chevrier, V. L., Hautier, G., Jain, A., Moore, C., Kim, S., et al. (2011). Voltage, Stability and Diffusion Barrier Differences between Sodium-Ion and Lithium-Ion Intercalation Materials. *Energy Environ. Sci.* 4 (9), 3680–3688. doi:10.1039/C1EE01782A
- Ou, X., Yang, C., Xiong, X., Zheng, F., Pan, Q., Jin, C., et al. (2017). A New rGO-Overcoated Sb₂Se₃ Nanorods Anode for Na+Battery: *In Situ* X-Ray Diffraction Study on a Live Sodiation/Desodiation Process. *Adv. Funct. Mater.* 27 (13), 1606242. doi:10.1002/adfm.201606242
- Pan, J., Zhang, Y., Li, L., Cheng, Z., Li, Y., Yang, X., et al. (2019). Polyanions Enhance Conversion Reactions for Lithium/Sodium-Ion Batteries: The Case of SbVO 4 Nanoparticles on Reduced Graphene Oxide. *Small Methods* 3 (10), 1900231. doi:10.1002/smt.201900231
- Poizat, P., Laruelle, S., Grugeon, S., Dupont, L., and Tarascon, J.-M. (2000). Nano-sized Transition-Metal Oxides as Negative-Electrode Materials for Lithium-Ion Batteries. *Nature* 407 (6803), 496–499. doi:10.1038/35035045
- Shadik, Z., Zhao, E., Zhou, Y. N., Yu, X., Yang, Y., Hu, E., et al. (2018). Advanced Characterization Techniques for Sodium-Ion Battery Studies. *Adv. Energ. Mater.* 8 (17), 1702588. doi:10.1002/aenm.201702588
- Shi, X., Chen, S. L., Fan, H. N., Chen, X. H., Yuan, D., Tang, Q., et al. (2019). Metallic-State SnS 2 Nanosheets with Expanded Lattice Spacing for High-Performance Sodium-Ion Batteries. *ChemSusChem* 12 (17), 4046–4053. doi:10.1002/cssc.201901355
- Shi, X., Liu, W., Xue, H., Chen, B., Wang, C., Sun, L., et al. (2021). An Exploration on the Improvement of Reversible Conversion and Capacity Retention of Sb₂O₃-Based Anode Materials for Alkali Metal-Ion Storage by Fe-C Co-hybridization. *J. Power Sourc.* 506, 230074. doi:10.1016/j.jpowsour.2021.230074
- Sottmann, J., Herrmann, M., Vajeston, P., Hu, Y., Ruud, A., Drathen, C., et al. (2016a). How Crystallite Size Controls the Reaction Path in Nonaqueous Metal Ion Batteries: The Example of Sodium Bismuth Alloying. *Chem. Mater.* 28 (8), 2750–2756. doi:10.1021/acs.chemmater.6b00491
- Sottmann, J., Herrmann, M., Vajeston, P., Ruud, A., Drathen, C., Emerich, H., et al. (2017). Bismuth Vanadate and Molybdate: Stable Alloying Anodes for Sodium-Ion Batteries. *Chem. Mater.* 29 (7), 2803–2810. doi:10.1021/acs.chemmater.6b04699
- Sottmann, J., Homs-Regojo, R., Wragg, D. S., Fjellvåg, H., Margadonna, S., and Emerich, H. (2016b). Versatile Electrochemical Cell for Li/Na-Ion Batteries and High-Throughput Setup for combined operando X-ray Diffraction and Absorption Spectroscopy. *J. Appl. Cryst.* 49 (6), 1972–1981. doi:10.1107/S160057671601428X
- Stephan, A. K. (2021). Standardized Battery Reporting Guidelines. *Joule* 5 (1), 1–2. doi:10.1016/j.joule.2020.12.026
- Stratford, J. M., Mayo, M., Allan, P. K., Pecher, O., Borkiewicz, O. J., Wiaderek, K. M., et al. (2017). Investigating Sodium Storage Mechanisms in Tin Anodes: A Combined Pair Distribution Function Analysis, Density Functional Theory, and Solid-State NMR Approach. *J. Am. Chem. Soc.* 139 (21), 7273–7286. doi:10.1021/jacs.7b01398
- Sun, W., Dacek, S. T., Ong, S. P., Hautier, G., Jain, A., Richards, W. D., et al. (2016). The Thermodynamic Scale of Inorganic Crystalline Metastability. *Sci. Adv.* 2 (11), e1600225. doi:10.1126/sciadv.1600225
- Sun, Y.-K. (2021). An Experimental Checklist for Reporting Battery Performances. *ACS Energ. Lett.* 6 (6), 2187–2189. doi:10.1021/acsenergylett.1c00870
- Surendran, A., Enale, H., Thottungal, A., Sarapulova, A., Knapp, M., Nishanthi, S. T., et al. (2022). Unveiling the Electrochemical Mechanism of High-Capacity Negative Electrode Model-System BiFeO₃ in Sodium-Ion Batteries: An in Operando XAS Investigation. *ACS Appl. Mater. Inter.* 14, 7856–7868. doi:10.1021/acsmi.1c20717
- Tan, H., Chen, D., Rui, X., and Yu, Y. (2019). Peering into Alloy Anodes for Sodium-Ion Batteries: Current Trends, Challenges, and Opportunities. *Adv. Funct. Mater.* 29 (14), 1808745. doi:10.1002/adfm.201808745
- Usiskin, R., Lu, Y., Popovic, J., Law, M., Balaya, P., Hu, Y.-S., et al. (2021). Fundamentals, Status and Promise of Sodium-Based Batteries. *Nat. Rev. Mater.* 6 (11), 1020–1035. doi:10.1038/s41578-021-00324-w
- Vaalma, C., Buchholz, D., Weil, M., and Passerini, S. (2018). A Cost and Resource Analysis of Sodium-Ion Batteries. *Nat. Rev. Mater.* 3 (4), 18013. doi:10.1038/natrevmats.2018.13
- Villeveille, C. (2022). Interfaces and Interphases in Batteries: How to Identify and Monitor Them Properly Using Surface Sensitive Characterization Techniques. *Adv. Mater. Inter.* 9, 2101865. doi:10.1002/admi.202101865
- Wang, L., Świątowska, J., Dai, S., Cao, M., Zhong, Z., Shen, Y., et al. (2019a). Promises and Challenges of alloy-type and Conversion-type Anode Materials for Sodium-Ion Batteries. *Mater. Today Energy* 11, 46–60. doi:10.1016/j.mtener.2018.10.017
- Wang, Q., Sarkar, A., Wang, D., Velasco, L., Azmi, R., Bhattacharya, S. S., et al. (2019b). Multi-anionic and -cationic Compounds: New High Entropy Materials for Advanced Li-Ion Batteries. *Energy Environ. Sci.* 12 (8), 2433–2442. doi:10.1039/C9EE00368A
- Wen, S., Zhao, J., Zhao, Y., Xu, T., and Xu, J. (2019). Reduced Graphene Oxide (RGO) Decorated Sb₂S₃ Nanorods as Anode Material for Sodium-Ion Batteries. *Chem. Phys. Lett.* 716, 171–176. doi:10.1016/j.cplett.2018.12.031
- Wu, C., Dou, S. X., and Yu, Y. (2018). The State and Challenges of Anode Materials Based on Conversion Reactions for Sodium Storage. *Small* 14 (22), 1703671. doi:10.1002/sml.201703671
- Wu, Q., and Wang, H. G. (2020). Sb₂MoO₆ Decorated on Graphene as an Anode Material for Lithium/Sodium-Ion Batteries. *J. Phys. Conf. Ser.* 1605 (1), 012176. doi:10.1088/1742-6596/1605/1/012176
- Wu, Y., Luo, W., Gao, P., Zhu, C., Hu, X., Qu, K., et al. (2020). Unveiling the microscopic origin of asymmetric phase transformations in (de)sodiated Sb₂Se₃ with *In Situ* transmission electron microscopy. *Nano Energy* 77, 105299. doi:10.1016/j.nanoen.2020.105299
- Xu, Y., Zhou, M., and Lei, Y. (2016). Nanoarchitected Array Electrodes for Rechargeable Lithium- and Sodium-Ion Batteries. *Adv. Energ. Mater.* 6 (10), 1502514. doi:10.1002/aenm.201502514
- Yang, L., Liao, H., Tian, Y., Hong, W., Cai, P., Liu, C., et al. (2019). Rod-Like Sb₂MoO₆: Structure Evolution and Sodium Storage for Sodium-Ion Batteries. *Small Methods* 3 (5), 1800533. doi:10.1002/smt.201800533
- Yang, Z., Sun, J., Ni, Y., Zhao, Z., Bao, J., and Chen, S. (2017). Facile Synthesis and *In Situ* Transmission Electron Microscopy Investigation of a Highly Stable Sb₂Te₃/C Nanocomposite for Sodium-Ion Batteries. *Energy Storage Mater.* 9, 214–220. doi:10.1016/j.ensm.2017.07.010
- Yao, S., Cui, J., Lu, Z., Xu, Z.-L., Qin, L., Huang, J., et al. (2017). Unveiling the Unique Phase Transformation Behavior and Sodiation Kinetics of 1D van der Waals Sb₂S₃ Anodes for Sodium Ion Batteries. *Adv. Energ. Mater.* 7 (8), 1602149. doi:10.1002/aenm.201602149
- Zhang, F., Shen, Y., Shao, M., Zhang, Y., Zheng, B., Wu, J., et al. (2020). SnSe₂ Nanoparticles Chemically Embedded in a Carbon Shell for High-Rate Sodium-Ion Storage. *ACS Appl. Mater. Inter.* 12 (2), 2346–2353. doi:10.1021/acsmi.9b16659
- Zhang, H., Hasa, I., and Passerini, S. (2018a). Beyond Insertion for Na-Ion Batteries: Nanostructured Alloying and Conversion Anode Materials. *Adv. Energ. Mater.* 8 (17), 1702582. doi:10.1002/aenm.201702582
- Zhang, L., Hu, X., Chen, C., Guo, H., Liu, X., Xu, G., et al. (2017). In Operando Mechanism Analysis on Nanocrystalline Silicon Anode Material for Reversible and Ultrafast Sodium Storage. *Adv. Mater.* 29 (5), 1604708. doi:10.1002/adma.201604708
- Zhang, X., Zhang, Z., Yao, S., Chen, A., Zhao, X., and Zhou, Z. (2018b). An Effective Method to Screen Sodium-Based Layered Materials for Sodium Ion Batteries. *Npj Comput. Mater.* 4 (1), 13. doi:10.1038/s41524-018-0070-2
- Zhang, Z., Zhang, X., Zhao, X., Yao, S., Chen, A., and Zhou, Z. (2019). Computational Screening of Layered Materials for Multivalent Ion Batteries. *ACS Omega* 4 (4), 7822–7828. doi:10.1021/acsomega.9b00482
- Zheng, S.-M., Tian, Y.-R., Liu, Y.-X., Wang, S., Hu, C.-Q., Wang, B., et al. (2021). Alloy Anodes for Sodium-Ion Batteries. *Rare Met.* 40 (2), 272–289. doi:10.1007/s12598-020-01605-z

Conflict of Interest: The authors declare that the research was conducted in the absence of any commercial or financial relationships that could be construed as a potential conflict of interest.

Publisher's Note: All claims expressed in this article are solely those of the authors and do not necessarily represent those of their affiliated organizations, or those of the publisher, the editors and the reviewers. Any product that may be evaluated in this article, or claim that may be made by its manufacturer, is not guaranteed or endorsed by the publisher.

Copyright © 2022 Skurtveit, Brennhagen, Park, Cavallo and Koposov. This is an open-access article distributed under the terms of the Creative Commons Attribution License (CC BY). The use, distribution or reproduction in other forums is permitted, provided the original author(s) and the copyright owner(s) are credited and that the original publication in this journal is cited, in accordance with accepted academic practice. No use, distribution or reproduction is permitted which does not comply with these terms.

Paper 2 – Review

Understanding the (de)sodiation mechanisms in Na-based batteries through Operando X-ray methods

A. Brennhagen, C. Cavallo, D. Wragg, J. Sottmann, A. Kuposov, and H. Fjellvåg

Batteries & Supercaps, **2021**, 4(7), 1039-1063.

2

Special
Collection

Understanding the (De)Sodiation Mechanisms in Na-Based Batteries through Operando X-Ray Methods

Anders Brennhagen,^[a] Carmen Cavallo,^{*[a]} David S. Wragg,^[a, b] Jonas Sottmann,^[c, d]
Alexey Y. Koposov,^[a, e] and Helmer Fjellvåg^[a]



Progress in the field of Na-based batteries strongly relies on the development of new advanced materials. However, one of the main challenges of implementing new electrode materials is the understanding of their mechanisms (sodiation/desodiation) during electrochemical cycling. *Operando* studies provide extremely valuable insights into structural and chemical changes within different battery components during battery operation. The present review offers a critical summary of the *operando* X-ray based characterization techniques used to

examine the structural and chemical transformations of the active materials in Na-ion, Na-air and Na-sulfur batteries during (de)sodiation. These methods provide structural and electronic information through diffraction, scattering, absorption and imaging or through a combination of these X-ray-based techniques. Challenges associated with cell design and data processing are also addressed herein. In addition, the present review provides a perspective on the future opportunities for these powerful techniques.

1. Introduction

Electrification of the energy sector represents a major challenge for society. Novel and powerful rechargeable batteries are an essential part of the solution. Li-ion batteries (LIBs) now dominate the market for transportation and portable electronics due to their high energy and power density.^[1,2] However, rapid growth of the LIB market may lead to shortage of some elements (including Li) currently utilized in LIBs, creating a need for complementary technologies. Non-aqueous Na-ion batteries (NIBs) are currently one of the most promising alternatives to LIBs representing a cheaper alternative, benefiting from the abundance of sodium in seawater and the earth's crust and its availability, which is not affected by geopolitical conflicts.^[3]

NIBs are inferior to LIBs in energy density, however, they are potential competitors to LIBs for large-scale stationary storage^[4] and applications where the lower cost of NIB's components becomes a significant factor. NIBs share the

“rocking chair” principle of LIBs and benefited from the massive body of research on the latter. The larger size of Na⁺ compared to Li⁺ results in differences between the two chemistries: for example, graphite, which is the most common commercial anode in LIBs, does not work in the same way for NIBs.^[5,6] Other materials are better suited for NIBs than for LIBs, such as Sn,^[7] Cu₃PS₄,^[8] Sb₂O₃ (better cycling stability)^[9] and NaNi_{1/2}Mn_{1/2}O₂ (faster kinetics).^[10] For both chemistries, the electrodes have three main working principles: intercalation/insertion, conversion and alloying.^[11,12] Cathodes usually have intercalation or insertion mechanisms, while anode materials utilize all three working principles (either separate or combined). This review is focused on the use of X-ray based *operando* methods (already used extensively for LIBs and to some degree for NIBs^[13–15]) for studying the chemical transformations of active materials during cycling of NIBs. Our review is not intended as an overview of materials for NIBs, as this can be found in several recent reviews.^[1,12,16]

During the last decade, *operando* and *in situ* experiments became powerful tools for understanding the electrochemistry and associated structural changes of NIB materials during sodiation and desodiation.

In situ means “in the original place” and refers to measurements of materials in their working environment. In synthetic chemistry and catalysis, it is used to describe structural measurements conducted during chemical reactions, but for battery materials, *in situ* is used to describe any experiment where the material remains inside the battery cell (or another environment used for electrochemistry). This has led to some confusion in the literature, especially among those with long experience of *in situ* studies in other fields. The opposite term, *ex situ* (“off-site” or “away” from the site), indicates that the characterization has been performed on a material removed from a battery.^[14,17,18]

Operando is best translated to “in operation” and refers to measurements performed under operating/working conditions with activity data collected simultaneously. This implies that measurements are conducted while the studied system is operated under conditions similar to a real application. For batteries, an *operando* experiment would involve logging electrochemical cycling data while simultaneously performing structural measurements with subsequent analysis linking the results together, as illustrated in Figure 1.^[14,17,18] This requires that the cycling continues during structural data collection, regardless of the C rate at which the battery is cycled. If the

[a] A. Brennhagen, C. Cavallo, D. S. Wragg, A. Y. Kozosov, H. Fjellvåg
 Centre for Material Science and Nanotechnology
 Department of Chemistry, University of Oslo
 PO Box 1033, Blindern, 0315, Oslo, Norway
 E-mail: carmen.cavallo@smn.uio.no

[b] D. S. Wragg
 Norwegian National Resource Centre for X-ray Diffraction and Scattering (RECX)
 Department of Chemistry, University of Oslo
 PO Box 1033, Blindern, 0315, Oslo, Norway

[c] J. Sottmann
 Physico-chimie des Électrolytes et Nanosystèmes Interfaciaux (PHENIX)
 Sorbonne Université, CNRS
 75005 Paris, France

[d] J. Sottmann
 Réseau sur le Stockage Electrochimique de l'Energie (RS2E)
 FR CNRS 3459
 80039 Amiens Cedex, France

[e] A. Y. Kozosov
 Department of Battery Technology
 Institute for Energy Technology (IFE)
 Instituttveien 18, 2007 Kjeller, Norway

Supporting information for this article is available on the WWW under <https://doi.org/10.1002/batt.202000294>

An invited contribution to a joint Special Collection between – ChemElectroChem and Batteries & Supercaps dedicated to research Beyond Lithium-Ion Batteries.

© 2021 The Authors. Batteries & Supercaps published by Wiley-VCH GmbH. This is an open access article under the terms of the Creative Commons Attribution License, which permits use, distribution and reproduction in any medium, provided the original work is properly cited.

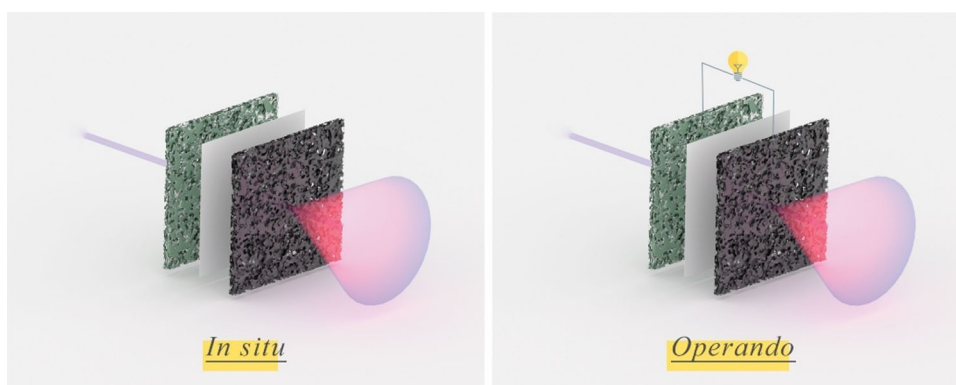


Figure 1. Scheme of *in situ* vs. *operando* experiments. *Operando* requires that the cycling be continuously performed and not stopped during the structural characterization.



Anders Brennhagen is currently pursuing his Ph.D. at the University of Oslo (UiO) in the field of Na-ion batteries focusing on conversion and alloying anode materials. A central part of the work is to use X-ray based *operando* characterization techniques to study the working mechanisms during cycling. He finished his B.Sc. degree in 2017 and M.Sc. degree in 2019, both within the field of battery materials at UiO. In his M.Sc. work he studied thin film cathodes for Li-ion batteries synthesized by atomic layer deposition.



Dr. Carmen Cavallo is an Associate Researcher at University of Oslo. She has a strong experience in batteries with more than 7 years of experience in the field. Currently, she is a battery scientist working on Li/Na/multivalent battery and capacitors materials, focusing on *operando* X-ray-based characterization. She worked as postdoctoral researcher fellow at Chalmers University of Technology, Sweden and a visiting scientist at the Commonwealth Scientific and Industrial Research Organization (CSIRO), Australia. She took her PhD in 2015 at the Sapienza University, Rome, supported by an intense collaboration with Stanford University (USA).



Dr. David Wragg is the manager of the Norwegian National Centre for X-ray Diffraction and Scattering (RECX). He holds a Ph.D. in chemistry from the University of St Andrews. His particular research interests lie in *operando* X-ray diffraction studies on functional materials like batteries and catalysts: analyzing data with rigorous crystallographic methods and applying new methods (e.g., PDF computed tomography) to understand the fundamental relationships between structure and properties in working materials.



Dr. Jonas Sottmann is a CNRS Associate Researcher in PHENIX Laboratory at Sorbonne University in Paris, France. After graduating from University Claude Bernard Lyon, France, he obtained his Ph.D. in electrochemistry and *operando* synchrotron studies of non-aqueous electrode materials from University of Oslo, Norway, in 2017. He then worked as a postdoctoral researcher under the guidance of Dr. Christine Martin in the CRISMAT laboratory in Caen, France. Since 2019, Dr. Sottmann has focused on the development of novel *in situ* tools to investigate electrolyte-electrode interfaces in batteries using synchrotron radiation.



Alexey Y. Koposov is Associate Professor of Chemistry at University of Oslo (UiO, Norway). He also holds a joined appointment as a Senior Scientist at the Institute for Energy Technology (IFE, Norway). He received his BS/MS degree in Materials Science from Moscow State University and PhD degree in Chemistry from University of Minnesota. After graduation, he worked in Los Alamos National Laboratory as a Postdoctoral Associate and later in 2011; he joined SHARP Corporation as a Senior Scientist. His current research interest includes synthesis and advanced characterization of new materials for emerging battery technologies.



Professor Helmer Fjellvåg, is head of Section for Nanostructures and Functional Materials at the Department of Chemistry, University of Oslo (UiO). After stays at the Max-Planck Institut für Festkörperforschung, Stuttgart and Institut Laue-Langevin, Grenoble, he started as Assoc. Prof. at UiO in 1987, as full professor since 1992. His field of expertise is solid state chemistry, with focus on synthesis of new compounds, structure-property relationships, combining experiment and modeling, and using synchrotron and neutron diffraction methods for detailed analyses, at *in situ* and *operando* conditions.

cycling is stopped while structural data are collected it becomes an *in situ* measurement. Based on more than 100 articles examined during the preparation of this review (Figure S1), we observed that the use of the term *operando* has gradually surpassed that of *in situ* and other related terms for studies on batteries during cycling. We therefore use the term *operando* to describe all the studies in this review.

Generally, *ex situ* measurements can be performed using standard instruments and, therefore, are substantially more accessible than the alternatives mentioned above. However, in order to create a comprehensive set of *ex situ* data describing chemical transformations during cycling, many batteries must be fabricated and stopped at different stages of cycling. Furthermore, several problems can occur before the sample can be measured *ex situ*. First, an active material can immediately relax from its active state as soon as cycling stops. Second, careless disassembly of cells can lead to short circuits, contamination or damage to the material of interest. Third, *ex situ* measurements performed under ambient conditions, compromise the chemical integrity of the studied samples (e.g., NaBi and Na₃Bi formed through sodiation of Bi-based anodes rapidly decompose in air^[19]). Finally, since only a few stages in the electrochemical process can reasonably be measured *ex situ*, it is easy to miss short-lived intermediates or unexpected non-linear behaviour of the chemical or structural transformations. The use of inert transfer chambers to preserve the sample while it is moved to the measurement instrument can further complicate *ex situ* measurements.

In situ and *operando* measurements do not require the removal of the studied materials from the battery, but they deliver their own disadvantages. Both types typically require the use of specially designed cells and equipment (see Section 5 of the present review).^[20–23] Such set-ups often have limited comparability to conventional cells and require slow charge and discharge to obtain high quality structural data.^[24] In addition, if high-energy radiation sources are used for data acquisition, heating and damage caused by the beam may affect the structure of the active material.^[25]

Frequently, the active materials in NIBs undergo a complex series of transformations including formation of intermediate phases, which influence their overall stability and cyclability. It is exceptionally difficult to detect these intermediate states with conventional *in situ* and *ex situ* characterization methods due to relaxation from the active state. *Operando* methods open up the possibility of following the path of structural changes for active material while cycling, allowing detection of the intermediates and therefore determine the mechanism of functionality.

Operando studies using X-rays have been utilized from the early stages of battery research. Chianelli *et al.* reported what could be described as the first *operando* study of a battery material in 1978. The use of continuous X-ray diffraction to study of LiTiS₂-based cathode during cycling, with the structural data being correlated to the electrochemistry in the analysis, is described by the authors as “dynamic X-ray diffraction”.^[26] It is noteworthy that this work was carried out only two years after Whittingham demonstrated a working rechargeable LIB with

TiS₂ as the cathode,^[27] and 24 years before the term *operando* was popularised in the catalysis community.^[28–31] As of today, a large ensemble of techniques used for *operando* characterization of batteries including diffraction/scattering, spectroscopy, imaging and combinations of these techniques. While several alternative techniques for *operando* studies, such as transmission electron microscopy (TEM), atomic force microscopy (AFM), nuclear magnetic resonance (NMR) and Raman spectroscopy, have become recently available, X-ray-based techniques are still the most popular choice in the battery research.

This review provides a summary of *operando* X-ray characterization techniques used for assessment of sodiation/desodiation mechanisms in NIBs. It is organized in three separate sections summarizing the most common *operando* X-ray techniques (diffraction/scattering, absorption/spectroscopy and imaging/combined techniques); and two more sections describing the design of *operando* cells and relevant data processing. It should be noted that some articles utilize several complementary techniques in the analysis of (de)sodiation mechanisms. Such results are grouped in this review according to the main *operando* technique used in the cited work.

2. X-Ray Diffraction and Scattering

X-ray diffraction (XRD) is the most common and accessible technique for *operando* studies of batteries and battery materials. The basics of XRD is covered in several textbooks^[32,33] and, therefore, omitted from this review.

X-ray total scattering, or pair distribution function (PDF) analysis is less common than XRD and uses both diffuse elastic scattering (short-range order) and inelastic scattering (due to movement of atoms) in addition to the Bragg peaks. This methodology allows to obtain not only information about the long-range crystal structure (as with XRD), but also information about the local structure. PDF is a powerful technique for studying amorphous battery materials.^[34]

Small-angle X-ray scattering (SAXS) utilizes the smallest angles in the X-ray scattering pattern (values of momentum transfer, q , $< \sim 1 \text{ \AA}^{-1}$). This provides information about size and shape of particles in a sample in the nm size range. SAXS is mainly used for characterizing porous materials or nanostructures with sizes in the range of 1–100 nm. The configuration of the SAXS instruments often allows the additional positioning of a regular XRD detector (often referred to as WAXS – wide-angle scattering in the SAXS community) and thus SAXS is often combined with XRD.

The active materials in NIBs operate according to three main classes of mechanisms: intercalation/insertion, conversion, and alloying. NIB cathode materials mainly operate through intercalation/insertion while a wide selection of anode materials utilize all three mechanism (separately or combined). The vast majority of materials used in NIBs are crystalline which makes XRD the most useful technique for *operando* characterization. These materials undergo a variety of phase transitions during (de)sodiation that are easy to observe through XRD.

Some electrode materials, however, are amorphous or become amorphous during cycling (usually materials with alloying or conversion mechanisms). In these cases, techniques that do not rely on long range order such as SAXS, PDF and XAS can help to understand the operation mechanisms of amorphous materials.

A summary of the most recent *operando* studies using X-ray scattering and diffraction techniques used for Na-ion and Na-metal batteries is shown in Table 1.

2.1. Layered Intercalation Materials

Operando XRD is a perfect technique for studying intercalation compounds. During cycling, the materials usually stay crystalline and undergo minor structural changes (volumetric changes and phase transitions), which are readily followed by XRD. *Operando* methods have therefore been deployed by several authors to detect the intermediate phases forming during (de)sodiation. Layered transition metal oxide (TMO) cathode materials are popular in NIBs due to their low Na^+ diffusion barriers. They have the general formula of Na_xMO_2 , where M is one or more transition metals (with a few exceptions) and through tuning of the lattice structure and chemical composition excellent Na-host materials can be obtained.^[148] Layered cathode materials frequently form structures based on edge shared MO_6 octahedra organized in layers that can intercalate Na-ions in either prismatic or octahedral sites. The transition metal ions are reduced and oxidized during sodiation and desodiation. Delmas *et al.*^[149] proposed a widely used classification system for the Na_xMO_2 materials based on the geometry of the Na sites (P for prismatic or O for octahedral) and the number of distinct MO_2 layers that form the stacking sequence. These materials can exhibit quite complex behaviour during cycling, because it is possible to change the stacking pattern with small shifts to adjacent MO_2 layers. This behaviour is strongly dependent on the chemical composition. The complexity and diversity of mechanisms found for this group of materials is difficult to predict from their compositions, or to infer from electrochemical data, and *operando* XRD has been crucial in revealing how their functionality is linked to their structure.

These layered materials can be divided into two subgroups based on the as synthesised structure: those with a pristine O3 phase and those with a pristine P2 phase. Fully sodiated materials ($x=1$ in Na_xMO_2) usually crystallise as O3-type phases, while sodium deficient materials (often $x=2/3$) generally form P2-type phases.^[150,151] During desodiation the O3 and P2 structures often transition to the related P3 and O2 structures, respectively; a series of *operando* studies, summarized below, revealed and confirmed these mechanisms. General crystal structures with O3, P3, P2 and O2 stacking sequences are shown in Figure 2.^[152]

Xie *et al.* demonstrated an O3-P3-O3 transition by *operando* XRD during cycling of $\text{NaNi}_{1/3}\text{Fe}_{1/3}\text{Mn}_{1/3}\text{O}_2$ up to 4.0 V (Figure 3a).^[99] Cycling to higher voltages (4.3 V) leads to different behaviour: above 4 V, the P3 phase transforms

further into a monoclinic distorted O3' phase, Figure 3b. During discharge from 4.3 V, the O3' phase transforms into a monoclinic distorted P3' phase before reverting to the initial, hexagonal O3 phase. Similar behaviour has been reported by Ding *et al.* for $\text{Na}[\text{Ni}_{0.6}\text{Fe}_{0.25}\text{Mn}_{0.15}]\text{O}_2$.^[70] However, this material transitions from O3 to P3 via an intermediate O'3 (monoclinic) phase. Above 4.0 V, the P3 phase transitions into a second hexagonal O3 phase (denoted O3''). This process is reversible and only the initial O3 phase was detected at end of discharge, as shown in Figure 3c-f. However, the full phase transition to O3'' lead to capacity degradation over time, and for long term stability it was beneficial to lower the cut-off voltage to 4.0 V. These two examples of materials with similar compositions show that these mechanisms cannot be generalized, as they are so sensitive to the combination of cations in the Na_xMO_2 structure. Several materials, including $\text{NaFe}_{0.25}\text{Mn}_{0.25}\text{Ni}_{0.25}\text{Ti}_{0.25}\text{O}_2$,^[88] $\text{Na}_x\text{Mn}_{1/3}\text{Fe}_{2/3}\text{O}_2$ ($x=0.77$)^[105] and $\text{NaNi}_{2/3}\text{Sb}_{1/3}\text{O}_2$,^[94] have also been reported to form O1 phases at high voltages, often in combination with P3. The complexity of the observed transformations particularly emphasizes the necessity of *operando* studies as the only method that can clearly reveal the important intermediate phases forming during (de)sodiation processes. The knowledge of the intermediates and when they are formed allows to explain the stability and cyclability of studied material and thus, provide further guidelines for material's improvements. There are several good examples where the results from *operando* XRD has been used to improve the cyclability of a material by implementing small changes. For example by controlling the potential window or coating the materials.^[70,74,90]

Operando XRD also revealed that P2 materials can follow several different structural routes during cycling. Some maintain their structure during cycling (solid solution behaviour),^[73,81,82,87] others reversibly transition into O2 phases,^[69,80,86,104] a third group stop at disordered intermediate phases termed "Z-" or "OP4".^[68,77,83,95] Jung *et al.* showed an example of the P2-O2-P2 transition for $\text{Na}_{0.7}\text{Fe}_{0.4}\text{Mn}_{0.4}\text{Co}_{0.2}\text{O}_2$, where the plateaus and slopes in the voltage plots clearly correspond to phase changes and lattice parameter variations respectively in the XRD data (Figure 4).^[104]

Sommerville *et al.* studied the Z phase in detail and described it as an intergrowth of P- and O-type layers.^[77] The OP4 phase is an ordered case of the Z-phase with a 50:50 intergrowth in which the P- and O-type layers alternate, as shown in Figure 5a. This study demonstrated that $\text{Na}_{2/3}[\text{Ni}_{1/6}\text{Mn}_{1/2}\text{Fe}_{1/3}]\text{O}_2$ transitions from the P2 phase through the Z phase and reaches the OP4 phase at around 4.3 V, as shown in Figure 5b-e. $\text{Na}_{0.66}\text{Li}_{0.22}\text{Ru}_{0.78}\text{O}_2$ ^[68] and $\text{Na}_x\text{Ni}_{0.3}\text{Mn}_{0.7}\text{O}_2$ ^[83] display similar behaviour, with the P2 phase reversibly transforming to the Z phase. These *operando* studies not only established the nature of the Z phase, but also explained its effect on the stability of the material during cycling: when transitioning through the Z phase the material undergoes less abrupt volumetric changes and thus the capacity retention is improved.

Table 1. Overview of scientific articles focused on *operando* X-ray diffraction and scattering.^[a]

Active Material	Type of Material	Technique(s) ^[b]	Cell type	X-ray window	S vs. H	T vs. R	Cycling rate	Acquisition time per scan	Ref.
Sb	Alloying	XRD	Coin cell	Be	H		50 mA g ⁻¹		[35]
Bi	Alloying	XRD	Coin cell	Kapton	H	T	50 mA g ⁻¹		[19]
a-P/C	Alloying	WAXS, SAXS	Swagelok	Kapton	S	T	C/10	60 s	[36]
Bi ₂ Sb ₄ , Bi ₂ Sb ₆	Alloying	XRD	Coin cell	Be	H		25 mA g ⁻¹		[37]
TiSb ₂	Alloying	XRD					C/30		[38]
Si	Alloying	XRD							[39]
P	Alloying	XRD/PDF-CT	Special/Tomography		S		C/2	7 min per slice	[40]
Bi	Alloying	XRD, TXM	Coin cell	Kapton	S			10 s	[41]
Bi	Alloying	XRD, XAS	Swagelok	Kapton	S	T	50 mA g ⁻¹	2 min	[42]
Sb	Alloying	PDF	AMPIX		S		C/20	180 s	[43]
Hard carbon	Carbon	PDF	Capillary		S	T	C/10	4.5 min	[44]
Hard carbon	Carbon	XRD	Special	Be	H	R	C/25	1 h	[45]
Graphite	Carbon	XRD	Special	Al	H		30 mA g ⁻¹		[46]
Graphite	Carbon	XRD	Special	Al	H		C/4–C/22		[47]
C (LCMH)	Carbon	XRD	Special	Kapton	H	R	100 mA g ⁻¹	2.5 min	[48]
Graphite	Carbon	XRD	Coin cell	Kapton	S		20 mA g ⁻¹	1 min	[49]
CuSO ₄	Conversion	XRD							[50]
Cu ₂ PS ₄	Conversion	XRD	Swagelok	Be	H	R	C/20	1 h	[8]
(Ni _{0.5} Co _{0.5}) ₂ S ₂ @NC	Conversion	XRD	Coin cell	Kapton	H		100 mA g ⁻¹		[51]
Pb ₃ Nb ₄ O ₁₃	Conversion	XRD			H				[52]
NiS _{1.03}	Conversion	XRD		Be					[53]
Ni ₂ S ₂	Conversion	XRD, TXM-XANES	Coin cell	Kapton	S				[54]
Co ₃ O ₄	Conversion	XRD, SAXS, XAS	Coin cell	Kapton	S	T	0.1 C	5 s	[55]
CoSe ₂	Conversion	XRD	Special	Be	H	R	100 mA g ⁻¹	10 min	[56]
NiSe ₂	Conversion	XRD	Special	Be	H	R			[57]
MoP	Conversion	XRD	Coin cell	Be	S				[58]
Cu _{1.5} TiOPO ₄ , Fe _{0.5} TiOPO ₄	Conversion	XRD	Special	Be	H	R	16.9 mA g ⁻¹		[59]
NiP ₃	Conversion	XRD	Swagelok	Be	H		C/3		[60]
FeSbO ₄	Conversion/alloying	XRD	Special	Al	H	R	30 mA g ⁻¹		[61]
SnS ₂	Conversion/alloying	XRD	Special		S		C/3		[62]
Sb ₂ O ₃ /rGO	Conversion/alloying	XRD			H		C/5		[9]
Sb ₂ Se ₃	Conversion/alloying	XRD-XAS	Special	Be	H	R	100 mA g ⁻¹	10 min	[63]
Bi ₂ S ₃	Conversion/alloying	XRD	Swagelok	Kapton	H, S	T	C/10	H: 20 min S: 1 min	[64]
FeSb ₂	Conversion/alloying	XRD	Swagelok	Be	H		C/6		[65]
FeSb ₂	Conversion/alloying	XRD	Coin cell	Kapton	H	R	C/50→C/200→C/40→C/120→C/30	4 h	[66]
Na _{2/3} Ni _{1/3} Mn _{2/3} O _{2-x} F _x	Layered	XRD	El-Cell	Kapton	H		C/10–C/20		[67]
Na _{0.66} Li _{0.22} Ru _{0.78} O ₂	Layered	XRD		Al	H				[68]
Na _{0.67} Mn _{0.6} Fe _{0.25} Co _{0.15} O ₂ + Na ₂ C ₆ O ₆	Layered	XRD	Special	Be	H	R	C/20	1 h	[69]
Na[Ni _{0.60} Fe _{0.22} Mn _{0.15}]O ₂	Layered	XRD	Special	Al	H		C/10		[70]
Na ₂ MnO ₂	Layered	XRD	Special		H	R	C/20	30 min	[71]
Li _{0.5} Na _{0.4} CoO ₂	Layered	XRD	Swagelok	Kapton	H	R	20 μV s ⁻¹		[72]
Li _{0.2} NaMn _{0.8} O ₂	Layered	XRD							[73]
NaMn _{0.35} Fe _{0.13} Ni _{0.35} O ₂	Layered	XRD							[74]
Na _{2/3} Mn _{0.8} Fe _{0.1} Ti _{0.1} O ₂	Layered	XRD	Swagelok	Be	S	T	26–526 mA g ⁻¹	40 s	[75]
Na _{1.5} Li _{0.5} IrO ₃	Layered	XRD	Swagelok	Be	H		C/20		[76]
Na _{2/3} [Ni _{1/3} Mn _{2/3}]O ₂	Layered	XRD	Special	Be	H	R	5 mA g ⁻¹		[77]
Na _{2/3} [Ni _{1/6} Mn _{1/2} Fe _{1/3}]O ₂									
Na _{2/3} Ni _{1/6} Mn _{2/3} Cu _{1/9} Mg _{1/18} O ₂	Layered	XRD	Swagelok	Al	H		C/10		[78]
Na _{0.7} Mn _{0.8} Mg _{0.2} O ₂	Layered	XRD	Coin cell	Kapton	S	T	15 mA g ⁻¹	3.5 min	[79]
Na _{2/3} Ni _{1/3} Mn _{2/3} O ₂	Layered	XRD			S		C/2		[80]
Na _{0.67} Mn _{0.65} Ni _{0.25} Co _{0.15} O ₂ , Na _{0.67} Mn _{0.65} Ni _{0.2} Mg _{0.15} O ₂	Layered	XRD	Coin cell		H		30 mA g ⁻¹		[81]
Na _{0.67} Mn _{0.5} Fe _{0.5} O ₂ (MgO coated)	Layered	XRD					0.2 mV s ⁻¹		[82]
Na ₂ Ni _{0.3} Mn _{0.7} O ₂	Layered	XRD	Coin cell		H	R	15 mA g ⁻¹	20 min	[83]
Na(TM)O ₂	Layered	XRD	Swagelok	Be	H		C/50, C/10	1 h	[84]
Na _{1.2} Ni _{0.2} Mn _{0.2} Ru _{0.4} O ₂	Layered	XRD	Swagelok		H		C/12		[85]
Na _{0.67} Mn _{0.6} Fe _{0.25} Al _{0.15} O ₂	Layered	XRD	Special	Be	H	R	C/13	1 h	[86]
Na _{0.6} Li _{0.2} Mn _{0.8} O ₂	Layered	XRD			H, S	R, T	H: C/30 S: C/5	H: 2 h S: 5 min	[87]
NaFe _{0.25} Mn _{0.25} Ni _{0.25} Ti _{0.25} O ₂	Layered	XRD		Al	H		0.4 C		[88]
Na[Li _{0.05} Ni _{0.3} Mn _{0.5} Cu _{0.1} Mg _{0.05}]O ₂	Layered	XRD	Swagelok	Al	H		C/10		[89]
Na _{0.9} Ca _{0.05} Ni _{1/3} Fe _{1/3} Mn _{1/3} O ₂	Layered	XRD			S		C/10		[90]
Na ₂ Ni ₂ SbO ₆	Layered	XRD	Swagelok	Al	H		C/20		[91]
MoO ₃	Layered	XRD	Capillary		S	T			[92]
Na _{2/3} Ni _{1/3-x} Fe _x Ti _{2/3} O ₂	Layered	XRD	Coin cell	Be	H		15 mA g ⁻¹	2.4–3.4 min	[93]
NaNi _{2/3} Sb _{1/3} O ₂	Layered	XRD		Be	H		C/5	15 min	[94]
Na _{2/3} Ni _{1/4} Mn _{2/3} Cu _{1/12} O ₂	Layered	XRD		Be	H		C/40		[95]
NaNiO ₂	Layered	XRD, TXM-XANES	Coin cell	Kapton	S	T	C/10	3 s	[96]
NaNi _{0.5} Cu _{0.05} Mn _{0.4} Ti _{0.1} O ₂	Layered	XRD	Special	Al	H				[97]
NaNiMn _{0.5-x} Ti _x O ₂ (0 ≤ x ≤ 0.5)	Layered	XRD	Swagelok	Al	H		C/20	30 min	[98]
NaNi _{1/3} Fe _{1/3} Mn _{1/3} O ₂	Layered	XRD	Coin cell	Kapton	S	T			[99]
NbS ₂	Layered	XRD	Special	Be	H	R	100 mA g ⁻¹	12.5 min	[100]
NaFe _{1/2} Co _{1/2} O ₂	Layered	XRD					6 mA g ⁻¹	35 min	[101]
NaFe _{1/3} Ni _{1/3} Ti _{1/3} O ₂	Layered	XRD	Special	Be	H	R	0.1 mV s ⁻¹	63 min	[102]
Na _{2.55} V ₆ O ₁₆ •0.6H ₂ O	Layered	XRD	Special	Al	H	R	10 mA g ⁻¹		[103]
Na _{0.7} Fe _{0.4} Mn _{0.4} Co _{0.2} O ₂	Layered	XRD	Capillary		S		40–80 mA g ⁻¹	25.7 s	[104]
Na ₂ Mn _{1/3} Fe _{2/3} O ₂	Layered	XRD, XANES	Special	Be	H		C/80	1 h	[105]
Na _{0.9} Cu _{0.22} Fe _{0.30} Mn _{0.48} O ₂	Layered	XRD	Special	Al	H		C/10		[106]
Na _{0.67} Mn _{0.8} Mg _{0.2} O ₂	Layered	XRD	Coin cell		S	T	12 and 100 mA g ⁻¹	4.4 s	[107]

Table 1. continued

Active Material	Type of Material	Technique(s) ^[b]	Cell type	X-ray window	S vs. H	T vs. R	Cycling rate	Acquisition time per scan	Ref.
$\text{Na}_{0.67}[\text{Mn}_{0.5}\text{Fe}_{0.5}]\text{O}_2$, $\text{Na}_{0.67}[\text{Mn}_{0.65}\text{Ni}_{0.15}\text{Fe}_{0.2}]\text{O}_2$	Layered	XRD	Special		H	R	13 mA g^{-1}	30 s	[108]
$\text{Na}_{0.84}\text{Fe}_{0.56}\text{Mn}_{0.44}\text{O}_2$	Layered	XRD	Special	Graphite	H	R	0.08 C and 0.17 C	18 min	[109]
NaNiO_2	Layered	XRD	Special	Be	H		C/70	20 min	[110]
Na_2VO_2	Layered	XRD	Special	Be	H		C/100	1 h	[111]
NaCrO_2	Layered	XRD	Special		S		C/12		[112]
$\text{Na}_{0.44}\text{Co}_{0.1}\text{Mn}_{0.5}\text{O}_2$	Layered and Network	XRD	Swagelok	Al	H				[113]
$\text{O}_2 + \text{CoO/CoP}$	Na-O2	XRD			S		200 mA g^{-1}		[114]
O_2	Na-O2	XRD	Special	Kapton	S	T	0.075 mA cm^{-2}	10 s	[115]
O_2	Na-O2	XRD	Special	Polyamide	H	R	0.2 mA cm^{-2}		[116]
S	Na-S	XRD	Coin cell	Kapton	S	T			[117]
$\text{Na}_3\text{MnTi}(\text{PO}_4)_3/\text{C@rGO}$	Network	XRD		Be	H		50 mA g^{-1}	120 s	[118]
$\text{Na}_{3-x}\text{Mn}_x\text{V}_{2-x}(\text{PO}_4)_3$ ($0 \leq x \leq 1$, $\Delta x = 0.2$)	Network	XRD		Be, Sapphire	H, S		C/8, C/5		[119]
$\text{Na}_x\text{Co}_3(\text{PO}_4)_2\text{P}_2\text{O}_7$	Network	XRD	Special		H				[120]
$\text{Na}_x\text{MnV}(\text{PO}_4)_3$	Network	XRD	Swagelok	Be	H		$1 \text{ Na}^+ / 10 \text{ h}$	55 min	[121]
NaTiOPO_4	Network	XRD	Special	Be	H		C/50	11 min	[122]
$\text{Na}_3(\text{VO})\text{Fe}(\text{PO}_4)_2\text{F}$	Network	XRD, XANES	Swagelok	Be	S		C/10		[123]
$\text{Na}_3\text{V}_2\text{O}_7(\text{PO}_4)_2\text{F}$	Network	XRD	Special	Sapphire	S		C/5	10 s	[124]
$\text{Na}_3\text{Fe}_2(\text{SO}_4)_3\text{C@GO}$	Network	XRD	Coin cell		S	T	50 mA g^{-1}		[125]
$\text{Na}_2\text{Co}_2(\text{SeO}_3)_3$	Network	XRD	Special		H	R	5 mA g^{-1}	30 min	[126]
TiO_2	Network	SAXS	Coin cell	Polyimide	S	T	C/12 and 1 C	0.6 s^*30	[127]
$\text{Na}_x\text{MnV}(\text{PO}_4)_3$	Network	XRD	Special	Sapphire	S	T	C/4		[128]
NaFePO_4	Network	XRD	Special	Be	H, S	R, T	C/60 and C/20, 1C	H: 30 min S: 2.3 min	[129]
$\text{Na}_3(\text{VOPO}_4)_2\text{F}$	Network	XRD	Special		H, S	T	C/10, C/6		[130]
$\text{Na}_x\text{V}_3\text{Al}(\text{P}_2\text{O}_7)_4(\text{PO}_4)$	Network	XRD	Swagelok	Be	H		C/20	1 h	[131]
$\text{Na}_3\text{V}_2(\text{PO}_4)_3\text{FO}_2$	Network	XRD	Special		H	R	C/40	2 h	[132]
$\text{Na}_3\text{VCr}(\text{PO}_4)_3$	Network	XRD	Coin cell	Kapton	S	T	C/10	14–15 min	[133]
$\text{Na}_{1.86}\text{Fe}_3(\text{PO}_4)_3$	Network	XRD	Swagelok	Be	H		C/10 and C/20		[134]
Gd_2TiO_5	Network	XRD	Coin cell	Kapton	S	T	4 mA g^{-1}	6.38 min	[135]
$\text{Na}[\text{FeTi}]_4\text{O}_4$	Network	XRD	Swagelok	Be	H		C/10	37 min	[136]
$\text{Na}_3\text{V}_2\text{O}_7(\text{PO}_4)_2\text{F}_{3-2x}$	Network	XRD	Coin cell	Kapton	S	T	C/2	4 min	[137]
NaFePO_4	Network	XRD	Special	Be	H	R	2.4 mA g^{-1}	9 min	[138]
Na_xFePO_4	Network	XRD	Swagelok	Be	S	T	$1 \text{ Na}^+ / 23 \text{ h}$	2 s scan^{-1}	[139]
$\text{Li}_4\text{Ti}_5\text{O}_{12}$	Network	XRD	Special	Mylar	S			15 min	[140]
$\text{Na}_3\text{V}_2(\text{PO}_4)_3$, Bi (full cell)	Network, Alloying	XRD							[141]
$\text{Na}_x\text{Mn}_{1-2x}\text{Sn}_x\text{Fe}(\text{CN})_6$	PBA ^[c]	XRD	Swagelok	Be	H		C/20		[142]
$\text{Na}_x\text{MnFe}(\text{CN})_6$	PBA ^[c]	XRD			H		60 mA h g^{-1}		[143]
$\text{Na}_{1.34}\text{Ni}[\text{Fe}(\text{CN})_6]_{0.81}$	PBA ^[c]	XRD			H		20 mA h g^{-1}		[144]
$\text{NaFeFe}(\text{CN})_6$	PBA ^[c]	XRD	Coin cell	Kapton	S	T	10 mA g^{-1}		[145]
$\text{Na}_{1.32}\text{Mn}[\text{Fe}(\text{CN})_6]_{0.83} \cdot z\text{H}_2\text{O}$	PBA ^[c]	XRD, XANES	Swagelok	Kapton	S	T	C/10	7 min	[146]
$\text{Fe}[\text{Fe}(\text{CN})_6]_{1-x}\text{FeCo}(\text{CN})_6$	PBA ^[c]	XRD	Coin cell	Kapton	S	T	0.05–0.2 mA	4.36 min	[147]

[a] S: synchrotron, H: home laboratory, T: transmission (Debye-Scherrer) geometry, R: reflection (Bragg-Brentano) geometry. [b] XRD: X-ray diffraction; WAXS: wide-angle X-ray scattering; SAXS: small-angle X-ray scattering; PDF: pair distribution function; CT: computed tomography; TXM: transmission X-ray microscopy; XAS: X-ray absorption spectroscopy; XANES: X-ray absorption near-edge spectroscopy. [c] PBA = Prussian blue analogues.

2.2. Insertion Network Materials

The most common three dimensional (3D) structured sodium insertion materials are polyanionic compounds (including Na superionic conductor, NASICON), titanates (TiO_2 , $\text{Li}_4\text{Ti}_5\text{O}_{12}$ and Gd_2TiO_5) and Prussian blue analogues (PBAs).

Polyanionic frameworks include phosphates, fluorophosphates and sulphates and are typically composed of XO_4 tetrahedra or trigonal XO_3 ($\text{X} = \text{P}, \text{S}$), and MO_6 octahedra (where M is 3d transition metal). NASICON-type materials (such as $\text{Na}_3\text{V}_2(\text{PO}_4)_3$), NaFePO_4 and $\text{Na}_2\text{Fe}_2(\text{SO}_4)_3$ are among the most promising cathode materials in this group. NaFePO_4 with the maricite structure has shown a capacity of 142 mA h g^{-1} and a capacity retention of 95% after 200 cycles.^[153] This is significantly better than olivine structured NaFePO_4 , which has a capacity of 125 mA h g^{-1} and slightly worse cycling stability.^[154] The olivine NaFePO_4 materials, have an average voltage around 3.0 V.^[155] $\text{Na}_2\text{Fe}_2(\text{SO}_4)_3$ is among the most promising sulfates for NIBs. In a composite with graphene oxide, $\text{Na}_2\text{Fe}_2(\text{SO}_4)_3$ demonstrates a capacity of approximately 100 mA h g^{-1} , stability for several hundred cycles, and an average voltage around 3.8 V.^[125]

Several groups showed that olivine NaFePO_4 exhibits a different behaviour than the well-studied olivine analogue of LiFePO_4 . Instead of one well-defined, two-phase transition (as for LiFePO_4), Na_xFePO_4 undergoes phase transitions with several intermediate phases revealed by *operando* XRD, and with more contribution from solid solution regions.^[129,138,139] Furthermore, such studies allowed the determination of different sodiation and desodiation mechanisms for the material.^[138] In comparison to orthophosphates, the pyrophosphates exhibit higher redox potentials for active elements, however, mass of the active material also increases with such substitution lowering the specific capacity.^[131] In the case of Co-based compounds: $\text{Na}_x\text{Co}_3(\text{PO}_4)_2\text{P}_2\text{O}_7$,^[120] a series of redox reactions occur between 4.3 and 4.7 V. This increased chemical complexity of the material results in several phase transitions during cycling, as demonstrated by *operando* XRD.

The NASICON-type compounds represent an interesting sub-group of phosphate materials. For the typical NASICON-type material, $\text{Na}_3\text{V}_2(\text{PO}_4)_3$, the structure consists of corner shared VO_6 octahedra and PO_4 tetrahedra. This gives a structure with several 3D channels for fast intercalation of Na^+ .^[16] This compound shows a capacity slightly above 100 mA h g^{-1} and a

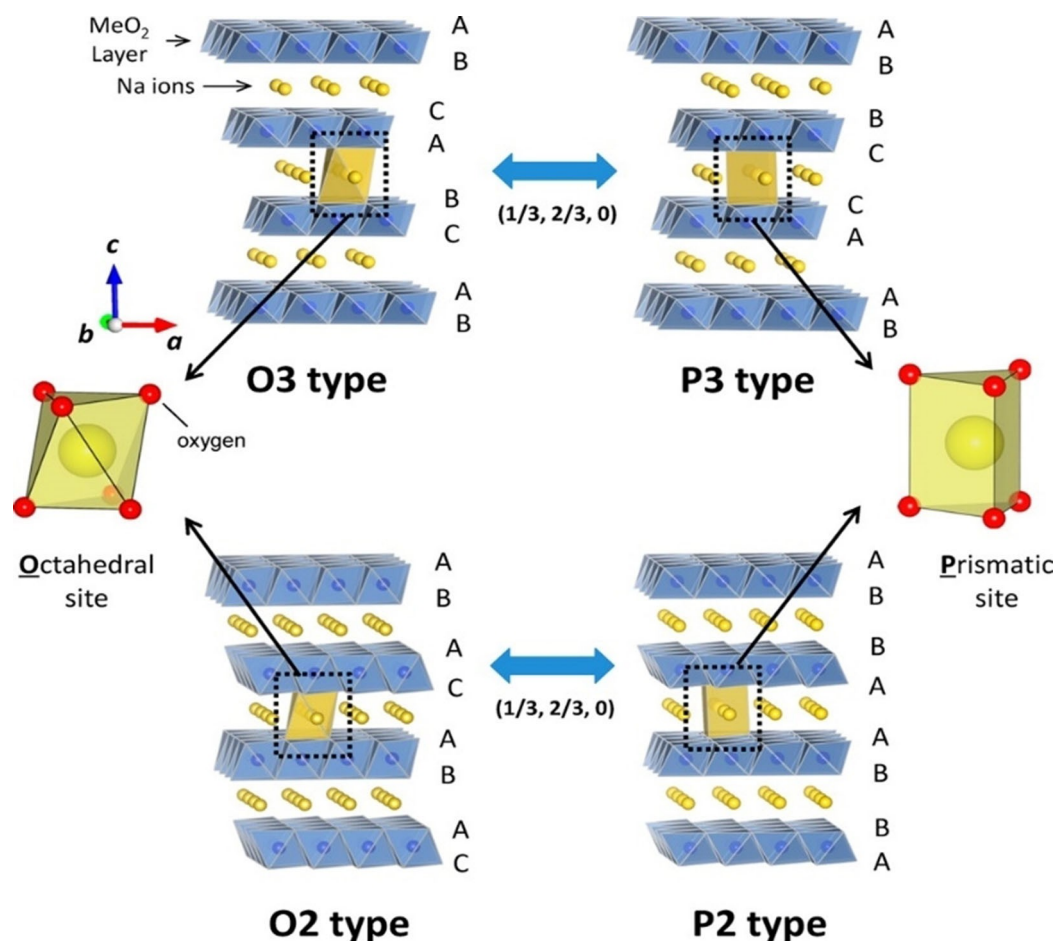


Figure 2. Layered O3, P3, O2 and P2 crystal structures with their respective stacking sequences. The blue and yellow spheres represent the transition metal and Na^+ ions in the O-type frameworks, respectively. Adapted from Ref. [152] with permission. Copyright (2014) American Chemical Society.

stable voltage plateau at 3.4 V. It has good cycle life and excellent rate capabilities where a capacity above 100 mAh g^{-1} can be maintained even at 2 Ag^{-1} .^[141] Unfortunately, vanadium compounds are toxic. Hence, replacing this with more benign elements is an important research target. To reflect that, Zakharkin *et al.* studied a series of $\text{Na}_{3+x}\text{Mn}_x\text{V}_{2-x}(\text{PO}_4)_3$ ($x=0, 0.2, 0.4, 0.6, 0.8$ and 1) with *operando* XRD.^[119,128] They showed that increased amount of Mn in the structure leads to small capacity improvements and more solid solution type behaviour. Pure vanadate materials clearly show a two-phase mechanism (Figure 6).^[119] The phase transitions in $\text{Na}_4\text{MnV}(\text{PO}_4)_3$ are highly dependent on the cut-off voltage. The transition from the monoclinic to the rhombohedral phase is reversible when charged to 3.8 V, but becomes irreversible when charged to 4.0 V.^[128] A similar study by Chen *et al.*^[121] supports this finding. Several *operando* XRD studies on fluorinated NASICON-type materials with general formula $\text{Na}_3\text{V}_2\text{O}_{2x}(\text{PO}_4)_2\text{F}_{3-2x}$ ($0 \leq x \leq 1$) were also reported.^[124,130,132,137] These materials demonstrate higher redox potentials than the non-fluorinated materials and good reversibility even when charged up to high voltages (4.3 V).

Prussian blue analogues (PBAs) have the general formula $\text{A}_x\text{MM}'(\text{CN})_6 \cdot n\text{H}_2\text{O}$, where A is a guest ion such as Na^+ , K^+ , Ca^{2+} ,

Mg^{2+} or a molecule of H_2O , M and M' are transition metals and the ambidentate CN^- ligands bridge the two metals M and M' in a corner-sharing octahedral configuration.^[156] This class of materials has great potential as cathode materials for NIBs, due to the large voids into which Na^+ can be inserted. PBAs also deliver good reversibility during (de)sodiation and, therefore, excellent cycling stability. However, their cubic crystal structure can be easily distorted by varying the level of water and CN^- vacancies. An *operando* XRD study on cubic and monoclinic $\text{Na}_x\text{MnFe}(\text{CN})_6$ by Tang *et al.* showed that the monoclinic version goes through several phase changes (monoclinic – cubic – tetragonal), which makes it unstable under cycling.^[143] The cubic phase, in contrast, maintains its structure during cycling, giving superior cycling stability. Several studies of other PBA modifications confirmed that the cubic phase has superior cycling stability relative to the distorted versions.^[142,146] However, a study of rhombohedral $\text{Na}_{1.34}\text{Ni}[\text{Fe}(\text{CN})_6]_{0.81}$ showed that the material goes through a highly reversible two-phase reaction from rhombohedral at low voltages to cubic at high voltages, which also gives great cycling stability.^[144] $\text{Na}_x\text{FeFe}(\text{CN})_6$ and $\text{Na}_x\text{FeCo}(\text{CN})_6$ were also studied with *operando* XRD showing only minor structural changes during cycling.^[145,147]

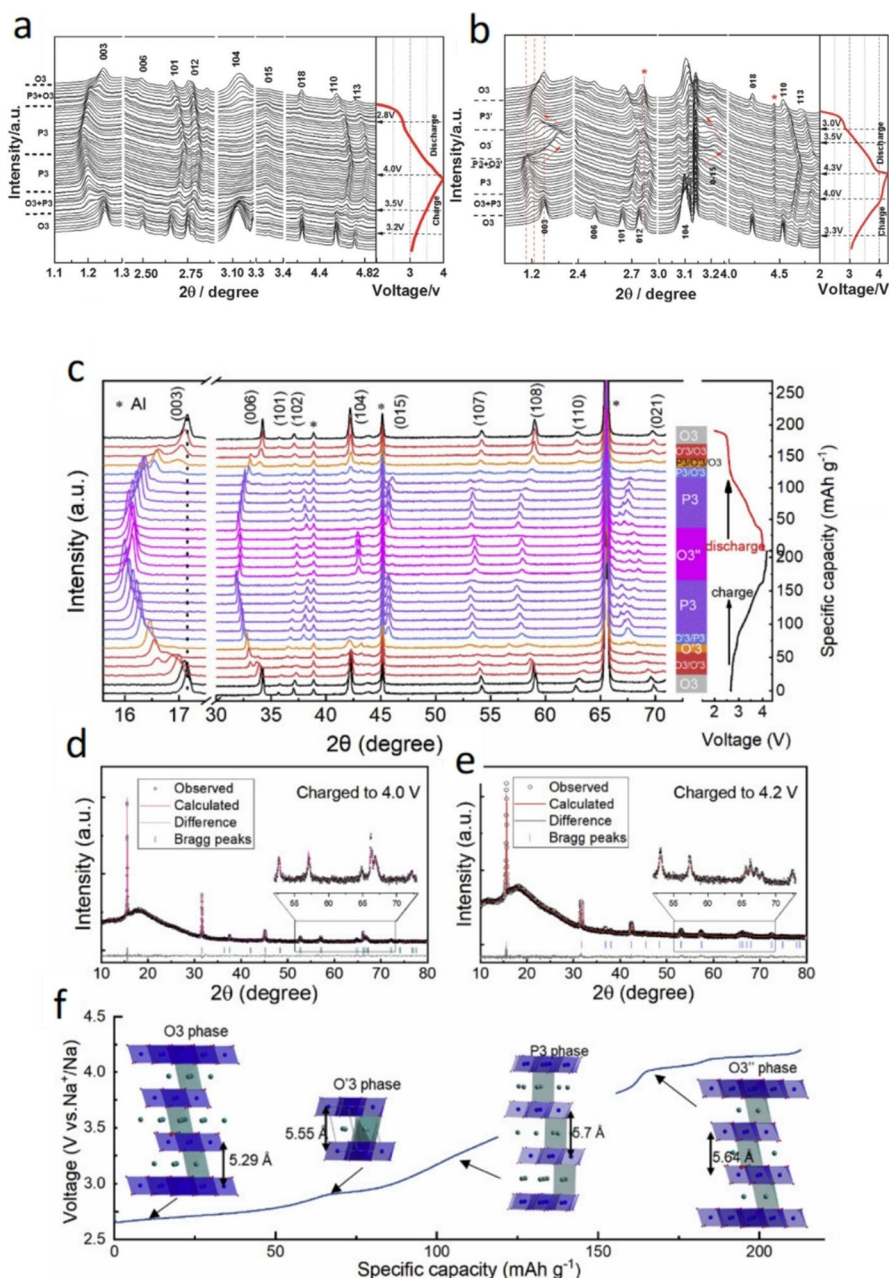


Figure 3. Operando XRD patterns collected from the first cycle of $\text{Na}_{1-x}\text{Ni}_{0.65}\text{Fe}_{0.25}\text{Mn}_{0.15}\text{O}_2$ electrode: a) between 2.0 and 4.0 V and b) between 2.0 and 4.3 V. Adapted from Ref. [99] with permission. Copyright (2016) Wiley-VCH. c) Operando XRD patterns collected during the first cycle of $\text{Na}_{1-x}\text{Ni}_{0.65}\text{Fe}_{0.25}\text{Mn}_{0.15}\text{O}_2$ in Na half-cell within the voltage range of 2.0–4.2 V. Corresponding phases and charge-discharge curves are given on the right side. d, e) Rietveld refinement patterns of powder XRD data for O3-NNFM cathode charged to 4.0 V and 4.2 V. f) Crystal structure evolution of O3-NNFM during desodiation. Adapted from Ref. [70] with permission. Copyright (2020) Elsevier.

Unlike the insertion materials discussed above, titanates are used as anodes rather than cathodes in NIBs. They are of interest due to their exceptional cycling stability. Santoro *et al.* performed an operando SAXS study on TiO_2 nanoparticles, showing that the particle size is preserved during cycling while the mean distance between the secondary nanoparticles changes.^[127] This is a rate-dependent phenomenon; at a low rate (C/12) the nanoparticles homogeneously drift apart, while at a higher rate (1C) nanoparticle aggregation is the dominant factor. Operando XRD was also utilized to demonstrate that titanate anodes such as Gd_2TiO_5 ,^[135] $\text{Na}_x[\text{FeTiO}_4]$ ^[136] and

$\text{Li}_4\text{Ti}_5\text{O}_{12}$ ^[140] display very small structural and volumetric changes upon (de)sodiation, leading to good cycling stability.

2.3. Carbon Materials

In the vast plethora of anode materials for NIBs, hard carbons are popular due to their low cost, high capacity and cycling stability.^[157] However, the amorphous nature of hard carbons limits the information that could be obtained by operando XRD. In such materials sodiation and desodiation result only in a

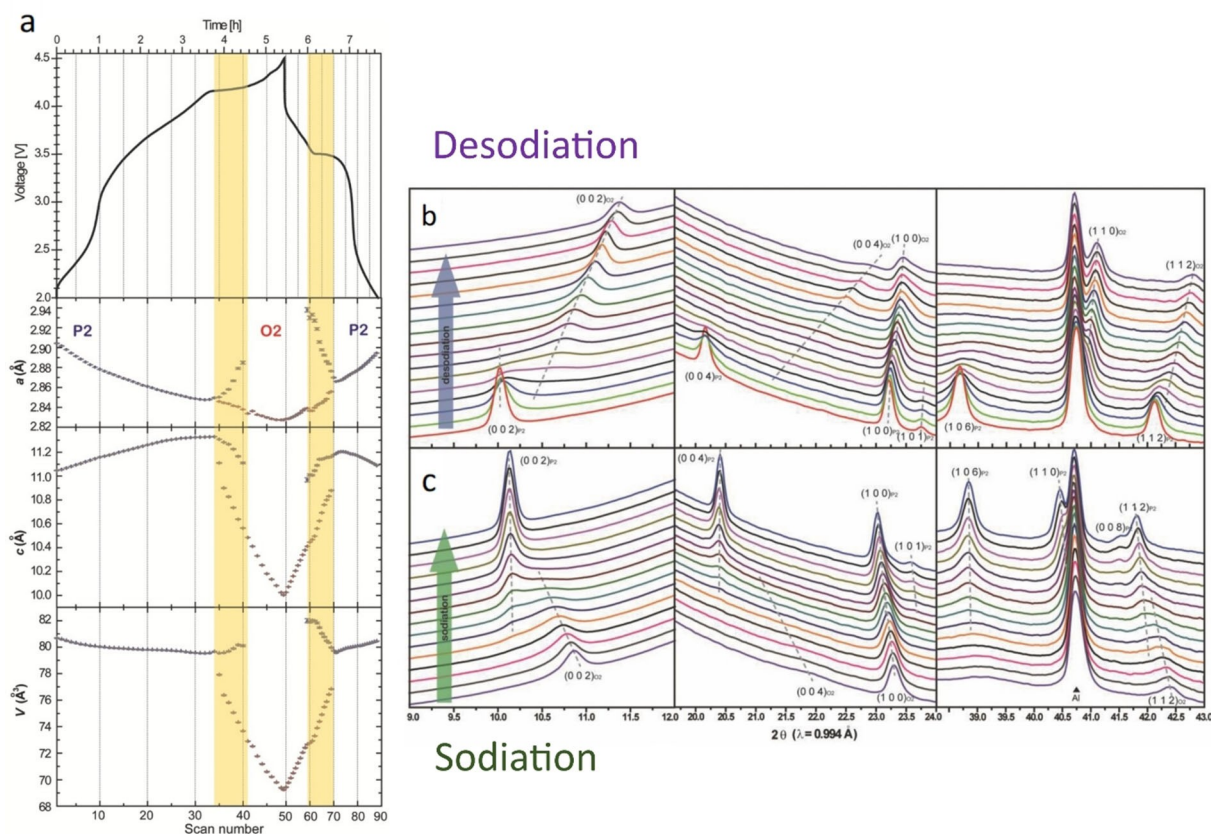


Figure 4. a) Charge discharge curves and the corresponding evolution of cell parameters and phases of the P2- $\text{Na}_{0.7}\text{Fe}_{0.4}\text{Mn}_{0.4}\text{Co}_{0.2}\text{O}_2$ electrode extracted from *operando* synchrotron XRD patterns: b) desodiation and c) sodiation. Adapted from Ref. [104] with permission. Copyright (2015) Wiley-VCH.

slight shift of the main broad diffraction peak, due to expansion and contraction.^[45,48] SAXS is a powerful tool for the study of hard carbons, able to detect the total porosity, (i.e., the surface (open) porosity, as well as the bulk (closed) porosity). However, the use of *operando* SAXS is far from routine for characterization of battery materials, probably due to the scarcity of lab-scale SAXS instruments.^[158] Therefore, complementary techniques are needed to study these materials in detail.

Stevens and Dahn^[150,160] were the first to attempt *operando* XRD and SAXS on carbon materials to study the intercalation of alkali metal ions. The historical model of sodium insertion into micropores was proposed after they conducted *operando* SAXS on sugar-derived hard carbons and observed a clear change in intensity of the SAXS signal. Alvin *et al.* revealed the mechanism of Na^+ cycling in hard carbon using a range of techniques including XRD, SAXS and Raman spectroscopy.^[161]

PDF analysis of total scattering data is a powerful technique for studying hard carbon materials since it allows the study of amorphous compounds. Mathiesen *et al.*^[44] successfully used *operando* PDF to study hard carbon (de)sodiation mechanisms. They observed changes to the interatomic distances both interplane and intraplane depending on the state of charge. They also showed an increasing level of disorder in the structure during cycling.

Although it is the most common anode for LIBs, graphite is a bad host material for Na^+ -ions with low preference for

intercalation. Graphite anodes for NIBs have nevertheless been studied with *operando* XRD. In this case, the use of diethylene glycol dimethyl ether (DEG-DME), and other “glymes”, as electrolytes enabled intercalation of solvated Na^+ -ions into graphite. Kim *et al.* reported one of the first studies, where they used a 1 M NaPF_6 in DEG-DME as electrolyte. *Operando* XRD revealed the structural evolution of the graphite during the solvated Na^+ intercalation.^[49] Further detailed *operando* XRD studies of the staging mechanism of solvated Na^+ into graphite were conducted, demonstrating sodium content of up to NaC_{18} .^[46,47]

A few other studies reported *operando* X-ray-based techniques^[162,163] for studying (de)sodiation mechanisms in carbon materials in NIBs. However, these are not discussed in this review, as the *operando* data were complementary to other techniques and were not a key part of the findings.

2.4. Conversion and Alloying Materials

Most conversion and alloying materials undergo a complex set of structural and chemical transformations during cycling. These are not always visible in conventional *ex situ* characterization. *Operando* XRD revealed the mechanisms of cycling for several conversion and alloying NIB anode materials and for some materials that combine these working mechanisms. Some

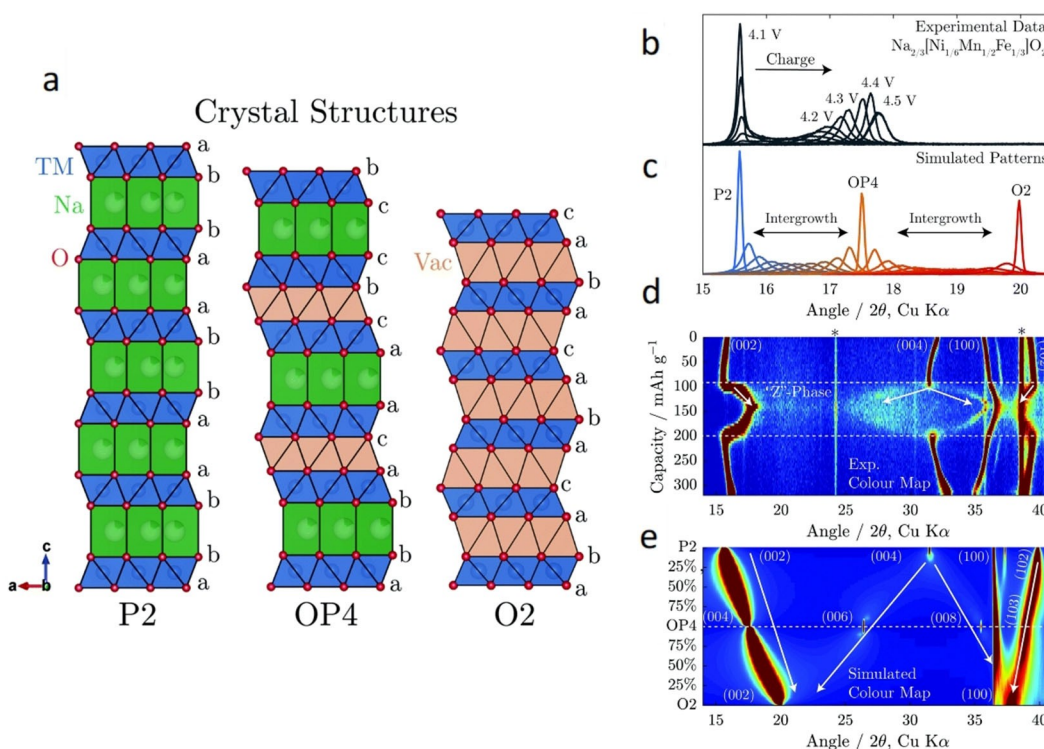


Figure 5. a) Illustration of the P2, OP4 and O2 phases showing the correlation between the structures. b) Experimental diffraction patterns at different voltages during the *operando* study of $\text{Na}_{2/3}[\text{Ni}_{1/6}\text{Mn}_{1/2}\text{Fe}_{1/3}]\text{O}_2$. c) Simulated diffraction patterns by using FAULTS for intergrowth structures composed of P2 and OP4, and OP4 and O2. d) Experimental diffraction data over a wider 2θ range as a colour map. e) Simulated diffraction data as a colour map. Adapted from Ref. [77] under the terms of the Creative Commons License. Copyright (2019) The Authors.

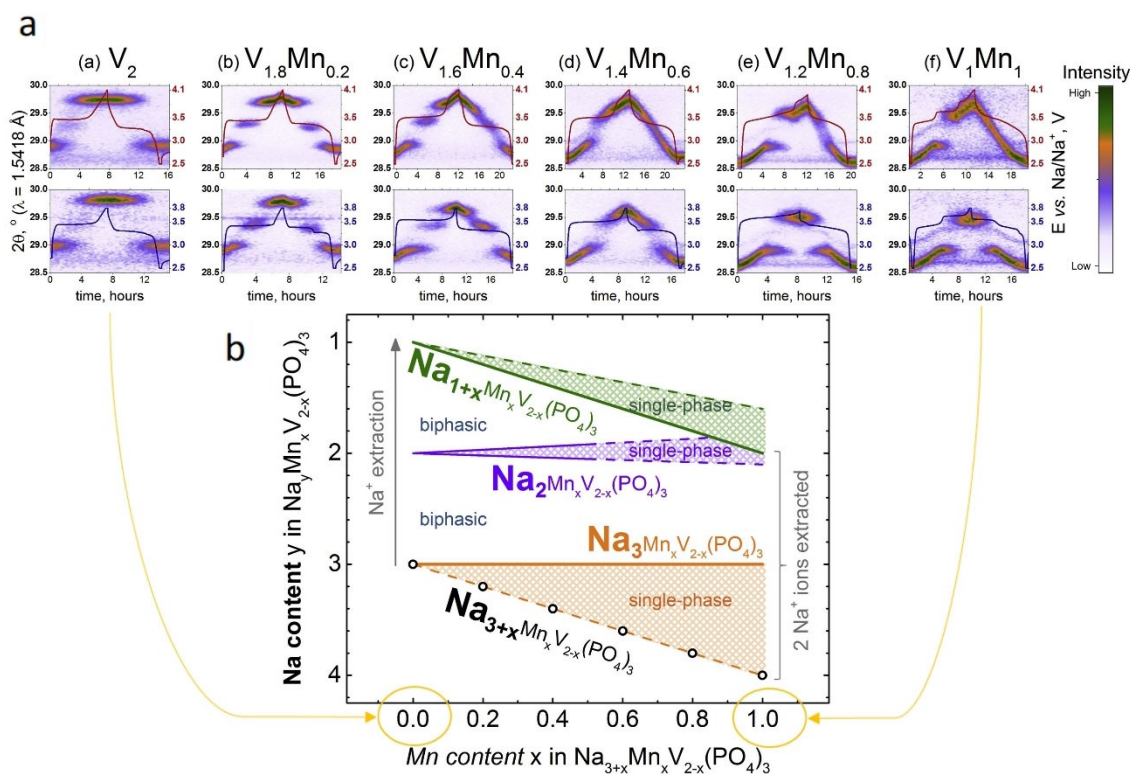


Figure 6. a) *Operando* XRD study on $\text{Na}_{3+x}\text{Mn}_x\text{V}_2(\text{PO}_4)_3$ with 5 different values of x with an increment of 0.2. The figure shows a selected region (024 reflection, $28.5\text{--}30.0^\circ$, $\text{CuK}\alpha_1/\text{K}\alpha_2$) of XRD patterns during (de)sodiation in the 2.5–3.8 V (bottom) and 2.5–4.1 V (top) voltage windows. b) Schematic illustration of the desodiation mechanisms based on the data from (a). Adapted from Ref. [119] with permission. Copyright (2020) Elsevier.

conversion and alloying materials are poorly suited for conventional XRD due to their amorphous nature or formation of amorphous phases during cycling. In these cases, PDF measurements can offer some hope for structural analysis.

Alloying anode materials for NIBs are generally composed of elements from the p-block of the periodic table (Sb, Sn, Bi, Si and P) or alloys composed of these elements (BiSb, TiSb₂). The sodiation of these materials often proceeds through formation of multiple crystalline phases, which can be tracked using *operando* XRD. For instance, several *operando* XRD studies performed on Bi alloying anodes confirmed the reversibility of Bi transitions to NaBi and Na₃Bi upon sodiation.^[19,41,141] The structure of Na₃Bi formed during cycling depends on the starting crystallite size of Bi. Nanosized Bi transforms into cubic Na₃Bi upon sodiation, while sodiation of larger Bi particles results in the formation of hexagonal Na₃Bi.^[42] The structure of the Na₃Bi phase affects the cycling stability, in which the cubic form is superior to the hexagonal form. A similar Na alloying mechanism was also proposed for BiSb-alloys based on *operando* XRD.^[37] However, elemental Sb has different cycling behaviour than Bi. Initially, Gao *et al.* demonstrated that Sb alloys with Cu from the current collector as well as Na, forming Na₃Cu_xSb_{1-x}.^[35] There is no evidence of a crystalline NaSb phase, but a detailed PDF study combined with *ex situ* NMR, conducted by Allan *et al.*, demonstrated the formation of several amorphous phases upon cycling.^[43] As shown in Figure 7 a–c, there are three different amorphous phases (Na_{1.7}Sb, Na_{1.0}Sb and Na_{3-x}Sb) in addition to the two crystalline phases (Sb and Na₃Sb). The study also showed the formation of amorphous Na_{3-x}Sb during sodiation only, while desodiation follows a different pathway.

A notable difference between sodiation and desodiation pathways were also observed for phosphorus alloying anodes, using *operando* SAXS/WAXS and PDF-CT (PDF = pair distribution function, CT = computed tomography).^[36,40] These studies demonstrated that sodiation of P-based electrodes follows the thermodynamic path via NaP to Na₃P, while during desodiation, the material takes a different pathway through the metastable Na_{2.6}P and Na_{2.36}P phases (desodiated forms of Na₃P) and directly back to amorphous P without forming NaP. The *operando* PDF study also demonstrated an enormous change in the crystallite size of phosphorous during cycling, which changes from 10 nm when P is fully sodiated to around 1 nm when fully desodiated.^[40] This study clearly illustrates the importance of *operando* studies for elucidation of (de)sodiation pathways that are not typically visible through conventional *ex situ* characterization.

Si is a very promising alloying material for LIBs but does not perform well in NIBs. Through nanostructuring of Si it is currently possible to obtain stable capacities slightly above 400 mAh g⁻¹,^[39] which is significantly less than for other alloying materials such as Sn and Sb (typical capacities around 600 mAh g⁻¹ over at least 100 cycles).^[164,165] An *operando* XRD study on nanocrystalline Si in NIBs showed a transformation into an amorphous phase upon sodiation.^[39] However, the sodiation mechanism in Si remains to be evaluated.

Conversion NIB anodes are of particular interest due to their high specific capacities. The materials undergo a reaction where the elements in the electrode material separate, and Na binds to the most electronegative element. The general reaction is given by Eq. (1)



where M is a transition metal (Fe, Ni, Co, Cu) and X is an electronegative non-metal (F, O, S, N, P, Se). Understanding the conversion process is extremely important for the rational design of future materials in this class. Thus, *operando* methods are particularly suitable for the task. To illustrate that, Ou *et al.* studied CoSe₂ and NiSe₂ with *operando* XRD. NiSe₂ showed a conversion reaction forming amorphous Ni-nanoparticles embedded in Na₂Se, with Na_xNiSe₂ as an intermediate.^[57] This reaction mechanism was confirmed through *operando* XRD and *ex situ* TEM. CoSe₂ showed similar behaviour by going through a two-step conversion reaction to CoSe and Co-metal with the formation of Na₂Se in both steps. The first step forming CoSe is quite reversible, while the full conversion to Co is difficult to reverse.^[56] Hollow spheres of NiS_{1.03},^[53] microcrystals of Ni₃S₂,^[54] (Ni_{0.5}Co_{0.5})₉S₈ nanoparticles embedded in nitrogen-doped porous carbon shells,^[51] powders of NiP₃^[60] and nanorods of MoP^[58] showed similar behaviour; the clusters of the transition metals are formed together with Na₂S or Na₃P. Many conversion materials also show signs of amorphous phases forming during cycling, which could be further studied with techniques other than XRD. For example, Xu *et al.* studied Co₃O₄ with *operando* XRD, SAXS and XANES (X-ray absorption near edge spectroscopy), showing transformation of Co₃O₄ into an amorphous phase during the conversion reaction.^[55] More complex conversion materials such as Cu₃PS₄,^[8] CuSO₄,^[50] Pb₃Nb₄O₁₃,^[52] Fe_{0.5}TiOPO₄ and Cu_{0.5}TiOPO₄^[59] were also studied with *operando* XRD and generally show the same behaviour.

The replacement of the transition metals in oxides and chalcogenides with more electronegative p-block elements (Sn, Sb and Bi) provides materials that combine conversion and alloying mechanisms. SnS₂,^[62] Bi₂S₃,^[64] Sb₂O₃/rGO,^[9] and Sb₂Se₃/rGO^[63] were studied by *operando* XRD confirming combined conversion and alloying as a sodiation mechanism. Such mechanism consists of initial conversion of the starting material into a stable matrix of sodium oxide, sulfide, or selenide with embedded (nano)particles of Sn, Bi or Sb. In subsequent cycles, the embedded particles are reversibly sodiated through alloying process. The conversion part of the reaction is only reversible at relatively high voltages (around 2 V for both Bi₂S₃ and Sb₂Se₃/rGO), meaning that it would be difficult to utilize this extra capacity in a full cell. Reversal of the initial conversion also negatively affects the cycling stability. The combined mechanism can also be achieved in alloys of transition metals with a p-block metal or similar mixed oxides. Examples are FeSb₂,^[65,66] and FeSbO₄,^[61] where Fe forms an electrochemically inactive amorphous phase during sodiation that helps to improve the cycling stability of the material driven by Sb – Na₃Sb alloying reaction.

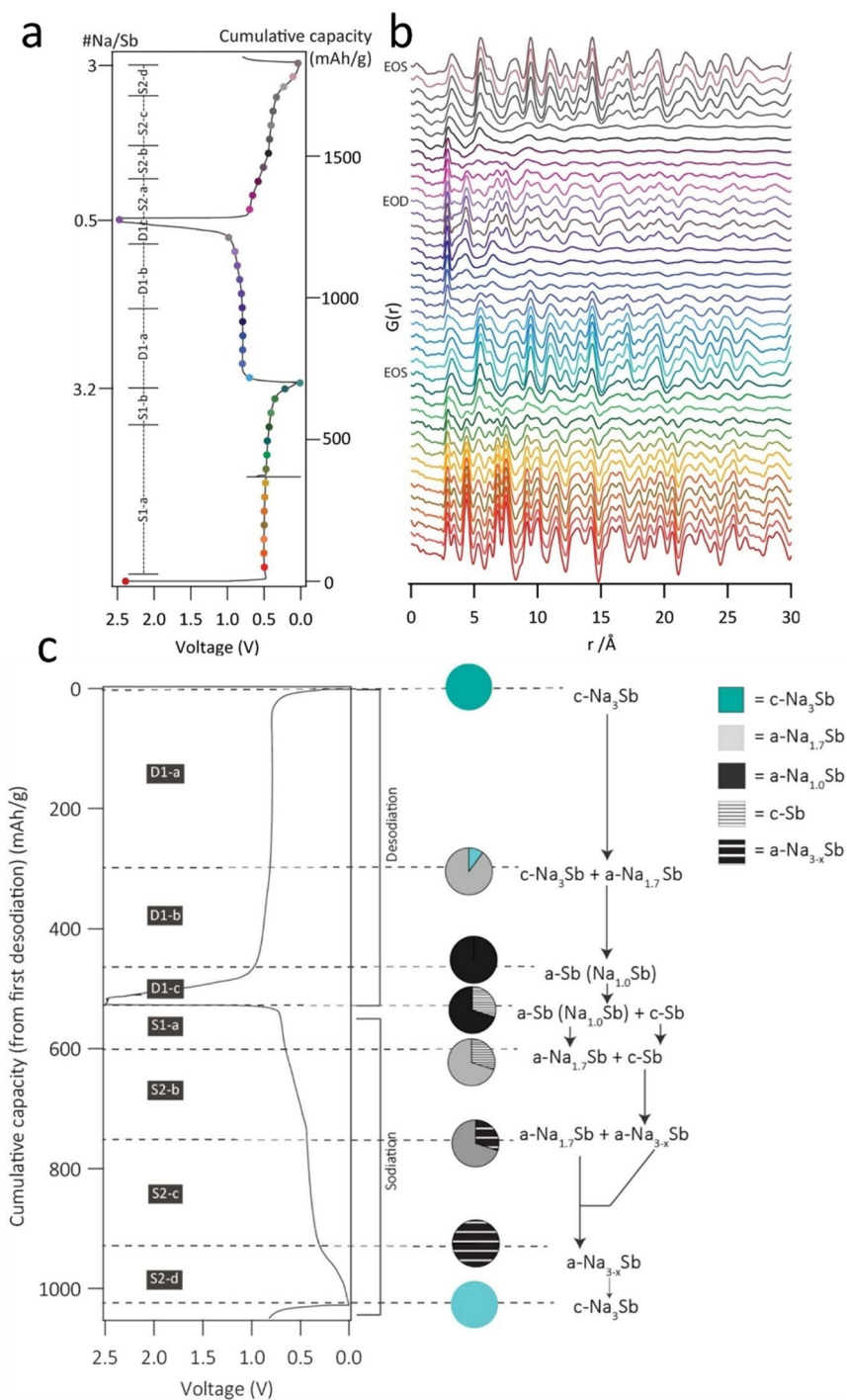


Figure 7. a) Charge-discharge curves and b) corresponding PDF graphs obtained from *operando* PDF measurements of Sb electrode during the *operando* PDF measurements. c) (de)sodiation mechanisms of Sb derived from the *operando* PDF measurements from the first desodiation and the second sodiation with a cycling rate of C/20. Adapted from Ref. [43] with permission. Copyright (2016) American Chemical Society.

2.5. Sulfur, Air, and Na Metal Batteries

Most *operando* studies on Na-based batteries in the literature are focused on NIBs. However, there are a few studies on Na-air, Na-S and Na-metal batteries. An *operando* XRD study performed by Pinedo *et al.* showed a different reaction mechanism for Na-air battery when cycling with dry O₂

compared to wet O₂. NaO₂ was the sole discharge product under dry conditions, while in wet conditions Na₂O₂·2H₂O and NaOH are formed.^[116] One of the major challenges in assessing the performance of Na-O₂ batteries is to understand the parasitic reactions that occur during cycling. Therefore, it is important to characterize and quantify the materials formed during cell operation and correlate these processes to the

charge accumulated during discharge/charge. In response to this challenge, Liu *et al.* performed *operando* XRD with an internal Si standard to quantify the formation of crystalline NaO₂ in a Na-air battery during the first discharge.^[115] The most recent *operando* study on Na-air batteries performed by Wang *et al.*, elucidated the presence of Na₂O₂, NaOH and Na₂CO₃ in the first cycle for a battery containing a CoO/CoP catalyst.^[114] To the best of our knowledge, only one *operando* XRD study has been performed on Na-S batteries, illustrating sodiation progress through the following phase transitions: S₈→Na₂S_x→Na₂S₄→Na₂S (x=8, 6, and 5). On desodiation, most of the S₈ phase is recovered, but over many cycles, nonconductive Na₂S accumulates leading to irreversible capacity loss.^[117]

3. X-Ray Absorption and Spectroscopy

X-ray absorption spectroscopy (XAS) is frequently used in *operando* studies of specific elements in battery materials. Electrons at the different energy levels of the atom are excited at characteristic photon energies measured in terms of intensity changes at the so called absorption edges. The X-ray energies are scanned across the “edge” of the target element. Usually, *operando* XAS experiments just concentrate on a single absorption edge, although with the optimized setup multiple edges can be probed reasonably fast.^[166]

The XAS spectrum can be split into regions before, close to and after the adsorption edge. XANES uses a small region close to (and including) one of the main absorption edges in the XAS-spectrum. From the energy and fine structure of the absorption edge, information about the oxidation state of the elements as it varies during cycling can be extracted. Information about element’s site symmetry and electronic structure can also be extracted from the XANES region (which includes the so-called “pre-edge” region just below the absorption edge). Extended X-ray absorption fine structure (EXAFS) uses the energy range from approximately 50 eV to > 600 eV above the absorption edge. EXAFS provides information about short-range order around the absorbing atom in the material: type, number, and distribution of neighbouring

atoms. In general, EXAFS analysis requires data with much better quality compared to XANES. A challenge with EXAFS analysis is the complexity of an average of a number of local structures that may change during the course of the cycling reactions. The active elements in NIB electrodes change their oxidation state and/or undergo chemical transformations during cycling. XAS can track these changes in crystalline or amorphous materials providing information on the local environment of a specific element. XAS becomes an especially strong tool when combined with other *operando* techniques. Several synchrotron beamlines are capable of performing such experiments, revealing the structural and electrochemical mechanisms that occur during cycling. Examples of *operando* XAS studies on NIB materials are summarized in Table 2.

An early *operando* XAS study of battery materials was reported by Pivko *et al.* in 2012.^[173] They compared two stable modifications of the A₃V₂(PO₄)₃ framework (A=Li, Na) by monitoring the vanadium oxidation states with V K-edge XANES and changes in the local environment of vanadium in Na₃V₂(PO₄)₃ during the first charge and discharge with V K-edge EXAFS. They showed that the average valence state of vanadium changes reversibly from V^{3.0+} to V^{3.8+} during cycling. In addition, a reversible structural deformation was observed, demonstrating the stability of Na₃V₂(PO₄)₃ for high-energy-density batteries.

Sodium-vanadium fluorophosphate compounds Na₃V₂(PO₄)₂F_{3-y}O_y (with y ranging from 0 to 2) are among the most promising polyanionic compounds for the use in NIBs.^[175] These materials were extensively studied by a number of methods including *operando* XAS. Broux *et al.*^[172] used *operando* XANES combined with solid-state NMR to confirm the disproportionation of V⁴⁺ into V³⁺ and V⁵⁺, which occurs upon the extraction of one Na⁺ ion from Na₃V₂(PO₄)₂F₃. The K edge XANES unambiguously confirmed that this phenomenon does not occur at the end of charging, but happens immediately after the extraction of one Na⁺ ion, i.e., after reaching the composition Na₂V^{III}V^{IV}(PO₄)₂F₃ (shown Figure 8a–b and 8c).^[172] The same research group also reported the substitution of V⁴⁺ with Fe³⁺ in Na₃V₂(PO₄)₂F₂ accompanied by subsequent *operando* studies.^[123] *Operando* XANES combined with EXAFS,

Table 2. Overview of scientific articles on *operando* X-ray absorption and spectroscopy techniques.^[a]

Active Material	Type of Material	Technique(s) ^[b]	Cell type	X-ray window	S vs. H	T vs. F	Cycling rate	Acquisition time per scan	Ref.
CuSO ₄	Conversion	XANES, EXAFS	Special	Glassy carbon	S	F	C/30 and C/40		[50]
SnO ₂	Conversion	XANES, EXAFS	Special	Glassy carbon	S	F	C/30 and C/40		[167]
Co ₃ O ₄	Conversion	XANES, EXAFS	Coin cell	Kapton	S	T	0.2 C	4 min	[55]
Bi ₂ O ₃	Conversion	XANES	Coin cell	Kapton	S	T	0.2 C	4 min	[168]
Na ₂ CoO ₂ (thin film)	Conversion	XPS	Special		H			2 h	[169]
Bi ₂ S ₃	Conversion/alloying	XANES, EXAFS	Swagelok	Kapton	S, H	T	C/10	2-7 min	[64]
FeSb ₂	Conversion/alloying	XANES, EXAFS	Swagelok	Be	S	T	C/2 and C/5		[170]
BiVO ₄ , Bi ₂ (MoO ₄) ₃	Conversion/alloying	XANES	Swagelok	Kapton	S	T	C/10	2 min	[171]
NaNi _{1/2} Fe _{1/2} Mn _{1/2} O ₂	Layered	XANES	Coin cell	Kapton	S	T			[99]
Na _{0.85} Li _{0.17} Ni _{0.21} Mn _{0.64} O ₂	Layered	XANES, EXAFS	Pouch cell	Aluminized Mylar	S	T			[166]
Na ₃ Mn _{1/3} Fe _{2/3} O ₂	Layered	XANES	Coin cell	Polyimide	S		C/50	30 min	[105]
Na ₃ V ₂ (PO ₄) ₂ F ₃	Network	XANES	Special	Kapton	S	F	C/10	4 min	[172]
Na ₃ V ₂ (PO ₄) ₃	Network	XANES, EXAFS	Pouch cell	Triplex	S	T	C/15	29 min	[173]
Na ₃ (VO)Fe(PO ₄) ₂ F ₃	Network	XANES	Special		S	T	C/10	6 min	[123]
NaFePO ₄	Network	XANES	Coin cell	Kapton	S	T			[174]
Na _{1.32} Mn[Fe(CN) ₆] _{0.83} ·2H ₂ O	PBA ^[c]	XANES	Swagelok	Kapton	S	T	C/10	3 min	[146]

[a] S: synchrotron, H: home laboratory, T: transmission (Debye-Scherrer) geometry, F: fluorescence geometry. [b] XANES: X-ray absorption near-edge, EXAFS: extended X-ray absorption fine spectroscopy, XPS: X-ray photoelectron spectroscopy. [c] PBA: Prussian blue analogue.

Mossbauer and solid-state NMR revealed that V^{4+} is completely oxidized to V^{5+} during the reversible single Na^+ extraction (in the voltage window from 2.5–4.3 V vs. Na^+/Na). Moreover, *operando* synchrotron XRD revealed that Na^+ -vacancy ordering during desodiation does not occur. This is the opposite of the behaviour previously reported for $Na_3V_2(PO_4)_2F_3$ and $Na_3(VO)_2(PO_4)_2F$.^[124]

Layered oxides, extensively discussed in Section 2, have also been studied by *operando* XAS. Karan *et al.* investigated the Na^+ cycling mechanism in P2-type $Na_{0.85}Li_{0.17}Ni_{0.21}Mn_{0.64}O_2$ based on the similarity between $LiMO_2$ and $NaMO_2$.^[166] Using a custom-made electrochemical cell for *operando* XAS to study the Ni and Mn edges, they demonstrated that Ni reversibly changes its oxidation states from Ni^{2+} to Ni^{3+} and Ni^{4+} while Mn^{4+} is electrochemically inactive. For materials where primary transition metal is partially substituted, *operando* XAS is the technique of choice allowing to assess the electrochemical functionality of each metal. For instance, the addition of Fe could rebalance the stoichiometry of Ni and Mn elements,

resulting in a special class of layered TMO materials.^[176,177] By employing *operando* XANES combined with *operando* Mössbauer spectroscopy, Mortemard de Boisse *et al.* demonstrated that the Fe^{3+}/Fe^{4+} couple is active at high voltages while the Mn^{4+}/Mn^{3+} couple is electrochemically active at low voltages and high sodium contents: $x > 0.67$ in $Na_xMn_{1/3}Fe_{2/3}O_2$.^[105]

Operando quasi-simultaneous XRD combined with XAS provide insight to the redox activity of PBA materials in NIBs. Sottmann *et al.*^[146] studied the (de)sodiation mechanism in $Na_{1.32}Mn[Fe(CN)_6]_{0.83} \cdot zH_2O$ with $z=3.0$ (monoclinic) or 2.2 (cubic). The monoclinic and cubic versions show similar redox behaviour for the Fe^{3+}/Fe^{2+} couple, but the cubic structure better utilizes the redox reactions of the Mn^{3+}/Mn^{2+} couple and, therefore, shows superior cycling stability. However, during cycling Mn in the active material is lost as $NaMnCl_3$ due to reaction with the $NaClO_4$ electrolyte, which causes capacity degradation. Moreover, the capacity loss is pushed by the coordinated water in $[Fe(CN)_6]$ vacancies and higher zeolitic water content in the pristine material.

Sb K-edge XAS and synchrotron Mössbauer spectroscopy (SMS) were combined for the first time to clarify the roles of iron and antimony in the electrochemical reaction mechanism of an $FeSb_2$ NIB anode.^[170] The study observed the formation of amorphous Na_3Sb and Fe nanoparticles containing a small fraction of Sb ($\leq 10\%$) in their lattice. After the first discharge, the amorphous/nanoconfined Sb is the active material leading to an alloy-type mechanism rather than a conversion reaction. Both *operando* and *ex situ* XAS were used to confirm the incomplete conversion and alloying reaction that SnO_2 undergoes during sodiation, due to the formation of a dense NaO_2 layer.^[167] Lee *et al.* identified the mechanism of the conversion reaction of $CuSO_4$ in a NIB using *operando* XANES and EXAFS. They discovered that during the initial charging/discharging, the oxidation states varies between Cu^{2+} and metallic Cu^0 . The simultaneous dissociation of the Cu–O bond and formation of the metallic Cu–Cu bond during initial discharging was confirmed from the Fourier transform of the EXAFS spectra.^[37]

Cobalt oxide was studied with *operando* EXAFS by Xu *et al.*,^[55] supported by complementary *operando* X-ray based characterizations. They confirmed the conversion of Co_3O_4 to Co and Na_2O upon sodiation. Compared with the lithiation process, the cobalt oxide undergoes smaller changes in pore structure, oxidation state, crystal structure and local structure during sodiation, which is attributed to the intrinsic low sodiation activity of Co_3O_4 .

Operando X-ray photoelectron spectroscopy (XPS) is not widely deployed due to the complexity of the cell design required. To the best of our knowledge, the first *operando* XPS study on oxide-based NIBs electrodes was conducted by Guhl *et al.*^[169] A novel cell setup was used to study the sodiation mechanism during charging of a $Na_xCoO_2/NASICON/Na$ battery half-cell NIB. The *operando* study validates the results obtained through *ex situ* analysis, which suggested the oxidation of Co^{3+} to Co^{4+} .^[169]

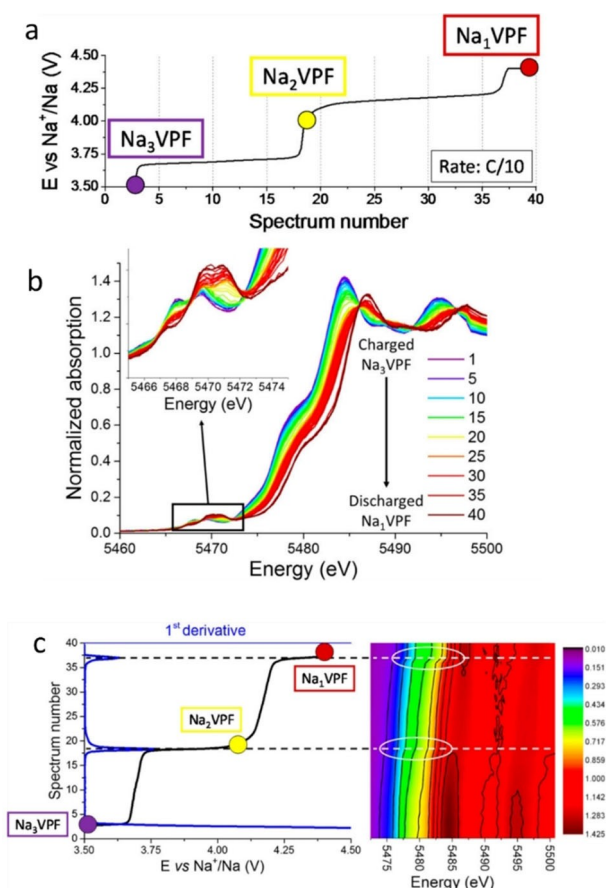


Figure 8. a) Voltage as a function of the time (spectrum number) obtained from *operando* XAS measurement during the first galvanostatic desodiation of $Na_3V_2(PO_4)_2F_3$ at C/10. b) Evolution of the vanadium K edge during desodiation obtained from *operando* XANES. The inset is focused on the pre-edge region c) Left: voltage (black line) as a function of the spectrum number (same as a)) with the associated first derivative (blue line). Right: 2D projection of the corresponding *operando* vanadium K edge XANES spectra emphasizing discontinuities at voltage jumps. Reprinted (adapted) from Ref. [172] with permission. Copyright (2017) American Chemical Society.

4. X-Ray Microscopy (TXM and STXM) and Tomography (XRT and CT)

X-ray microscopy can be used to image samples by detecting reflected or transmitted X-rays. Full-field transmission X-ray microscopy (TXM) or scanning transmission X-ray microscopy (STXM) are two main techniques in X-ray microscopy. To assess chemical information about the sample TXM uses XAS or SAXS data while STXM uses energy dispersive X-ray spectroscopy (EDX), Auger spectroscopy and other methods commonly used for scanning electron microscopy (SEM). TXM and STXM allow imaging of thicker samples than is possible with electrons, with lower radiation damage however with sacrifice of resolution (maximum of around 10 nm).^[178] Higher resolution (around 5 nm) can be achieved in coherent STXM by using ptychography.^[179–182]

Tomographic reconstruction methods can be used on imaging data to create 3D models of battery components and particles. They can be applied to X-ray radiography,^[183] microscopy^[7] or space resolved diffraction/scattering^[184,185] and microfocus XAS data.^[186] Examples of imaging techniques used for *operando* studies of battery materials are shown in Table 3.

Xie *et al.* analysed the phase transformation of $\text{NaNi}_{1/3}\text{Fe}_{1/3}\text{Mn}_{1/3}\text{O}_2$ during Na-ion intercalation through *operando* TXM combined with XRD.^[99] A non-equilibrium solid-solution reaction occurs during desodiation, while during sodiation, the XRD patterns suggest that the phase transformation of $\text{Na}_{1-x}\text{Ni}_{1/3}\text{Fe}_{1/3}\text{Mn}_{1/3}\text{O}_2$ follows a reversible O3-P3-O3 sequence during cycling. Finally, *ex situ* XANES shows that only the $\text{Ni}^{2+}/\text{Ni}^{3+}$ redox couple is electrochemically active between 2.0 and 4.0 V, while $\text{Ni}^{3+}/\text{Ni}^{4+}$ and $\text{Fe}^{3+}/\text{Fe}^{4+}$ are active between 4.0 and 4.3 V. By combining these techniques, they monitored both the structural and the morphological changes of the particles, creating chemical maps of a region in the sample showing the phase changes.

The same techniques were used to reveal the electrochemical behaviour of NaNiO_2 (Figure 9).^[96] Two phase transitions ($\text{NaNiO}_2 - \text{Na}_x\text{NiO}_2 - \text{Na}_{0.19}\text{NiO}_2$) were detected during the cycling process and phase sensitive imaging showed that the changes spread from the outer shell to the core of the particles during both sodiation and desodiation (Figure 9 f and g).

The same group further explored the use of a TXM microscope, combining it with XANES analysis, to elucidate the

Na^+ cycling mechanism of FeS through mapping of the chemical phase transformation.^[187] Similar to NaNiO_2 , sodiation spreads gradually from the surface into the core of the particles, in a partially irreversible process.

While the surface-to-core sodiation patterns commonly observed in *operando* TXM-XANES studies could be predicted, experiments also show that the formation of core-shell structures during sodiation do not indicate the same mechanism for all materials. For instance, in CuO ,^[188] the sodiation happens only in the surface layers and the core becomes inactive (immobilized) to the sodiation. In Ni_3S_2 ,^[54] the sodiation first occurs in the outer regions of the particles and gradually proceeds into the core. However, the sodiation of the core leads to volume expansion and particle cracking ultimately increasing the surface area. This process opens desodiation pathways through the cracked particles. The analysis reveals another reason for the high irreversible capacity of this material: while four Na-ions are inserted during sodiation, only 1.95 Na^+ can be extracted during the first desodiation.

Operando imaging techniques are extremely useful for analysis of transformations in alloying anodes. Wang *et al.*^[7] used *operando* full-field TXM tomography to image Sn particles in an alloying NIB anode in 3D during cycling. Larger particles were observed to expand and crack during sodiation, leading to poor cycling life, while particles smaller than 0.5 μm are less prone to cracking and can be cycled for longer (Figure 10).

Lim *et al.*^[41] combined TXM with XRD to analyse a Bi electrode during sodiation. A core-shell pattern (similar to that of the materials described above) is observed, accompanied by a sudden volume change, which leads to cracking. The particles do not shrink significantly on desodiation, leaving behind a porous microstructure.

Sottmann *et al.*^[40] were the first to use *operando* XRD/PDF computed tomography (XRD/PDF-CT) to study specific NIB components, separating the contributions of the different components (e.g., electrodes, current collectors, electrolyte, and binders). This provided PDF data of very high-quality for mechanistic studies on the anode (see Section 2.4 above) and allowed mapping of the structural variations in the crystalline Na_3P using Rietveld analysis.

Table 3. An overview of scientific articles on *operando* X-ray imaging and combined X-ray techniques used on sodium ion batteries.^[a]

Active Material	Type of Material	Techniques ^[b]	Cell type	X-ray window	S vs. H	T	Cycling rate	Acquisition time	Ref.
Sn	Alloying	XRT, TXM	Coin cell	Kapton	S	T	5 mA g ⁻¹	10 s	[7]
Bi	Alloying	TXM-XRD	Coin cell	Kapton	S	T		60 s	[41]
P	Alloying	XRD/PDF-CT	Special/Tomography		S	T	C/2	7 min per slice	[40]
FeS	Conversion	TXM-XANES	Coin cell	Kapton	S	T		10 s	[187]
Ni_3S_2	Conversion	TXM-XANES	Coin cell	Kapton	S	T	C/10	15 s	[54]
CuO	Conversion	TXM-XANES	Coin cell		S	T		10 s	[188]
$\text{NaNi}_{1/3}\text{Fe}_{1/3}\text{Mn}_{1/3}\text{O}_2$	Layered	TXM-XANES	Coin cell	Kapton	S	T		20 s	[99]
NaNiO_2	Layered	TXM-XANES	Coin cell	Kapton	S	T	C/10	20 s	[96]

[a] S: synchrotron, H: home laboratory, T: transmission (Debye-Scherrer) geometry, F: fluorescence geometry. [b] XRT: X-ray tomography, TXM: full-field transmission X-ray microscopy, XRD: X-ray diffraction, PDF-CT: pair distribution function-computed tomography, XANES: X-ray absorption near-edge spectroscopy.

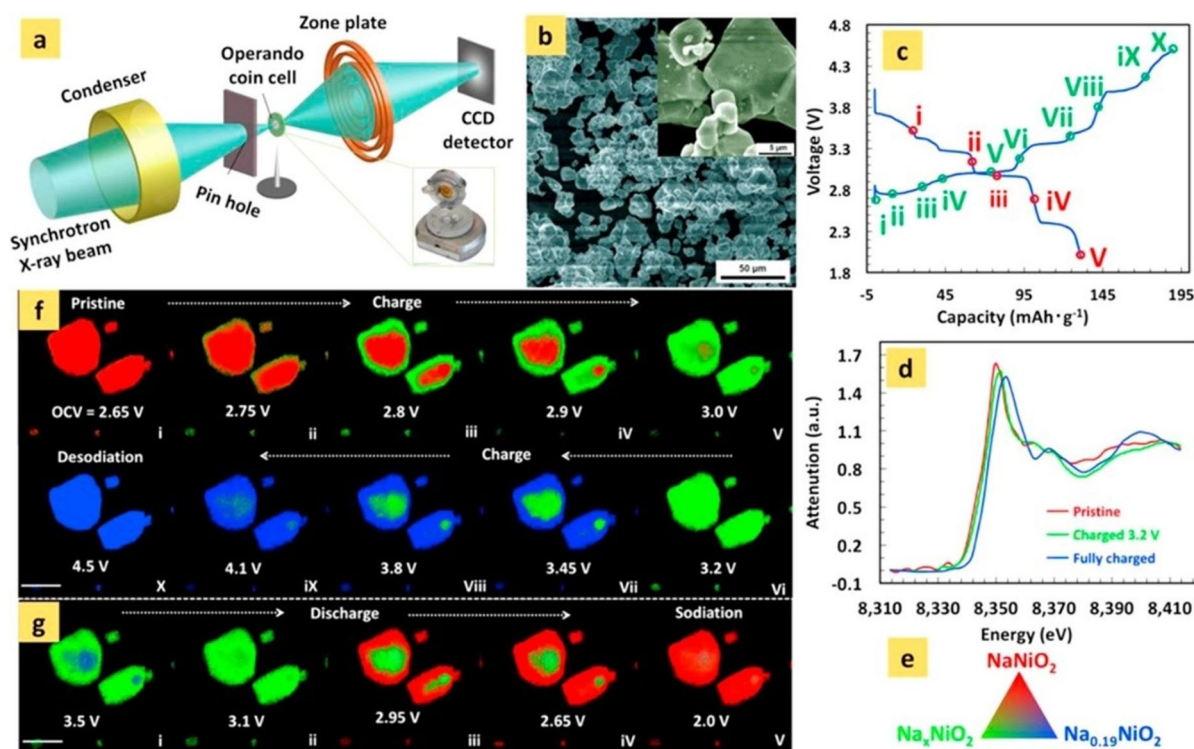


Figure 9. Operando hard X-ray spectro-imaging of two-dimensional microstructural evolution of NaNiO_2 cathode. a) Schematic illustration of the TXM experimental setup. b) Scanning electron micrographs of the NaNiO_2 . Inset is the magnified graph of the NaNiO_2 . c) Charge and discharge profiles of the operando cell. The cell was cycled at the rate of $C/10$ between 2.0 V and 4.5 V. The small circles correspond to the states of charge where the data were collected and fitted as chemical mapping. d) Reference XANES spectra selected from three different operando charged states. e) The reference colour indicates the three phases in the chemical mapping. f) and g) are the two-dimensional chemical phase mapping during the first charge and discharge process. Scale bar: 10 μm . Reprinted from Ref. [96] with permission. Copyright (2017) Elsevier.

5. Experimental Setup, Operando Cells

Operando measurements on batteries require specially designed electrochemical cells and setups that are adapted to the inherent constraints of the instrument used for measurements (within the present review: X-ray diffraction/scattering, absorption and imaging).^[20–23] These X-ray transparent electrochemical cells should ideally mimic the configuration of real batteries in terms of pressure on the stack of battery components, volume of electrolyte with respect to electrode material and thickness of the working electrode. Thus, many of the reported cells are modifications of standard electrochemical cells used in the research laboratory (coin, pouch and Swagelok cells). For meaningful operando characterization, the cell should reproduce a typical electrochemical operation of a common electrochemical test cell. Air and moisture sensitive battery components need to be hermetically sealed in inert atmosphere and shielded from air. The container and window materials should further be chemically inert with respect to the other battery components. The operando cell should also be designed for easy assembly/disassembly. The cell design for the operando X-ray diffraction/scattering, absorption and imaging mainly varies in the orientation of the stack of battery components with respect to the X-ray beam, the type of X-ray transparent window/container materials that can be used and the dimensions of the electrodes.

X-ray diffraction/scattering and XAS measurements are commonly performed perpendicular to the plane of the electrode layers; this geometry only allows one to observe changes in the working electrode if signals from other cell components can be removed, masked or ignored. The stack of battery components is typically pressed together by parts containing X-ray transparent windows.^[21,189] The cell designs can be separated into disposable (coin^[190] or pouch cell)^[191,192] and reusable (Swagelok-type).^[189,193–196] For some of these cells automated sample changers are available, which permits more efficient use of experimental time.^[189–191,193] For the disposable cells, Kapton (polyimide) film or Parafilm can be used as X-ray windows, Figure 11a.^[190,192] However, depending on the film thickness, their flexibility can reduce the homogeneity of pressure across electrode layer, with corresponding variations in chemistry.^[197–199] These issues can be avoided in the reusable Swagelok-type cells, where besides Kapton^[189,195] and aluminum foils^[196] also, more costly but rigid and electrically conducting window materials such as glassy carbon^[193] or beryllium (Be)^[194] can be used, as shown in Figure 11b and 11c. It should be noted that Be and its compounds are highly toxic, and must be handled with extreme care. Another disadvantage of Be windows is their Bragg peaks, which could overlap with those of active material. Aluminum foil (often placed between the Be window and positive electrode materials to prevent oxidation of Be)^[194] also introduces diffraction peaks. Glassy carbon is

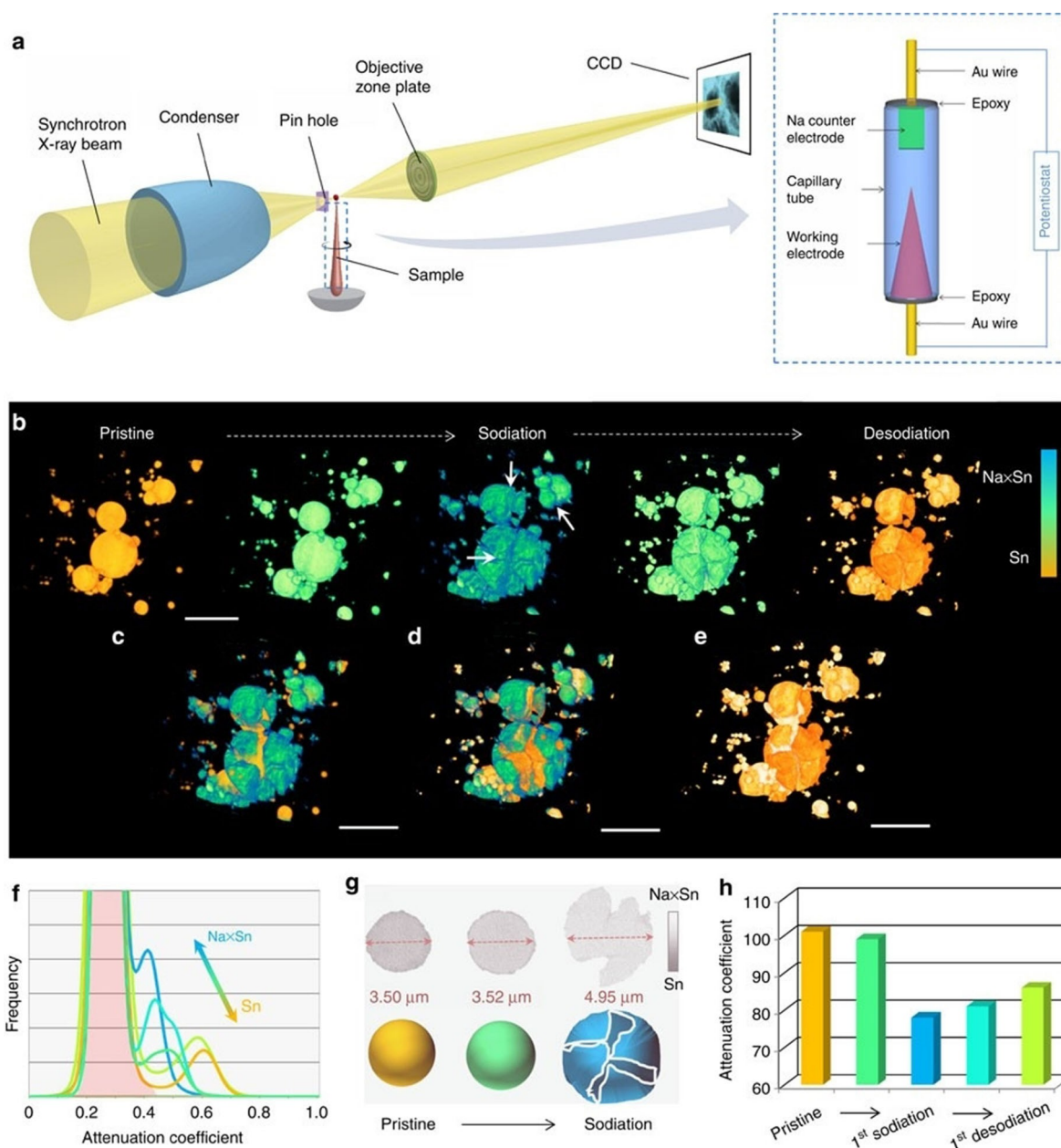


Figure 10. a) Experimental setup and electrochemical cells for *operando* TXM. b) 3D morphological change of Sn particles during the first sodiation and desodiation. The colours represent the attenuation coefficient variation, shown in (h), within the reconstructed images. Overlapped 3D images of Sn particles at different cycling stages: c) pristine/sodiated, d) sodiated/desodiated, and e) pristine/desodiated. The contrasts of the overlapping colours (c–e) are adjusted for better visualization. f) Normalized X-ray attenuation coefficient graph during the first cycle. g) Schematic illustration showing the volume expansion and cracking during the sodiation process supported by the cross-section images of selected particles (shown in grey). h) Histogram of attenuation coefficient change correlated to the 3D morphological and chemical changes. Scale bar: 10 μm. Reprinted (adapted) from Ref. [7] under the terms of the Creative Commons License. Copyright (2015) Springer Nature.

amorphous, resulting in a broad background contribution (no Bragg peaks) and is non-hazardous. Be is less absorbing than glassy carbon.

For XAS, particularly in the energy range of transition metal K-edges, Be and Kapton are the preferred window materials due to their higher transmission. In some cases, holes are punched through the current collectors, counter electrode and separator. The volume of electrolyte can also be reduced, to further improve beam transmission.^[200] With these optimiza-

tions, XAS spectra of most transition metals and alloying elements can be obtained in transmission geometry. For the lighter elements and/or small concentrations, however, fluorescence mode (reflection geometry) is preferable.

Higher energies are typically used for diffraction/scattering experiments, compared to XAS, (at the synchrotron or with e.g. Mo radiation on laboratory diffractometers)^[189] so transmission through the cell (Debye–Scherrer geometry) is usually not a problem. It is then possible to collect scattering data from both

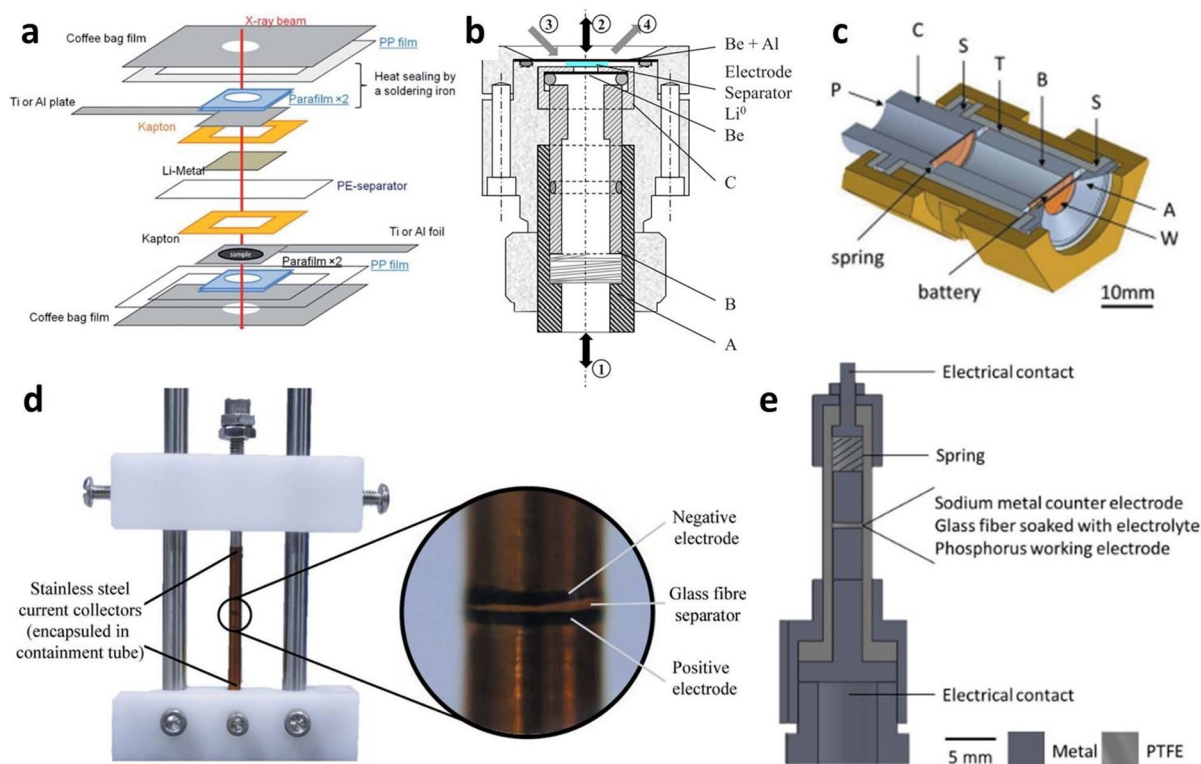


Figure 11. Illustration of *operando* cell designs based on a) pouch cells (reproduced from Ref. [192] with permission, copyright (2014) Royal Chemical Society), b) Swagelok-type cell with Be window (reproduced from Ref. [194] with permission, copyright (2010) The Electrochemical Society), and c) Kapton (reproduced from Ref. [189] with permission, copyright (2016) International Union of Crystallography); 3D imaging cells with d) alignment rods reproduced from Ref. [205] with permission, copyright (2016) International Union of Crystallography), and e) PTFE casing reproduced from Ref. [206] with permission, copyright (2017) Wiley-VCH.

electrodes in a full-cell simultaneously. Some cells use a reflection configuration (Bragg–Brentano geometry), which is commonly available in laboratory X-ray diffractometers with Cu radiation. In such experiments, a surface layer with an angle- and composition-dependent depth is sampled instead of the entire depth of the working electrode as in transmission geometry. The available cell designs include a reusable Swagelok-type cell with a Be window,^[201] a reusable cell with glassy carbon windows,^[202] a reusable cell with a graphite dome as the window,^[109] a disposable coin cell with a Kapton window^[203] and a pouch cell with an Al/Ti metal foil window.^[192] The similarities between the cell designs for X-ray diffraction/scattering and absorption make parallel XRD and XAS experiments possible on some beamlines. This enables deep insights into electrochemical processes by both structural and chemical characterization of the electrode material(s) quasi-simultaneously (at the same voltage or state of charge) in the same cell.^[189,204]

X-ray imaging is performed in full-field or scanning modes. Each cell design was modified to minimize adsorption of hard X-rays, allowing an unobstructed view of the region of interest (e.g., a few electrode particles, a slice of the electrode or the entire stack of battery components).^[22,23] For three-dimensional (3D) imaging rotation of the object (ideally at least 180°) is required. The rotation axis is typically chosen perpendicular to the stack of components and the X-ray beam is oriented in the

plane of the electrode layer(s). *Operando* cells for 3D imaging typically, therefore, have a cylindrical shape. The container walls are made of thin, mechanically stable, electrochemically inert, electrically insulating, X-ray transparent and texture-free materials, e.g., Kapton, quartz glass, PEEK (polyether ether ketone) and PTFE (polytetrafluoroethylene). The diameter of the cell has to be sufficiently small to reduce absorption of the X-rays in the selected energy range by electrode materials and electrolyte. Smaller versions can be built from quartz glass capillaries (~1 mm in diameter). The electrodes are attached to metal wires glued into the capillary with epoxy, which also hermetically seals the cell. Planar cells, e.g. pouch cells,^[207] and cylindrical cells with alignment rods (Figure 11d–e),^[205] can be used for tomographic imaging with less than 180° rotation. However, the missing angular wedge may cause artefacts, some of which can be removed with sophisticated reconstruction algorithms.^[208]

6. Methods for Analysis of *Operando* Data and New Experimental Methodologies

Fitting the large volumes of data produced by modern *operando* experiments is a significant task. Modern computing and software make this process significantly easier, and several

methods developed recently are extremely applicable for *operando* NIB studies. At the time of writing, only a few of these methods have been applied to NIBs. Therefore, this section will cast its net wider in terms of chemistries studied than the bulk of the review.

Batch fitting methods have been used since the early days of *in situ* and *operando* studies, for example, fitting of Bragg peak intensities to obtain crystallisation kinetics during zeolite structure transformations.^[209] In a batch (or sequential) pattern fitting process, the initial structural model is refined against the starting dataset and the refined model is taken as the starting point for refinement against the next dataset in the series. In this way, the model “evolves” through the process as it is refined against each dataset. This method was applied to diffraction, scattering and spectroscopic data series.^[210,211] Some Rietveld and PDF refinement software packages, e.g., Fullprof^[212,213] and PDFGUI^[251] include specific tools for batch refinement, or function with software designed by others to facilitate it.^[214] Batch refinement was used by Gaubicher *et al.* in an early *operando* study on NIBs.^[139] Batch processing is also part of the popular ATHENA^[215] suite for XAS data processing, used in the first *operando* XAS study of NIBs.^[216]

The surface/parametric approach to pattern fitting developed by Stinton and Evans^[217] has been applied in several *operando* studies of NIB materials.^[42,206,216–220] In this method, the entire series of diffraction patterns or spectra are treated simultaneously. Parameters like the instrumental peak shape and diffractometer zero point can be refined globally against all the data, while parameters that can vary during the experiment are refined separately for each diffraction pattern/spectrum. The approach is especially useful for *operando* diffraction computed tomography studies,^[221] which produce massive volumes of data, as the number of refined parameters can be significantly reduced compared to batch methods. An example is the XRD-CT mapping presented by Sottmann *et al.* on a working phosphorus NIB anode.^[206] Linking less interesting, well understood parameters to equations which describe their physical behaviour can further improve the stability and precision of parametric fits.^[222] An intriguing extension of this approach is the direct least-squares reconstruction (DLSR) method for XRD-CT recently described by Vamvakeros *et al.*^[223] Here, the reconstruction and Rietveld refinement are carried out simultaneously using a parametric approach in which the groups of measured diffraction patterns merged to reconstruct each voxel, are refined simultaneously against a single physical model for the relevant voxel. DLSR allows reconstruction of larger objects without blurring at the periphery of the tomograms caused by parallax artefacts. This has obvious benefits for electrochemistry, as the use of larger, more realistic cells reduces inaccuracies in e.g. calculated capacity from electrode mass, as larger masses are easier to measure accurately, not to mention being easier to handle.

The use of structures from density functional theory (DFT) calculations (energy minimisations both of known structures from databases and invented structures produced, e.g. by replacement of certain atom types in a known structure) has already proved important in interpreting *operando* data from

NIBs.^[42,43,171,206,218,224–226] We expect such methods to find new applications as *operando* experiments develop further and come into wider use. The development of databases of computed properties like Materials Project^[227] and machine learning approaches to prediction of materials with desirable properties will also accelerate this process.

Principle component analysis (PCA) is a statistical multivariate curve resolution (MCR) method that has been used for several decades to analyse spectroscopic data^[228] and has more recently been applied to diffraction^[229,230] and PDF.^[231] PCA takes a dataset with many variables and extracts a small number of new variables that express the bulk of the variance.^[232] In *operando* battery cycling studies, where we expect to see variations in the structure and composition of the active components during the experiment, PCA can extract the signals responsible for most of the variance in the data series without any prior knowledge of the chemistry. These principal components should represent the signals of the active components that change during the experiment.

PCA is a very powerful tool for rapidly determining the key sources variance in a series of many spectra/patterns. An interesting recent example is the use of *in situ* XRD/PDF/fiber optic reflectance spectroscopy in an attempt to determine the lost recipe of the ancient pigment Mayan blue.^[233] PCA has also been used for automatic extraction of kinetic data from *in situ* experiments combining Raman spectroscopy and XRD,^[234] and for efficient analysis of a large series of *in situ* single crystal datasets collected during the adsorption of CO₂ on zeolite-Y.^[235] The team behind many of these developments has produced a software package, RootProf,^[236] for PCA analysis of diffraction and spectroscopy data.

In multivariate curve resolution with alternating least squares (MCR-ALS),^[172,237,238] a set of factors describing the data, obtained from an MCR method like PCA, singular-value decomposition^[239] or cluster analysis^[240] is fitted to the data using a constrained least squares refinement.^[241] The power of this approach lies in the possibility of inserting constraints obtained from other measurements on the same sample, allowing the combination of data from a range of sources and techniques. Application of this method to large *operando* battery XAS datasets suggests it may prove very useful in the future.^[172,237,238] Recently, Rekhinta *et al.* used MCR-ALS to extract and study the variable components of a PDF data series collected during the decomposition of magnesium hydroxycarbonate. They revealed, with no prior information, the existence of an amorphous intermediate phase in the process that was not evident from other examinations of the experimental PDFs. Although PCA and MCR-ALS are yet to be applied to *operando* battery PDF data, we believe that they will prove very useful in future for extracting signals from weakly scattering but highly variable amorphous components that appear during cycling.

Modulation excitation is another technique that makes a virtue of the huge number of data points obtained from an *operando* experiment. In this case, there is an experimental element as well as statistical analysis. A series of structural data (spectra, diffraction patterns, etc.) are collected from a sample while a modulated external stimulus is applied. This could be

anything from a switchable electric field to a changing series of reactive gases.^[242] The variations in the structural data are then plotted against the frequency of modulation of the stimulus. When the series of data is processed correctly against the modulation frequency, signals which do not vary with the external stimulus collapse to zero intensity, leaving only the signals from parts of the sample that vary along with it. This can significantly simplify the data by wiping out the contribution of spectator species that might otherwise have a strong contribution to the spectra/patterns. The approach was first applied to spectroscopy by Urakawa and co-workers^[243] and subsequently developed for diffraction data,^[244] but has not thus far been applied to a large range of systems. The potential for processing *operando* data on battery cycling with this method is obvious, as a modulated stimulus is already an integral part of the experiment. Chernyshov *et al.* recently compared the use of PCA and modulation excitation analysis for synchrotron diffraction data on gas loading of the porous framework gamma Mg(BH₄)₂.^[245]

The potential of machine learning (ML) and artificial intelligence (AI) methods for spotting trends in massive datasets, which might be ignored by careless humans, is immense but is currently untapped in the field of *operando* NIB studies. An indication of the possibilities comes from the use of machine learning to carry out an extensive statistical analysis of tomographic data on the detachment of NMC particles in an LIB cathode from their conductive carbon support.^[246]

7. Main Challenges and Future Perspective

In the ongoing search for alternatives to LIBs, NIBs (and potentially Na-air and Na-S batteries) offer promise for several applications. However, NIBs still lack the performance required to be truly competitive with LIBs. Therefore, the search for more efficient, stable, cheap, and environmentally friendly materials continues. The rational design of NIB materials requires a deep understanding of their behaviour in electrochemical systems that are as close as possible to real applications. *Operando* X-ray methodologies deliver valuable information about the structural, atomistic, and morphological changes while the battery is actually in its working state. In some cases, data can be obtained with spatial resolution. Although X-ray methods have limitations (limited resolution, beam damage, lack of surface sensitivity) several of which are accentuated when they are used for *operando* characterization, the methods described above are suitable for a wide range of both crystalline and amorphous materials. In particular, beam damage remains a bottleneck in the *in situ* and *operando* characterizations, not only for NIBs but also for all kind of battery systems.^[25,247,248]

Crystalline TMO cathodes, in particular, are perfect samples for both XRD and XAS methods. Furthermore, PDF has proved to be an extremely powerful technique for analysis of conversion and alloying anode materials, which often become amorphous during cycling. One practical problem specific to *operando* XRD/PDF measurements on NIB half-cells with Na

metal counter electrodes is the very strong scattering from the Na foil. This signal can have very strong preferred orientation effects (often giving single crystal-like diffraction spots), which move during the experiment due to expansion and contraction of the active material(s). This problem is most commonly addressed by masking out the areas of the diffraction pattern where the Na peaks are observed, however, this can lead to the loss of valuable sample information. We expect that in the near future *operando* XRD/PDF CT methods will increase in popularity as they provide an extraordinary amount of information for understanding NIB performance. These methods also directly target the components of interest, removing the contributions from electrolyte, current collectors, sodium metal half-cell electrodes etc. MCR methods like PCA and modulation enhanced diffraction/spectroscopy also offer the promise of extracting signals for the active materials while excluding the Na metal signal. An obvious experimental solution to problems with Na metal counter electrodes, is, of course, to use full cells for *operando* studies. This, however, adds another significant and variant contribution to the data.

A broad range of *operando* X-ray methods can now be applied both at synchrotrons and in home laboratories, and many electrochemical cell designs are available. These offer tremendous scope for new *operando* investigations of working and degradation mechanisms in NIBs. Analysis of the sometimes extremely large datasets generated during these measurements (e.g. XRD-CT) will continue to become easier as advanced analysis tools develop and gain wider acceptance. A significant gap in the sensitivity of *operando* battery methods remains the detection of thin layers and coatings, both those formed during cycling and those applied to battery components to improve their properties. We expect that ongoing improvements in X-ray brilliance and focussing of smaller beams at synchrotron sources, along with new sample cell developments will address this in the next few years.

While X-ray based methods are well established for *operando* characterization of battery materials, the *operando* application of other, complementary methods will allow even more complete characterisation of these complex systems. In the near future we expect to see the use of techniques combining X-ray methods with TEM, AFM and Raman for *operando* NIB studies. In combination, this suite of *operando* methods will provide very complete descriptions of NIBs.

Further optimization and development of the new materials and chemistries will require understanding not only of bulk processes, but also of the interfaces between various materials and components. Thus, we expect the rise of surface *operando* techniques such as Raman and Fourier transform infrared (FTIR) spectroscopies as well as X-ray surface methods in the near future. *Operando* HAXPES^[249] (hard X-ray photoelectron spectroscopy) has already been used for LIBs and synchrotron-based SOXPES (soft X-ray photoelectron spectroscopy)^[250] has been applied in the study of SEI (solid-electrolyte interface) formation in NIBs, but only *in situ*.

Operando methods deliver chemical and structural information of such high value that a growing number of researchers consider them worthwhile, despite the complexity of the

experimental setups and data processing. Considering the importance of battery science, we predict further expansion of their use, providing the basis for further materials and technology development.

Acknowledgements

The authors thank the Research Council of Norway (NFR) for funding through the NanoName project (number 287480). This work was performed within MoZEEs, a Norwegian Centre for Environment-friendly Energy Research (FME), co-sponsored by the Research Council of Norway (project number 257653) and 40 partners from research, industry and public sector. D.S.W. thanks Antony Vamvakeros, Wouter Van Beek, and Dmitri Chernyshov for discussions on DLSR, modulation excitation and PCA methods. C.C. would like to thank Dr. Muhammad Abdelhamid for helping with the graphics.

Conflict of Interest

The authors declare no conflict of interest.

Keywords: *operando* X-ray methods · sodiation and desodiation mechanism · cell design · data analysis for *operando* · Na-ion batteries

- [1] I. Hasa, S. Mariyappan, D. Saurel, P. Adelhelm, A.Y. Kuposov, C. Masquelier, L. Croguennec, M. Casas-Cabanas, *J. Power Sources* **2021**, *482*, 228872.
- [2] C. Vaalma, D. Buchholz, M. Weil, S. Passerini, *Nat. Rev. Mater.* **2018**, *3*, 18013.
- [3] M. I. James, A. S. Prakash, *J. Power Sources* **2018**, *378*, 268–300.
- [4] X. Yin, S. Sarkar, S. Shi, Q.-A. Huang, H. Zhao, L. Yan, Y. Zhao, J. Zhang, *Adv. Funct. Mater.* **2020**, *30*, 1908445.
- [5] K. Nobuhara, H. Nakayama, M. Nose, S. Nakanishi, H. Iba, *J. Power Sources* **2013**, *243*, 585–587.
- [6] Z. Wang, S. M. Selbach, T. Grande, *RSC Adv.* **2014**, *4*, 4069–4079.
- [7] J. Wang, C. Eng, Y. C. K. Chen-Wiegart, J. Wang, *Nat. Commun.* **2015**, *6*, 7596.
- [8] W. Brehm, A. L. Santhosha, Z. Zhang, C. Neumann, A. Turchanin, A. Martin, N. Pinna, M. Seyring, M. Rettenmayr, J. R. Buchheim, P. Adelhelm, *Adv. Funct. Mater.* **2020**, *30*, 1910583.
- [9] H. Li, K. Qian, X. Qin, D. Liu, R. Shi, A. Ran, C. Han, Y.-B. He, F. Kang, B. Li, *J. Power Sources* **2018**, *385*, 114–121.
- [10] E. de la Llave, V. Borgel, K.-J. Park, J.-Y. Hwang, Y.-K. Sun, P. Hartmann, F.-F. Chesneau, D. Aurbach, *ACS Appl. Mater. Interfaces* **2016**, *8*, 1867–1875.
- [11] Y. Lu, Q. Zhang, J. Chen, *Sci. China Chem.* **2019**, *62*, 533–548.
- [12] X. Pu, H. Wang, D. Zhao, H. Yang, X. Ai, S. Cao, Z. Chen, Y. Cao, *Small* **2019**, *15*, 1805427.
- [13] W. Zhu, Y. Wang, D. Liu, V. Gariépy, C. Gagnon, A. Vijn, M. L. Trudeau, K. Zaghib, *Energies* **2018**, *11*, 2963.
- [14] D. Liu, Z. Shadike, R. Lin, K. Qian, H. Li, K. Li, S. Wang, Q. Yu, M. Liu, S. Ganapathy, *Adv. Mater.* **2019**, *31*, 1806620.
- [15] G. Zhang, T. Xiong, L. He, M. Yan, K. Zhao, X. Xu, L. Mai, *J. Mater. Sci.* **2017**, *52*, 3697–3718.
- [16] S. Mukherjee, S. Bin Mujib, D. Soares, G. Singh, *Materials* **2019**, *12*, 1952.
- [17] A. M. Tripathi, W.-N. Su, B. J. Hwang, *Chem. Soc. Rev.* **2018**, *47*, 736–851.
- [18] J. Li, C. Arbizzani, S. Kjelstrup, J. Xiao, Y.-y. Xia, Y. Yu, Y. Yang, I. Belharouak, T. Zawodzinski, S.-T. Myung, *J. Power Sources* **2020**, *452*, 227824.
- [19] H. Gao, W. Ma, W. Yang, J. Wang, J. Niu, F. Luo, Z. Peng, Z. Zhang, *J. Power Sources* **2018**, *379*, 1–9.
- [20] S.-M. Bak, Z. Shadike, R. Lin, X. Yu, X.-Q. Yang, *NPG Asia Mater.* **2018**, *10*, 563–580.
- [21] R. D. Marco, J.-P. Veder, *TrAC Trends Anal. Chem.* **2010**, *29*, 528–537.
- [22] L. Wang, J. Wang, P. Zuo, *Small Methods* **2018**, *2*, 1700293.
- [23] J. Nelson Weker, M. F. Toney, *Adv. Funct. Mater.* **2015**, *25*, 1622–1637.
- [24] P. Harks, F. Mulder, P. Notten, *J. Power Sources* **2015**, *288*, 92–105.
- [25] J. Conder, C. Marino, P. Novák, C. Villevieille, *J. Mater. Chem. A* **2018**, *6*, 3304–3327.
- [26] R. R. Chianelli, *J. Electrochem. Soc.* **1978**, *125*, 1563.
- [27] M. S. Whittingham, *Science* **1976**, *192*, 1126–1127.
- [28] B. M. Weckhuysen, *Phys. Chem. Chem. Phys.* **2003**, *5*, 4351–4360.
- [29] M. A. Bañares, M. O. Guerrero-Pérez, J. L. G. Fierro, G. G. Cortez, *J. Mater. Chem.* **2002**, *12*, 3337–3342.
- [30] M. Bañares, I. Wachs, *J. Raman Spectrosc.* **2002**, *33*, 359–380.
- [31] M. Guerrero-Pérez, M. Bañares, *Chem. Commun.* **2002**, *12*, 1292–1293.
- [32] C. Giacovazzo, H. L. Monaco, D. Viterbo, F. Scordari, G. Gilli, G. Zanotti, M. Catti, *Fundamentals of crystallography*, Vol. 7, Oxford University Press Oxford, **2002**.
- [33] C. Suryanarayana, M. G. Norton, *X-Ray Diffraction*, Springer, **1998**.
- [34] T. Egami, S. J. Billinge, *Underneath the Bragg peaks: structural analysis of complex materials*, Newnes, **2012**.
- [35] H. Gao, X. Yan, J. Niu, Y. Zhang, M. Song, Y. Shi, W. Ma, J. Qin, Z. Zhang, *Chem. Eng. J.* **2020**, *388*, 124299.
- [36] M. Povia, J. Sottmann, G. Portale, K. D. Knudsen, S. Margadonna, S. Sartori, *J. Phys. Chem. C* **2018**, *122*, 5917–5923.
- [37] H. Gao, J. Niu, C. Zhang, Z. Peng, Z. Zhang, *ACS Nano* **2018**, *12*, 3568–3577.
- [38] M. Arnaiz, J. L. Gómez-Cámer, J. Ajuria, F. Bonilla, B. Acebedo, M. Jáuregui, E. Goikolea, M. Galceran, T. Rojo, *Chem. Mater.* **2018**, *30*, 8155–8163.
- [39] L. Zhang, X. Hu, C. Chen, H. Guo, X. Liu, G. Xu, H. Zhong, S. Cheng, P. Wu, J. Meng, *Adv. Mater.* **2017**, *29*, 1604708.
- [40] J. Sottmann, M. Di Michiel, H. Fjellvåg, L. Malavasi, S. Margadonna, P. Vajeeston, G. B. Vaughan, D. S. Wragg, *Angew. Chem. Int. Ed.* **2017**, *56*, 11385–11389; *Angew. Chem.* **2017**, *129*, 11543–11547.
- [41] C.-H. Lim, B. Selvaraj, Y.-F. Song, C.-C. Wang, J.-T. Jin, S.-S. Huang, C.-H. Chuang, H.-S. Sheu, Y.-F. Liao, N.-L. Wu, *J. Mater. Chem. A* **2017**, *5*, 21536–21541.
- [42] J. Sottmann, M. Herrmann, P. Vajeeston, Y. Hu, A. Ruud, C. Drathen, H. Emerich, H. Fjellvåg, D. S. Wragg, *Chem. Mater.* **2016**, *28*, 2750–2756.
- [43] P. K. Allan, J. M. Griffin, A. Darwiche, O. J. Borkiewicz, K. M. Wiaderek, K. W. Chapman, A. J. Morris, P. J. Chupas, L. Monconduit, C. P. Grey, *J. Am. Chem. Soc.* **2016**, *138*, 2352–2365.
- [44] J. K. Mathiesen, R. Väli, M. Härmas, E. Lust, J. Fold von Bülow, K. M. Ø. Jensen, P. Norby, *J. Mater. Chem. A* **2019**, *7*, 11709–11717.
- [45] A. Beda, C. Villevieille, P.-L. Taberna, P. Simon, C. M. Ghimbeu, *J. Mater. Chem. A* **2020**, *8*, 5558–5571.
- [46] H.-J. Liang, B.-H. Hou, W.-H. Li, Q.-L. Ning, X. Yang, Z.-Y. Gu, X.-J. Nie, G. Wang, X.-L. Wu, *Energy Environ. Sci.* **2019**, *12*, 3575–3584.
- [47] L. Seidl, N. Bucher, E. Chu, S. Hartung, S. Martens, O. Schneider, U. Stimming, *Energy Environ. Sci.* **2017**, *10*, 1631–1642.
- [48] T. Yang, X. Niu, T. Qian, X. Shen, J. Zhou, N. Xu, C. Yan, *Nanoscale* **2016**, *8*, 15497–15504.
- [49] H. Kim, J. Hong, G. Yoon, H. Kim, K.-Y. Park, M.-S. Park, W.-S. Yoon, K. Kang, *Energy Environ. Sci.* **2015**, *8*, 2963–2969.
- [50] Y. Lee, C.-H. Jo, J.-K. Yoo, J. U. Choi, W. Ko, H. Park, J. H. Jo, D. O. Shin, S.-T. Myung, J. Kim, *Energy Storage Mater.* **2020**, *24*, 458–466.
- [51] X.-M. Lin, J.-H. Chen, J.-J. Fan, Y. Ma, P. Radjenovic, Q.-C. Xu, L. Huang, S. Passerini, Z.-Q. Tian, J.-F. Li, *Adv. Energy Mater.* **2019**, *9*, 1902312.
- [52] Z. Chen, X. Cheng, H. Yu, H. Zhu, R. Zheng, T. Liu, J. Zhang, M. Shui, J. Shu, *Ceram. Int.* **2018**, *44*, 17094–17101.
- [53] C. Dong, J. Liang, Y. He, C. Li, X. Chen, L. Guo, F. Tian, Y. Qian, L. Xu, *ACS Nano* **2018**, *12*, 8277–8287.
- [54] L. Wang, J. Wang, F. Guo, L. Ma, Y. Ren, T. Wu, P. Zuo, G. Yin, J. Wang, *Nano Energy* **2018**, *43*, 184–191.
- [55] G.-L. Xu, T. Sheng, L. Chong, T. Ma, C.-J. Sun, X. Zuo, D.-J. Liu, Y. Ren, X. Zhang, Y. Liu, *Nano Lett.* **2017**, *17*, 953–962.
- [56] X. Ou, X. Liang, F. Zheng, P. Wu, Q. Pan, X. Xiong, C. Yang, M. Liu, *Electrochim. Acta* **2017**, *258*, 1387–1396.

- [57] X. Ou, J. Li, F. Zheng, P. Wu, Q. Pan, X. Xiong, C. Yang, M. Liu, *J. Power Sources* **2017**, *343*, 483–491.
- [58] Z. Huang, H. Hou, C. Wang, S. Li, Y. Zhang, X. Ji, *Chem. Mater.* **2017**, *29*, 7313–7322.
- [59] P. Bleith, H. Kaiser, P. Novák, C. Villevieille, *Electrochim. Acta* **2015**, *176*, 18–21.
- [60] J. Fullenwarth, A. Darwiche, A. Soares, B. Donnadié, L. Monconduit, *J. Mater. Chem. A* **2014**, *2*, 2050–2059.
- [61] E. Edison, P. K. Gogoi, Y. Zheng, S. Sreejith, S. J. Pennycook, C. T. Lim, M. Srinivasan, *ACS Appl. Mater. Interfaces* **2019**, *11*, 20082–20090.
- [62] X. Shi, S.-L. Chen, H.-N. Fan, X.-H. Chen, D. Yuan, Q. Tang, A. Hu, W.-B. Luo, H.-K. Liu, *ChemSusChem* **2019**, *12*, 4046–4053.
- [63] X. Ou, C. Yang, X. Xiong, F. Zheng, Q. Pan, C. Jin, M. Liu, K. Huang, *Adv. Funct. Mater.* **2017**, *27*, 1606242.
- [64] J. Sottmann, R. Homs-Regojo, D. S. Wragg, H. Fjellvåg, S. Margadonna, H. Emerich, *J. Appl. Crystallogr.* **2016**, *49*, 1972–1981.
- [65] A. Darwiche, M. Toiron, M. T. Sougrati, B. Fraisse, L. Stievano, L. Monconduit, *J. Power Sources* **2015**, *280*, 588–592.
- [66] L. Baggetto, H.-Y. Hah, C. E. Johnson, C. A. Bridges, J. A. Johnson, G. M. Veith, *Phys. Chem. Chem. Phys.* **2014**, *16*, 9538–9545.
- [67] K. Liu, S. Tan, J. Moon, C. J. Jafta, C. Li, T. Kobayashi, H. Lyu, C. A. Bridges, S. Men, W. Guo, *Adv. Energy Mater.* **2020**.
- [68] X. Cao, H. Li, Y. Qiao, X. Li, M. Jia, J. Cabana, H. Zhou, *Adv. Energy Mater.* **2020**, 1903785.
- [69] E. Marelli, C. Marino, C. Bolli, C. Villevieille, *J. Power Sources* **2019**, *450*, 227617.
- [70] F. Ding, C. Zhao, D. Zhou, Q. Meng, D. Xiao, Q. Zhang, Y. Niu, Y. Li, X. Rong, Y. Lu, L. Chen, Y.-S. Hu, *Energy Storage Mater.* **2020**, *30*, 420–430.
- [71] A. Kulka, C. Marino, K. Walczak, C. Borca, C. Bolli, P. Novák, C. Villevieille, *J. Mater. Chem. A* **2020**, *8*, 6022–6033.
- [72] C. Heubner, B. Matthey, T. Lein, F. Wolke, T. Liebmann, C. Lämmel, M. Schneider, M. Herrmann, A. Michaelis, *Energy Storage Mater.* **2020**, *27*, 377–386.
- [73] Y. Zhu, W. Nie, P. Chen, Y. Zhou, Y. Xu, *Int. J. Energy Res.* **2020**, *44*, 3253–3259.
- [74] Y. Yu, W. Kong, Q. Li, D. Ning, G. Schuck, G. Schumacher, C. Su, X. Liu, *ACS Appl. Mater. Interfaces* **2020**, *3*, 933–942.
- [75] D. Goonetilleke, S. Wang, E. Gonzalo, M. Galcerán, D. Saurel, S. J. Day, F. Fauth, T. Rojo, N. Sharma, *J. Mater. Chem. A* **2019**, *7*, 12115–12125.
- [76] A. J. Perez, G. I. Rousse, J.-M. Tarascon, *Inorg. Chem.* **2019**, *58*, 15644–15651.
- [77] J. W. Somerville, A. Sobkowiak, N. Tapia-Ruiz, J. Billaud, J. G. Lozano, R. A. House, L. C. Gallington, T. Ericsson, L. Häggström, M. R. Roberts, *Energy Environ. Sci.* **2019**, *12*, 2223–2232.
- [78] Y. Xiao, Y.-F. Zhu, H.-R. Yao, P.-F. Wang, X.-D. Zhang, H. Li, X. Yang, L. Gu, Y.-C. Li, T. Wang, Y.-X. Yin, X.-D. Guo, B.-H. Zhong, Y.-G. Guo, *Adv. Energy Mater.* **2019**, *9*, 1803978.
- [79] D. Sehwat, S. Cheong, A. Rawal, A. M. Glushenkov, H. E. A. Brand, B. Cowie, E. Gonzalo, T. Rojo, P. J. P. Naeyaert, C. D. Ling, M. Avdeev, N. Sharma, *CrystEngComm* **2019**, *21*, 172–181.
- [80] Q. Liu, Z. Hu, M. Chen, C. Zou, H. Jin, S. Wang, Q. Gu, S. Chou, *J. Mater. Chem. A* **2019**, *7*, 9215–9221.
- [81] Y. Wen, J. Fan, C. Shi, P. Dai, Y. Hong, R. Wang, L. Wu, Z. Zhou, J. Li, L. Huang, S.-G. Sun, *Nano Energy* **2019**, *60*, 162–170.
- [82] W. Kong, H. Wang, L. Sun, C. Su, X. Liu, *Appl. Surf. Sci.* **2019**, *497*, 143814.
- [83] S. Kjeldgaard, S. Birgisson, A. G. Kielland, B. B. Iversen, *J. Appl. Crystallogr.* **2018**, *51*, 1304–1310.
- [84] X. Chen, S. Hwang, R. Chisnell, Y. Wang, F. Wu, S. Kim, J. W. Lynn, D. Su, X. Li, *Adv. Funct. Mater.* **2018**, *28*, 1803896.
- [85] N. Su, Y. Lyu, B. Guo, *Electrochem. Commun.* **2018**, *87*, 71–75.
- [86] E. Marelli, C. Villevieille, S. Park, N. Héroult, C. Marino, *ACS Appl. Mater. Interfaces* **2018**, *1*, 5960–5967.
- [87] L. Yang, X. Li, X. Ma, S. Xiong, P. Liu, Y. Tang, S. Cheng, Y.-Y. Hu, M. Liu, H. Chen, *J. Power Sources* **2018**, *381*, 171–180.
- [88] X. Zhang, K. Jiang, S. Guo, X. Mu, X. Zhang, P. He, M. Han, H. Zhou, *Chem. Commun.* **2018**, *54*, 12167–12170.
- [89] Y. Xiao, P.-F. Wang, Y.-X. Yin, Y.-F. Zhu, Y.-B. Niu, X.-D. Zhang, J. Zhang, X. Yu, X.-D. Guo, B.-H. Zhong, Y.-G. Guo, *Adv. Mater.* **2018**, *30*, 1803765.
- [90] L. Sun, Y. Xie, X.-Z. Liao, H. Wang, G. Tan, Z. Chen, Y. Ren, J. Gim, W. Tang, Y.-S. He, K. Amine, Z.-F. Ma, *Small* **2018**, *14*, 1704523.
- [91] P. F. Wang, H. R. Yao, Y. You, Y. G. Sun, Y. X. Yin, Y. G. Guo, *Nano Res.* **2018**, *11*, 3258–3271.
- [92] S. N. Lou, N. Sharma, D. Goonetilleke, W. H. Saputera, T. M. Leoni, P. Brockbank, S. Lim, D. W. Wang, J. Scott, R. Amal, *Adv. Energy Mater.* **2017**, *7*, 1700545.
- [93] H. Ma, H. Su, K. Amine, X. Liu, S. Jaffer, T. Shang, L. Gu, H. Yu, *Nano Energy* **2018**, *43*, 1–10.
- [94] H. Dai, C. Yang, X. Ou, X. Liang, H. Xue, W. Wang, G. Xu, *Electrochim. Acta* **2017**, *257*, 146–154.
- [95] K. Kubota, Y. Yoda, S. Komaba, *J. Electrochem. Soc.* **2017**, *164*, A2368–A2373.
- [96] L. Wang, J. Wang, X. Zhang, Y. Ren, P. Zuo, G. Yin, J. Wang, *Nano Energy* **2017**, *34*, 215–223.
- [97] H.-R. Yao, P.-F. Wang, Y. Gong, J. Zhang, X. Yu, L. Gu, C. OuYang, Y.-X. Yin, E. Hu, X.-Q. Yang, E. Stavitski, Y.-G. Guo, L.-J. Wan, *J. Am. Chem. Soc.* **2017**, *139*, 8440–8443.
- [98] P.-F. Wang, H.-R. Yao, X.-Y. Liu, J.-N. Zhang, L. Gu, X.-Q. Yu, Y.-X. Yin, Y.-G. Guo, *Adv. Mater.* **2017**, *29*, 1700210.
- [99] Y. Xie, H. Wang, G. Xu, J. Wang, H. Sheng, Z. Chen, Y. Ren, C. J. Sun, J. Wen, J. Wang, *Adv. Energy Mater.* **2016**, *6*, 1601306.
- [100] X. Ou, X. Xiong, F. Zheng, C. Yang, Z. Lin, R. Hu, C. Jin, Y. Chen, M. Liu, *J. Power Sources* **2016**, *325*, 410–416.
- [101] K. Kubota, T. Asari, H. Yoshida, N. Yaabuuchi, H. Shiiba, M. Nakayama, S. Komaba, *Adv. Funct. Mater.* **2016**, *26*, 6047–6059.
- [102] J. Wang, X. He, D. Zhou, F. Schappacher, X. Zhang, H. Liu, M. C. Stan, X. Cao, R. Kloepsch, M. S. Sofy, G. Schumacher, J. Li, *J. Mater. Chem. A* **2016**, *4*, 3431–3437.
- [103] S. Hartung, N. Bucher, R. Bucher, M. Srinivasan, *Rev. Sci. Instrum.* **2015**, *86*, 086102.
- [104] Y. H. Jung, A. S. Christiansen, R. E. Johnsen, P. Norby, D. K. Kim, *Adv. Funct. Mater.* **2015**, *25*, 3227–3237.
- [105] B. M. de Boisse, J.-H. Cheng, D. Carlier, M. Guignard, C.-J. Pan, S. Bordere, D. Filimonov, C. Drathen, E. Suard, B.-J. Hwang, *J. Mater. Chem. A* **2015**, *3*, 10976–10989.
- [106] L. Mu, S. Xu, Y. Li, Y. S. Hu, H. Li, L. Chen, X. Huang, *Adv. Mater.* **2015**, *27*, 6928–6933.
- [107] N. Sharma, N. Tapia-Ruiz, G. Singh, A. R. Armstrong, J. C. Pramudita, H. E. A. Brand, J. Billaud, P. G. Bruce, T. Rojo, *Chem. Mater.* **2015**, *27*, 6976–6986.
- [108] E. Talaie, V. Duffort, H. L. Smith, B. Fultz, L. F. Nazar, *Energy Environ. Sci.* **2015**, *8*, 2512–2523.
- [109] Y. Shen, E. E. Pedersen, M. Christensen, B. B. Iversen, *Rev. Sci. Instrum.* **2014**, *85*, 104103.
- [110] M. H. Han, E. Gonzalo, M. Casas-Cabanas, T. Rojo, *J. Power Sources* **2014**, *258*, 266–271.
- [111] M. Guignard, C. Didier, J. Darriet, P. Bordet, E. Elkaïm, C. Delmas, *Nat. Mater.* **2013**, *12*, 74–80.
- [112] Y.-N. Zhou, J.-J. Ding, K.-W. Nam, X. Yu, S.-M. Bak, E. Hu, J. Liu, J. Bai, H. Li, Z.-W. Fu, *J. Mater. Chem. A* **2013**, *1*, 11130–11134.
- [113] Y. Xiao, Y. F. Zhu, W. Xiang, Z. G. Wu, Y. C. Li, J. Lai, S. Li, E. Wang, Z. G. Yang, C. L. Xu, B. H. Zhong, X. D. Guo, *Angew. Chem. Int. Ed.* **2020**, *59*, 1491–1495.
- [114] J. Wang, R. Gao, L. Zheng, Z. Chen, Z. Wu, L. Sun, Z. Hu, X. Liu, *ACS Catal.* **2018**, *8*, 8953–8960.
- [115] C. Liu, D. Rehnlund, W. R. Brant, J. Zhu, T. R. Gustafsson, R. Younesi, *ACS Energy Lett.* **2017**, *2*, 2440–2444.
- [116] R. Pinedo, D. A. Weber, B. Bergner, D. Schröder, P. Adelhelm, J. Janek, *J. Phys. Chem. C* **2016**, *120*, 8472–8481.
- [117] Y.-X. Wang, J. Yang, W. Lai, S.-L. Chou, Q.-F. Gu, H. K. Liu, D. Zhao, S. X. Dou, *J. Am. Chem. Soc.* **2016**, *138*, 16576–16579.
- [118] T. Zhu, P. Hu, C. Cai, Z. Liu, G. Hu, Q. Kuang, L. Mai, L. Zhou, *Nano Energy* **2020**, *70*, 104548.
- [119] M. V. Zakharkin, O. A. Drozhzhin, S. V. Ryazantsev, D. Chernyshov, M. A. Kirsanova, I. V. Mikhchev, E. M. Pazhetnov, E. V. Antipov, K. J. Stevenson, *J. Power Sources* **2020**, *470*, 228231.
- [120] M. Zarrabeitia, M. A. Jáuregui, N. Sharma, J. C. Pramudita, M. Casas-Cabanas, *Chem. Mater.* **2019**, *31*, 5152–5159.
- [121] F. Chen, V. M. Kovrugin, R. David, O. Mentre, F. Fauth, J. N. Chotard, C. Masquelier, *Small Methods* **2019**, *3*, 1800218.
- [122] M. Galceran, J. Rikarte, M. Zarrabeitia, M. C. Pujol, M. Aguiló, M. Casas-Cabanas, *ACS Appl. Mater. Interfaces* **2019**, *2*, 1923–1931.
- [123] L. H. B. Nguyen, J. Olchowka, S. Belin, P. Sanz Camacho, M. Duttine, A. Iadecola, F. Fauth, D. Carlier, C. Masquelier, L. Croguennec, *ACS Appl. Mater. Interfaces* **2019**, *11*, 38808–38818.
- [124] D. Burova, I. Shakhova, P. Morozova, A. Iarchuk, O. A. Drozhzhin, M. G. Rozova, S. Praneetha, V. Murugan, J.-M. Tarascon, A. M. Abakumov, *RSC Adv.* **2019**, *9*, 19429–19440.

- [125] M. Chen, D. Cortie, Z. Hu, H. Jin, S. Wang, Q. Gu, W. Hua, E. Wang, W. Lai, L. Chen, S.-L. Chou, X.-L. Wang, S.-X. Dou, *Adv. Energy Mater.* **2018**, *8*, 1800944.
- [126] S. Y. Kim, D. Kundu, L. F. Nazar, *Adv. Energy Mater.* **2018**, *8*, 1701729.
- [127] G. Santoro, J. M. Amarilla, P. Tartaj, M. B. Vázquez-Santos, *Mater. Today* **2018**, *10*, 23–27.
- [128] M. V. Zakharkin, O. A. Drozhzhin, I. V. Tereshchenko, D. Chernyshov, A. M. Abakumov, E. V. Antipov, K. J. Stevenson, *ACS Appl. Mater. Interfaces* **2018**, *10*, 23–27.
- [129] D. Saurel, M. Galceran, M. Reynaud, H. Anne, M. Casas-Cabanas, *Int. J. Energy Res.* **2018**, *42*, 3258–3265.
- [130] Y. Qi, Z. Tong, J. Zhao, L. Ma, T. Wu, H. Liu, C. Yang, J. Lu, Y.-S. Hu, *Joule* **2018**, *2*, 2348–2363.
- [131] V. M. Kovrugin, J.-N. Chotard, F. Fauth, A. Jamali, R. David, C. Masquelier, *J. Mater. Chem. A* **2017**, *5*, 14365–14376.
- [132] M. Bianchini, P. Xiao, Y. Wang, G. Ceder, *Adv. Energy Mater.* **2017**, *7*, 1700514.
- [133] R. Liu, G. Xu, Q. Li, S. Zheng, G. Zheng, Z. Gong, Y. Li, E. Kruskop, R. Fu, Z. Chen, K. Amine, Y. Yang, *ACS Appl. Mater. Interfaces* **2017**, *9*, 43632–43639.
- [134] R. Essehli, H. Ben Yahia, K. Maher, M. T. Sougrati, A. Abouimrane, J. B. Park, Y. K. Sun, M. A. Al-Maadeed, I. Belharouak, *J. Power Sources* **2016**, *324*, 657–664.
- [135] J. C. Pramudita, R. Aughterson, W. M. Dose, S. W. Donne, H. E. Brand, N. Sharma, *J. Mater. Res.* **2015**, *30*, 381–389.
- [136] J. Wang, B. Qiu, X. He, T. Risthaus, H. Liu, M. C. Stan, S. Schulze, Y. Xia, Z. Liu, M. Winter, J. Li, *Chem. Mater.* **2015**, *27*, 4374–4379.
- [137] P. Serras, V. Palomares, T. Rojo, H. E. Brand, N. Sharma, *J. Mater. Chem. A* **2014**, *2*, 7766–7779.
- [138] M. Galceran, D. Saurel, B. Acebedo, V. V. Roddatis, E. Martin, T. Rojo, M. Casas-Cabanas, *Phys. Chem. Chem. Phys.* **2014**, *16*, 8837–8842.
- [139] J. Gaubicher, F. Boucher, P. Moreau, M. Cuisinier, P. Soudan, E. Elkaim, D. Guyomard, *Electrochem. Commun.* **2014**, *38*, 104–106.
- [140] X. Yu, H. Pan, W. Wan, C. Ma, J. Bai, Q. Meng, S. N. Ehrlich, Y.-S. Hu, X.-Q. Yang, *Nano Lett.* **2013**, *13*, 4721–4727.
- [141] C. Wang, D. Du, M. Song, Y. Wang, F. Li, *Adv. Energy Mater.* **2019**, *9*, 1900022.
- [142] J. Li, X. He, S. Ostendorp, L. Zhang, X. Hou, D. Zhou, B. Yan, D. M. Meira, Y. Yang, H. Jia, *Electrochim. Acta* **2020**, *342*, 135928.
- [143] Y. Tang, W. Li, P. Feng, M. Zhou, K. Wang, Y. Wang, K. Zaghbi, K. Jiang, *Adv. Funct. Mater.* **2020**, *30*, 1908754.
- [144] B. Xie, L. Wang, J. Shu, X. Zhou, Z. Yu, H. Huo, Y. Ma, X. Cheng, G. Yin, P. Zuo, *ACS Appl. Mater. Interfaces* **2019**, *11*, 46705–46713.
- [145] W. Tang, Y. Xie, F. Peng, Y. Yang, F. Feng, X. Z. Liao, Y. S. He, Z. F. Ma, Z. Chen, Y. Ren, *J. Electrochem. Soc.* **2018**, *165*, A3910–A3917.
- [146] J. Sottmann, F. L. M. Bernal, K. V. Yuseenko, M. Herrmann, H. Emerich, D. S. Wragg, S. Margadonna, *Electrochim. Acta* **2016**, *200*, 305–313.
- [147] J. C. Pramudita, S. Schmid, T. Godfrey, T. Whittle, M. Alam, T. Hanley, H. E. Brand, N. Sharma, *Phys. Chem. Chem. Phys.* **2014**, *16*, 24178–24187.
- [148] Z. Dai, U. Mani, H. T. Tan, Q. Yan, *Small Methods* **2017**, *1*, 1700098.
- [149] C. Delmas, C. Fouassier, P. Hagenmuller, *Physica B + C* **1980**, *99*, 81–85.
- [150] M. Bianchini, J. Wang, R. J. Clément, B. Ouyang, P. Xiao, D. Kitchaev, T. Shi, Y. Zhang, Y. Wang, H. Kim, M. Zhang, J. Bai, F. Wang, W. Sun, G. Ceder, *Nat. Mater.* **2020**, *19*, 1088–1095.
- [151] M. H. Han, E. Gonzalo, G. Singh, T. Rojo, *Energy Environ. Sci.* **2015**, *8*, 81–102.
- [152] N. Yabuuchi, K. Kubota, M. Dahbi, S. Komaba, *Chem. Rev.* **2014**, *114*, 11636–11682.
- [153] J. Kim, D.-H. Seo, H. Kim, I. Park, J.-K. Yoo, S.-K. Jung, Y.-U. Park, W. A. Goddard III, K. Kang, *Energy Environ. Sci.* **2015**, *8*, 540–545.
- [154] S.-M. Oh, S.-T. Myung, J. Hassoun, B. Scrosati, Y.-K. Sun, *Electrochem. Commun.* **2012**, *22*, 149–152.
- [155] Y. Zhu, Y. Xu, Y. Liu, C. Luo, C. Wang, *Nanoscale* **2013**, *5*, 780–787.
- [156] H.-W. Lee, R. Y. Wang, M. Pasta, S. W. Lee, N. Liu, Y. Cui, *Nat. Commun.* **2014**, *5*, 1–6.
- [157] A. Ponrouch, A. Goñi, M. R. Palacin, *Electrochem. Commun.* **2013**, *27*, 85–88.
- [158] X. Dou, I. Hasa, D. Saurel, C. Vaalma, L. Wu, D. Buchholz, D. Bresser, S. Komaba, S. Passerini, *Mater. Today* **2019**, *23*, 87–104.
- [159] D. Stevens, J. Dahn, *J. Electrochem. Soc.* **2001**, *148*, A803.
- [160] D. Stevens, J. Dahn, *J. Electrochem. Soc.* **2000**, *147*, 4428.
- [161] S. Alvin, D. Yoon, C. Chandra, H. S. Cahyadi, J.-H. Park, W. Chang, K. Y. Chung, J. Kim, *Carbon* **2019**, *145*, 67–81.
- [162] Z. V. Bobyleva, O. A. Drozhzhin, K. A. Dosaev, A. Kamiyama, S. V. Ryazantsev, S. Komaba, E. V. Antipov, *Electrochim. Acta* **2020**, *354*, 136647.
- [163] M. Anji Reddy, M. Helen, A. Groß, M. Fichtner, H. Euchner, *ACS Energy Lett.* **2018**, *3*, 2851–2857.
- [164] M. Fukunishi, N. Yabuuchi, M. Dahbi, J.-Y. Son, Y. Cui, H. Oji, S. Komaba, *J. Phys. Chem. C* **2016**, *120*, 15017–15026.
- [165] L. Liang, Y. Xu, C. Wang, L. Wen, Y. Fang, Y. Mi, M. Zhou, H. Zhao, Y. Lei, *Energy Environ. Sci.* **2015**, *8*, 2954–2962.
- [166] N. K. Karan, M. D. Slater, F. Dogan, D. Kim, C. S. Johnson, M. Balasubramanian, *J. Electrochem. Soc.* **2014**, *161*, A1107.
- [167] D. Dixon, M. Ávila, H. Ehrenberg, A. Bhaskar, *ACS Omega* **2019**, *4*, 9731–9738.
- [168] M.-K. Kim, S.-H. Yu, A. Jin, J. Kim, I.-H. Ko, K.-S. Lee, J. Mun, Y.-E. Sung, *Chem. Commun.* **2016**, *52*, 11775–11778.
- [169] C. Guhl, P. Kehne, Q. Ma, F. Tietz, L. Alff, P. Komissinskiy, W. Jaegermann, R. Hausbrand, *Rev. Sci. Instrum.* **2018**, *89*, 073104.
- [170] M. Fehse, D. Bessas, A. Darwiche, A. Mahmoud, G. Rahamim, C. La Fontaine, R. P. Hermann, D. Zitoun, L. Monconduit, L. Stievano, *Batteries & Supercaps* **2019**, *2*, 66–73.
- [171] J. Sottmann, M. Herrmann, P. Vajeeston, A. Ruud, C. Drathen, H. Emerich, D. S. Wragg, H. Fjellvåg, *Chem. Mater.* **2017**, *29*, 2803–2810.
- [172] T. Broux, T. Bamine, L. Simonelli, L. Stievano, F. O. Fauth, M. Ménétrier, D. Carlier, C. Masquelier, L. Croguennec, *J. Phys. Chem.* **2017**, *121*, 4103–4111.
- [173] M. Pivko, I. Arcon, M. Bele, R. Dominko, M. Gaberscek, *J. Power Sources* **2012**, *216*, 145–151.
- [174] W. Tang, X. Song, Y. Du, C. Peng, M. Lin, S. Xi, B. Tian, J. Zheng, Y. Wu, F. Pan, K. P. Loh, *J. Mater. Chem. A* **2016**, *4*, 4882–4892.
- [175] Z. Jian, W. Han, X. Lu, H. Yang, Y. S. Hu, J. Zhou, Z. Zhou, J. Li, W. Chen, D. Chen, *Adv. Energy Mater.* **2013**, *3*, 156–160.
- [176] D. Kim, E. Lee, M. Slater, W. Lu, S. Rood, C. S. Johnson, *Electrochem. Commun.* **2012**, *18*, 66–69.
- [177] S.-M. Oh, S.-T. Myung, C. S. Yoon, J. Lu, J. Hassoun, B. Scrosati, K. Amine, Y.-K. Sun, *Nano Lett.* **2014**, *14*, 1620–1626.
- [178] W. Chao, P. Fischer, T. Tyliczczyk, S. Rekawa, E. Anderson, P. Naulleau, *Opt. Express* **2012**, *20*, 9777–9783.
- [179] D. A. Shapiro, Y.-S. Yu, T. Tyliczczyk, J. Cabana, R. Celestre, W. Chao, K. Kaznatcheev, A. D. Kilcoyne, F. Maia, S. Marchesini, *Nat. Photonics* **2014**, *8*, 765.
- [180] R. Falcone, C. Jacobsen, J. Kirz, S. Marchesini, D. Shapiro, J. Spence, *Contemp. Phys.* **2011**, *52*, 293–318.
- [181] J. Nelson Weker, M. F. Toney, *Adv. Funct. Mater.* **2015**, *25*, 1622–1637.
- [182] M. Wolf, B. M. May, J. Cabana, *Chem. Mater.* **2017**, *29*, 3347–3362.
- [183] D. P. Finegan, M. Scheel, J. B. Robinson, B. Tjaden, I. Hunt, T. J. Mason, J. Millichamp, M. Di Michiel, G. J. Offer, G. Hinds, D. J. L. Brett, P. R. Shearing, *Nat. Commun.* **2015**, *6*, 6924.
- [184] S. D. M. Jacques, M. Di Michiel, S. A. J. Kimber, X. Yang, R. J. Cernik, A. M. Beale, S. J. L. Billinge, *Nat. Commun.* **2013**, *4*, 2536.
- [185] G. Harding, J. Kosanetzky, U. Neitzel, *Med. Phys.* **1987**, *14*, 515–525.
- [186] S. W. T. Price, K. Ignatyev, K. Geraki, M. Basham, J. Filik, N. T. Vo, P. T. Witte, A. M. Beale, J. F. W. Mosselmans, *Phys. Chem. Chem. Phys.* **2015**, *17*, 521–529.
- [187] J. Wang, L. Wang, C. Eng, J. Wang, *Adv. Energy Mater.* **2017**, *7*, 1602706.
- [188] Z. Yu, J. Wang, L. Wang, Y. Xie, S. Lou, Z. Jiang, Y. Ren, S. Lee, P. Zuo, H. Huo, G. Yin, Q. Pan, J. Wang, *ACS Energy Lett.* **2019**, *4*, 2007–2012.
- [189] J. Sottmann, R. Homs-Regojo, D. S. Wragg, H. Fjellvåg, S. Margadonna, H. Emerich, *J. Appl. Crystallogr.* **2016**, *49*, 1972–1981.
- [190] M. Herklotz, J. Weiss, E. Ahrens, M. Yavuz, L. Mereacre, N. Kiziltas-Yavuz, C. Drager, H. Ehrenberg, J. Eckert, F. Fauth, L. Giebeler, M. Knapp, *J. Appl. Crystallogr.* **2016**, *49*, 340–345.
- [191] F. Rosciano, M. Holzapfel, H. Kaiser, W. Scheifele, P. Ruch, M. Hahn, R. Kotz, P. Novak, *J. Synchrotron Radiat.* **2007**, *14*, 487–491.
- [192] C. Villevieille, T. Sasaki, P. Novak, *RSC Adv.* **2014**, *4*, 6782–6789.
- [193] O. J. Borkiewicz, B. Shyam, K. M. Wiaderek, C. Kurtz, P. J. Chupas, K. W. Chapman, *J. Appl. Crystallogr.* **2012**, *45*, 1261–1269.
- [194] J. B. Leriche, S. Hamelet, J. Shu, M. Morcrette, C. Masquelier, G. Ouvrard, M. Zerrouki, P. Soudan, S. Belin, E. Elkaïm, F. Baudalet, *J. Electrochem. Soc.* **2010**, *157*, A606–A610.
- [195] C. Baetz, T. Buhrmester, N. N. Bramnik, K. Nikolowski, H. Ehrenberg, *Solid State Ionics* **2005**, *176*, 1647–1652.
- [196] K. Nikolowski, C. Baetz, N. N. Bramnik, H. Ehrenberg, *J. Appl. Crystallogr.* **2005**, *38*, 851–853.

- [197] O. J. Borkiewicz, K. M. Wiaderek, P. J. Chupas, K. W. Chapman, *The J. Phys. Chem. Letters* **2015**, *6*, 2081–2085.
- [198] G. Ouvrard, M. Zerrouki, P. Soudan, B. Lestriez, C. Masquelier, M. Morcrette, S. Hamelet, S. Belin, A. M. Flank, F. Baudelet, *J. Power Sources* **2013**, *229*, 16–21.
- [199] O. J. Borkiewicz, K. W. Chapman, P. J. Chupas, *Phys. Chem. Chem. Phys.* **2013**, *15*, 8466–8469.
- [200] L. H. B. Nguyen, A. Iadecola, S. Belin, J. Olchowka, C. Masquelier, D. Carlier, L. Croguennec, *J. Phys. Chem. C* **2020**, *124*, 23511–23522.
- [201] J. Leriche, S. Hamelet, J. Shu, M. Morcrette, C. Masquelier, G. Ouvrard, M. Zerrouki, P. Soudan, S. Belin, E. Elkaim, *J. Electrochem. Soc.* **2010**, *157*, A606.
- [202] J. Sottmann, V. Pralong, N. Barrier, C. Martin, *J. Appl. Crystallogr.* **2019**, *52*, 485–490.
- [203] K. Rhodes, M. Kirkham, R. Meisner, C. M. Parish, N. Dudney, C. Daniel, *Rev. Sci. Instrum.* **2011**, *82*, 075107.
- [204] P. Bleith, W. van Beek, H. Kaiser, P. Novák, C. Villevieille, *J. Phys. Chem. C* **2015**, *119*, 3466–3471.
- [205] H. Liu, P. K. Allan, O. J. Borkiewicz, C. Kurtz, C. P. Grey, K. W. Chapman, P. J. Chupas, *J. Appl. Crystallogr.* **2016**, *49*, 1665–1673.
- [206] J. Sottmann, M. Di Michiel, H. Fjellvåg, L. Malavasi, S. Margadonna, P. Vajeeston, G. B. M. Vaughan, D. S. Wragg, *Angew. Chem. Int. Ed.* **2017**, *56*, 11385–11389; *Angew. Chem.* **2017**, *129*, 11543–11547.
- [207] J. Nelson, S. Misra, Y. Yang, A. Jackson, Y. Liu, H. Wang, H. Dai, J. C. Andrews, Y. Cui, M. F. Toney, *JACS* **2012**, *134*, 6337–6343.
- [208] D. Verhoeven, *Appl. Opt.* **1993**, *32*, 3736–3754.
- [209] P. Norby, *J. Am. Chem. Soc.* **1997**, *119*, 5215–5221.
- [210] M. A. Newton, W. van Beek, *Chem. Soc. Rev.* **2010**, *39*, 4845–4863.
- [211] J. Hanson, P. Norby, in *In-situ Characterization of Heterogeneous Catalysts*, Wiley Online Library, **2013**, pp. 121–146.
- [212] N. Döbelin, “XrdBatch Manual”, can be found under <http://www.doe-belien.org/nic/tools/xrdbatch/xrdbatch01.pdf>, **2009**.
- [213] J. Rodríguez-Carvajal, in *Abstracts of the Satellite Meeting on Powder Diffraction of the XV Congress of the IUCr*, Toulouse, France, **1990**, p. 127.
- [214] P. Rajiv, R. E. Dinnebier, M. Jansen, *Mater. Sci. Forum* **2010**, *651*, 97–104.
- [215] B. Ravel, M. Newville, *J. Synchrotron Radiat.* **2005**, *12*, 537–541.
- [216] N. K. Karan, M. D. Slater, F. Dogan, D. Kim, C. S. Johnson, M. Balasubramanian, *J. Electrochem. Soc.* **2014**, *161*, A1107–A1115.
- [217] G. W. Stinton, J. S. O. Evans, *J. Appl. Crystallogr.* **2007**, *40*, 87–95.
- [218] A. Ruud, J. Sottmann, P. Vajeeston, H. Fjellvåg, *J. Mater. Chem. A* **2019**, *7*, 17906–17913.
- [219] P. B. Samarasingha, J. Sottmann, S. Margadonna, H. Emerich, O. Nilsen, H. Fjellvåg, *Acta Mater.* **2016**, *116*, 290–297.
- [220] J. Sottmann, R. Homs-Regojo, D. S. Wragg, H. Fjellvåg, S. Margadonna, H. Emerich, *J. Appl. Crystallogr.* **2016**, *49*, 1972–1981.
- [221] D. S. Wragg, M. G. O’Brien, M. Di Michiel, F. Lønstad-Bleken, *J. Appl. Crystallogr.* **2015**, *48*, 1719–1728.
- [222] G. Agostini, C. Lamberti, L. Palin, M. Milanesio, N. Danilina, B. Xu, M. Janousch, J. A. Van Bokhoven, *J. Am. Chem. Soc.* **2010**, *132*, 667–678.
- [223] A. Vamvakeros, A. A. Coelho, D. Matras, H. Dong, Y. Odarchenko, S. W. T. Price, K. T. Butler, O. Gutowski, A.-C. Dippel, M. Zimmermann, I. Martens, J. Drnec, A. M. Beale, S. D. M. Jacques, *J. Appl. Crystallogr.* **2020**, *53*, 1531–1541.
- [224] A. Ruud, J. Sottmann, P. Vajeeston, H. Fjellvåg, *Phys. Chem. Chem. Phys.* **2018**, *20*, 29798–29803.
- [225] L. Marbella, M. Evans, M. Groh, J. Nelson, K. Griffith, A. Morris, C. Grey, *J. Am. Chem. Soc.* **2018**, *140*, 7994–8004.
- [226] J. Stratford, M. Mayo, P. Allan, O. Pecher, O. Borkiewicz, K. Wiaderek, K. Chapman, C. Pickard, A. Morris, C. Grey, *J. Am. Chem. Soc.* **2017**, *139*, 7273–7286.
- [227] A. Jain, S. P. Ong, G. Hautier, W. Chen, W. D. Richards, S. Dacek, S. Cholia, D. Gunter, D. Skinner, G. Ceder, K. A. Persson, *APL Mater.* **2013**, *1*, 011002.
- [228] G. Musumarra, G. Scarlata, S. Wold, *Gazz. Chim. Ital.* **1981**, *111*, 499–502.
- [229] R. Caliandro, G. Di Profio, O. Nicolotti, *J. Pharm. Biomed. Anal.* **2013**, *78–79*, 269–279.
- [230] A. Rizzuti, R. Caliandro, V. Gallo, P. Mastroianni, G. Chita, M. Latronico, *Food Chem.* **2013**, *141*, 1908–1915.
- [231] K. W. Chapman, S. H. Lapidus, P. J. Chupas, *J. Appl. Crystallogr.* **2015**, *48*, 1619–1626.
- [232] A. M. C. Davies, T. Fearn, *Spectrosc. Eur.* **2004**, *16*, 20.
- [233] R. Caliandro, V. Toson, L. Palin, E. Conterposito, M. Aceto, V. Gianotti, E. Boccaleri, E. Dooryhee, M. Milanesio, *Chem. Eur. J.* **2019**, *25*, 11503–11511.
- [234] P. Guccione, L. Palin, B. D. Belviso, M. Milanesio, R. Caliandro, *Phys. Chem. Chem. Phys.* **2018**, *20*, 19560–19571.
- [235] E. Conterposito, L. Palin, R. Caliandro, W. van Beek, D. Chernyshov, M. Milanesio, *Acta Crystallogr. Sect. A* **2019**, *75*, 214–222.
- [236] R. Caliandro, D. B. Belviso, *J. Appl. Crystallogr.* **2014**, *47*, 1087–1096.
- [237] A. Darwiche, F. Murgia, M. Fehse, A. Mahmoud, A. Iadecola, S. Belin, C. La Fontaine, V. Briois, R. P. Hermann, B. Fraisse, R. Berthelot, M. T. Sougrati, L. Monconduit, L. Stievano, *Energy Storage Mater.* **2019**, *21*, 1–13.
- [238] L. H. Nguyen, A. Iadecola, S. Belin, J. Olchowka, C. Masquelier, D. Carlier, L. Croguennec, *J. Phys. Chem. C* **2020**, *124*, 23511–23522.
- [239] J. Felten, H. Hall, J. Jaumot, R. Tauler, A. de Juan, A. Gorzsás, *Nat. Protoc.* **2015**, *10*, 217–240.
- [240] H. Motegi, Y. Tsuboi, A. Saga, T. Kagami, M. Inoue, H. Toki, O. Minowa, T. Noda, J. Kikuchi, *Sci. Rep.* **2015**, *5*, 15710.
- [241] M. Garrido, F. X. Rius, M. S. Larrechí, *Anal. Bioanal. Chem.* **2008**, *390*, 2059–2066.
- [242] P. Müller, I. Hermans, *Ind. Eng. Chem. Res.* **2017**, *56*, 1123–1136.
- [243] A. Urakawa, T. Bürgi, A. Baiker, *Chem. Eng. Sci.* **2008**, *63*, 4902–4909.
- [244] D. Chernyshov, V. Dyadkin, W. van Beek, A. Urakawa, *Acta Crystallogr. Sect. A* **2016**, *72*, 500–506.
- [245] D. Chernyshov, I. Dovgaliuk, V. Dyadkin, W. van Beek, *Crystals* **2020**, *10*, 581.
- [246] Z. Jiang, J. Li, Y. Yang, L. Mu, C. Wei, X. Yu, P. Pianetta, K. Zhao, P. Cloetens, F. Lin, Y. Liu, *Nat. Commun.* **2020**, *11*, 2310.
- [247] V. Shapovalov, A. Guda, V. Butova, I. Shukaev, A. Soldatov, *Nanomaterials* **2021**, *11*, 156.
- [248] J.-Q. Huang, X. Guo, J. Huang, H. Tan, X. Du, Y. Zhu, B. Zhang, *J. Power Sources* **2021**, *481*, 228916.
- [249] B. T. Young, D. R. Heskett, C. C. Nguyen, M. Nie, J. C. Woicik, B. L. Lucht, *ACS Appl. Mater. Interfaces* **2015**, *7*, 20004–20011.
- [250] L. A. Ma, A. J. Naylor, L. Nyholm, R. Younesi, *Angew. Chem. Int. Ed.* **2021**, *60*, 4855.
- [251] C. L. Farrow, P. Juhas, J. W. Liu, D. Bryndin, E. S. Božin, J. Bloch, T. Proffen, S. J. L. Billinge, *J. Phys. Condens. Matter* **2007**, *19*, 335219.

Manuscript received: November 30, 2020

Revised manuscript received: February 17, 2021

Accepted manuscript online: February 17, 2021

Version of record online: March 16, 2021

Batteries & Supercaps

Supporting Information

Understanding the (De)Sodiation Mechanisms in Na-Based Batteries through Operando X-Ray Methods

Anders Brennhagen, Carmen Cavallo,* David S. Wragg, Jonas Sottmann, Alexey Y. Kozlov, and Helmer Fjellvåg

Supporting Information

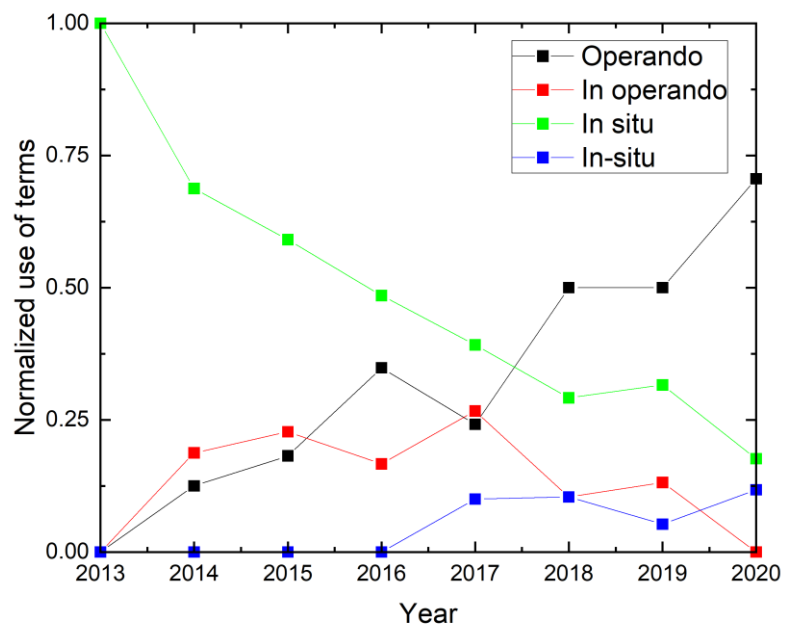


Figure S1. Normalized use of the terms *operando*, *in operando*, *in situ* and *in-situ* to describe scattering/diffraction X-ray techniques applied during electrochemical cycling. Data are collected from the articles in Table 1.

Paper 3

Operando XRD studies on Bi_2MoO_6 as anode material for Na-ion batteries

A. Brennhagen, C. Cavallo, D. S. Wragg, P. Vajeeston, A. O. Sjøstad, A. Y. Kuposov, and H. Fjellvåg

Nanotechnology, **2022**, 33(18), 185402.

3

This article has a corrigendum:

A. Brennhagen, C. Cavallo, D. S. Wragg, P. Vajeeston, A. O. Sjøstad, A. Y. Kuposov and H. Fjellvåg, "Corrigendum: Operando XRD studies on Bi_2MoO_6 as anode material for Na-ion batteries (2022 *Nanotechnology* 33 185402)," *Nanotechnology*, **2022**, 33(35), 359501.

Operando XRD studies on Bi_2MoO_6 as anode material for Na-ion batteries

Anders Brennhagen¹ , Carmen Cavallo^{1,*} , David S. Wragg^{1,2} ,
Ponniiah Vajeeston¹ , Anja O. Sjøstad¹ , Alexey Y. Kopusov^{1,3}  and
Helmer Fjellvåg^{1,*} 

¹ Centre for Material Science and Nanotechnology, Department of Chemistry, University of Oslo, PO Box 1033, Blindern, N-0315, Oslo, Norway

² Norwegian National Resource Centre for x-ray Diffraction and Scattering (RECX), Department of Chemistry, University of Oslo, PO Box 1033, Blindern, N-0315, Oslo, Norway

³ Department of Battery Technology, Institute for Energy Technology (IFE), Instituttveien 18, 2007, Kjeller, Norway

E-mail: carmen.cavallo@smn.uio.no and helmer.fjellvag@kjemi.uio.no

Received 22 November 2021, revised 21 January 2022

Accepted for publication 25 January 2022

Published 10 February 2022



CrossMark

Abstract

Based on the same rocking-chair principle as rechargeable Li-ion batteries, Na-ion batteries are promising solutions for energy storage benefiting from low-cost materials comprised of abundant elements. However, despite the mechanistic similarities, Na-ion batteries require a different set of active materials than Li-ion batteries. Bismuth molybdate (Bi_2MoO_6) is a promising NIB anode material operating through a combined conversion/alloying mechanism. We report an *operando* x-ray diffraction (XRD) investigation of Bi_2MoO_6 -based anodes over 34 (de)sodiation cycles revealing both basic operating mechanisms and potential pathways for capacity degradation. Irreversible conversion of Bi_2MoO_6 to Bi nanoparticles occurs through the first sodiation, allowing Bi to reversibly alloy with Na forming the cubic Na_3Bi phase. Preliminary electrochemical evaluation in half-cells *versus* Na metal demonstrated specific capacities for Bi_2MoO_6 to be close to 300 mAh g^{-1} during the initial 10 cycles, followed by a rapid capacity decay. *Operando* XRD characterisation revealed that the increased irreversibility of the sodiation reactions and the formation of hexagonal Na_3Bi are the main causes of the capacity loss. This is initiated by an increase in crystallite sizes of the Bi particles accompanied by structural changes in the electronically insulating Na–Mo–O matrix leading to poor conductivity in the electrode. The poor electronic conductivity of the matrix deactivates the Na_xBi particles and prevents the formation of the solid electrolyte interface layer as shown by post-mortem scanning electron microscopy studies.

Supplementary material for this article is available [online](#)

Keywords: Na-ion batteries, SEI, PDF, Conversion-alloy anode materials, Post-mortem SEM, *Operando* XRD

(Some figures may appear in colour only in the online journal)

* Authors to whom any correspondence should be addressed.



Original content from this work may be used under the terms of the [Creative Commons Attribution 4.0 licence](#). Any further distribution of this work must maintain attribution to the author(s) and the title of the work, journal citation and DOI.

1. Introduction

Li-ion batteries (LIBs) dominate the rechargeable battery market due to their high energy and power densities. However, Na-ion batteries (NIBs) have recently emerged as a promising alternative to LIBs due to the high abundance and low cost of Na [1, 2]. While there are many similarities

between LIBs and NIBs, some well-established LIB materials perform poorly for NIBs. Graphite as an anode material is a key example. The challenges associated with the use of graphite in NIBs led to a search for alternatives, where materials utilizing conversion and/or alloying reactions show promising performance [3]. Among those, Bi is a promising alloying anode material with a high theoretical capacity (385 mAh g^{-1}) and low operating potential ($\sim 0.5 \text{ V}$) versus Na/Na^+ . Unfortunately, like most alloying electrode materials, Bi suffers from poor cycling stability. Several strategies have been tested to stabilise the cycling behaviour of Bi. One of the most promising is the preparation of Bi-based materials that combine conversion and alloying in their cycling mechanisms. Bi-metallates, with a general formula of $\text{Bi}_x\text{TM}_y\text{O}_z$ (TM = transition metal), are examples of these. Their operating mechanism consists of an irreversible conversion reaction during the first sodiation followed by reversible alloying of sodium ions with Bi formed in the initial conversion. The conversion reaction also appears to create a protective matrix around the Bi. The cycling stability of BiVO_4 and $\text{Bi}_2(\text{MoO}_4)_3$ is better than that of pure Bi [4, 5]. These materials show stable capacities of around 350 mAh g^{-1} for 100 cycles and 79% retained capacity after 1000 cycles [4]. Other Bi-metallates such as BiFeO_3 [6] and Bi_2MoO_6 [7] demonstrate capacities between 500 and 600 mAh g^{-1} during the first cycles, but stable long term cycling has not been achieved.

Operando x-ray absorption spectroscopy (XAS) and x-ray diffraction (XRD) investigations of the first 1.5 cycles of Bi-metallate NIB anodes suggest that the cycling mechanism involves the conversion of $\text{Bi}_x\text{TM}_y\text{O}_z$ into small clusters of Bi metal and an amorphous Na-TM-O matrix during the first sodiation. The Bi then alloys reversibly with Na from pure Bi to Na_3Bi , while the Na-TM-O has low electrochemical activity [4].

Similar results are observed for Bi-metallate anodes in LIBs [8, 9], and the Bi to Na_3Bi cycling is also seen in NIBs with Bi metal [5, 10] and Bi_2S_3 [11] anodes. The examples above, like most *operando* battery studies [12–15], only cover the first 1–2 cycles, however, significant structural changes that are crucial for long-term electrochemical performance can occur at later stages. In this work, we have performed an *operando* XRD evaluation of Bi_2MoO_6 over 34 cycles, to obtain structural insight into both the cycling mechanisms and capacity degradation. This approach allows us to correlate cycling stability and capacity degradation with structural changes.

The solid electrolyte interface (SEI) on the anode surface in NIBs is believed to be crucial for cycling stability, and its instability contributes to capacity degradation. Ideally, it should be electrically insulating, have good ionic conductivity and be mechanically, electrochemically and thermally stable [16]. SEIs are complex and contain several different species that are highly dependent on the electrolyte, electrodes, binders and additives. The exact compositions remain uncertain, but Na_2O , Na_2CO_3 and NaF are often detected [17, 18]. Previous studies showed that the SEI formation in NIBs are

different from LIBs [19], where higher solubility of SEI components in NIB electrolytes is a big challenge [20].

By studying a large number of cycles *operando*, we confirm that the main cycling mechanism of Bi_2MoO_6 is similar to the mechanism proposed in literature [4], but furthermore, initiate a discussion on what impacts the different phase changes have on capacity degradation. We also explore the formation and dissolution of the SEI layer on the Bi_2MoO_6 surface as an alternative contributor to the capacity decay. By post-mortem scanning electron microscopy (SEM) studies, we observe the formation and dissolution of the SEI layer at different stages of cycling. The work provides a new perspective on the cycling mechanism of Bi_2MoO_6 and, more generally, of conversion/alloying materials for Na-ion batteries.

2. Experimental

2.1. Materials

$\text{Bi}(\text{NO}_3)_3 \cdot 5\text{H}_2\text{O}$ (98%), ethylene glycol (99.8%), N-methyl-2-pyrrolidone (NMP) (99.5%), ethylene carbonate (EC) (99%), diethyl carbonate (DEC) (99%), fluoroethylene carbonate (FEC) (99%), sodium metal and sodium carboxymethylcellulose (CMC) were purchased from Sigma Aldrich and $\text{Na}_2\text{MoO}_4 \cdot 2\text{H}_2\text{O}$ (99%) from Merck. We also bought Ethanol (99.7%) from VWR, Super P from Timical, Kynar polyvinylidene fluoride (PVDF) from Arkema, double-sided dendritic Cu foil (99.9%, $10 \mu\text{m}$ thick) from Schlenk and NaPF_6 from Fluorochem. The home laboratory production facility provided distilled H_2O (Resistivity $> 1 \text{ M}\Omega \text{ cm}$). Na, FEC, DEC, EC and NaPF_6 were stored in an Ar-filled glovebox (M-Braun, H_2O and O_2 levels below 0.1 ppm) while ethylene glycol and NMP had protective caps. We used all the chemicals as purchased without any further purification or treatments, except when stated otherwise in the following sections.

2.2. Synthesis of Bi_2MoO_6

The synthesis is a modified procedure of a method previously reported in literature by Xin *et al* [7]. To synthesise Bi_2MoO_6 we dissolved 1.26 g (5.2 mmol) $\text{Na}_2\text{MoO}_4 \cdot 2\text{H}_2\text{O}$ and 5.06 g (10.4 mmol) $\text{Bi}(\text{NO}_3)_3 \cdot 5\text{H}_2\text{O}$ in two separate beakers each with 15 ml of ethylene glycol under stirring for half an hour. Consecutively, the two solutions were mixed in a third container and 60 ml of ethanol was added dropwise followed by continuous stirring for an additional 1.5 h. Then we transferred the solution to a Teflon-lined stainless steel autoclave with an inner volume of 180 ml. The autoclave was heated in an oven at $160 \text{ }^\circ\text{C}$ for 24 h and then naturally cooled down to room temperature. Finally, we obtained the Bi_2MoO_6 microspheres by filtering, washing three times with ethanol and drying at $60 \text{ }^\circ\text{C}$ in air. In the course of this work, we carried out several other solvothermal Bi_2MoO_6 syntheses with different temperatures and heating times. The results of those syntheses and discussion of the structure, morphology and electrochemical performance of the products can be

found in section S1.1, S1.2 and figures S6-S12 (available online at stacks.iop.org/NANO/33/185402/mmedia) in the supporting information (SI).

2.3. Material characterisation

X-ray diffraction (XRD) and pair distribution function (PDF) measurements on the pristine Bi_2MoO_6 in a 0.7 mm borosilicate glass capillary were performed at beamline ID15A of the European Synchrotron (ESRF) in Grenoble. We used a Dectris Pilatus 3X 2M CdTe detector and monochromatic radiation with a wavelength of 0.1425 Å [21]. The 2D diffraction data were integrated with PyFai [22] and converted to PDFs with PDFgetX3 [23] after subtraction of a background measurement on an empty 0.7 mm borosilicate glass capillary. For pattern fitting of the XRD and PDF data, we used Topas v6 [24], while Vesta [25, 26] was utilized for visualization of the structure. We further investigated the morphology of the Bi_2MoO_6 particles with a high-resolution Hitachi SU8230 cold-field emission scanning electron microscope (SEM), generating images using secondary electrons. We used an acceleration voltage of 5 kV, magnifications from 500 to 250,000 and a working distance of 8–10 mm. Carbon tape on the SEM holders ensured good conductivity and held the powder in place during the measurements.

2.4. Electrode preparation

For electrode preparation, we mixed 80 wt% active material (Bi_2MoO_6) with 10 wt% Super P and 10 wt% PVDF binder in NMP in a Thinky® mixer (ARE 250). The slurry was cast on a 10 µm thick double-sided dendritic Cu foil using a motorised K control coater (RK) with a stainless steel doctor blade with the thickness set to 300 µm. After casting, we dried the electrodes (cut to 15 mm diameter, ~2 mg cm⁻² active material) overnight under ambient conditions in a fume hood followed by drying in a Buchi oven at 80 °C under dynamic vacuum for 4 h and then transferred to an Ar-filled glovebox (MBRAUN, H₂O and O₂ levels below 0.1 ppm).

2.5. Electrochemical analysis

The electrochemical performance of the electrodes was tested in Na-ion half-cells, using Na metal as a counter electrode. We assembled coin cells using CR2032 stainless steel housings (304, Pi-Kem) with glass microfiber separators (17 mm, Whatman), soaked with 80 µl of electrolyte during cell assembly. The electrolyte was prepared in the glovebox with 1 M NaPF₆ in a 1:1 (volume ratio) mixture of EC and DEC with 5% FEC as additive. We prepared Na metal electrodes by removing the oxide layer from Na blocks (Sigma-Aldrich) with a scalpel, rolling them to form thin sheets (roughly 0.5 mm thick) and punching the discs with a diameter of 14 mm. An automatic coin cell crimper (Hohsen) pressed and sealed the cells. Galvanostatic cycling (GC) was performed using a battery tester (CT-4008T-5V10mA-164, Neware) with a voltage range of 0.01–2.00 V *versus* Na/Na⁺, specific current of 100 mA g⁻¹ and 12 h rest before cycling. For cyclic voltammetry (CV), we employed an MPG2 battery

cycler (BioLogic) with a voltage range of 0.01–2.00 V *versus* Na/Na⁺ and a sweep rate of 0.1 mV s⁻¹.

2.6. Electrode preparation for operando cell assembly and characterisation

For the *operando* XRD experiments, we used a laboratory manufactured cell similar to the one presented by Drozhzhin *et al* [27], with glassy carbon windows. The electrodes had CMC as a binder and distilled H₂O as solvent. We added the slurry dropwise directly on the glassy carbon window (glued to the cathode half of the *operando* cell) with a glass pipette. The subsequent preparation steps were identical to the methodology described in section 2.3. The preparation procedure of the electrodes for the *operando* cells did not permit accurate determination of the active materials' mass. Therefore, the absolute, rather than specific, currents and capacities are presented for these measurements. We assembled the *operando* cells with Na metal as counter electrodes, glass fiber separator, 80 µl of 1 M NaPF₆ in EC:DEC (1:1) with 5% FEC as the electrolyte, and the studied electrode. GC measurements were performed with a current of 250 µA between 0.01 and 2.00 V using an SP150 battery cycler (BioLogic). We performed *operando* XRD measurements by continuous still scans (10 min scan⁻¹, Q = 1.26–3.65 Å⁻¹) with a D8 Advance diffractometer (Bruker, Mo source, λ = 0.7093) using a Dectris Eiger 2R detector in 1D mode.

2.7. Preparation of post-mortem samples for SEM

The electrodes and cells for post mortem SEM analysis were prepared as described in sections 2.3 and 2.4. The batteries cycled with a specific current of 100 mA g⁻¹ in the range of 0.01–2.00 V *versus* Na/Na⁺, except when stated otherwise in section 3.4 and figure 5. We stopped the measurement at certain stages of cycling as specified in section 3.4. To ensure that the ongoing electrochemical reactions at the given voltages were completed, we kept the voltage at the endpoint constant until the measured current was below 0.02 mA.

After disassembling the batteries with a coin cell disassembling tool (Hoshen) inside the glovebox, we carefully extracted the electrodes and cleaned them with 0.5 ml DEC. The drying process was carried out in the small glovebox antechamber under a dynamic vacuum. To minimize the air exposure, we mounted the electrodes to the sample holder inside the glovebox and transferred them into a glass container covered with parafilm and a latex glove to the SEM. The samples were exposed to air for less than 3 s during the transfer from the glass container to the SEM, which we expect to have minimal impact on their morphology.

3. Result and discussions

3.1. Structural and morphological characterisation

We characterised the as-synthesised Bi_2MoO_6 sample by using XRD, PDF and SEM. Pattern fitting of the XRD and PDF measurements (figures 1(a) and (b)) confirmed that the sample

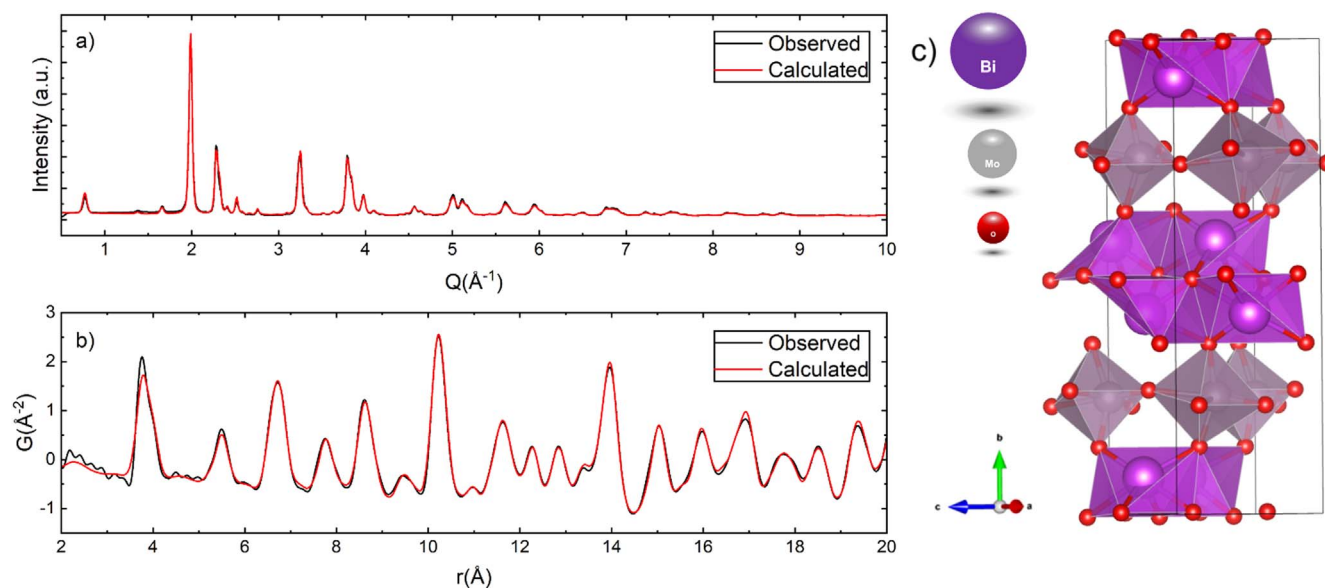


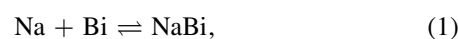
Figure 1. Pattern fitting of (a) XRD data and (b) PDF pattern of Bi_2MoO_6 [28]. (c) visualization of the structure including coordination polyhedra where purple, grey and red spheres represent Bi, Mo and O atoms, respectively.

is phase-pure and composed of orthorhombic Bi_2MoO_6 (spacegroup: $\text{Pca}2_1$; COD ID: 1530868). The structure consists of layers of distorted Mo-O6 octahedra connected by corner-sharing (figure 1(c)). Bi atoms bond to six oxygen atoms and are organised in a double layer between the Mo layers. Table S1 (SI) provides more structural details. The SEM images of Bi_2MoO_6 showed agglomerates of spherical particles with sizes between roughly 1–3 μm (figures 2(a) and (b)). A more detailed analysis of the particles revealed the substructure comprised of nanoplatelets with an approximate thickness of 20 nm ordered in a ‘house-of-cards’ morphology (figures 2(c) and (d)). The 2D character of the nanoplatelets probably reflects the layered nature of the Bi_2MoO_6 structure (figure 1(c)). Besides, the sample contained ~ 100 nm thick spikes growing out of the particles (figure 2(d)). While the particle size, distribution of spikes and the size of the nanoplatelets varies through the sample, the thickness of the nanoplatelets is almost identical between the particles even when the microstructure differs (figure S1).

3.2. Electrochemical characterisation (sodiation and desodiation)

To investigate the electrochemical performance of Bi_2MoO_6 we extracted selected sodiation-desodiation curves (figure 3(a)) and the corresponding dQ/dV plot (figure 3(b)) from a representative GC measurement. During the 1st sodiation, the material reached a specific capacity of 650 mAh g^{-1} (calculated from the mass of Bi_2MoO_6) while during the 2nd sodiation only a capacity of 350 mAh g^{-1} was measured. This capacity loss is attributed to the irreversible *in situ* conversion of Bi_2MoO_6 into Bi metal and a Mo-containing matrix as well as the formation of SEI layers. For cycles 2, 5 and 10, we observe 2 distinct plateaus (figure 3(a)) in the (de) sodiation curves and 2 peaks in the dQ/dV plot (figure 3(b))

corresponding to the following alloying reactions:



Reaction (1) corresponds to the dQ/dV peak at around 0.6 V during sodiation and 0.8 V during desodiation. Reaction (2) occurs around 0.4 V (sodiation) and 0.6 V (desodiation). This part of the reaction mechanism is similar to that of other Bi-metallates [4]. The theoretical capacity of reaction (1) and (2) combined is 264 mAh g^{-1} . This is significantly less than the observed specific capacity during the first 3 cycles, which is above 300 mAh g^{-1} . However, between cycles 3 and 10, the specific capacity is in the range of $245\text{--}285 \text{ mAh g}^{-1}$ (both sodiation and desodiation), indicating that the observed capacity is almost exclusively derived from reactions (1) and (2). The origin of the extra capacity observed during the first 3 cycles is still uncertain, but redox reactions in the Mo-containing matrix may be involved. We evaluated the contribution of the conductive carbon additive, Super P, to the total capacity of the anode (section S2 and figure S13). It was approximately 15 mAh g^{-1} .

After 10 (de)sodiation cycles, the capacity of the Bi_2MoO_6 -based electrodes exhibit a substantial decay (figure 3(c)). To elucidate the electrochemical changes occurring during this decay we extracted the (de)sodiation curves for cycles 9–14 (figure 3(d)). Inspection of those graphs clearly shows the complete disappearance of the plateaus corresponding to reaction (1), followed by a reduction of the second plateau corresponding to reaction (2).

Further tests were conducted on ball-milled Bi_2MoO_6 to study the effect on cycling stability. As reported in sections S3.1, S3.2 and figures S14–S16, the materials did not perform better than the as-synthesised Bi_2MoO_6 . We, therefore, proceeded with *operando* studies on the as-synthesised material only.

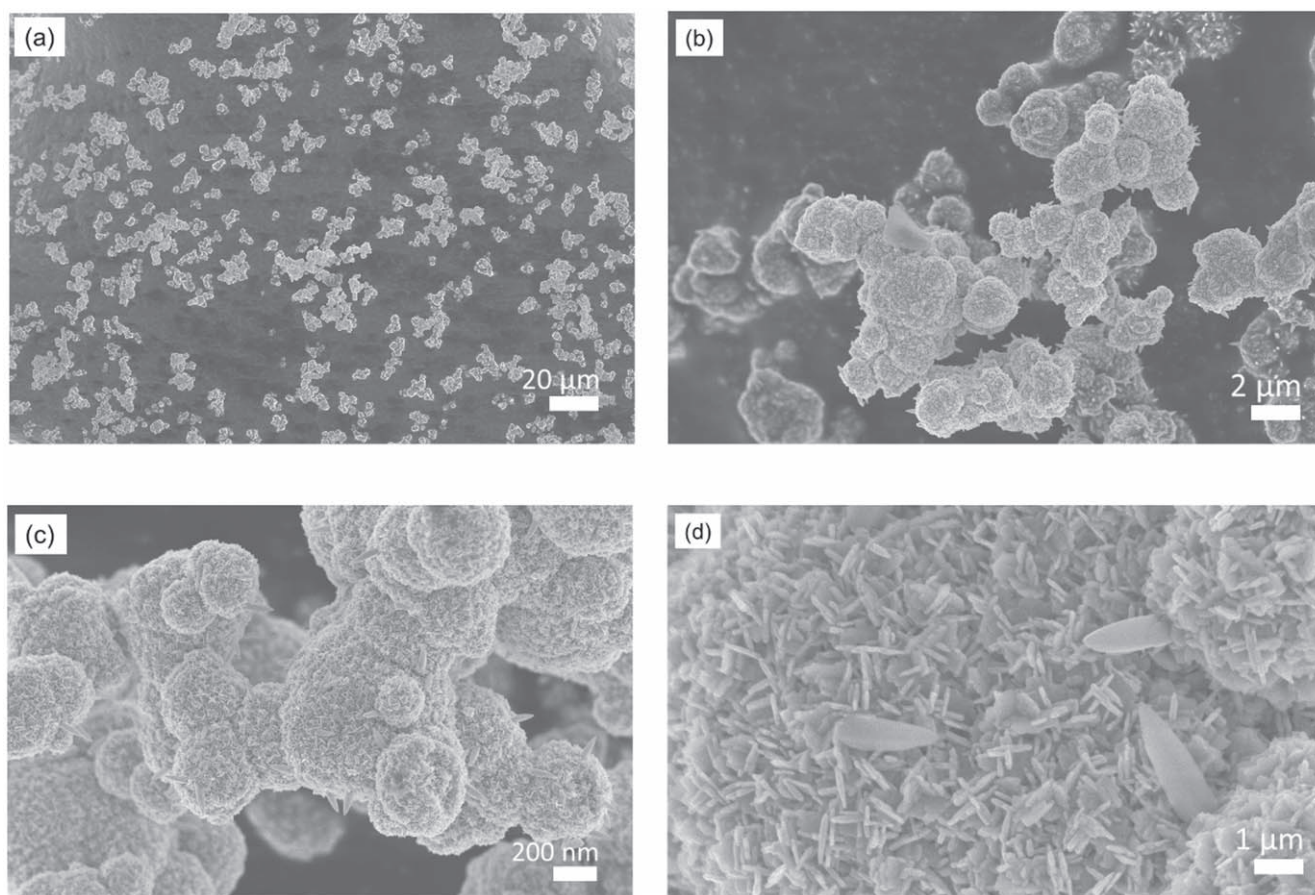


Figure 2. SEM images of the Bi_2MoO_6 particles generated by secondary electrons at different magnifications: (a) $\times 500$, (b) $\times 5000$, (c) $\times 10,000$ and (d) $\times 50,000$.

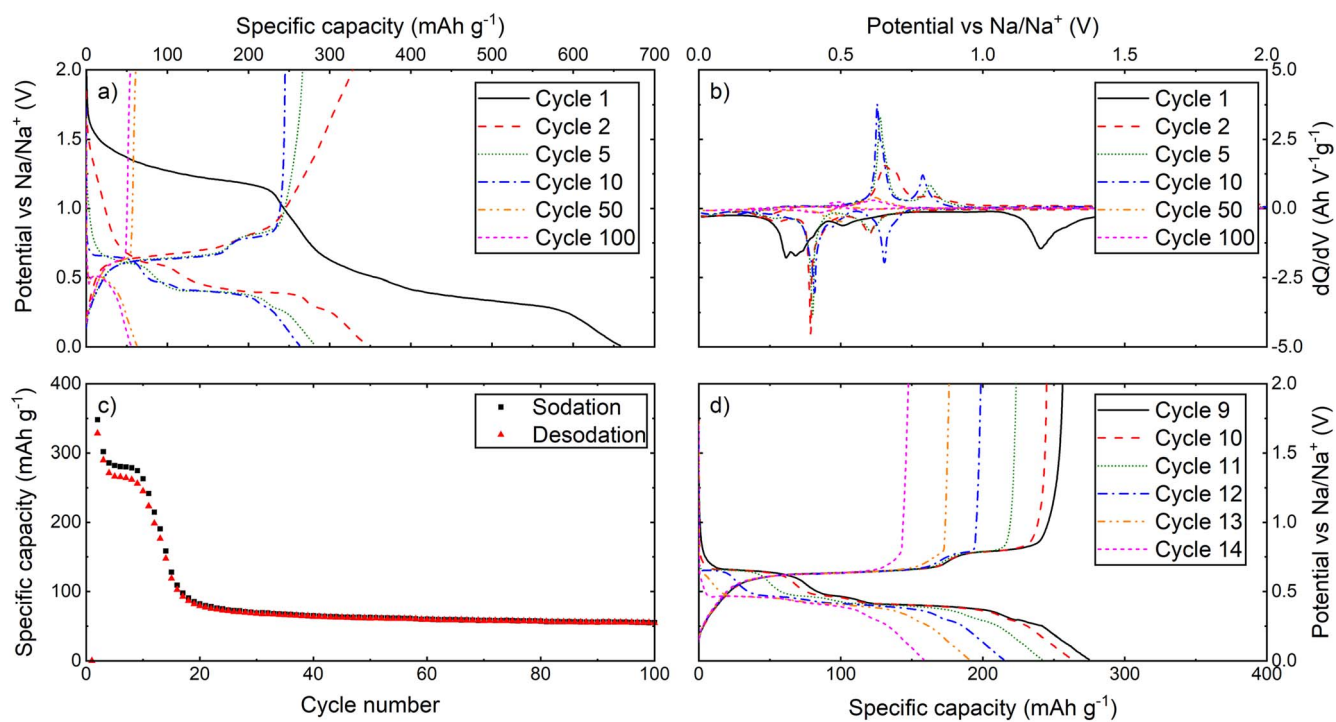


Figure 3. (a) (de)sodiation curves and (b) corresponding dQ/dV plot of selected cycles, (c) specific capacity over the first 100 cycles, (d) (de)sodiation curves of cycle 9–14 highlighting the region with rapid capacity decay. All graphs are derived from galvanostatic cycling (GC) measurements performed with a specific current of 100 mA g^{-1} with a voltage range of 0.01–2.00 V versus Na/Na^+ .

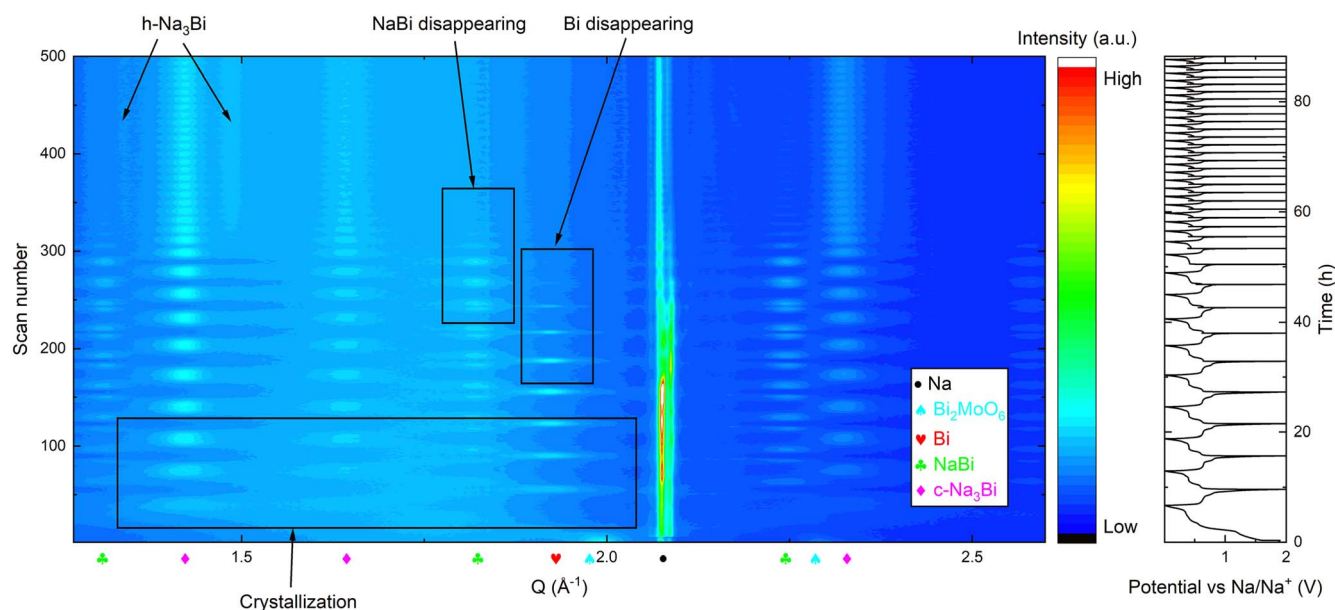


Figure 4. Operando XRD over 34 cycles of Bi_2MoO_6 in Na half-cell obtained from GC measurements between 0.01–2.00 V versus Na/Na^+ and a current of 250 μA .

3.3. Cycling mechanism and capacity fade (operando XRD)

To further investigate the cycling mechanism of Bi_2MoO_6 and understand the origin of capacity fading we performed operando XRD measurements over 34 cycles with GC (figure 4). The data in figure 4, and the extended contour plot in figure S4, unambiguously confirmed the main cycling reactions suggested in section 3.2: Bi_2MoO_6 converts into Bi (COD: 2310889) at the start of the first sodiation. The Bi then reversibly alloys with Na to form NaBi (ICSD: 58816) and Na_3Bi . The Na_3Bi phase formed in the initial formation is the cubic phase of Na_3Bi (c- Na_3Bi) with the spacegroup Fm-3m and not the hexagonal phase (h- Na_3Bi) (COD: 1010291), which forms from microcrystalline Bi metal [5] (figure S5). Detailed information about the structures is reported in Table S1 (SI).

We also observe that the Bi peaks that appear during the first sodiation are significantly broader than those of the Bi_2MoO_6 that disappear. Along with the observation of c- Na_3Bi , this indicates that the Bi metal formed during the initial sodiation of Bi_2MoO_6 is nanocrystalline. The operando data also provides insight into the chemical mechanism of degradation. During the first cycle, we observed that Bi, and the corresponding sodiated phases, are nanocrystalline. During the first 5 (de)sodiation cycles the peaks corresponding to Bi, NaBi and Na_3Bi gradually become sharper indicating an increase in the crystallite sizes. Around cycle 8, the diffraction peaks corresponding to metallic Bi gradually disappear. This corresponds to the start of the capacity decay. The exact point where the capacity decay starts may vary slightly between different cells; in the operando cell, the capacity decay begins a few cycles earlier than for the conventional coin cell described in section 3.2. The disappearance of the Bi XRD peaks together with the disappearance of the Bi–NaBi plateau in the (de)sodiation curves confirms that reaction (1)

gradually becomes irreversible and Bi is no longer formed during desodiation after cycle 8. Over the next few cycles, similar irreversibility occurs for reaction (2) as more and more NaBi converts into Na_3Bi during sodiation but is not recovered during desodiation. That process is accompanied by the formation of the h- Na_3Bi phase in addition to c- Na_3Bi . The appearance of h- Na_3Bi could be explained by the increased crystallite size of active domains, as Sottmann *et al* showed for Bi metal [5]. The same study also showed that the h- Na_3Bi has poor cycling stability compared to the cubic phase, due to a structural mismatch with NaBi. Our results suggest that for Bi_2MoO_6 the reversibility of cycling to/from c- Na_3Bi is also greatly reduced in later cycles, as the corresponding diffraction peaks vary only slightly in intensity and do not disappear during desodiation. Therefore, we believe that the mechanism of capacity decay is primarily driven by the Mo-containing matrix formed during the initial sodiation, rather than by the formation of large h- Na_3Bi crystallites.

The operando XRD data provided full insight into the crystalline phases formed throughout the cycle life of our battery, however, it does not reveal information regarding the amorphous phases. There is no sign of Mo-containing phases in the observed diffractograms, confirming its amorphous nature after the first sodiation. During the crystal growth of the Bi particles, it is likely that structural changes happen to the Na–Mo–O matrix. A set of Na–Mo–O compounds was previously screened by ‘The Materials Project’ [29], showing that all of them are electronic insulators. Therefore, it is reasonable to assume that structural transformations that take place during cycling result in a thicker matrix of Na–Mo–O around Bi, NaBi and Na_3Bi sub-particles, inhibiting the desodiation process. We will, in future studies, investigate this aspect with techniques like PDF and extended x-ray absorption fine structure (EXAFS) that are sensitive to amorphous phases.

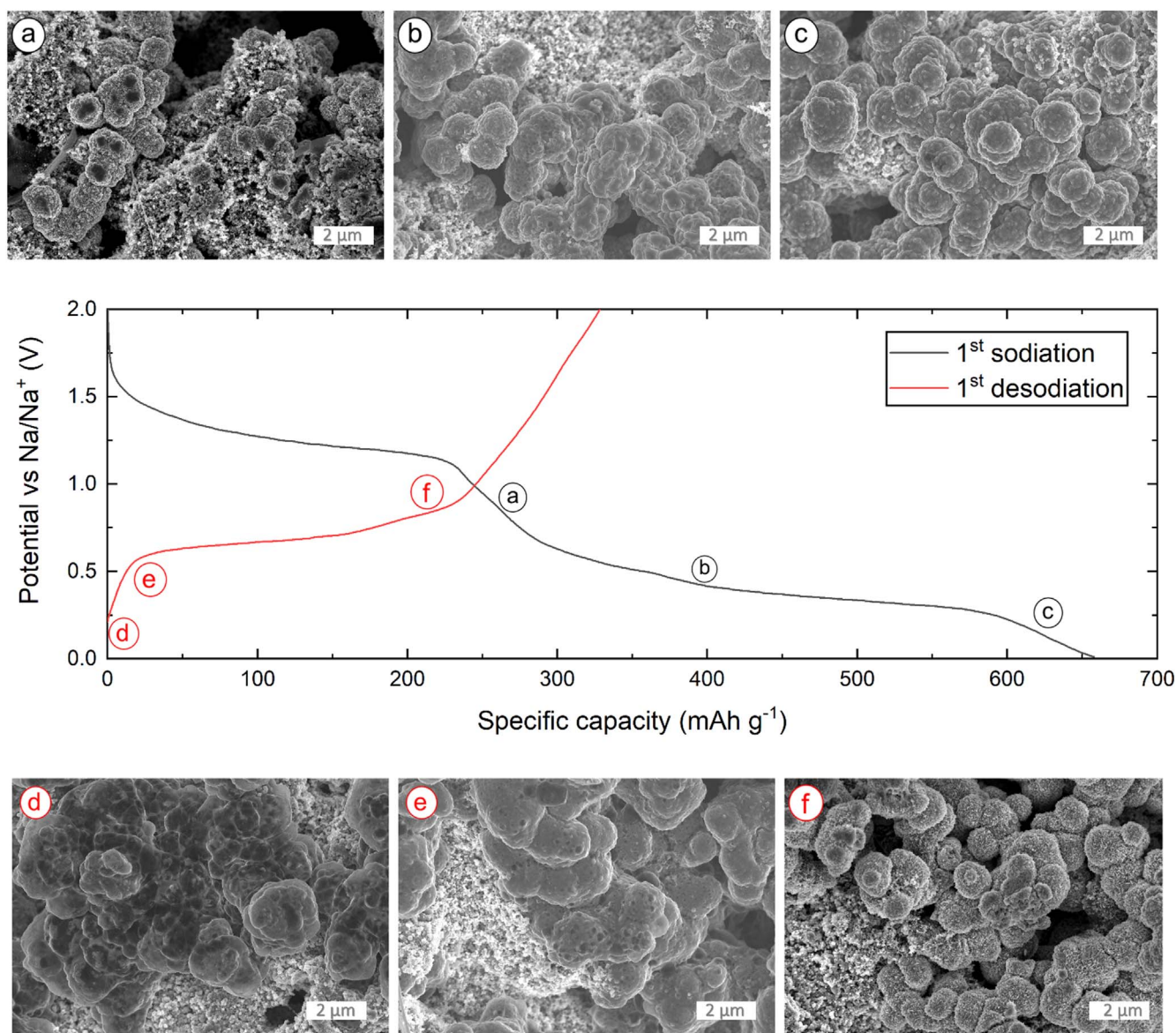


Figure 5. Post-mortem SEM images captured with a secondary electron detector at different sodiation states during the first cycle. (a) sodiated to 1.00 V, (b) sodiated to 0.50 V, (c) sodiated to 0.35 V, (d) fully sodiated to 0.01 V, (e) desodiated to 0.50 V and (f) desodiated to 0.90 V *versus* Na/Na⁺.

3.4. Post-mortem SEM

Dissolution of the SEI is a common problem for NIB anode materials [20]. To study the SEI formation, we performed post-mortem SEM on electrodes extracted at different states of charge (figure 5). During the 1st sodiation, the SEI layer starts to form already above 1 V *versus* Na/Na⁺, visible as dark spots in figure 5(a). However, the SEI only covers a few areas of the electrode surface at this stage of cycling. At 0.50 and 0.35 V, the particles are completely covered, as they have a smooth surface showing no characteristic signs of the nanoplatelets from the pristine material (figures 5(b) and (c)). This confirms that the formation of the SEI layer mostly occurs between 1.00 and 0.50 V during the 1st sodiation. During the 1st desodiation, the SEI layer is still intact at 0.50 V, but it is not present above 0.90 V as the nanoplatelets are again observed (figure 5(d)). This means that the SEI layer

forms and dissolves in the same voltage range as the alloying reactions between Na and Bi occur. Hence, we are unable to avoid the formation and dissolution of the SEI layer with our current electrolyte composition. To determine the role of the SEI on cycling stability, we extracted desodiated (2.00 V) and sodiated (0.01 V) samples at different stages of cycling. There is clearly an SEI forming on the surface of the particles in the samples imaged after the 1st, 2nd and 10th sodiation (figures S2(a), (b) and (c), respectively). After the 1st sodiation, the particles are quite uniformly coated as the main particle shapes are still visible, as opposed to the 2nd sodiation where the SEI covers whole agglomerates. After the 10th sodiation, the particle shapes become more visible again as the SEI layer becomes thinner and covers less of the surface. There are also certain areas where particles without a visible SEI layer are present. After the 20th sodiation (figure S2d, SI) the SEI layer is almost completely gone.

When studying the desodiated samples from the corresponding cycles (figure S3, SI) it is evident that the SEI layer disappears during the desodiation process. This indicates that the SEI layer is formed in every sodiation and dissolved in every desodiation during at least the first 10 cycles. This reaction consumes Na ions and may explain why the sodiation capacity is higher than the desodiation capacity during the first 10 cycles (figure 3(c)). When the SEI layer struggles to reform after 10 cycles it is reasonable to assume that this process is linked to the capacity decay observed between cycles 10 and 20. One theory we considered is that the repeated formation and dissolution of the SEI consumes vital components in the electrolyte during the first 10 cycles. When these components are depleted, the SEI no longer forms possibly leading to the structural changes observed in the *operando* XRD and the capacity decay. However, electrochemical measurements performed on Bi₂MoO₆ samples (section S4, figure S17, SI) with different amounts of electrolyte indicates that the rapid loss of electrochemical performance does not depend on the amount of the electrolyte used. Even in a cell where we replaced both the electrolyte and the Na counter electrode after 10 cycles, the decay in capacity continued in the same fashion. The capacity decay does not, therefore, originate from the consumption of critical electrolyte components. The structural changes discussed in section 3.3 thus appear to be the main cause of both the capacity degradation and the changes in SEI formation.

A common degradation mechanism for alloying materials is particle fracturing and pulverization caused by large volume changes during cycling [30–33]. From the SEM images in this study (figure 5, S2 and S3), we do not observe any signs of cracking. We believe this is due to the protective effect of the Na-TM-O matrix, which mitigates the strain caused by the volume changes.

During the SEM study, we also observed an increasing amount of charging effects, with cycle number, leading to dark stripes in the images (figure S3(d)), which indicates poor electronic conductivity. This is also supported by electrochemical impedance spectroscopy measurements performed on the cells after the 1st and 20th desodiation, where the last cell showed much higher impedance (section S5, figure S18). This poor conductivity is most likely the leading cause of the capacity decay and can explain why the SEI layer no longer forms during the 20th sodiation. The question of exactly which structural changes in the material lead to this poor conductivity needs to be addressed in future studies.

4. Conclusions and perspectives

Bi₂MoO₆ is a potentially promising anode material for NIBs but requires further studies with appropriate nanostructuring and carbon additives to enhance the electronic conductivity. We have yet to find the perfect approach to ensure a long cycle life. However, by using *operando* XRD over a large number of cycles and post-mortem SEM, we have elucidated the cycling and degradation mechanism in this material and possibly a general trend in Bi-metallates as anode materials

for Na-ion batteries. The reversible cycling between Bi and c-Na₃Bi through NaBi is the main cycling mechanism for the 10 first cycles, where the capacity is stable and close to 300 mAh g⁻¹. Following this, a rapid capacity decay occurs as the Bi–NaBi and NaBi–Na₃Bi reactions become more irreversible followed by the formation of h-Na₃Bi. At the same stage of cycling the SEI layer stops forming during sodiation. We postulate that the sudden onset of capacity loss is driven by structural changes, crystallite growth in the Na_xBi particles and growth of a thick, insulating Na–Mo–O matrix, with the disappearance of the SEI being a symptom of these rather than the cause of capacity loss.

Future studies on the structure and electrochemical properties of the amorphous Na–Mo–O will further improve our understanding of the cycling and degradation mechanisms of Bi₂MoO₆, and help to find an approach that could improve the cycling stability of this and similar materials.




Acknowledgments

This work was performed with support from the Research Council of Norway (NFR) through the NanoName project (number 287480). We acknowledge the use of the Norwegian national infrastructure for x-ray diffraction and Scattering (RECX) where we performed all our *operando* measurements. We acknowledge the European Synchrotron Radiation Facility (ESRF) for the provision of beamtime on ID15A and we would like to thank Stefano Checchia for the support during our beam time.

Data availability statement

All data that support the findings of this study are included within the article (and any supplementary files).

ORCID iDs

Anders Brennhagen  <https://orcid.org/0000-0003-4467-6750>
Carmen Cavallo  <https://orcid.org/0000-0003-1931-3018>
David S. Wragg  <https://orcid.org/0000-0001-8502-7912>
Ponniiah Vajeeston  <https://orcid.org/0000-0002-5566-2429>
Anja O. Sjøstad  <https://orcid.org/0000-0001-9280-541X>
Alexey Y. Kuposov  <https://orcid.org/0000-0001-5898-3204>
Helmer Fjellvåg  <https://orcid.org/0000-0001-6045-7211>

References

- [1] Hasa I *et al* 2021 Challenges of today for Na-based batteries of the future: from materials to cell metrics *J. Power Sources* **482** 228872
- [2] Vaalma C, Buchholz D, Weil M and Passerini S 2018 A cost and resource analysis of sodium-ion batteries *Nat. Rev. Mater.* **3** 18013

- [3] Zhang H, Hasa I and Passerini S 2018 Beyond insertion for na-ion batteries: nanostructured alloying and conversion anode materials *Adv. Energy Mater.* **8** 1702582
- [4] Sottmann J et al 2017 Bismuth vanadate and molybdate: stable alloying anodes for sodium-ion batteries *Chem. Mater.* **29** 2803–10
- [5] Sottmann J et al 2016 How crystallite size controls the reaction path in nonaqueous metal ion batteries: the example of sodium bismuth alloying *Chem. Mater.* **28** 2750–6
- [6] Xia H, Yan F, Lai M O, Lu L and Song W 2009 Electrochemical properties of BiFeO₃ thin films prepared by pulsed laser deposition *Funct. Mater. Lett.* **2** 163–7
- [7] Xu X, Li M and Yu T 2020 Facile synthesis of Bi₂MoO₆ nanosheets@nitrogen and sulfur codoped graphene composites for sodium-ion batteries *Chem. Res. Chin. Univ.* **36** 115–9
- [8] Ruud A, Sottmann J, Vajeeston P and Fjellvåg H 2018 Operando investigations of lithiation and delithiation processes in a BiVO₄ anode material *Phys. Chem. Chem. Phys.* **20** 29798–803
- [9] Ruud A, Sottmann J, Vajeeston P and Fjellvåg H 2019 Direct observation of reversible conversion and alloying reactions in a Bi₂(MoO₄)₃-based lithium-ion battery anode *J. Mater. Chem. A* **7** 17906–13
- [10] Gao H et al 2018 Sodium storage mechanisms of bismuth in sodium ion batteries: An operando x-ray diffraction study *J. Power Sources* **379** 1–9
- [11] Sottmann J, Homs-Regojo R, Wragg D S, Fjellvåg H, Margadonna S and Emerich H 2016 Versatile electrochemical cell for Li/Na-ion batteries and high-throughput setup for combined operando x-ray diffraction and absorption spectroscopy *J. Appl. Crystallogr.* **49** 1972–81
- [12] Liu D et al 2019 Review of recent development of *in situ* /operando characterization techniques for lithium battery research *Adv. Mater.* **31** 1806620
- [13] Zhang G et al 2017 Electrochemical *in situ* x-ray probing in lithium-ion and sodium-ion batteries *J. Mater. Sci.* **52** 3697–718
- [14] Zhu W et al 2018 Application of operando x-ray diffractometry in various aspects of the investigations of lithium/sodium-ion batteries *Energies* **11** 2963
- [15] Brennhagen A, Cavallo C, Wragg D S, Sottmann J, Kuposov A Y and Fjellvåg H 2021 Understanding the (De) Sodiation mechanisms in na-based batteries through operando x-ray methods *Batteries Supercaps* **4** 1039–63
- [16] Huang Y, Zhao L, Li L, Xie M, Wu F and Chen R 2019 Electrolytes and electrolyte/electrode interfaces in sodium-ion batteries: from scientific research to practical application *Adv. Mater.* **31** 1808393
- [17] Bommier C and Ji X 2018 Electrolytes, SEI formation, and binders: a review of nonelectrode factors for sodium-ion battery anodes *Small* **14** 1703576
- [18] Fondard J, Irisarri E, Courrèges C, Palacin M R, Ponrouch A and Dedryvère R 2020 SEI composition on hard carbon in na-ion batteries after long cycling: influence of salts (NaPF₆, NaTFSI) and additives (FEC, DMCF) *J. Electrochem. Soc.* **167** 070526
- [19] Philippe B, Valvo M, Lindgren F, Rensmo H and Edström K 2014 Investigation of the electrode/electrolyte interface of Fe₂O₃ composite electrodes: li versus na batteries *Chem. Mater.* **26** 5028–41
- [20] Ma L A, Naylor A J, Nyholm L and Younesi R 2021 Strategies for mitigating dissolution of solid electrolyte interphases in sodium-ion batteries *Angew. Chem.* **133** 4905–13
- [21] Vaughan G B M et al 2020 ID15A at the ESRF—a beamline for high-speed operando x-ray diffraction, diffraction tomography and total scattering *Journal of Synchrotron Radiation* **27** 515–28
- [22] Ashiotis G et al 2015 The fast azimuthal integration Python library: pyFAI *Journal of Applied Crystallography* **48** 510–9
- [23] Juhás P, Davis T, Farrow C L and Billinge S J L 2013 PDFgetX3: a rapid and highly automatable program for processing powder diffraction data into total scattering pair distribution functions *Journal of Applied Crystallography* **46** 560–6
- [24] Coelho A A and IUCr 2018 TOPAS and TOPAS-Academic: an optimization program integrating computer algebra and crystallographic objects written in C++ *Journal of Applied Crystallography* **51** 210–8
- [25] Momma K and Izumi F 2008 VESTA: a three-dimensional visualization system for electronic and structural analysis *Journal of Applied Crystallography* **41** 653–8
- [26] Momma K and Izumi F 2011 VESTA 3 for three-dimensional visualization of crystal, volumetric and morphology data *Journal of Applied Crystallography* **44** 1272–6
- [27] Drozhzhin O A, Tereshchenko I V, Emerich H, Antipov E V, Abakumov A M and Chernyshov D 2018 An electrochemical cell with sapphire windows for operando synchrotron x-ray powder diffraction and spectroscopy studies of high-power and high-voltage electrodes for metal-ion batteries *J. Synchrotron Radiat* **25** 468–72
- [28] Wragg D, Brennhagen A, Villeveille C and Checchia S 2021 Modulation enhanced operando pdf for battery materials *European Synchrotron Radiation Facility (ESRF)* (<https://doi.org/10.15151/ESRF-ES-433977821>)
- [29] Jain A et al 2013 Commentary: the materials project: a materials genome approach to accelerating materials innovation *APL Mater.* **1** 011002
- [30] Lao M, Zhang Y, Luo W, Yan Q, Sun W and Dou S X 2017 Alloy-based anode materials toward advanced sodium-ion batteries *Adv. Mater.* **29** 1700622
- [31] Liu X H, Zhong L, Huang S, Mao S X, Zhu T and Huang J Y 2012 Size-dependent fracture of silicon nanoparticles during lithiation *ACS Nano* **6** 1522–31
- [32] Ulvestad A et al 2021 Stoichiometry-controlled reversible lithiation capacity in nanostructured silicon nitrides enabled by *in situ* conversion reaction *ACS Nano* **15** 16777–87
- [33] Wang J, Eng C, Chen-Wiegart Y K and Wang J 2015 Probing three-dimensional sodiation–desodiation equilibrium in sodium-ion batteries by *in situ* hard x-ray nanotomography *Nat. Commun.* **6** 1–9



Corrigendum: Operando XRD studies on Bi_2MoO_6 as anode material for Na-ion batteries (2022 *Nanotechnology* 33 185402)

Anders Brennhagen¹, Carmen Cavallo^{1,*} , David S Wragg^{1,2},
Ponniiah Vajeeston¹, Anja O Sjøstad¹, Alexey Y Kopusov^{1,3}  and
Helmer Fjellvåg^{1,*}

¹ Centre for Material Science and Nanotechnology, Department of Chemistry, University of Oslo, PO Box 1033, Blindern, N-0315, Oslo, Norway

² Norwegian National Resource Centre for X-ray Diffraction and Scattering (RECX), Department of Chemistry, University of Oslo, PO Box 1033, Blindern, N-0315, Oslo, Norway

³ Department of Battery Technology, Institute for Energy Technology (IFE), Instituttveien 18, 2007, Kjeller, Norway

E-mail: carmen.cavallo@smn.uio.no and helmer.fjellvag@kjemi.uio.no

Received 6 May 2022

Accepted for publication 23 May 2022

Published 14 June 2022

(Some figures may appear in colour only in the online journal)

1. Structural and morphological characterization

Figure 2 reports the correct label for panels (c) and (d), which were inverted in the primary submission. ' Bi_2MoO_6 ' in the caption instead of Bi_2MoO_6 .

Figure 3 reports the correct label: 'Sodiation and Desodiation', which were wrong in the primary submission (sodation and desodation).

1.1. Post-mortem SEM

'During the 1st desodiation, the SEI layer is still intact at 0.50 V (figure 5(e)).' Figure 5(e) was missing in the primary submission.

'but it is not present above 0.90 V as the nanoplatelets are again observed (figure 5(f))'. Figure 5(f) was missing in the primary submission.

In the caption of figure 5: ('b) sodiated'. It was written sodiated with an extra *t*.

Figure 5: post-mortem SEM images captured with a secondary electron detector at different sodiation states during the first cycle. (a) sodiated to 1.00 V, (b) sodiated to 0.50 V, (c) sodiated to 0.35 V, (d) fully sodiated to 0.01 V, (e) desodiated to 0.50 V and (f) desodiated to 0.90 V versus Na/Na⁺.

* Authors to whom any correspondence should be addressed.

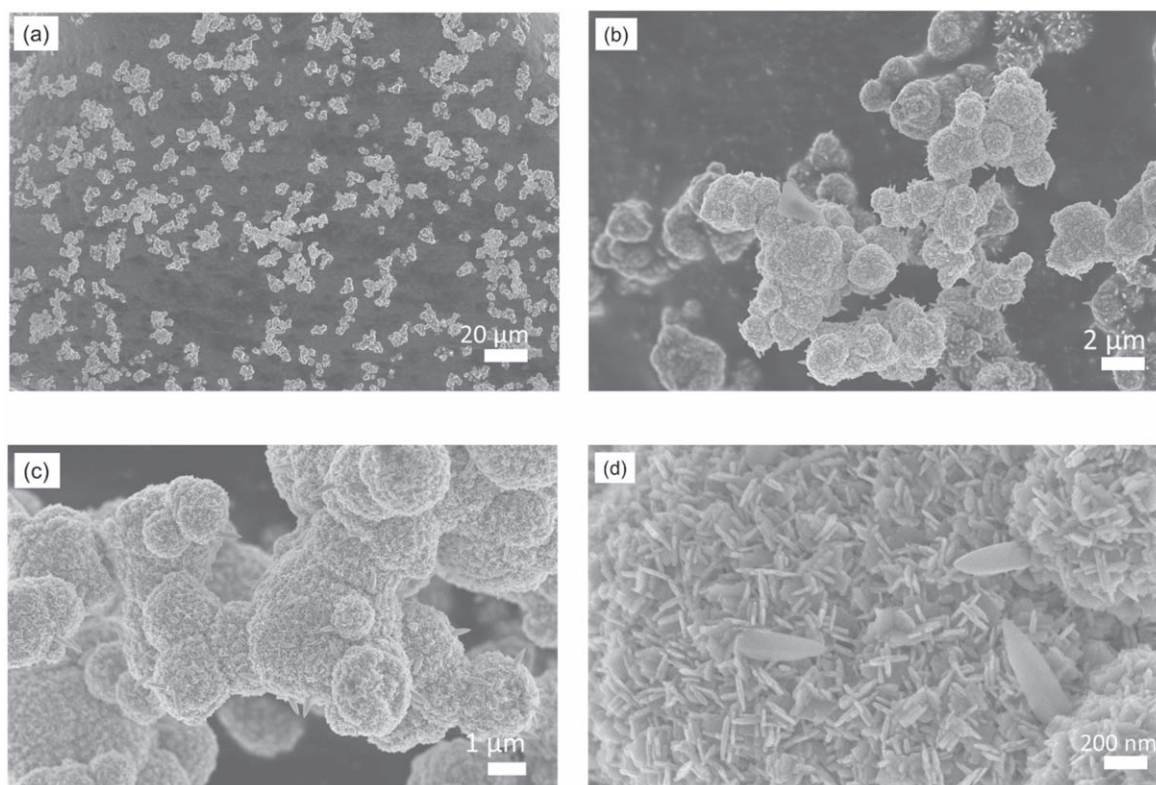


Figure 2. SEM images of the Bi_2MoO_6 particles generated by secondary electrons at different magnifications: (a) $\times 500$, (b) $\times 5\,000$, (c) $\times 10\,000$ and (d) $\times 50\,000$.

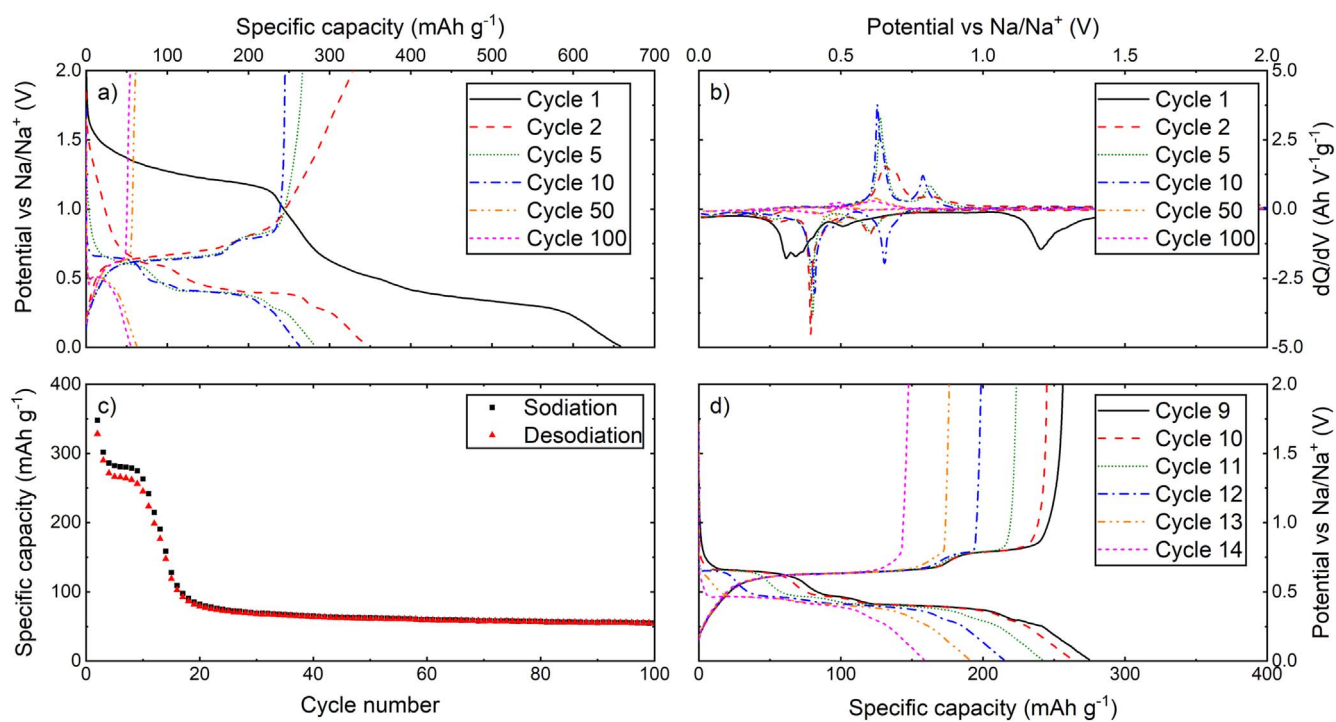


Figure 3. (a) (de)sodiation curves and (b) corresponding dQ/dV plot of selected cycles, (c) specific capacity over the first 100 cycles, (d) (de)sodiation curves of cycles 9–14 highlighting the region with rapid capacity decay. All graphs are derived from galvanostatic cycling (GC) measurements performed with a specific current of 100 mA g^{-1} with a voltage range of 0.01–2.00 V versus Na/Na^+ .

Supporting information

Operando XRD studies on Bi₂MoO₆ as anode material for Na-ion batteries

Anders Brennhagen¹, Carmen Cavallo*¹, David S. Wragg^{1,2}, Ponniah Vajeeston¹, Anja O. Sjøstad¹, Alexey Y. Koposov^{1,3} and Helmer Fjellvåg*¹

¹Centre for Material Science and Nanotechnology, Department of Chemistry, University of Oslo, PO Box 1033, Blindern, N-0315, Oslo, Norway.

²Norwegian National Resource Centre for X-ray Diffraction and Scattering (RECX), Department of Chemistry, University of Oslo, PO Box 1033, Blindern, N-0315, Oslo, Norway.

³Department of Battery Technology, Institute for Energy Technology (IFE), Instituttveien 18, 2007, Kjeller, Norway.

E-mail: carmen.cavallo@smn.uio.no, helmer.fjellvag@kjemi.uio.no

Table S1: Structural information of the phases used for XRD analysis

Phase	Space group	Z	Unit cell parameters (Å)	Atomic sites					Source
				Atom	Wyckoff	x	y	z	
Bi ₂ MoO ₆	Pca2 ₁ (29)	4	a = 5.4896 b = 16.22658 c = 5.5131	Bi1 Bi2 Mo1 O1 O2 O3 O4 O5 O6		0.519 0.483 0.001 0.049 0.259 0.242 0.698 0.207 0.572	0.4231 0.0786 0.2479 0.1428 0.9956 0.5048 0.2297 0.2624 0.3602	0.983 0.989 0 0.091 0.271 0.272 0.251 0.36 0.575	COD: 1530868
Bi	R-3m (166)	6	a = 4.546 c = 11.862	Bi1	2g	0	0	0.23389	COD: 2310889
NaBi	P4/mmm (123)	1	a = 3.46 c = 4.8	Bi1 Na1	1a 1d	0 1/2	0 1/2	0 1/2	ICSD: 58816
h-Na ₃ Bi	P6 ₃ /mmc (194)	2	a = 5.448 c = 9.655	Bi1 Na1 Na2	2c 2b 4f	1/3 0 1/3	2/3 0 2/3	1/4 1/4 0.583	COD: 1010291
c-Na ₃ Bi	Fm-3m (225)	4	a = 7.66526	Bi1 Na1 Na2	4a 4b 8c	0 1/2 1/4	0 1/2 1/4	0 1/2 1/4	[1]

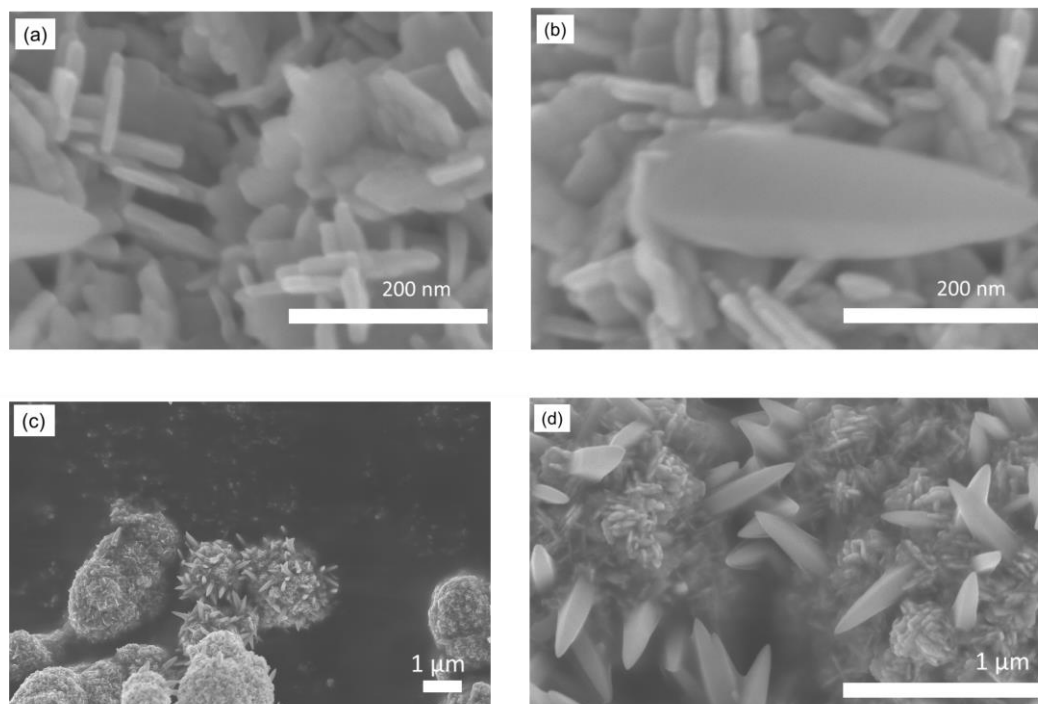


Figure S1: SEM images of the pristine Bi_2MoO_6 : a) nanoplatelets, b) an example of spike-type particle, c) low-resolution images demonstrating particles with slightly different morphology and d) particles with a high concentration of spikes and less developed nanoplatelets.

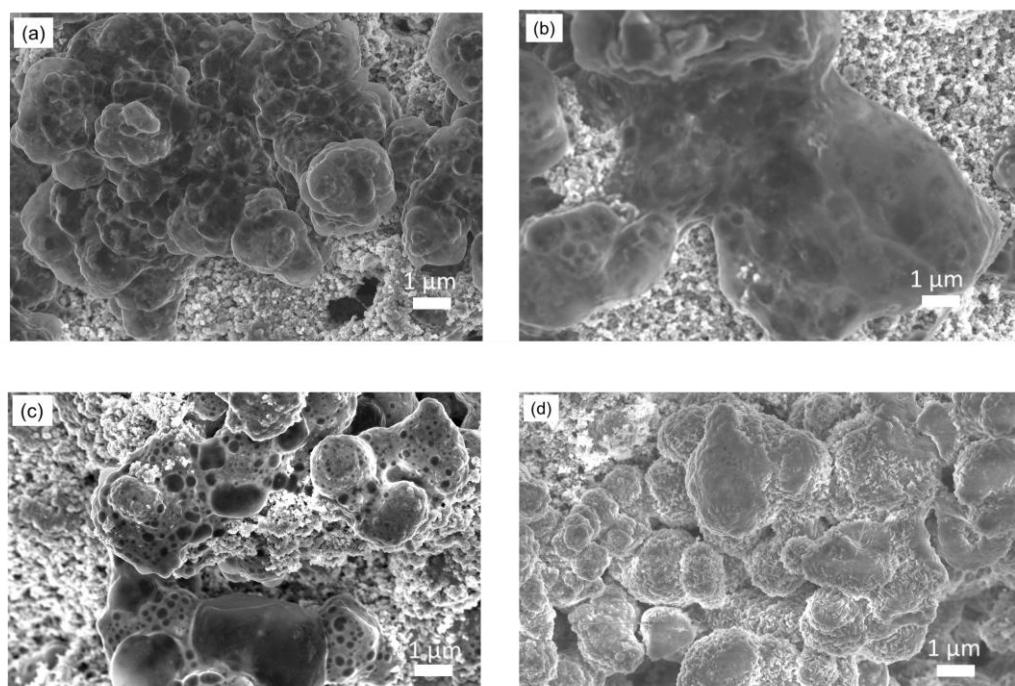


Figure S2: Post-mortem SEM top-view images of Bi_2MoO_6 -based electrodes sodiated to 0.01 V vs Na/Na^+ at different stages of cycling. After a) 1st sodiation, b) 2nd sodiation, c) 10th sodiation and d) 20th sodiation.

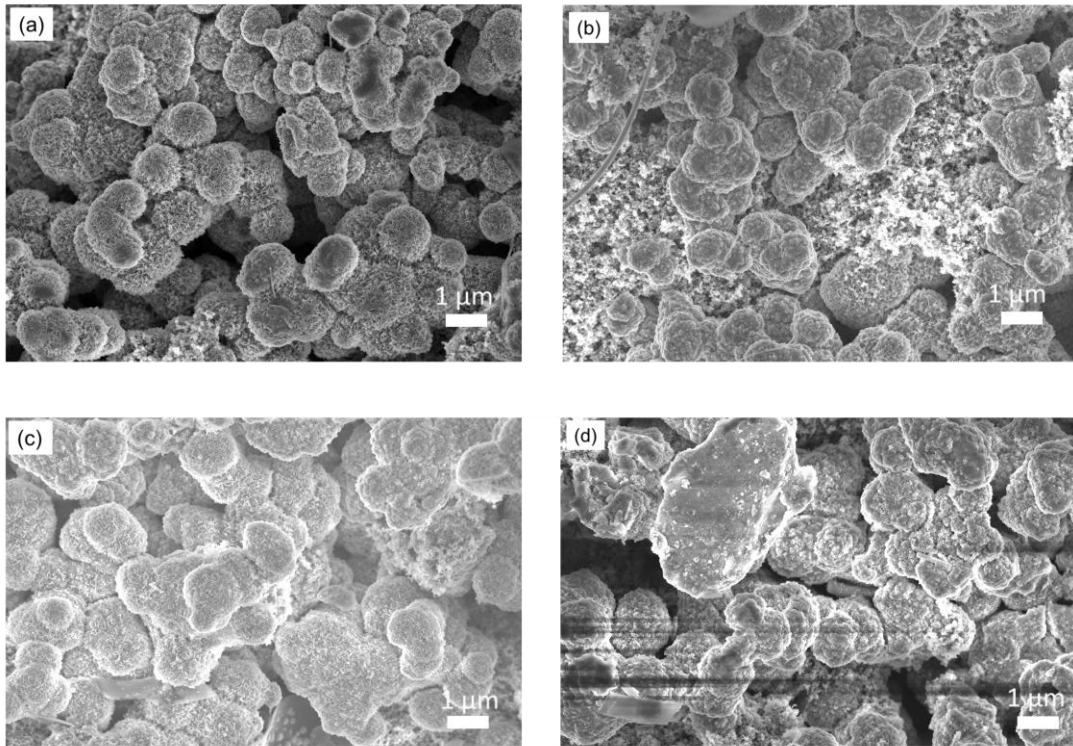


Figure S3: Post-mortem SEM top-view images of Bi_2MoO_6 -based electrodes desodiated to 2.00 V vs Na/Na^+ at different stages of cycling. After a) 1st desodiation, b) 2nd desodiation, c) 10th desodiation and d) 20th desodiation.

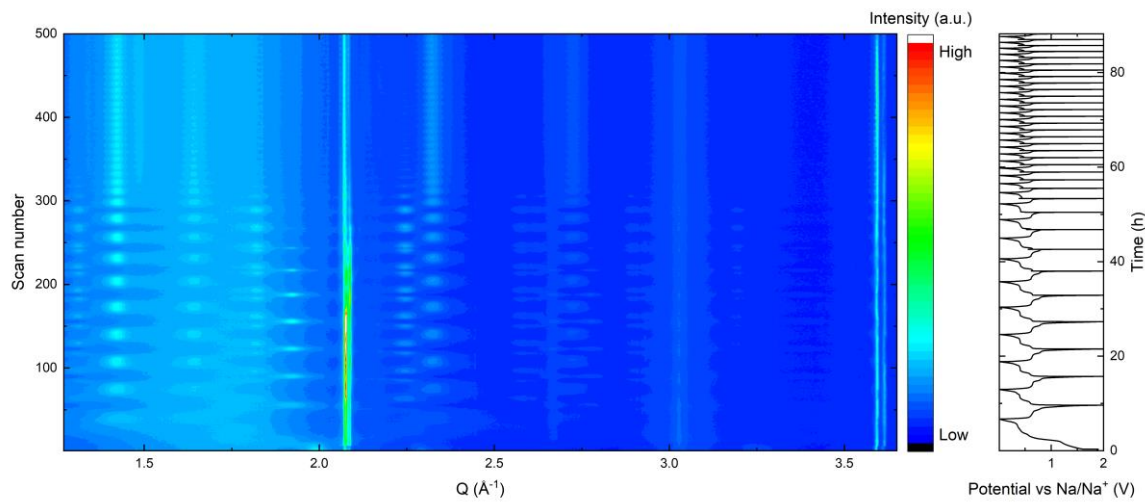


Figure S4: The complete operando XRD contour plot of Bi_2MoO_6 -based electrode cycled for 34 cycles against Na metal.

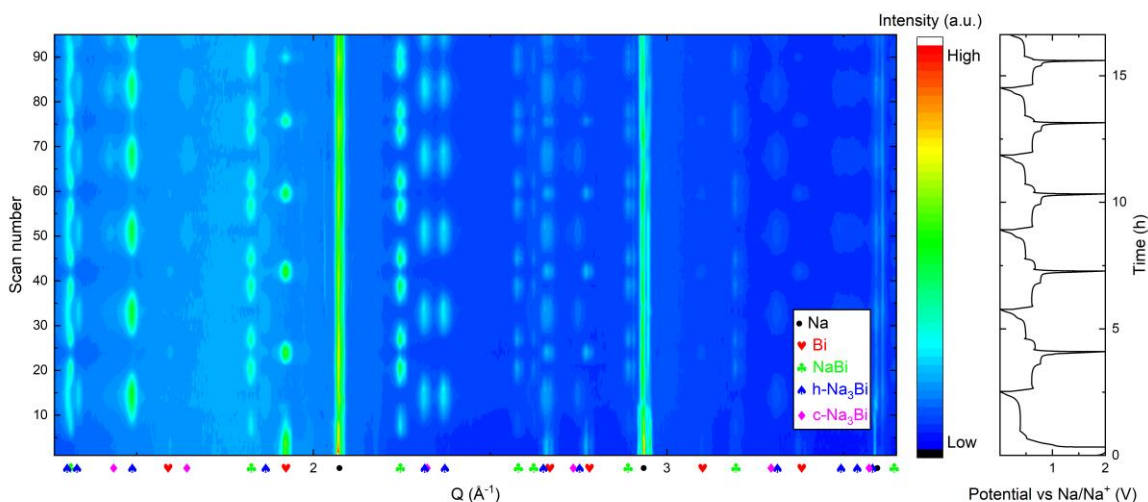


Figure S5: The complete operando XRD contour plot of Bi-metal-based electrode cycled for 6 cycles against Na metal. The procedure is identical to the one described in section 2.6 in the main article.

Section S1.1: Alternative solvothermal syntheses of Bi_2MoO_6 (structural and morphological characterisation)

As a part of this study, in an attempt to improve the electrochemical performance, we performed six solvothermal syntheses in addition to the main synthesis described in the article. The procedure was similar to what we described in section 2.1 in the main article, except for the temperatures and reaction times. Four syntheses were performed at 160 °C and retrieved from the oven after 15 min, 30 min, 1 h and 6 h. We also synthesised two compounds at 200 °C with reaction times of 6 h and 24 h.

From the XRD patterns shown in Figure S6, we observe that the syntheses performed at 160 °C with a reaction time of 15 or 30 min mostly contained Bi_2O (and possibly $\text{Bi}_{3.2}\text{Mo}_{0.8}\text{O}_{7.5}$) while the others (1 h and 6 h) mainly led to the formation of Bi_2MoO_6 . However, the sample synthesised at 160 °C for the duration of 1 h have XRD peaks that are slightly shifted, and possibly another Bi_2MoO_6 phase has formed compared to the syntheses carried out for longer times. It should also be noted that the XRD peaks corresponding to Bi_2MoO_6 , Bi_2O_3 and $\text{Bi}_{3.2}\text{Mo}_{0.8}\text{O}_{7.5}$ overlap, making it difficult to accurately determine the ratio between these phases in the final materials.

The SEM images captured at different magnifications demonstrated that the different synthesis parameters do not have much effect on the morphology of the samples as shown in Figures S7-S10. All the samples consist of agglomerates formed by primary particles with sizes roughly between 1 and 3 μm . The morphology of the particles varies between quite smooth surfaces formed by small nanoplatelets (Figure S9) to particles with a rough surface formed consisting of larger platelets (Figure S10). This was observed for all synthesised materials.

We prepared electrodes from all the synthesised materials and performed electrochemical evaluation in the same way as described in sections 2.3 and 2.4 of the main article, except for the electrolyte used. For the materials synthesised at 160 °C we used 1 M NaPF_6 in EC:DMC, for the material synthesised at 200 °C for 6 h we used 1 M NaPF_6 in PC and for 200 °C at 24 h we used 1 M NaClO_4 in EC:DMC. All electrolytes had in addition 5% FEC. Throughout the work of this study, we have not noticed any significant difference in the electrochemical performance when different electrolytes were used. Even though the materials have different phases, they show very similar behaviour as anode materials. The sodiation-desodiation curves and the dQ/dV plots (Figure S11) show that all the materials have the two characteristic plateaus/peaks corresponding to the Bi-NaBi and NaBi-Na₃Bi reactions. The Bi-NaBi reaction gradually disappears, but for the material synthesised for 6 h or more, it is maintained slightly longer than for the others. This explains why these materials show higher capacity around cycle 5-15 (as shown in Figure S12) before they experience the rapid capacity decay.

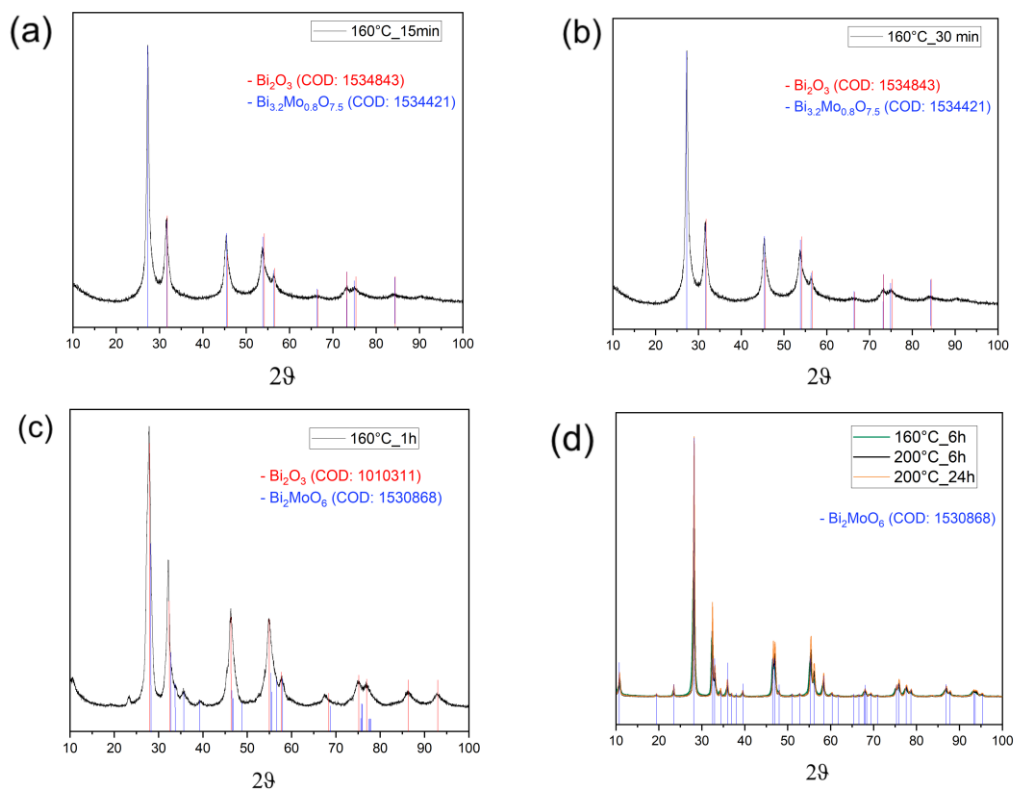


Figure S6: XRD patterns of pristine materials from solvothermal synthesis at different temperatures and times. (a) 160 °C for 15 min, (b) 160 °C for 30 min, (c) 160 °C for 1 h, (d) 160 °C for 6 h, 200 °C for 6 h, 200 °C for 24 h.

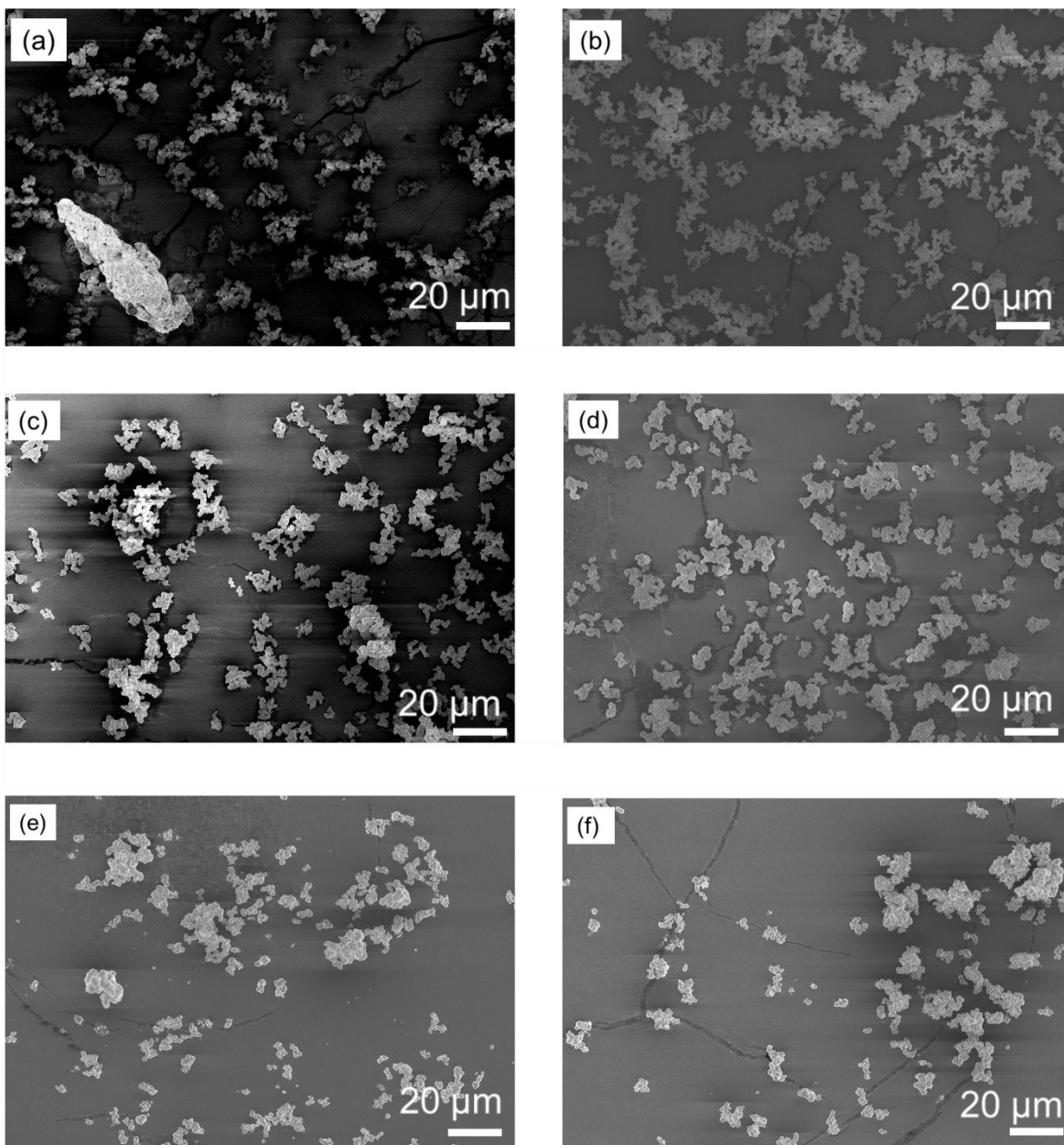


Figure S7: low resolution SEM images demonstrating an overview of the Bi_2MoO_6 particles prepared under different conditions. (a) 160 °C for 15 min, (b) 160 °C for 30 min, (c) 160 °C for 1 h, (d) 160 °C for 6 h, (e) 200 °C for 6 h, (f) 200 °C for 24 h.

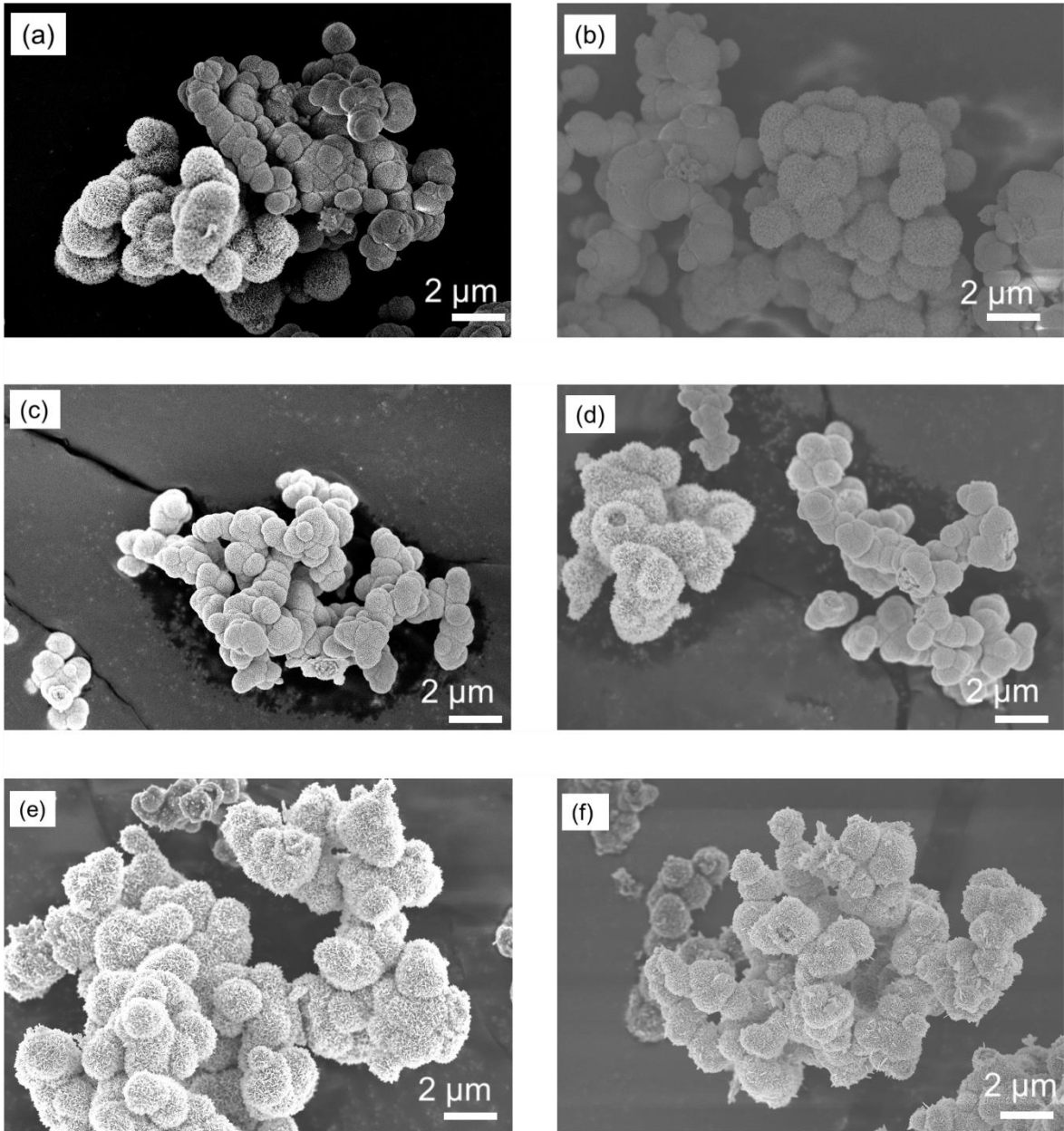


Figure S8: SEM images demonstrating sizes and shapes of selected Bi_2MoO_6 particles prepared under different conditions. (a) 160 °C for 15 min, (b) 160 °C for 30 min, (c) 160 °C for 1 h, (d) 160 °C for 6 h, (e) 200 °C for 6 h, (f) 200 °C for 24 h.

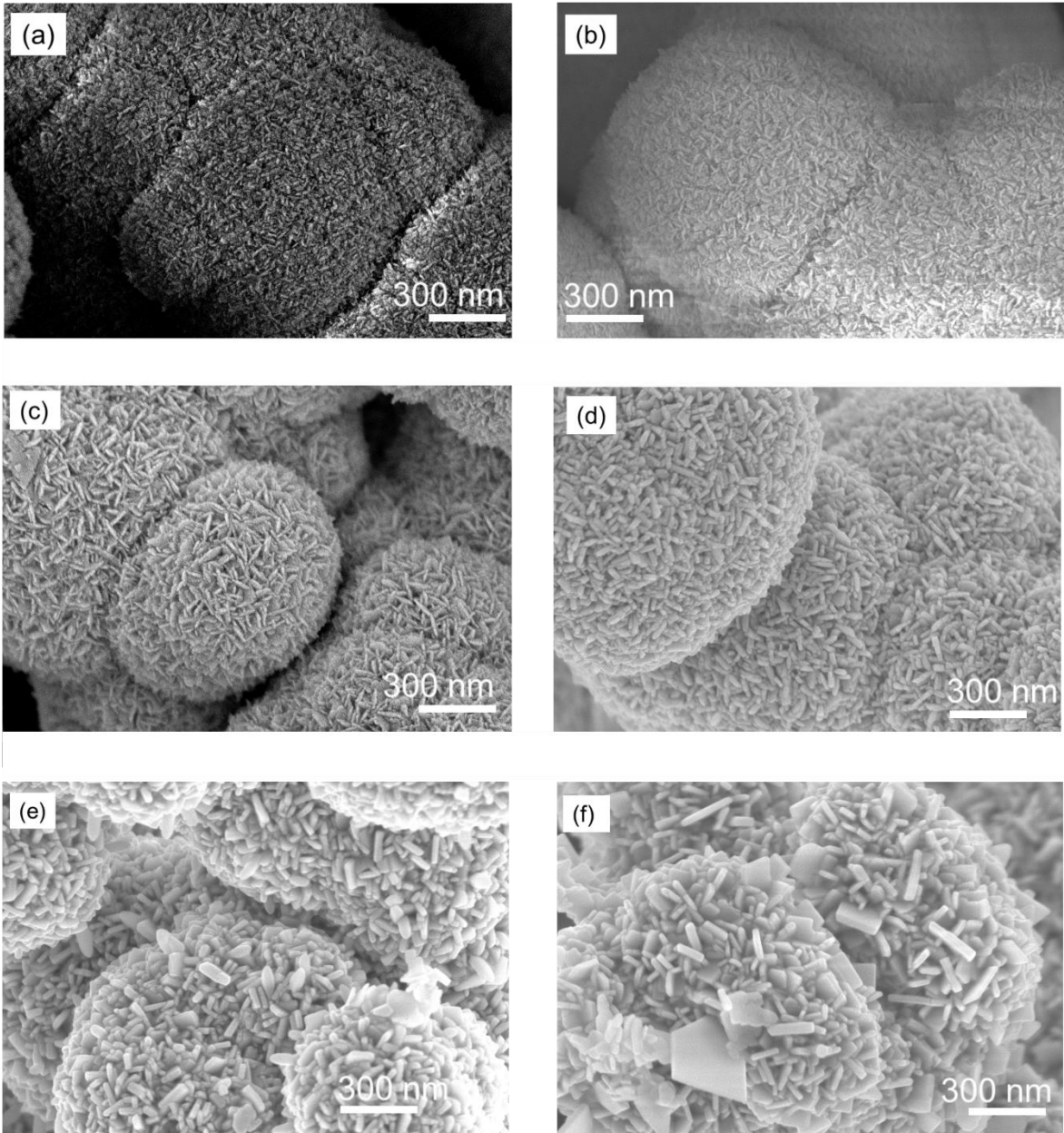


Figure S9: High resolution SEM images illustrating the details at the surface of the Bi_2MoO_6 particles consisting of small nanoplatelets. (a) 160 °C for 15 min, (b) 160 °C for 30 min, (c) 160 °C for 1 h, (d) 160 °C for 6 h, (e) 200 °C for 6 h, (f) 200 °C for 24 h.

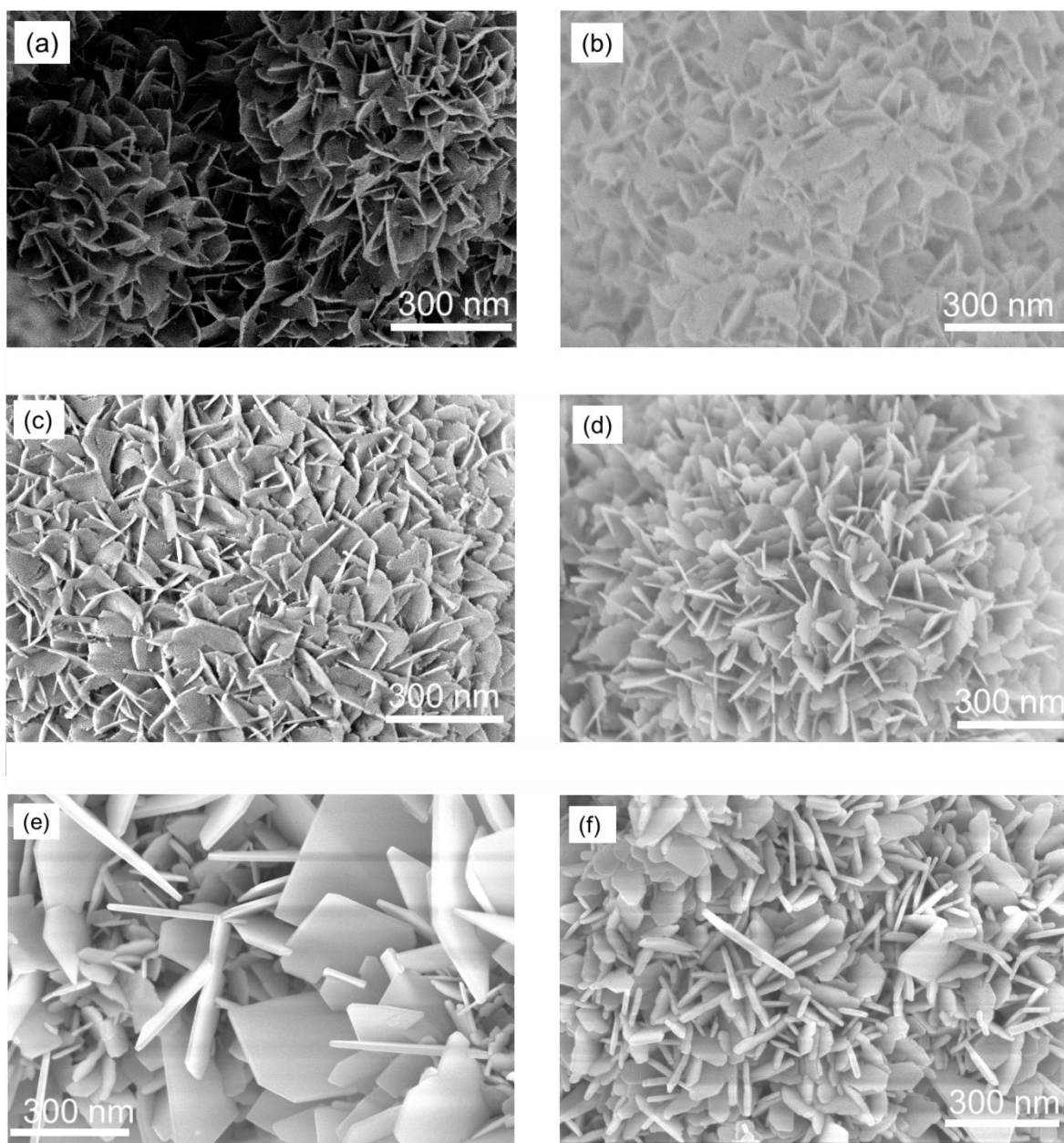


Figure S10: High resolution SEM images illustrating details at the surface of the Bi_2MoO_6 particles consisting of larger platelets. (a) 160 °C for 15 min, (b) 160 °C for 30 min, (c) 160 °C for 1 h, (d) 160 °C for 6 h, (e) 200 °C for 6 h, (f) 200 °C for 24 h.

Section S1.2: Alternative solvothermal syntheses of Bi_2MoO_6 (electrochemical characterisation)

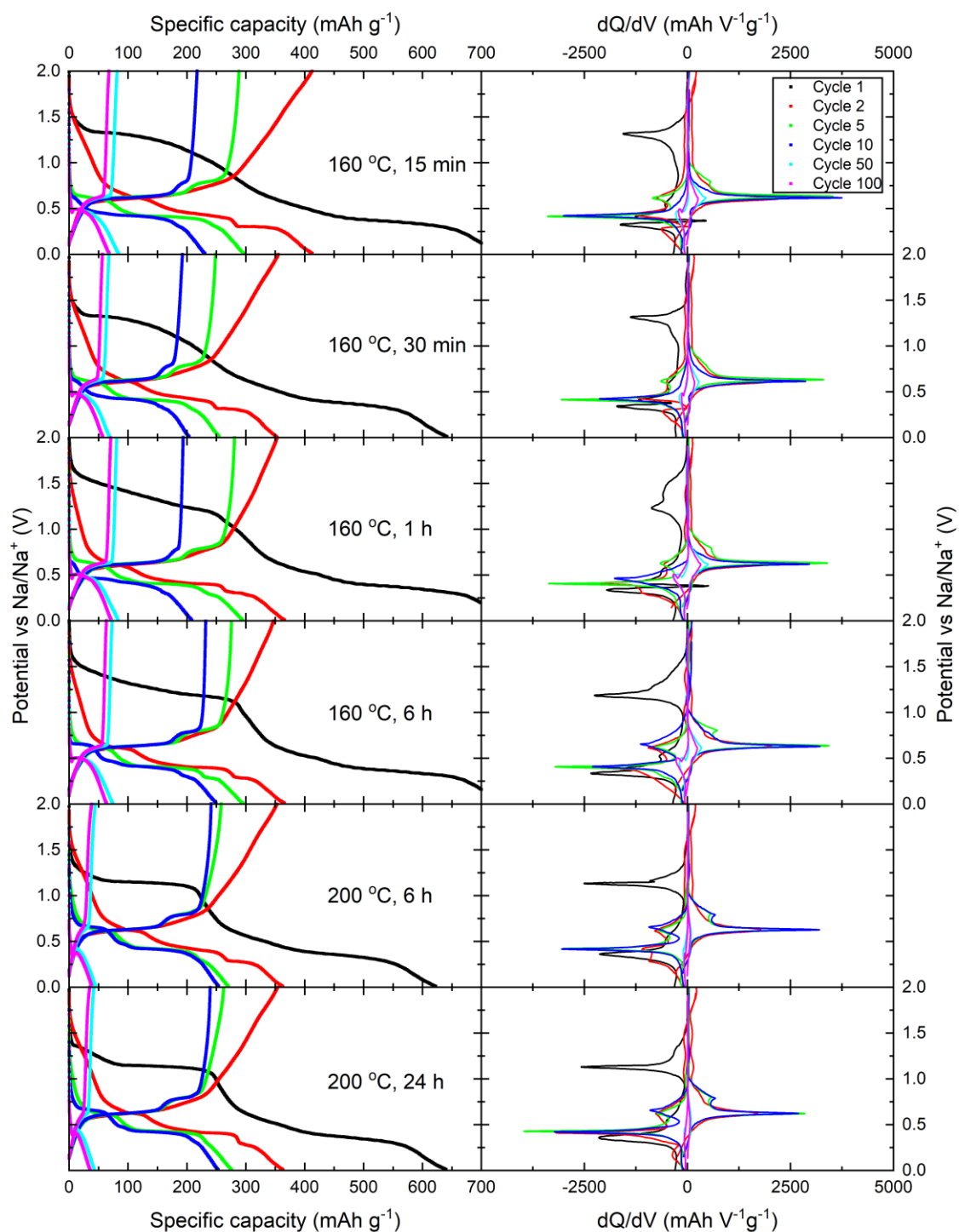


Figure S11: Sodiatio-desodiation curves (left) and dQ/dV plot (right) extracted from GC measurements performed against Na-metal with a voltage range of 0.01-2.00 V vs Na/Na^+ and a specific current of 100 mA g^{-1} on Bi-Mo-O compounds obtained by solvothermal syntheses. The variable synthesis parameters are shown in the figure.

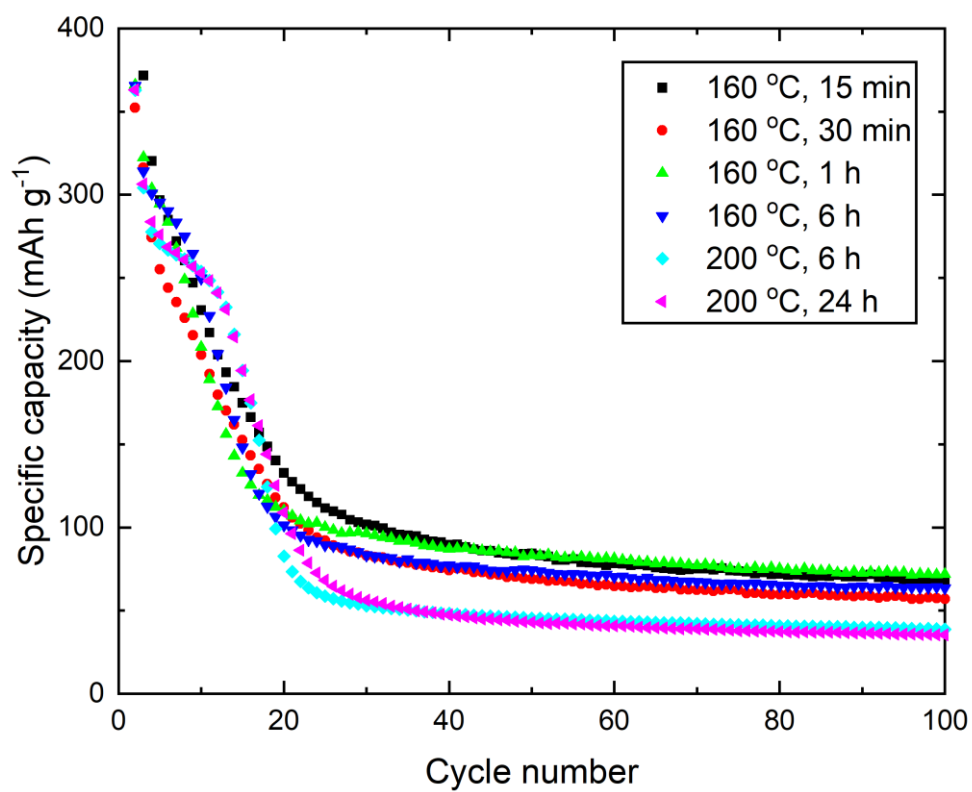


Figure S12: Capacity per cycle plot corresponding to the measurement in Figure S11. The variable synthesis parameters are shown in the figure legend.

Section S2: Super P capacity contribution and uncertainties

Super P, which we use as a conductive additive in our electrodes, does also contribute some to the capacity. To measure this capacity, we prepared electrodes with 80% Super P and 20% PVDF and performed GC measurements on 3 coin cells following the same procedure as for Bi_2MoO_6 (Section 2.5). The active mass of the electrodes was between 1 and 1.2 mg. As we can see from Figure S13, Super P has a very stable specific capacity around 150 mAh g^{-1} for at least 50 cycles. This means that we can subtract approximately 15 mAh g^{-1} from the obtained specific capacities of the other batteries (since we used 10% Super P in the electrodes) to obtain the true capacity contribution of our active material. We also observe that the specific capacity varies a bit between the batteries even though they are constructed to be identical. This means that we have some uncertainties in our specific capacities, and in the case of this dataset, it seems to be around 15%. The most likely explanation for this is that we use a scale in the glovebox to measure the weight of the electrodes, which has an intrinsic uncertainty of 0.1 mg. In practice, this uncertainty might be a bit larger since the scale seems to have some fluctuations while being inside the glovebox. When we work with active masses of only a few mg, this uncertainty will have some influence on the results. After testing many cells, we rarely see deviations larger than 10% and this is good enough for us in this stage of research.

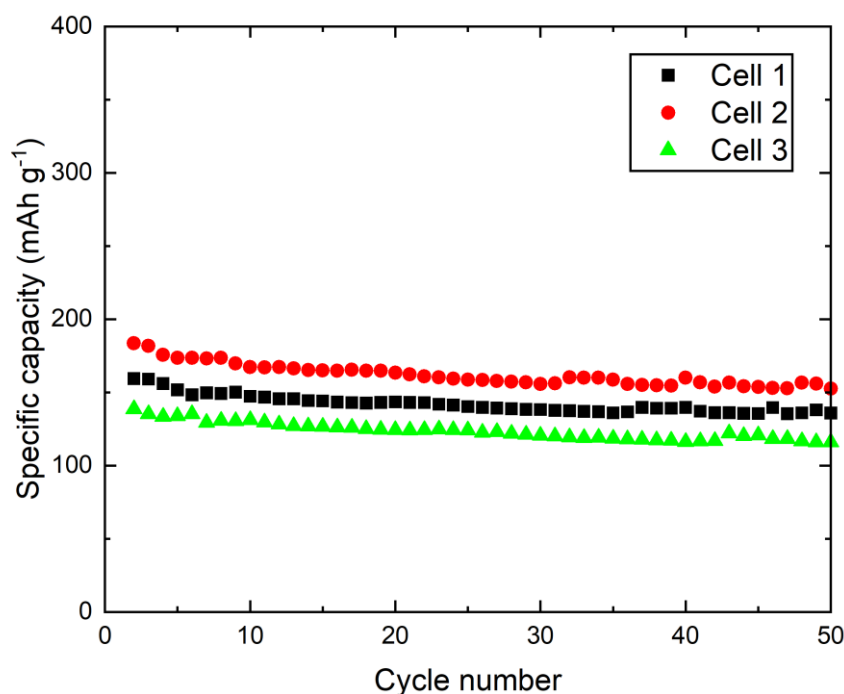


Figure S13: Sodiation capacity per cycle of Super P as active material in Na-half cell measured in 3 independent cells.

Section S3.1: Ball milling of pristine Bi_2MoO_6 , synthesised at 160 °C for 24 h

In an attempt to improve the electrochemical performance of the Bi_2MoO_6 material through nanosizing, we tried ball milling at different speeds and durations. We performed the ball milling with a Pulverisette 7 premium line planetary micro mill (Fritsch) with 3 mm stainless steel balls and a container made of stainless steel. The samples and the balls were introduced to and sealed in the container inside an Argon filled glovebox (MBRAUN, H_2O and O_2 levels were less than 0.1 ppm). We prepared three different samples. One with ball milling for 30 min at 300 rpm, one for 20 min at 700 rpm and one sample ball milled twice for 20 min at 700 rpm. The two last samples are from the same batch. We ball-milled first for 20 min at 700 rpm, then brought the container back inside the glovebox and extracted some of the powder. Following this, we closed the container with the rest of the powder and continued the ball milling for another 20 min. The sample thus produced is referred to in the figures below as “2·20 min at 700 rpm”.

From the XRD patterns (Figure S14), we observed that the sample ball milled for 30 min at 300 rpm have much broader diffraction peaks than the pristine Bi_2MoO_6 . The peak positions for ball-milled Bi_2MoO_6 are the same as for the pristine material indicating the identity of the phase. However, the material that we ball milled for 20 min and twice for 20 min at 700 rpm have formed some metallic Bi in addition to small particles of Bi_2MoO_6 , according to the XRD analysis.

We performed the electrode preparation and GC measurements for ball-milled materials in the same way as described in sections 2.3 and 2.4 of the main article except for the electrolyte where we used 1 M NaClO_4 in EC:DMC and 5% FEC. The (de)sodiation curves and the dQ/dV plots as well as the capacity per cycle plot (Figure S15) demonstrate that the ball-milled materials behave worse than the pristine material.

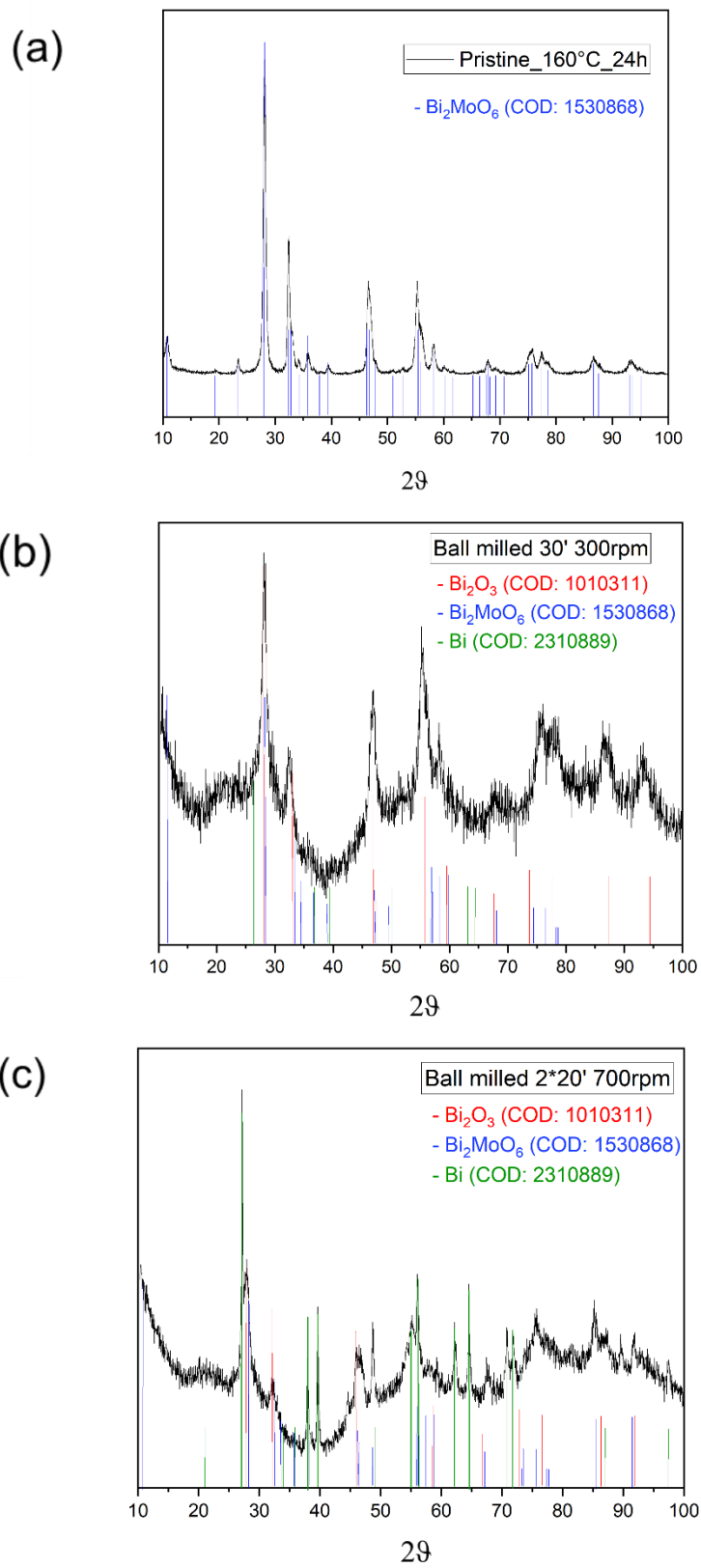


Figure S14: XRD patterns of (a) pristine Bi_2MoO_6 synthesised at 160°C for 24 h, (b) ball milled for 30 min at 300 rpm, (c) ball milled for 2*20 min at 700 rpm.

Section S3.2: Electrochemical evaluation of ball-milled Bi_2MoO_6 materials

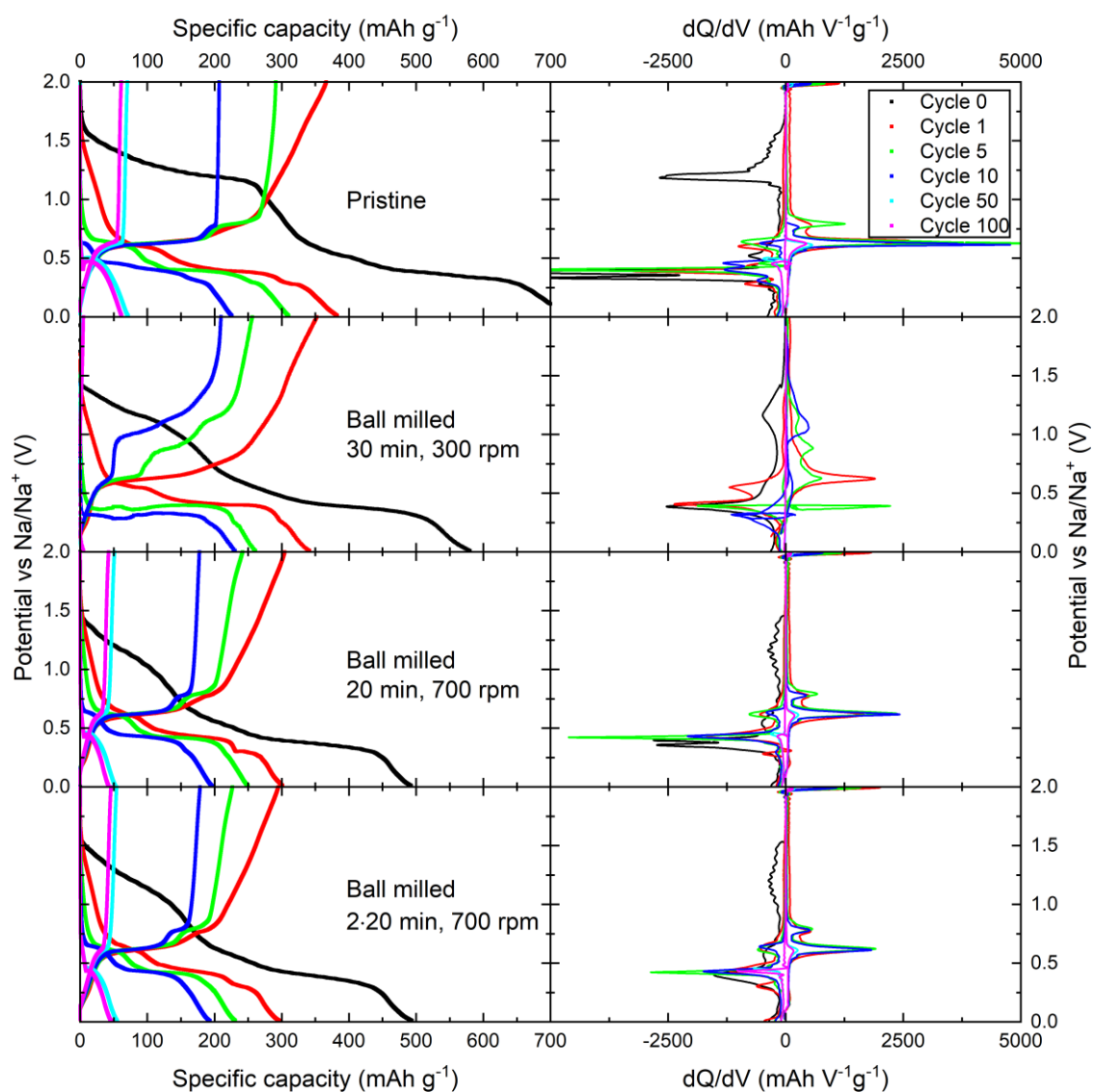


Figure S15: Sodiatio-desodiation curves (left) and dQ/dV plots (right) of pristine and ball-milled Bi_2MoO_6 from GC measurements performed against Na-metal with a voltage range of 0.01-2.00 V vs Na/Na⁺ and a specific current of 100 mA g⁻¹. The conditions for ball milling are shown as figure legends.

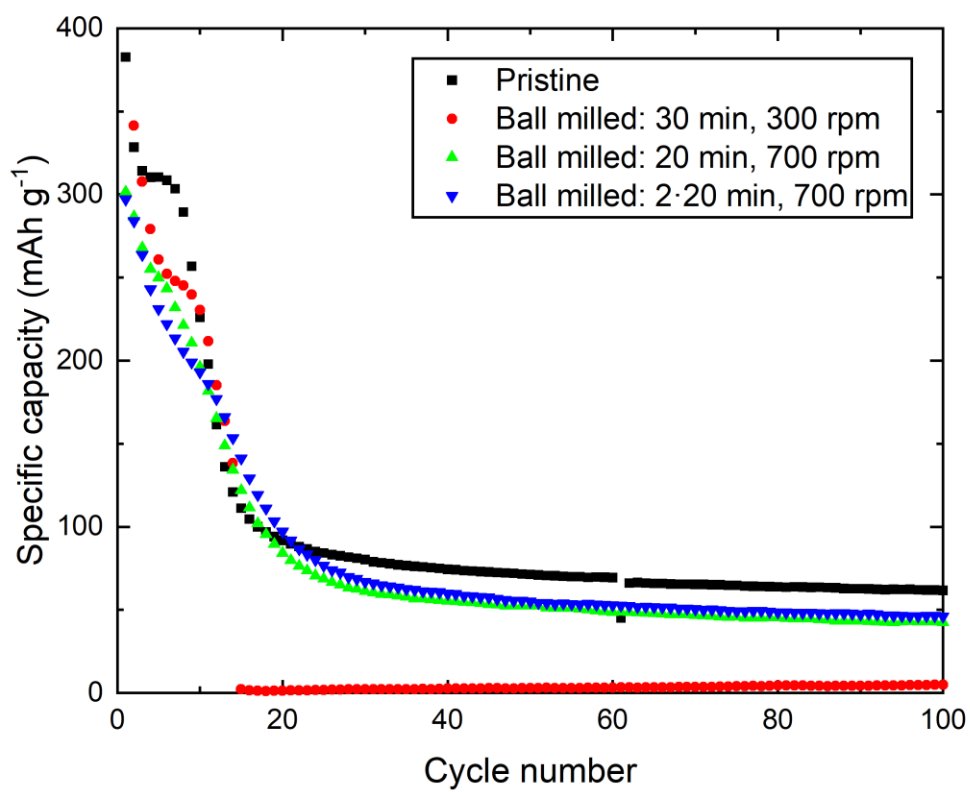


Figure S16: Capacity per cycle for pristine Bi_2MoO_6 (black), ball milled for 30 min at 300 rpm (red), ball milled for 20 min at 700 rpm (green) and 2·20 min at 700 rpm (blue).

Section S4: Effect of amount of electrolyte

To determine the cause of the capacity decay we studied a similar Bi_2MoO_6 material (synthesised at 200 C for 6 h), in terms of the consumption of electrolyte.

We prepared cells containing 80 μL (the standard amount used in this work) and 120 μL of electrolyte. Furthermore, we fabricated one more cell containing 80 μL of electrolyte, but after 10 cycles we extracted the electrode and placed it in a new cell with fresh electrolyte (80 μL) and fresh Na counter electrode. The electrolyte used was 1 M NaPF_6 in EC:DMC and 5% FEC and the cells were cycled with 100 mA g^{-1} between 0.01 and 2.00 V vs Na/Na^+ and a 12 h rest before the start of cycling. The cells did not show any significant difference in electrochemical performance and all of the cells experienced a rapid capacity decay between cycles 10 and 20 (Figure S17).

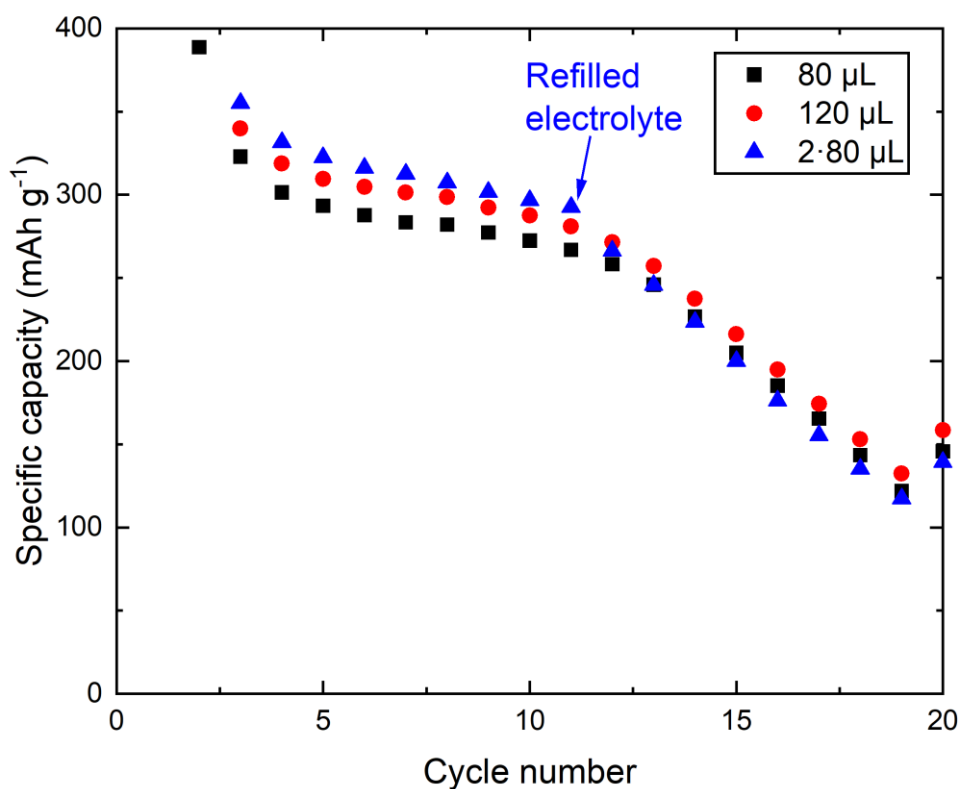


Figure S17: Specific sodiation capacity of Bi_2MoO_6 vs Na counter electrode with different amounts of electrolyte.

Section S5: Impedance spectroscopy

To characterise the changes in conductivity during cycling we performed electrochemical impedance spectroscopy (EIS) on the studied cells after the 1st sodiation and the 20th sodiation (Figure S18). The EIS spectra were collected by using an MPG2 (Biologic) with frequencies ranging from 20 kHz and 100 mHz with an amplitude of 10 mV.

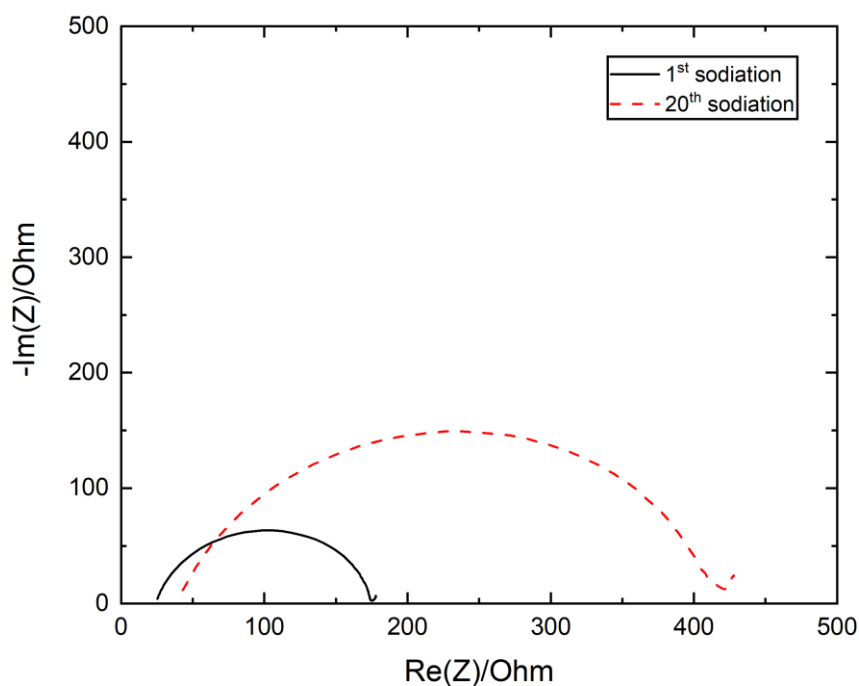


Figure S18: Nyquist plot of Bi_2MoO_6 -based electrodes after 1st sodiation and 20th desodiation to 0.01 V vs Na/Na⁺. The studied samples correspond to the post-mortem SEM images in Figure S2a and S2d, respectively.

References:

- [1] J. Sottmann *et al.*, "How Crystallite Size Controls the Reaction Path in Nonaqueous Metal Ion Batteries: The Example of Sodium Bismuth Alloying," *Chemistry of Materials*, vol. 28, no. 8, pp. 2750–2756, 2016, doi: 10.1021/acs.chemmater.6b00491.

Paper 4

Unravelling the (de)sodiation mechanisms of BiFeO₃ at a high rate with *operando* XRD

A. Brennhagen, C. Skautvedt, C. Cavallo, D. S. Wragg, A. Y. Kopusov, A. O. Sjøstad, and H. Fjellvåg

Accepted by *ACS Applied Materials & Interfaces*

Unravelling the (de)sodiation mechanisms of BiFeO₃ at a high rate with *operando* XRD

Anders Brennhagen^{1*}, Casper Skautvedt¹, Carmen Cavallo², David S. Wragg^{1,3}, Alexey Y. Kuposov^{1,3}, Anja O. Sjøstad¹, Helmer Fjellvåg^{1*}.

¹Centre for Materials Science and Nanotechnology, Department of Chemistry, University of Oslo, PO Box 1033, Blindern, N-0315, Oslo, Norway

²CENATE, Centrifugal Nanotechnology, Rakkestadveien 1, 1814, Askim, Norway

³Department of Battery Technology, Institute for Energy Technology (IFE), Instituttveien 18, 2007, Kjeller, Norway

E-mail: anders.brennhagen@smn.uio.no and helmer.fjellvag@kjemi.uio.no

Keywords: BiFeO₃, Na-ion battery, *operando* XRD, high rate cycling, conversion-alloying materials

ABSTRACT

Development of new anode materials for Na-ion batteries strongly depends on detailed understanding of their cycling mechanism. Due to instrumental limitations, the majority of mechanistic studies focus on *operando* materials' characterisation at low cycling rates. In this work, we evaluate and compare the (de)sodiation mechanisms of BiFeO₃ in Na-ion batteries at different current densities using *operando* X-ray diffraction (XRD) and *ex situ* X-ray absorption spectroscopy (XAS). BiFeO₃ is a conversion-alloying anode material with high initial sodiation capacity of ~600 mAh g⁻¹, when cycled at 0.1 A g⁻¹. It does not change its performance and cycling mechanism, except for minor losses in capacity, when the current density is increased to 1 A g⁻¹. In addition, *operando* XRD characterisation carried out over multiple cycles shows that the Bi ⇌ NaBi (de)alloying reaction and the oxidation of Bi at the interface with Na-Fe-O matrix are detrimental for cycling stability. The isolated NaBi ⇌ Na₃Bi reaction is less damaging for the cycling stability of the material.

Introduction

Na-ion batteries (NIBs) have been long viewed as promising alternatives to modern Li-ion batteries (LIBs), due to the high abundance and low cost of Na that can make up for the slightly lower energy densities [1-3]. The application of NIBs is particularly promising in stationary energy storage, where high power is necessary and energy density is less crucial [4]. However, further optimisation of NIBs for high power applications requires development of suitable anode materials, which performance will not suffer at elevated cycling rates. High rate capabilities and ability to achieve a good compromise between high capacity and cycling stability make conversion-alloying materials (CAMs) a promising group of compounds [5-7]. However, their complex cycling and degradation mechanisms, often involving formation of amorphous phases, make them challenging to develop further. In order to determine the (de)sodiation mechanisms of these materials it is essential to use *operando* methods, where the structural characterisation is performed during electrochemical cycling. This methodology is superior to *ex situ* characterisation due to potential structural relaxation of active materials and risk of side reactions with the environment when the materials are extracted from coin cells during preparation of *ex situ* samples [8-10].

The general cycling mechanism of CAMs at low cycling rates ($<150 \text{ mA g}^{-1}$) has been revealed through several studies on LIBs and NIBs with *operando* techniques including X-ray diffraction (XRD), X-ray absorption spectroscopy (XAS) and total scattering computed tomography (TSCT) coupled with *ex situ* and *in situ* transmission electron microscopy (TEM) [11-19]. These studies have confirmed a conversion reaction during the first sodiation/lithiation, which leads to a phase separation with formation of nanosized particles of the alloying element (Si, Ge, Sn, Sb, Bi) distributed in a Na_xX ($\text{X} = \text{O, S, Se, Te, P, oxometallates}$) matrix [6]. During the following cycles the particles of the alloying element are the main contributors to the capacity. However, there are reports of partially reversible conversion reactions in the binary CAMs [11, 18] and electrochemical activity in the transition metal in the matrix of ternary CAMs adding to the capacity [13, 20, 21].

Bi metallates are a group of ternary CAMs, which exhibit high capacities as anode materials in NIBs. BiFeO_3 , $\text{Bi}_2(\text{MoO}_4)_3$, BiVO_4 and Bi_2MoO_6 have previously been explored with primary focus on cycling stability [14, 20, 22, 23]. In line with the general cycling mechanism of CAMs, Bi metallates undergo an irreversible conversion reaction during the first sodiation to produce Bi nanoparticles embedded in a Na-TM-O (TM = transition metal) matrix. The Bi particles then reversibly transform into Na_3Bi (*via* NaBi as an intermediate phase) during sodiation [20, 22]. There are two known polymorphs of Na_3Bi , hexagonal (h- Na_3Bi) and cubic (c- Na_3Bi). The h- Na_3Bi phase is thermodynamically stable and has been observed to form from microcrystalline NaBi particles, while c- Na_3Bi forms in nanocrystalline NaBi particles (for example those formed in Bi metallates) [20, 24]. The buildup of h- Na_3Bi during prolonged cycling of Bi-metallates has been linked to particle growth and capacity degradation [22]. Despite significant efforts, we still lack a generalised understanding of the evolution of Na_xBi particles and the Na-TM-O matrix during cycling [14, 20, 21].

BiFeO_3 is perhaps the most straightforward chemical system among Bi metallates. It has shown reversible (de)sodiation capacities up to 600 mAh g^{-1} , but its cycling stability is limited and the operating mechanism is still disputed [14, 25]. Surendran *et al.* performed *operando* XAS on BiFeO_3 and proposed the formation of metallic Fe in addition to Na_2O and an Fe-based oxide during the initial conversion reaction [14]. The same study also showed the presence of Bi-O bonds after the first desodiation, indicating a partial oxidation of Bi metal as was determined by Fourier transformed (FT) extended X-ray absorption fine structure (EXAFS) [14].

The majority of *operando* studies of CAMs has been performed at low current densities and, to the best of our knowledge, there are no *operando* studies addressing the cycling mechanisms of these materials at high cycling rates. This lack of insight is due to the challenges associated with conducting *operando* measurements at high rates: performing reliable electrochemistry in an *operando* cell with an electrode thick enough to obtain sufficient intensity of X-ray signals. Another limiting factor is the availability of X-ray sources, as synchrotron radiation is needed to obtain high quality data with high time resolution. In this article, we conducted *operando* XRD measurements, with current densities of 0.1 A g^{-1} and 1 A g^{-1} , to elucidate and compare the electrochemical cycling mechanism of BiFeO_3 at low and high rates. We also deployed *operando* XRD over 27 (de)sodiation cycles combined with *ex situ* XAS to gain further understanding of the interplay between the Na_xBi alloying particles and the Na-Fe-O matrix and their influence on the cycling stability of BiFeO_3 .

Results and Discussion

Materials and electrochemical characterisation

Synthesis of phase pure BiFeO_3 is recognised as challenging owing to competing ternary phases [25]. After optimisation of the reaction conditions, we managed to synthesise BiFeO_3 with small amounts of Bi_2O_3 ($\sim 12 \text{ wt}\%$ according to Rietveld refinement) by means of a sol-gel synthesis route (Figure S1, Section S1, SI). The Bi_2O_3 impurities were successfully removed by leaching with nitric acid (Figure S2, SI), but the resulting product showed poor electrochemical performance (Figure S3, SI). Therefore, the unleached product was used for further work.

The electrochemical performance of BiFeO_3 was evaluated at different cycling rates with both galvanostatic cycling (GC) and cyclic voltammetry (CV) (Figure S4, Section S2, SI). The initial sodiation capacity of BiFeO_3 , obtained from GC measurements, was $\sim 600 \text{ mAh g}^{-1}$ at 0.1 A g^{-1} , comparable to that of literature reports [14, 25]. In addition, fast cycling was undertaken at 1 A g^{-1} where BiFeO_3 maintained reasonable performance. The cycling stability, even at 0.1 A g^{-1} , is nevertheless challenging and the capacity drops from $\sim 450 \text{ mAh g}^{-1}$ to $\sim 130 \text{ mAh g}^{-1}$ after 25 cycles.

Elucidation of cycling mechanism at low and high rates

Due to experimental limitations, *operando* studies are typically performed under slow cycling conditions, often quite different from the cycling protocols that electrode materials are subjected to in normal use. *Operando* characterisation at high cycling rates is rare, despite the fact that understanding of the material's behaviour under such conditions is critical for the development of batteries with high power [26, 27]. Several CAMs have shown promising electrochemical performance at high rates [25, 28, 29], but their cycling mechanisms at these high current densities have not been studied with *operando* structural methods. To address this problem, we performed *operando* XRD on BiFeO_3 -based electrodes using synchrotron radiation at BM31 at the European Synchrotron Radiation Facility (ESRF) during electrochemical cycling at 1 A g^{-1} in half cell configuration using Na foil as a counter electrode (Figure 1a-c). Surprisingly, BiFeO_3 is fully sodiated to Na_3Bi in the first sodiation despite the high current density, confirming that BiFeO_3 can maintain the same cycling mechanism and capacity at 1 A g^{-1} as at lower cycling rates [14, 25]. Overall, the cycling mechanism was found to be similar to that proposed previously for BiFeO_3 and confirmed by *operando* and *post-mortem* studies in other Bi metallates [14, 20, 22, 25]. The minor, but significant difference for BiFeO_3 compared to other Bi metallates is the formation of both h- Na_3Bi and c- Na_3Bi phases

during the first sodiation, regardless of the current density. This is different from what was shown for BiVO_4 , $\text{Bi}_2(\text{MoO}_4)_3$ and Bi_2MoO_6 as they formed only c- Na_3Bi during the first cycles [20, 22]. The formation of h- Na_3Bi has been shown to form in microsized NaBi particles, while c- Na_3Bi forms from nanosized NaBi particles [24]. Therefore, the presence of h- Na_3Bi phase after the first sodiation is rather unusual, as the presence of h- Na_3Bi has been linked to long-term deactivation of the Bi metallates [22, 24]. Furthermore, this suggests that the Bi particles formed after sodiation are slightly larger than what has been observed for other materials with similar chemistry. This indicates that the size and mobility of the alloying particles could be tuned by customising the surrounding matrix.

To look for possible variations in the cycling mechanism at different rates, another *operando* measurement was performed with a current density of 0.1 A g^{-1} (Figure 1d-f). As expected, the measurements at 0.1 and 1 A g^{-1} showed the same general cycling mechanism. However, one significant difference was observed: At 1 A g^{-1} the diffraction peaks for the Na-Bi phases are less defined than for the 0.1 A g^{-1} measurement. The challenges with performing a high-rate *operando* XRD measurement forced us to find an acceptable compromise between counting statistics and time resolution, while maintaining the electrochemical performance, which results in less defined diffraction peaks. However, an alternative explanation arises from the lack of time required for the crystallisation of the observed phases at high cycling rates, and, therefore, the corresponding peaks do not reach their maximum intensity and sharpness. The limited intensity of the diffraction peaks observed at the 1 A g^{-1} measurement made the h- Na_3Bi phase difficult to deconvolute from c- Na_3Bi and was therefore not included in the surface Rietveld refinement.

In addition to the rate comparison, the measurement conducted at 0.1 A g^{-1} provided more detailed insight into the cycling mechanism. Because of the sharper and more intense diffraction peaks it was easy to distinguish all the different Na_xBi phases and determine the exact moment of their formation. Phase fractions obtained from surface Rietveld refinement show that the c- Na_3Bi phase forms before h- Na_3Bi (Figure 1f). This is likely because the nucleation of Na_3Bi within the NaBi particles results in the c- Na_3Bi phase, a transformation shown to be more kinetically favourable than that from NaBi to the thermodynamically stable h- Na_3Bi [24]. The formation of h- Na_3Bi starts later and proceeds at the cost of c- Na_3Bi indicating a transformation from the cubic to the hexagonal phase, possibly when the Na_3Bi crystallites grow to a certain size. Another explanation is that a significant Na deficiency may stabilise in the c- Na_3Bi structure and that h- Na_3Bi forms as full sodiation is achieved: Towards the end of sodiation there is a significant timeslot after the disappearance of NaBi where only the two Na_3Bi phases are present, while the electrochemistry is still active (grey areas in Figure 1f). This transformation cannot be treated as a relaxation process as it is electrochemically driven: *Ex situ* XRD measurements of a sodiated sample conducted two weeks after cell disassembly confirmed the presence of c- Na_3Bi and h- Na_3Bi phases in approximately 7:2 ratio (Figure S5).

Another notable observation is that the time that the NaBi phase is present is significantly shorter during desodiation than sodiation. This could be explained by the formation and dissolution of the SEI layer for each cycle as shown for Bi_2MoO_6 in our previous study [22]. The formation of SEI during sodiation consumes Na ions and, therefore, contributes to the capacity. This formation prolongs the duration of the sodiation, while the dissolution process during desodiation does not contribute significantly to the capacity. Another possibility is that the reaction paths during desodiation is slightly different than for sodiation, which has previously been shown for the alloying reactions between Na and P [30].

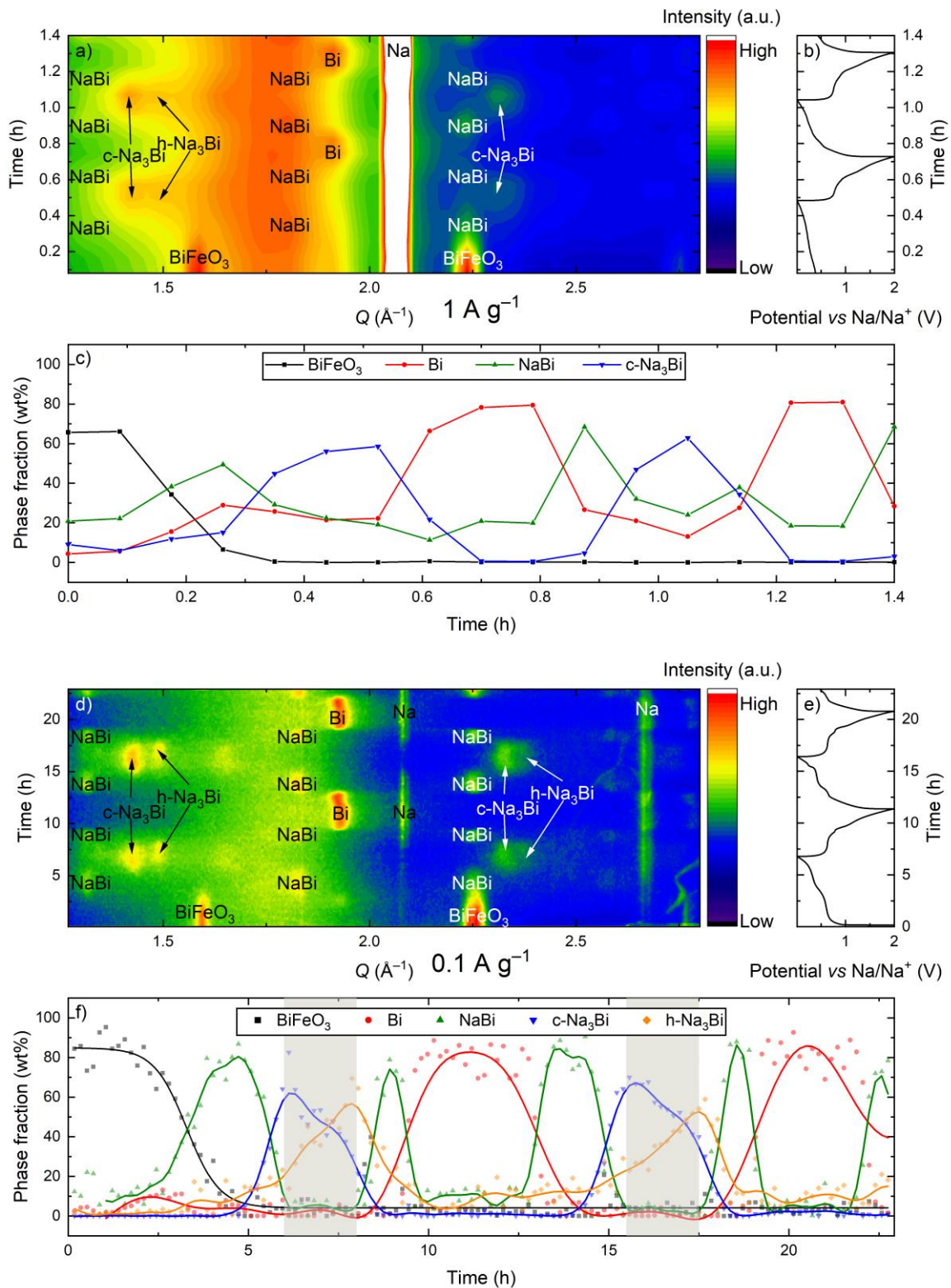


Figure 1: a) Contour plot derived from high-rate *operando* XRD measurement of 2 (de)sodiation cycles of BiFeO₃, measured with synchrotron radiation at BM31 at ESRF, b) corresponding (de)sodiation curves measured at 1 A g⁻¹. c) Phase fractions in wt% retrieved from surface Rietveld refinement of the diffraction patterns plotted in a), showing the evolution of the Bi-containing phases as a function of scan number. The h-Na₃Bi phase is omitted from the surface Rietveld refinement due to limited data quality at the high data collection rate. d)-f) Corresponding graphs for *operando* XRD measurement from the home lab with a current density of 0.1 A g⁻¹. The grey areas in f) highlights the regions where only c-Na₃Bi and h-Na₃Bi is present.

Oxidation of Bi and the nature of the Na-Fe-O matrix

Most of the works on CAMs have been primarily focused on the electrochemically active materials, while the chemistry of matrix and its interaction with the active component is still poorly understood. The XRD data described above combined with *ex situ* XAS measurements provided information of the local structure in the matrix material, the nature of its chemical interaction with the alloying particles and how they influence each other.

In the desodiated state between ~10–13 h (>1 V) the only detectable XRD peak from the working electrode is the peak corresponding to Bi metal (Figure 1d-f). However, a significant capacity (~200 mAh g⁻¹) is observed when assessing the contribution above 1 V during the first desodiation (Figure S4c), which suggests that additional chemical transformations other than (de)sodiation of Na_xBi particles take place at this voltage window. The *ex situ* XAS measurements of the Bi L3 edge, confirmed that the oxidation state of Bi in the fully desodiated sample is higher than 0 (Figure S6). The FT EXAFS analysis also shows a clear peak corresponding to Bi-O bonds, together with Bi-Bi bonds similar to that observed for the Bi-metal reference (Figure S6b and d). Thus, the capacity contribution above 1 V vs Na/Na⁺ is attributed to the oxidation of Bi, which was also shown by Surendran *et al.* through *operando* XAS measurements [14]. This oxidation of Bi can be explained by Bi-O bonds at the interface between the Bi particles and the Na-Fe-O matrix. The contribution from the Bi-O bonds will be significant as long as the Bi particles are relatively small (<10 nm) so that the surface-to-volume ratio is large. In the region where Bi has a positive oxidation state the main diffraction peak of Bi seems to shift slightly towards higher Q values during desodiation, and back again during sodiation (Figure 1d). At this point, we are not able to explain this phenomenon.

There are no signs of the Na-Fe-O matrix in the *operando* XRD measurements, as all the peaks in the XRD pattern can be assigned to the alloying particles (Na_xBi phases) and the Na metal used as a counter electrode. The *operando* XAS study of Surendran *et al.* showed that Fe was redox active and contributed some to the capacity during electrochemical cycling of BiFeO₃ [14]. However, there are no clear plateaus in the (de)sodiation curves in our measurements that should correspond to the reduction/oxidation of Fe. Given the amorphous nature of the Fe-containing phase(s), it would likely exhibit a very gradual redox reaction that is difficult to observe in the (de)sodiation processes dominated by electrochemistry of Bi. Our *ex situ* X-ray absorption near edge spectroscopy (XANES) measurements on cycled samples showed a shift in the edge position of Fe proving that it is electrochemically active (Figure S7), even though it is to a smaller extent than what Surendran *et al.* showed in their *operando* measurement [14]. The apparent differences between Surendran's and our results could originate from different morphology of the particles and/or inherent differences between *ex situ* vs *operando* measurements. The XANES data also indicate a significant change in local coordination around the Fe atoms, where a pre-edge peak appears during the first sodiation (Figure S7a). This pre-edge feature is characteristic for tetrahedral coordination of Fe, similar to that in Fe₃O₄, as opposed to the octahedrally coordinated Fe in BiFeO₃ that shows no significant pre-edge feature (Figure S7a). Apart from this small change in oxidation state and coordination of Fe, it is difficult to assess the Fe-containing phase(s). However, these results still suggest a dynamic nature of the Na-Fe-O matrix, which might be responsible for the degradation of the material.

Material degradation

To further understand the degradation processes in BiFeO₃, we performed *operando* XRD for 27 cycles between 0.01–2.00 V in half cell configuration using Na foil as a counter electrode (Figure S8). Since BiFeO₃ has the same cycling mechanism at different current densities, a

current density of 0.2 A g^{-1} was selected to obtain a good compromise between total measurement time, time resolution and data quality. Detailed analysis of the *operando* XRD data was combined with *ex situ* XAS measurements of the Bi L3 edge (Figure 2 and Figure S9, SI). Based on the behaviour of BiFeO_3 , the degradation mechanism could be divided into 3 well defined regions, where each region is characterised by one specific redox reaction that determines the capacity decay.

Region 1 corresponds to the first 6 cycles and is assigned based on the disappearance of the oxidation of Bi (region 1 in Figure 2a and b). The XAS data from samples extracted after the 1st and 5th desodiation supports the statement that the capacity decay in this region is due to disappearance of Bi–O bonds at the interface between the Bi particles and the Na–Fe–O matrix (Figure 2c and d). All desodiated samples show characteristic signals for Bi–Bi bonds between 2–3.4 Å in the FT EXAFS graphs, indicating the presence of Bi metal (Figure 2d). At the same time, the position of the Bi XANES edge after 1st desodiation is between the position of Bi metal (Bi^0) and BiFeO_3 (Bi^{3+}), meaning that Bi in this sample has a positive average oxidation state roughly between 1–2 (Figure 2c). Furthermore, there are clear signals in the FT EXAFS graphs of Bi–O bonds after the 1st desodiation between R values 1–2 Å, which mostly disappear after the 5th desodiation likely due to coalescence of Bi leading to larger particles inside the Na–Fe–O matrix. The analysis of the diffraction patterns in the fully desodiated state reveals that the diffraction peaks corresponding to the Na_xBi alloys become more pronounced as cycling progresses, confirming increase of crystallite size (Figure S8, SI). This provides a rationale for the disappearance of the oxidation reaction as bigger particles will have a smaller surface-to-volume ratio and, therefore, fewer Bi–O bonds.

Between cycles 6–15 (region 2) the diffraction peaks of Bi gradually disappear together with the (de)sodiation plateaus corresponding to the $\text{Bi} \rightleftharpoons \text{NaBi}$ reaction (Figure 2a and b). The same was observed for Bi_2MoO_6 between cycles 4–9 (Figure S10, SI) [22]. From cycle 15–26 for BiFeO_3 (Figure 2a and b) and cycle 9–13 for Bi_2MoO_6 (Figure S10, SI) the intensities of the NaBi peaks are also greatly reduced indicating that the $\text{NaBi} \rightleftharpoons \text{Na}_3\text{Bi}$ alloying reaction becomes partially irreversible and that the system locks itself in the sodiated state (region 3). Following this, the capacity stabilises at $\sim 20\%$ of its initial desodiation capacity and the main capacity contribution comes from some redox activity between NaBi and Na_3Bi .

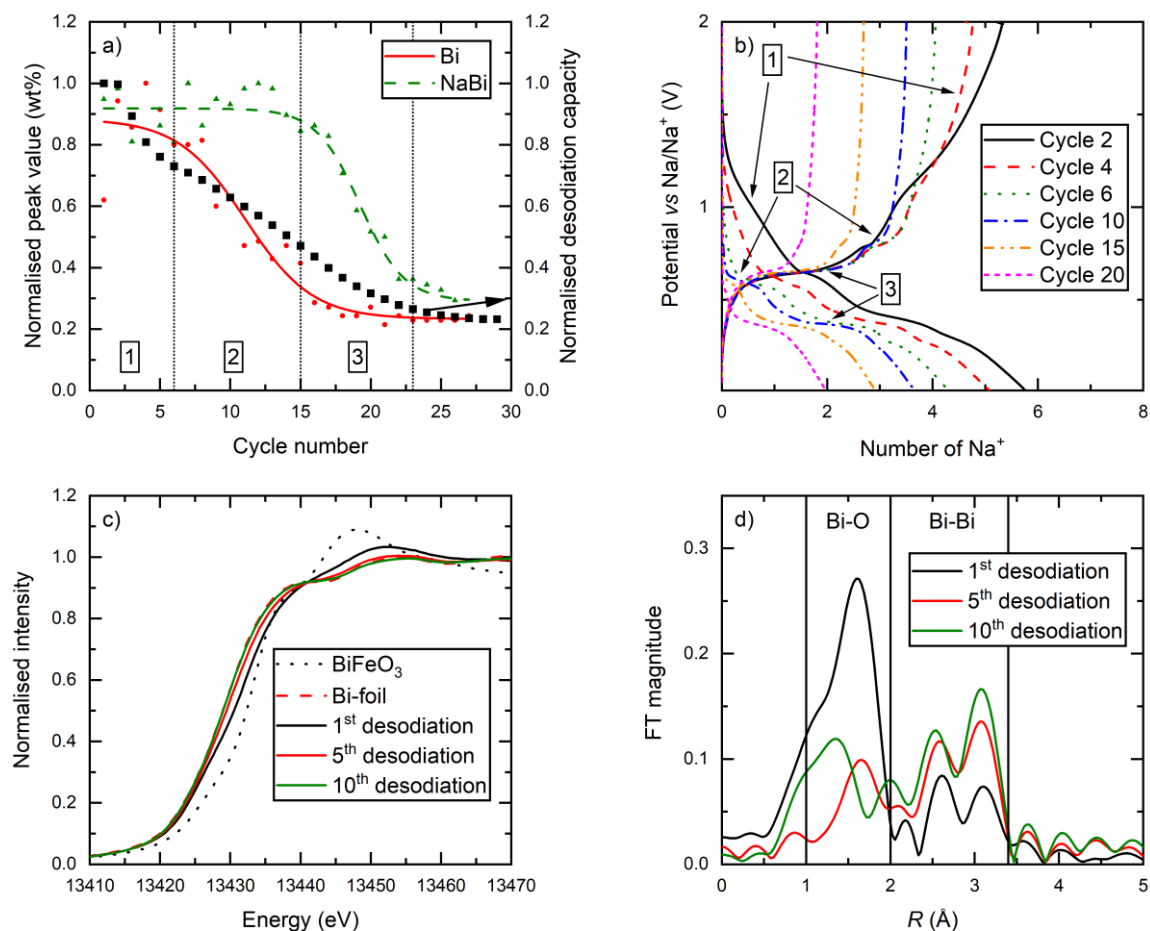


Figure 2: a) Maximum normalised phase fractions for Bi and NaBi vs cycle number extracted from surface Rietveld refinement on *operando* XRD of BiFeO₃ for the first 27 (de)sodiation cycles performed with a specific current of 0.2 A g⁻¹ and a voltage range of 0.01–2.00 V. b) Selected (de)sodiation curves plotted as potential vs Na/Na⁺ against the calculated number of Na⁺ ions transferred per formula unit obtained from the *operando* measurements shown in a) highlighting the capacity decay between cycle 2–20. c) XANES spectra of the Bi L₃ edge for desodiated BiFeO₃ at different stages of cycling compared to pristine BiFeO₃ and Bi metal as references. d) Corresponding FT EXAFS spectra showing the changes in Bi–O bonds.

Regions 1–3, described above, separate the capacity degradation according to the key chemical processes determining the capacity fading, with the main trigger being growth of the alloying particles inside the Na–Fe–O matrix. This increase of the particle size is most likely driven by the electrochemical sintering of the Na_xBi particles. In the pursuit of the origin of the capacity degradation, we reduced the upper cut-off voltage to 0.7 V to cycle the material only between NaBi and Na₃Bi using a current density of 0.1 A g⁻¹ (Figure 3a and c). This new cut-off voltage limited the reversible capacity to a maximum of ~230 mAh g⁻¹, but increased the cycling stability significantly as the capacity was only reduced to ~140 mAh g⁻¹ after 100 cycles. The performance at high-rate (1 A g⁻¹) was also well maintained (Figure 3b and c). This performance is still not sufficient to be of commercial interest, however, it demonstrates that the electrochemical isolation of the NaBi ⇌ Na₃Bi reaction leads to stable cycling. Galvanostatic cycling up to 0.90 V vs Na/Na⁺ was also performed, but showed similar capacity fading as during cycling to 2.00 V vs Na/Na⁺ (Figure S11). This showed that the Bi ⇌ NaBi reaction and the oxidation of Bi are the main contributors to the capacity degradation.

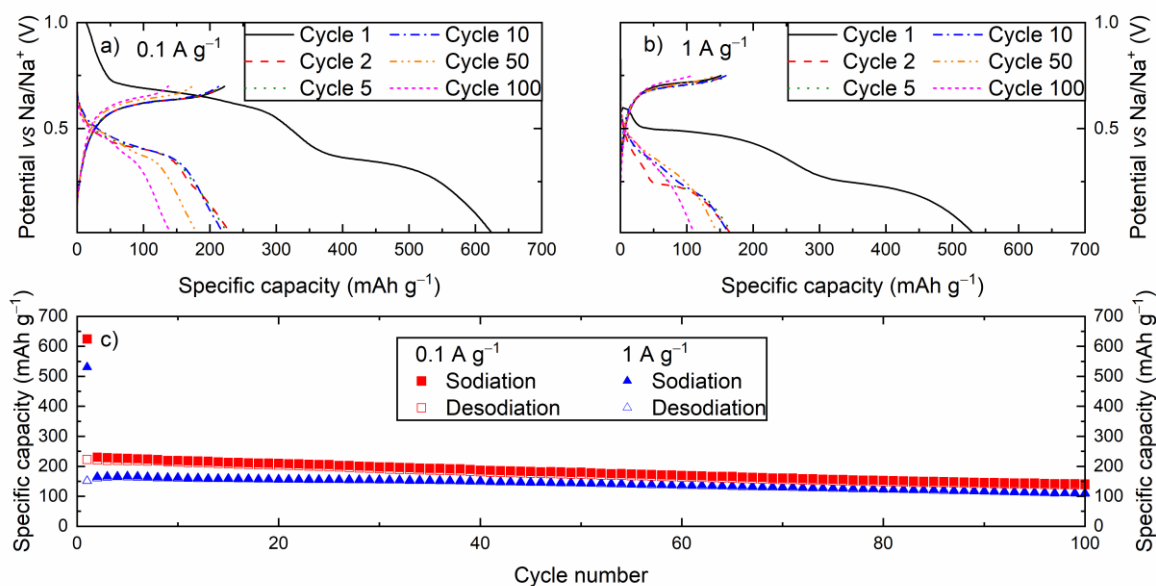


Figure 3: Selected (de)sodiation curves of BiFeO_3 cycled at a) 0.1 A g^{-1} with a voltage range of $0.01\text{--}0.70 \text{ V}$ and b) 1 A g^{-1} with a voltage range of $0.01\text{--}0.75 \text{ V}$. c) specific (de)sodiation capacity per cycle derived from the measurements in a) and b).

The exact reason why the capacity from the $\text{Bi} \rightleftharpoons \text{NaBi}$ reaction and the surface oxidation of Bi decays so quickly is difficult to know with certainty, but it is likely that the large structural changes occurring during cycling are involved. The large volume expansion of $\sim 250\%$ for the $\text{Bi} \rightleftharpoons \text{h-Na}_3\text{Bi}$ reaction could lead to particle cracking, which is potentially the main reason for the poor cycling stability of pure Bi metal [24, 31]. The Na-Fe-O matrix surrounding the Bi nanoparticles formed during the conversion reaction should mitigate some of these problems, but the growth of the alloying particles and the structural changes of the matrix including redox activity on Fe still leads to limited cycling stability. It may be that the matrix and the alloying particles are stable when cycling between NaBi and Na_3Bi , but that the transition between Bi and NaBi leads to significant movements in the matrix allowing the alloying particles to agglomerate and induce capacity degradation. A more detailed understanding of the structural changes in the matrix and the growth of the Bi particles, especially above 0.7 V , could provide the knowledge needed to stabilise the full two-step (de)alloying reaction to reach an acceptable specific capacity. Finding a material that forms a stable matrix, which can keep the Bi particles in place while still allowing the alloying reactions to occur will probably be the recipe for a CAM anode with good cycling stability.

Conclusion

Using *operando* XRD, both at high rates and over 27 (de)sodiation cycles, we have revealed some new insights into the cycling mechanism of BiFeO_3 . The results reveal that the general cycling mechanism is the same at 1 and 0.1 A g^{-1} . The first sodiation shows an irreversible conversion reaction forming Bi nanoparticles embedded in a Na-Fe-O matrix. During the following cycles, the main contributor to the capacity is the two-staged alloying mechanisms going from Bi to NaBi and Na_3Bi . We observe both the hexagonal and cubic versions of Na_3Bi , where c- Na_3Bi forms before h- Na_3Bi during sodiation. There is also a significant capacity contribution above 1 V during desodiation, attributed to the oxidation of the Bi nanoparticles, resulting in Bi-O bonds on the interface towards the Na-Fe-O matrix. This contribution gradually disappears during the first 6 cycles. The following capacity decay is explained by the

increasing irreversibility of the alloying reactions where the equilibrium is shifted towards the sodiated phases. Especially for the $\text{Bi} \rightleftharpoons \text{NaBi}$ reaction, which disappears completely. When reducing the upper cut-off voltage to isolate the $\text{NaBi} \rightleftharpoons \text{Na}_3\text{Bi}$ reaction the cycling stability was significantly improved and the high-rate performance was maintained, showing that this reaction in itself is stable. There is still not much knowledge of the Na-Fe-O matrix, but *ex situ* XAS showed that Fe is electrochemically active and contributes a bit to the capacity. More detailed structural studies are needed to fully understand the nature of the Na-Fe-O matrix and the movement and growth of the Bi particles. This will hopefully enable us to design CAMs with good cycling stability combined with the already established benefits of high capacity and good rate capabilities.

Experimental

Synthesis

BiFeO_3 was synthesised by a sol-gel method based on the study of Ma *et al.* [32], where 1.2×10^{-2} mol (5.822 g) $\text{Bi}(\text{NO}_3)_3 \cdot 5\text{H}_2\text{O}$ (98%, Sigma-Aldrich) and 1.0×10^{-2} mol (4.040 g) $\text{Fe}(\text{NO}_3)_3 \cdot 9\text{H}_2\text{O}$ ($\geq 98\%$, Sigma-Aldrich) were mixed with 8–10 mL of ethylene glycol (99.8%, Sigma-Aldrich) under magnetic stirring at 100 rpm and 60 °C for 1 h. Subsequently the temperature was increased to 100 °C to allow a slow evaporation of the solvent *via* autocombustion. The resulting dry gel was then transferred to an Al_2O_3 crucible and calcined in air at 350 °C for 3 h in a muffle oven (Carbolite Furnaces CWF 1200) and cooled down to room temperature. The product was then crushed to powder in an agate mortar, pressed to a pellet and treated at 650 °C for 8 h. To decrease the particle size, 2 g of the obtained product was ball milled with 85 g of 3 mm stainless steel balls in a Pulverisette 7 Premium Line (Fritsch) for 20 min at 250 rpm in Argon atmosphere.

Materials characterisation

The XRD samples were prepared by mixing the obtained product with isopropanol ($\geq 99.7\%$, VWR) and dispersing it on a flat glass plate mounted on the sample holder. All XRD patterns of uncycled samples were collected using a D8 Discover diffractometer (Bruker, Cu-source, $\lambda = 1.5406 \text{ \AA}$) with a point detector and fluorescence correction in the 2θ range 10–100 ° ($Q = 0.71\text{--}6.25 \text{ \AA}^{-1}$). One scan lasted ~ 3 h. The morphology of the BiFeO_3 particles was investigated with a high-resolution Hitachi SU8230 cold-field emission SEM operated with an acceleration voltage of 5 kV. The images were generated by secondary electrons, with a working distance of 8.8 mm and magnifications ranging from 1000–25 000. The powder was spread out on a carbon tape, attached to the sample holder, to fix the powder and ensure good conductivity.

Electrode preparation

The battery electrodes were made by combining the active material (BiFeO_3), binder (carboxymethylcellulose sodium salt, CMC, Sigma-Aldrich), conductive agent (Carbon black, Super P, Timcal) and solvent (distilled H_2O) in an 8:1:1 ratio into a slurry in a Thinky mixer (ARE 250). The mixing procedure consisted of 5 min mixing at a speed of 2000 rpm followed by a defoaming step for 1.5 min at 750 rpm. After the mixing procedure, which was repeated if necessary, the slurry was coated onto dendritic Cu foil (Schlenk, 10 μm thick) with a coating height of 300 μm . The resulting electrode sheets were dried in air overnight, cut into 15 mm discs the following day and were further dried in a Büchi oven at 60 °C under dynamic vacuum

for 3 h. Afterwards the electrodes were placed into a glovebox (MBraun Labmaster, H₂O and O₂ < 0.1 ppm) for coin cell assembly.

Electrochemical characterisation

Electrochemical characterisation was performed in half-cells with metallic Na as the counter electrode. Na chunks (Sigma-Aldrich) were cut into smaller pieces, rolled flat and then stamped into 14 mm discs. The discs were then brushed on each side with a toothbrush (medium, First Price) to ensure a fresh surface. Each Na disc was placed in a coin cell (CR2032, stainless steel, 304, Pi-Kem) together with separator (Whatman GE, 16 mm), wetted with 80 µl of electrolyte, and the working electrode before the battery was closed using an automatic coin cell crimper (Hohsen). The electrolyte was mixed inside the glovebox and consisted of 1 M NaPF₆ (Fluorochem) in propylene carbonate (PC, 99.7%, Sigma-Aldrich) with 5% fluoroethylene carbonate (FEC, 99%, Sigma-Aldrich) as additive.

Galvanostatic cycling (GC) of the batteries was carried out with a Neware battery tester (CT-4008T-5V10mA-164) at 25 °C with a lower cut-off voltage of 0.01 V and current densities of 0.1 and 1 A g⁻¹ with respect to the mass of BiFeO₃. The active mass loading of the electrodes was between 1–2 mg cm⁻². The upper cut-off voltage was 2 V for most of the measurements, but it was reduced to 0.7 V for one measurement at 0.1 A g⁻¹ and to 0.75 at 1 A g⁻¹ in order to isolate the NaBi ⇌ Na₃Bi reaction. The higher upper cut-off voltage for the 1 A g⁻¹ measurement was chosen to account for the increased overpotential at higher current densities. Cyclic voltammetry (CV) measurements were performed with an MPG2 battery cyler (BioLogic) using a voltage window of 0.01–2.00 V and sweep rates of 0.1 and 1 mV s⁻¹.

Operando XRD

Laboratory manufactured *operando* cells similar to the one presented by Drozhzhin *et al.* with glassy carbon windows were used for the *operando* XRD measurements [33]. The electrode for the *operando* measurement over the course of 2 (de)sodiation cycles at 0.1 A g⁻¹ was made by drop casting the slurry directly onto one of the cell halves to optimise the XRD signals. The measurement over 27 cycles used normal electrodes on Cu foil to ensure good electrochemical performance. Apart from this the assembly was performed as similar as possible to the normal coin cells. The GC measurements of these two *operando* measurements were performed using an SP150 battery cyler (BioLogic) with a voltage range of 0.01–2.00 V and current densities of 0.1 A g⁻¹ (2 cycles) and 0.2 A g⁻¹ (27 cycles). The XRD measurements were performed simultaneously with continuous still scans (10 min scan⁻¹, Q = 1.26–3.65 Å⁻¹) using a Dectris Eiger2 R 500K detector on a Bruker D8 Advance diffractometer (Mo source, λ_{Kα1} = 0.7093 Å, λ_{Kα2} = 0.7136 Å, focussing mirror primary optic).

The high rate *operando* XRD measurement with a current density of 1 A g⁻¹ and voltage range of 0.01–2.00 V was also performed over the course of 2 cycles. This measurement was performed with synchrotron radiation at BM31, which is a part of the Swiss-Norwegian Beam Lines (SNBL), at ESRF with a wavelength of 0.24486 Å and a Pilatus CdTe 2M detector from DECTRIS. Each scan had an exposure time of 20 s with 15 repetitions that was averaged, giving a total measurement time of 5 min per data point. The electrode used for this measurement was coated with a wet thickness of 500 µm on Cu foil.

Ex situ XAS

Electrodes for *ex situ* XAS were prepared in the same way as for normal coin cells. The batteries were cycled at 0.1 A g⁻¹ between 0.01–2.00 V until the desired stage of cycling (specified in main text) where they then went through a constant voltage step where the cut-off voltage was held until the current was below 20 µA. The coin cells were then transferred to

the glovebox and disassembled with a coin cell disassembling tool (Hoshen). The electrodes were carefully extracted from the disassembled coin cells, cleaned with ~0.5 mL DEC per electrode and dried for 1 h inside the glovebox. Following this, the electrode material was scraped from the Cu foil, ground carefully in a mortar and filled in 1 mm borosilicate glass capillaries that were sealed with UV glue (Bondic). The XAS measurements on the Bi L3 edge were performed in transmission mode with ion chamber detectors in the energy range of 13.32–14.10 keV, 0.7 eV step size and 200 ms exposure giving a measurement time of 3 min and 44 s per scan. Each sample was measured with 2 repetitions, which were averaged in Athena [34]. The Fe K edge was measured in fluorescence mode with an energy range of 7.05–7.26 keV, 0.3 eV step size and 200 ms exposure leading to a total measurement time of 2 min and 20 s.

Software and data treatment

To visualise the crystal structure of BiFeO₃ we utilised Vesta [35, 36]. J-edit and Topas v6 [37] were used for Rietveld refinements, while EC-lab and software from Neware were used to process electrochemistry data. Python 3 and Origin 2020 were utilised for further processing and plotting of the data, including python scripts provided by the BM31 staff. The Athena software was used for processing and analysing the XAS data [34].

SUPPORTING INFORMATION

XRD and SEM data of pristine BiFeO₃; (de)sodiation curves and cycling voltammograms at different cycling conditions; *ex situ* XRD and XAS data from cycled BiFeO₃ samples; contour plot from *operando* XRD of BiFeO₃ over 27 cycles with corresponding dQ/dV curves; results from surface Rietveld refinement of *operando* XRD of Bi₂MoO₆

ASSOCIATED CONTENT

All the background data for this publication including procedures and scripts for data treatment are available at dataverse.no [38]. Additional data and analysis from the BiFeO₃ system are also available [39].

AUTHOR INFORMATION

Corresponding Author

Contact information for the author(s) to whom correspondence should be addressed.

Anders Brennhagen, anders.brennhagen@smn.uio.no

Helmer Fjellvåg, helmer.fjellvag@kjemi.uio.no

Author Contributions

The manuscript was written through contributions of all authors. All authors have given approval to the final version of the manuscript. †These authors contributed equally.

Funding Sources

Norges Forskningsråd (The Research Council of Norway, NFR) through NanoName: Improving sodium ion battery performance with nanostructured metalate anodes (Project number: 287480) and RECX (Norwegian National Resource Centre for X-ray Diffraction and Scattering) for usage of X-ray radiation facilities (Funded by NFR, project number: 208896).

ACKNOWLEDGMENT

Salah Bra Amedi is acknowledged for assisting in the synthesis of BiFeO₃. The Swiss Norwegian beamlines (SNBL, ESRF) are acknowledged for provision of beamtime and its staff for invaluable support. The BM31 setup was funded by the Swiss National Science Foundation (grant 206021_189629) and the Research Council of Norway.

ABBREVIATIONS

Conversion-alloying material	CAM
Carboxymethylcellulose sodium salt	CMC
Cyclic voltammetry	CV
European Synchrotron Radiation Facility	ESRF
Extended X-ray absorption fine structure	EXAFS
Fluoroethylene carbonate	FEC
Fourier transform	FT
Galvanostatic cycling	GC
Li-ion battery	LIB
Na-ion battery	NIB
Norges Forskningsråd (The Research Council of Norway)	NFR
Propylene carbonate	PC
Resource Centre for X-ray Diffraction and Scattering	RECX
Scanning electron microscopy	SEM
Solid electrolyte interface	SEI
Swiss-Norwegian beamlines	SNBL
Total scattering computed tomography	TSCT
Transition electron microscopy	TEM
Transition metal	TM
X-ray absorption near edge spectroscopy	XANES
X-ray absorption spectroscopy	XAS
X-ray diffraction	XRD

REFERENCES

- [1] Vaalma, C.; Buchholz, D.; Weil, M.; Passerini, S. A Cost and Resource Analysis of Sodium-Ion Batteries. *Nature reviews materials*, **2018**, 3(4), 1-11.
- [2] Hasa, I.; Mariyappan, S.; Saurel, D.; Adelhelm, P.; Kuposov, A. Y.; Masquelier, C.; Croguennec, L.; Casas-Cabanas, M. Challenges of Today for Na-Based Batteries of the Future: From Materials to Cell Metrics. *Journal of Power Sources*, **2021**, 482, 228872.

- [3] Mukherjee, S.; Bin Mujib, S.; Soares, D.; Singh, G. Electrode Materials for High-Performance Sodium-Ion Batteries. *Materials*, **2019**, *12*(12), 1952.
- [4] Chayambuka, K.; Mulder, G.; Danilov, D. L.; Notten, P. H. From Li-Ion Batteries toward Na-Ion Chemistries: Challenges and Opportunities. *Advanced Energy Materials*, **2020**, *10*(38), 2001310.
- [5] Zhang, H.; Hasa, I.; Passerini, S. Beyond Insertion for Na-Ion Batteries: Nanostructured Alloying and Conversion Anode Materials. *Advanced Energy Materials*, **2018**, *8*(17), 1702582.
- [6] Skurtveit, A.; Brennhagen, A.; Park, H.; Cavallo, C.; Kozosov, A. Benefits and Development Challenges for Conversion-Alloying Anode Materials for Na-Ion Batteries. *Frontiers in Energy Research*, **2022**, *10*.
- [7] Fang, L.; Bahlawane, N.; Sun, W.; Pan, H.; Xu, B. B.; Yan, M.; Jiang, Y. Conversion-Alloying Anode Materials for Sodium Ion Batteries. *Small*, **2021**, *17*(37), 2101137.
- [8] Liu, D.; Shadike, Z.; Lin, R.; Qian, K.; Li, H.; Li, K.; Wang, S.; Yu, Q.; Liu, M.; Ganapathy, S. Review of Recent Development of In Situ/Operando Characterization Techniques for Lithium Battery Research. *Advanced Materials*, **2019**, *31*(28), 1806620.
- [9] Brennhagen, A.; Cavallo, C.; Wragg, D. S.; Sottmann, J.; Kozosov, A. Y.; Fjellvåg, H. Understanding the (De)Sodiation Mechanisms in Na-Based Batteries through Operando X-Ray Methods. *Batteries & Supercaps*, **2021**, *4*(7), 1039-1063.
- [10] Gao, H.; Ma, W.; Yang, W.; Wang, J.; Niu, J.; Luo, F.; Peng, Z.; Zhang, Z. Sodium Storage Mechanisms of Bismuth in Sodium Ion Batteries: An Operando X-Ray Diffraction Study. *Journal of Power Sources*, **2018**, *379*, 1-9.
- [11] Sottmann, J.; Homs-Regojo, R.; Wragg, D. S.; Fjellvåg, H.; Margadonna, S.; Emerich, H. Versatile Electrochemical Cell for Li/Na-Ion Batteries and High-Throughput Setup for Combined Operando X-Ray Diffraction and Absorption Spectroscopy. *Journal of Applied Crystallography*, **2016**, *49*(6), 1972-1981.
- [12] Ou, X.; Yang, C.; Xiong, X.; Zheng, F.; Pan, Q.; Jin, C.; Liu, M.; Huang, K. A New Rgo-Overcoated Sb₂Se₃ Nanorods Anode for Na⁺ Battery: In Situ X-Ray Diffraction Study on a Live Sodiation/Desodiation Process. *Advanced Functional Materials*, **2017**, *27*(13), 1606242.
- [13] Ruud, A.; Sottmann, J.; Vajeeston, P.; Fjellvåg, H. Operando Investigations of Lithiation and Delithiation Processes in a BiVO₄ Anode Material. *Physical Chemistry Chemical Physics*, **2018**, *20*(47), 29798-29803.
- [14] Surendran, A.; Enale, H.; Thottungal, A.; Sarapulova, A.; Knapp, M.; Nishanthi, S.; Dixon, D.; Bhaskar, A. Unveiling the Electrochemical Mechanism of High-Capacity Negative Electrode Model-System BiFeO₃ in Sodium-Ion Batteries: An in Operando XAS Investigation. *ACS applied materials & interfaces*, **2022**, *14*(6), 7856-7868.
- [15] Sottmann, J.; Ruud, A.; Fjellvåg, Ø. S.; Vaughan, G. B. M.; Di Michel, M.; Fjellvåg, H.; Lebedev, O. I.; Vajeeston, P.; Wragg, D. S. 5D Total Scattering Computed Tomography Reveals the Full Reaction Mechanism of a Bismuth Vanadate Lithium Ion Battery Anode. *Physical Chemistry Chemical Physics*, **2022**, *24*(44), 27075-27085.
- [16] Dixon, D.; Ávila, M.; Ehrenberg, H.; Bhaskar, A. Difference in Electrochemical Mechanism of SnO₂ Conversion in Lithium-Ion and Sodium-Ion Batteries: Combined in Operando and Ex Situ XAS Investigations. *ACS Omega*, **2019**, *4*(6), 9731-9738.

- [17] Kim, Y.; Kim, Y.; Choi, A.; Woo, S.; Mok, D.; Choi, N.-S.; Jung, Y. S.; Ryu, J. H.; Oh, S. M.; Lee, K. T. Tin Phosphide as a Promising Anode Material for Na-Ion Batteries. *Advanced Materials*, **2014**, *26*(24), 4139-4144.
- [18] Wu, Y.; Luo, W.; Gao, P.; Zhu, C.; Hu, X.; Qu, K.; Chen, J.; Wang, Y.; Sun, L.; Mai, L.; Xu, F. Unveiling the Microscopic Origin of Asymmetric Phase Transformations in (De)Sodiated Sb_2Se_3 with in Situ Transmission Electron Microscopy. *Nano Energy*, **2020**, *77*, 105299.
- [19] Ma, C.; Xu, J.; Alvarado, J.; Qu, B.; Somerville, J.; Lee, J. Y.; Meng, Y. S. Investigating the Energy Storage Mechanism of SnS_2 -RGO Composite Anode for Advanced Na-Ion Batteries. *Chemistry of Materials*, **2015**, *27*(16), 5633-5640.
- [20] Sottmann, J.; Herrmann, M.; Vajeeston, P.; Ruud, A.; Drathen, C.; Emerich, H.; Wragg, D. S.; Fjellvåg, H. Bismuth Vanadate and Molybdate: Stable Alloying Anodes for Sodium-Ion Batteries. *Chemistry of Materials*, **2017**, *29*(7), 2803-2810.
- [21] Ruud, A.; Sottmann, J.; Vajeeston, P.; Fjellvåg, H. Direct Observation of Reversible Conversion and Alloying Reactions in a $\text{Bi}_2(\text{MoO}_4)_3$ -Based Lithium-Ion Battery Anode. *Journal of Materials Chemistry A*, **2019**, *7*(30), 17906-17913.
- [22] Brennhagen, A.; Cavallo, C.; Wragg, D. S.; Vajeeston, P.; Sjøstad, A. O.; Kopolov, A. Y.; Fjellvåg, H. Operando Xrd Studies on Bi_2MoO_6 as Anode Material for Na-Ion Batteries. *Nanotechnology*, **2022**, *33*(18), 185402.
- [23] Xu, X.; Li, M.; Yu, T. Facile Synthesis of Bi_2MoO_6 Nanosheets@ Nitrogen and Sulfur Codoped Graphene Composites for Sodium-Ion Batteries. *Chemical Research in Chinese Universities*, **2020**, *36*(1), 115-119.
- [24] Sottmann, J.; Herrmann, M.; Vajeeston, P.; Hu, Y.; Ruud, A.; Drathen, C.; Emerich, H.; Fjellvåg, H.; Wragg, D. S. How Crystallite Size Controls the Reaction Path in Nonaqueous Metal Ion Batteries: The Example of Sodium Bismuth Alloying. *Chemistry of Materials*, **2016**, *28*(8), 2750-2756.
- [25] Durai, L.; Moorthy, B.; Thomas, C. I.; Kim, D. K.; Bharathi, K. K. Electrochemical Properties of BiFeO_3 Nanoparticles: Anode Material for Sodium-Ion Battery Application. *Materials Science in Semiconductor Processing*, **2017**, *68*, 165-171.
- [26] Zhang, X.; van Hulzen, M.; Singh, D. P.; Brownrigg, A.; Wright, J. P.; van Dijk, N. H.; Wagemaker, M. Direct View on the Phase Evolution in Individual LiFePO_4 Nanoparticles During Li-Ion Battery Cycling. *Nature Communications*, **2015**, *6*(1), 8333.
- [27] Liu, H.; Strobridge, F. C.; Borkiewicz, O. J.; Wiaderek, K. M.; Chapman, K. W.; Chupas, P. J.; Grey, C. P. Capturing Metastable Structures During High-Rate Cycling of LiFePO_4 Nanoparticle Electrodes. *Science*, **2014**, *344*(6191), 1252817.
- [28] Kim, M.-K.; Yu, S.-H.; Jin, A.; Kim, J.; Ko, I.-H.; Lee, K.-S.; Mun, J.; Sung, Y.-E. Bismuth Oxide as a High Capacity Anode Material for Sodium-Ion Batteries. *Chemical Communications*, **2016**, *52*(79), 11775-11778.
- [29] Lu, X.; Wang, Z.; Liu, K.; Luo, J.; Wang, P.; Niu, C.; Wang, H.; Li, W. Hierarchical Sb_2MoO_6 Microspheres for High-Performance Sodium-Ion Battery Anode. *Energy Storage Materials*, **2019**, *17*, 101-110.
- [30] Sottmann, J.; Di Michiel, M.; Fjellvåg, H.; Malavasi, L.; Margadonna, S.; Vajeeston, P.; Vaughan, G. B. M.; Wragg, D. S. Chemical Structures of Specific Sodium Ion Battery Components Determined by Operando Pair Distribution

- Function and X-Ray Diffraction Computed Tomography. *Angewandte Chemie International Edition*, **2017**, 56(38), 11385-11389.
- [31] Lim, C.-H.; Selvaraj, B.; Song, Y.-F.; Wang, C.-C.; Jin, J.-T.; Huang, S.-S.; Chuang, C.-H.; Sheu, H.-S.; Liao, Y.-F.; Wu, N.-L. Insight into Microstructural and Phase Transformations in Electrochemical Sodiation–Desodiation of a Bismuth Particulate Anode. *Journal of Materials Chemistry A*, **2017**, 5(40), 21536-21541.
- [32] Ma, C.-J.; Li, N.; Song, W.-L. Tailoring the Electrochemical Behaviors of Bismuth Ferrite Using Ca Ion Doping. *Frontiers in Materials*, **2020**, 7, 15.
- [33] Drozhzhin, O. A.; Tereshchenko, I. V.; Emerich, H.; Antipov, E. V.; Abakumov, A. M.; Chernyshov, D. An Electrochemical Cell with Sapphire Windows for Operando Synchrotron X-Ray Powder Diffraction and Spectroscopy Studies of High-Power and High-Voltage Electrodes for Metal-Ion Batteries. *Journal of Synchrotron Radiation*, **2018**, 25(2), 468-472.
- [34] Ravel, B.; Newville, M. ATHENA, ARTEMIS, HEPHAESTUS: Data Analysis for X-Ray Absorption Spectroscopy Using IFEFFIT. *Journal of Synchrotron Radiation*, **2005**, 12(4), 537-541.
- [35] Momma, K.; Izumi, F. Vesta: A Three-Dimensional Visualization System for Electronic and Structural Analysis. *Journal of Applied Crystallography*, **2008**, 41(3), 653-658.
- [36] Momma, K.; Izumi, F. Vesta 3 for Three-Dimensional Visualization of Crystal, Volumetric and Morphology Data. *Journal of applied crystallography*, **2011**, 44(6), 1272-1276.
- [37] Coelho, A. A. Topas and Topas-Academic: An Optimization Program Integrating Computer Algebra and Crystallographic Objects Written in C++. *Journal of Applied Crystallography*, **2018**, 51(1), 210-218.
- [38] Brennhagen, A.; Nafuma. *Experimental Data for the Nanoname Project*, DataverseNO, 2023, <https://doi.org/10.18710/ZFADJS>.
- [39] Skautvedt, C. E., "Syntese og Karakterisering av BiFeO₃ som Anodemateriale i Na-lonebatterier," Master thesis, University of Oslo, 2022.

Supporting Information: “Unravelling the (de)sodiation mechanisms of BiFeO₃ at a high rate with *operando* XRD”

Anders Brennhagen^{1*}, Casper Skautvedt¹, Carmen Cavallo², David S. Wragg^{1,3}, Alexey Y. Koposov^{1,3}, Anja O. Sjøstad¹, Helmer Fjellvåg^{1*}.

¹Centre for Materials Science and Nanotechnology, Department of Chemistry, University of Oslo, PO Box 1033, Blindern, N-0315, Oslo, Norway

²CENATE, Centrifugal Nanotechnology, Rakkestadveien 1, 1814, Askim, Norway

³Department of Battery Technology, Institute for Energy Technology (IFE), Instituttveien 18, 2007, Kjeller, Norway

E-mail: anders.brennhagen@smn.uio.no and helmer.fjellvag@kjemi.uio.no

Section S1: Structural and morphological characterisation

BiFeO₃ takes a distorted perovskite structure described in space group R3c using a hexagonal unit cell (Figure S1b, Table S1). Due to the inert lone pair of the 6s orbitals of Bi³⁺ the FeO₆ and the BiO₁₂ polyhedra are significantly distorted compared to the ideal perovskite structure. The secondary particles of the synthesised BiFeO₃ had a wide distribution in particle sizes between 1–500 μm in diameter, as shown by scanning electron microscopy (SEM), and they consisted of primary particles with sizes ranging from 100–500 nm (Figure S1c and d). To improve the electrochemical performance of the material, the sample was ball milled for 20 min at 250 rpm to pulverise the largest secondary particles without drastically changing the nanostructures of the material. The SEM images of the ball milled sample showed that the largest secondary particles after ball milling were <20 μm in diameter, while the primary particles were of the same size as the pristine sample (Figure S1e and f). The XRD pattern of the ball-milled sample was similar to the pristine sample (Figure S1a). The only significant difference was some peak broadening, which is probably due to strain from the ball milling.

Table S1: Structural information of the phases used for XRD analysis

Phase	Space group	Z	Unit cell parameters (Å)	Atomic sites					Source
				Atom	Wyckoff	x	y	z	
BiFeO ₃	R3c:H (161)	4	a = 5.57893 c = 13.86953	Bi1	6a	0	0	0	ICSD: 192511
				Fe1	6a	0	0	0.2206	
				O1	18b	0.444	0.018	0.9525	
Bi ₂ O ₃	P2 ₁ /c (14)	4	a = 5.8486 b = 8.1661 c = 7.5097	Bi1	4e	0.5240	0.1831	0.3613	COD: 9012546
				Bi2	4e	0.0409	0.0425	0.7762	
				O1	4e	0.7800	0.3000	0.7100	
				O2	4e	0.2420	0.0440	0.1340	
				O3	4e	0.2710	0.0240	0.5130	
Bi	R-3m (166)	6	a = 4.546 c = 11.862	Bi1	2g	0	0	0.23389	COD: 2310889
NaBi	P4/mmm (123)	1	a = 3.46 c = 4.8	Bi1	1a	0	0	0	ICSD: 58816
h-Na ₃ Bi	P6 ₃ /mmc (194)	2	a = 5.448 c = 9.655	Bi1	2c	1/3	2/3	1/4	COD: 1010291
				Na1	2b	0	0	1/4	
				Na2	4f	1/3	2/3	0.583	
c-Na ₃ Bi	Fm-3m (225)	4	a = 7.66526	Bi1	4a	0	0	0	[1]
				Na1	4b	1/2	1/2	1/2	
				Na2	8c	1/4	1/4	1/4	

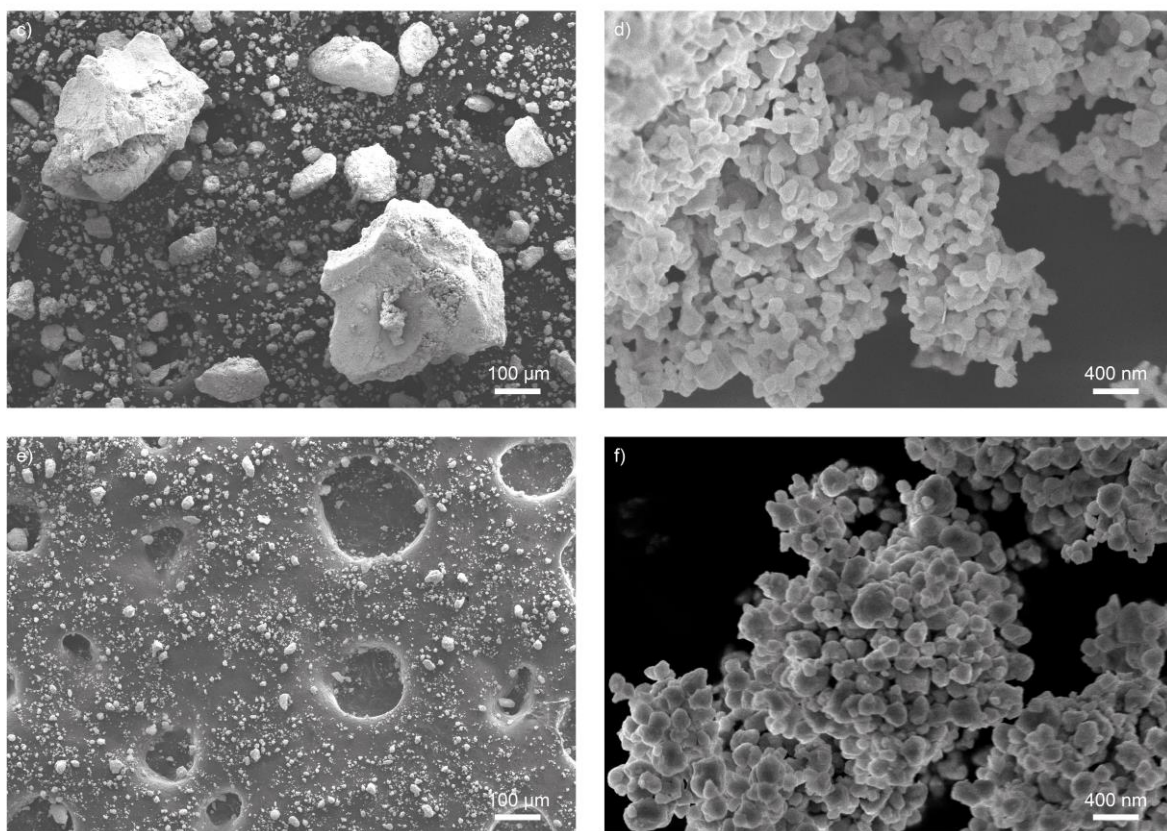
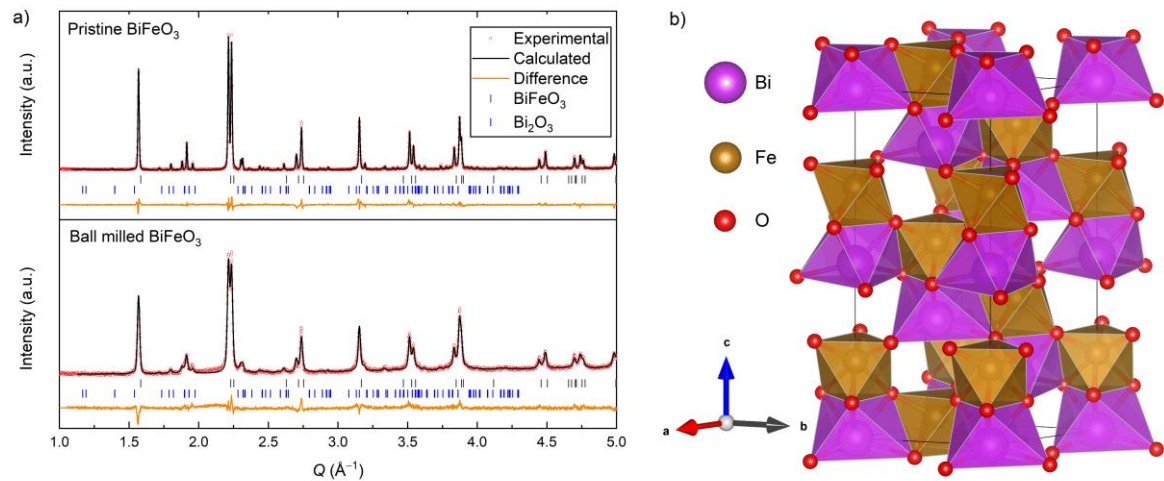


Figure S1: a) XRD with Rietveld refinement of pristine BiFeO₃ and the sample after ball milling for 20 min at 250 rpm. b) Visualisation of the crystal structure of BiFeO₃ (space group: R3c). SEM images of c) pristine BiFeO₃ particles with magnification of 100 x, d) pristine BiFeO₃ at 25 000 x, e) ball milled BiFeO₃ at 100 x, f) ball milled BiFeO₃ at 25 000 x. All SEM images are generated by secondary electrons.

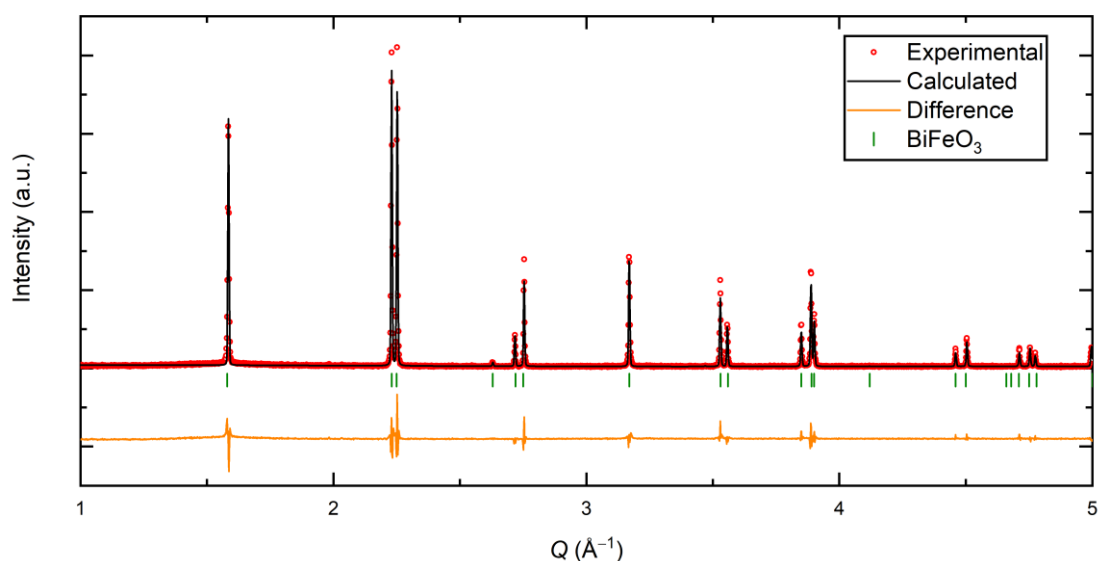


Figure S2: XRD pattern fitted with Rietveld refinement of pure BiFeO_3 obtained by sol-gel synthesis followed by leaching with an aqueous solution of 10% HNO_3 .

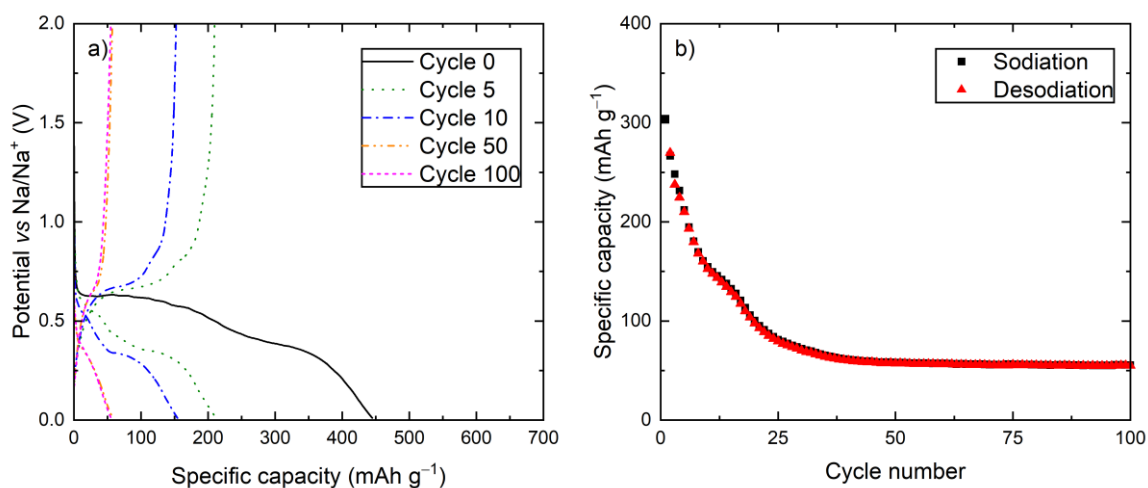
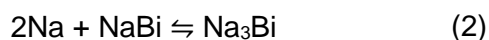


Figure S3: Galvanostatic cycling of leached BiFeO_3 . a) (De)sodiation curves plotted as voltage vs specific capacity and b) specific capacity per cycle plot.

Section S2: Electrochemical characterisation

To evaluate the electrochemical performance of ball milled BiFeO_3 in NIBs, we conducted several cyclic voltammetry (CV) and galvanostatic cycling (GC) measurements in half cells vs Na/Na^+ . CV measurements with a sweep rate of 0.1 mV s^{-1} showed two distinct peaks during sodiation at ~ 0.6 and $\sim 0.3 \text{ V}$ (Figure S4a). The peak at $\sim 0.6 \text{ V}$ is larger during the first sodiation than in the following cycles, and it has a clear shoulder on the right side starting around 1 V . This peak (and shoulder) should correspond to the conversion reaction from BiFeO_3 to Bi and the first step of the alloying reaction forming NaBi (reaction (1)). In addition, some solid electrolyte interface (SEI) formation likely occurs in this region. The second peak is characteristic of the second alloying step where NaBi transforms into Na_3Bi (reaction (2)).



During desodiation, the peaks corresponding to the dealloying reaction of Na_3Bi to NaBi is present at ~ 0.7 V and the peak at ~ 0.8 V corresponds to the formation of Bi (Figure S4a). In addition to these two peaks, there is a bump between 1.00 and 1.25 V that is related to the further oxidation of Bi [2]. At the higher sweep rate of 1 mV s^{-1} , the peaks are broader and shifted towards lower voltages during sodiation and higher voltages for desodiation compared to the measurement at 0.1 mV s^{-1} (Figure S4b). This is most pronounced during the first sodiation where the curve peaks around 0.1 V (shifted with 0.5 V), indicating that the initial conversion reaction has limited kinetics. The peaks corresponding to the alloying reactions during the following cycles are not shifted as much (roughly 0.1 V), indicating a lower overpotential and better kinetics.

To further evaluate the electrochemical performance of BiFeO_3 at different rates, GC measurements at 0.1 and 1 A g^{-1} were performed (Figure S4c and d). The initial sodiation capacity of BiFeO_3 was $\sim 600 \text{ mAh g}^{-1}$ at 0.1 A g^{-1} . The measured capacity is higher than the theoretical capacity of the conversion and alloying to Na_3Bi and a Na-Fe-O matrix with Fe^{3+} , which is 514 mAh g^{-1} . Some of this deviation between theoretical and experimental capacity could be explained by redox activity of Fe, which is known to happen for BiFeO_3 [2]. The rest of the deviation probably comes from SEI formation, sodiation of the conductive carbon and uncertainty from weighing of the electrodes. The contribution from the conductive carbon is estimated to be $\sim 15 \text{ mAh g}^{-1}$ and the uncertainty of the weighing is $\sim 10\%$ for the electrodes used in this study [3]. The most pronounced difference at the different cycling rates is the conversion reaction during the first sodiation where the reaction starts at ~ 1.0 V in the 0.1 A g^{-1} measurement compared to ~ 0.5 V at 1 A g^{-1} . This is consistent with the CV measurements (Figure S4a and b), which also showed a significant difference in the first sodiation. Apart from this, the measurements at the two current densities are very similar, showing that the material can handle high current densities without compromising on performance. The cycling stability of BiFeO_3 is challenging as the capacity drops from $\sim 450 \text{ mAh g}^{-1}$ at the second cycle to approximately $\sim 130 \text{ mAh g}^{-1}$ after 25 cycles (Figure S4e). Following this, the capacity is reasonably stable up to at least 100 cycles, where the capacity ends up at $\sim 120 \text{ mAh g}^{-1}$ and $\sim 70 \text{ mAh g}^{-1}$ for 0.1 A g^{-1} and 1 A g^{-1} , respectively (Figure S4f). We have $\sim 12 \text{ wt}\%$ Bi_2O_3 in our sample, which is known to be electrochemically active in NIBs and show similar performance as BiFeO_3 [4-6]. The Bi_2O_3 impurities introduces some uncertainties to the specific capacities presented in this paper, but should not alter the key findings.

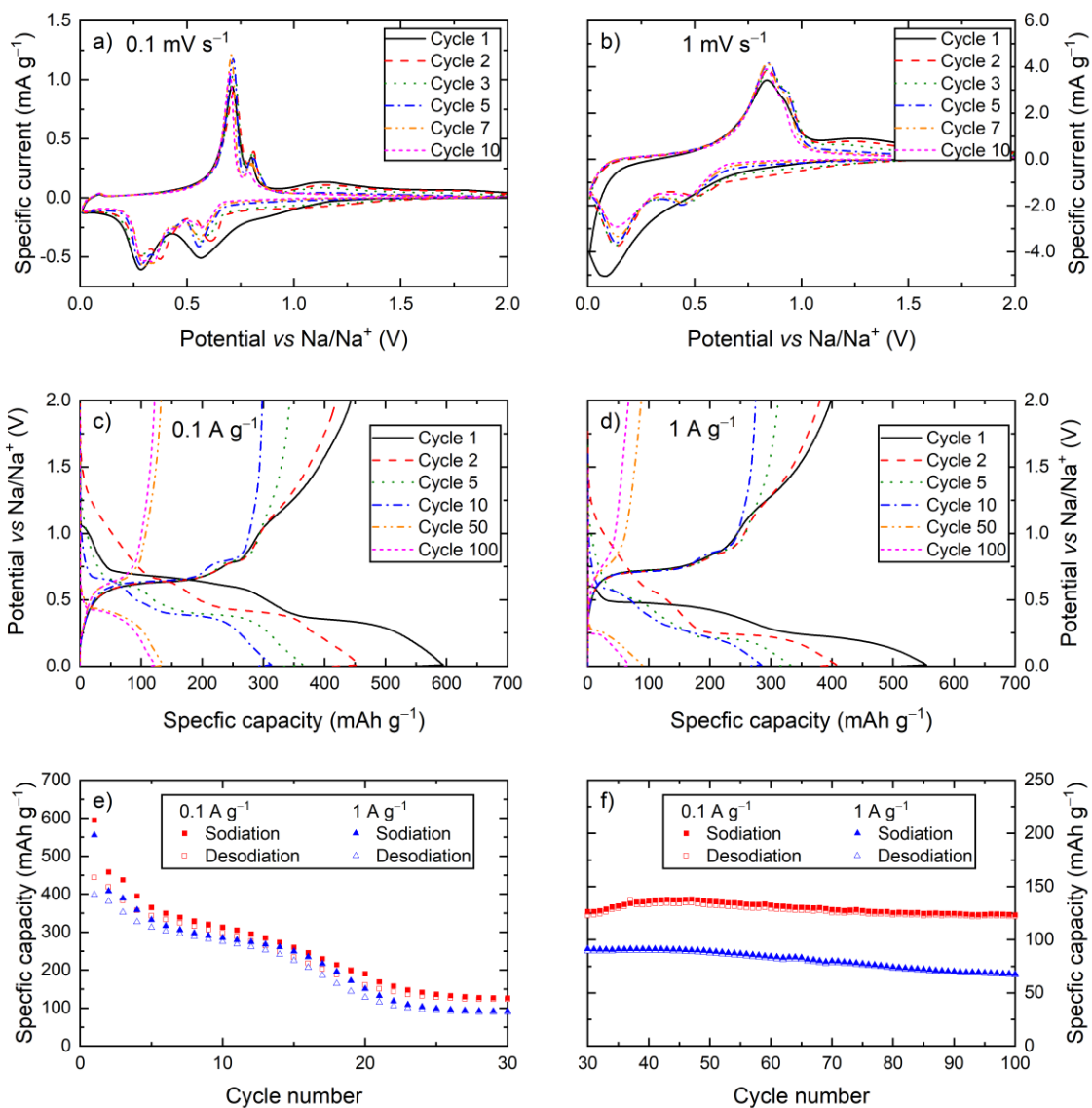


Figure S4: Electrochemical characterisation of ball milled BiFeO_3 . a) and b) cyclic voltammograms obtained from CV measurements with a voltage range of 0.01–2.00 V and sweep rates of 0.1 mV s^{-1} and 1 mV s^{-1} , respectively. c) and d) (de)sodiation curves of selected cycles derived from GC measurements with current densities of 0.1 A g^{-1} and 1 A g^{-1} , respectively. e) and f) capacity per cycle plot comparing the cycling behaviour at the different current rates, derived from the GC measurements.

Section S3: Other supporting figures and tables

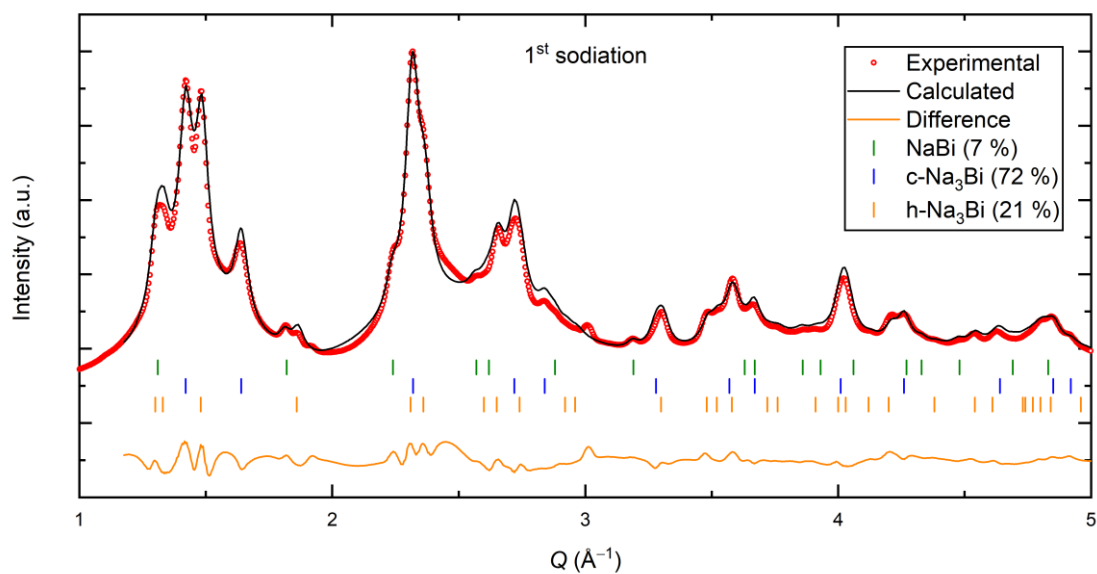


Figure S5: *Ex situ* XRD measured on a sealed capillary with BiFeO₃ extracted after the 1st sodiation. The sample was extracted from 5 coin cells, cycled at 0.1 A g⁻¹ to 0.01 V, to obtain enough powder. Rietveld refinement with corresponding phase fractions in wt% provided in the legend.

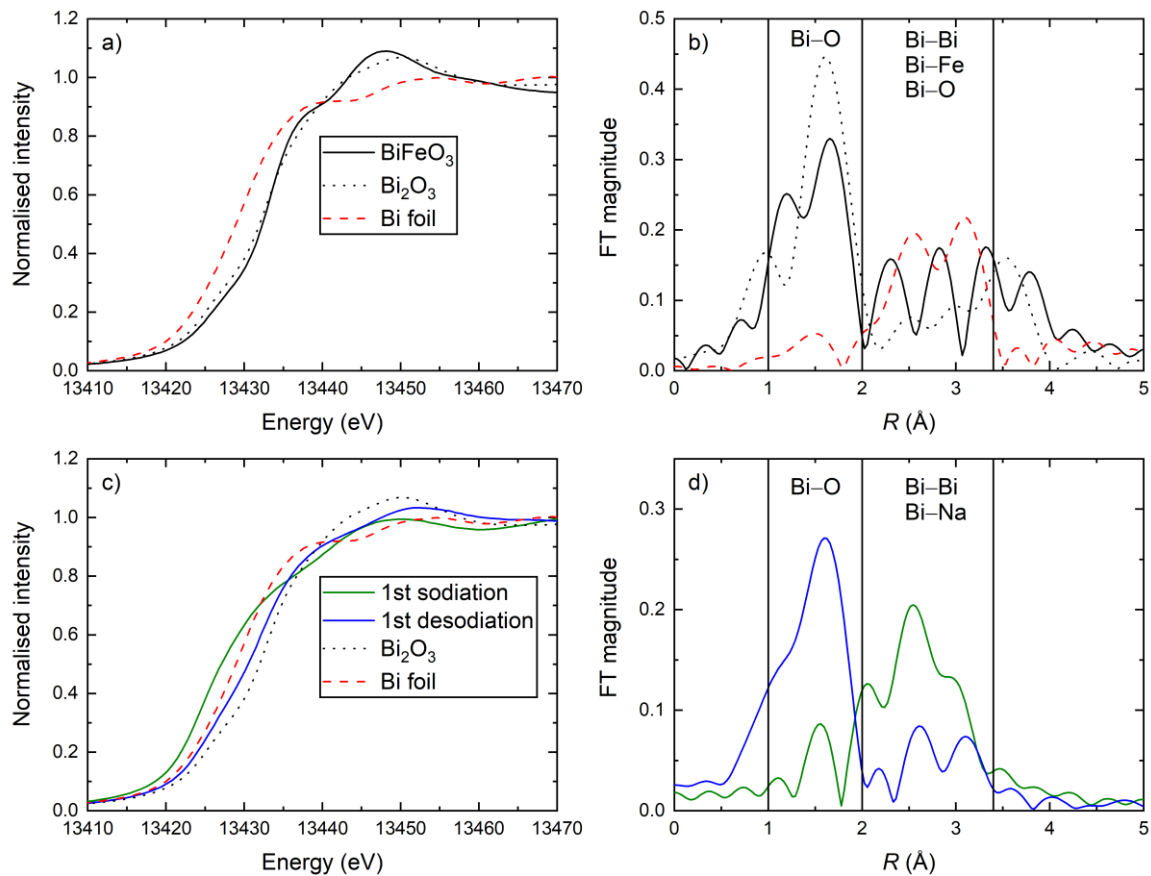


Figure S6: XAS measurements of the Bi L3 edge. a) XANES and b) FT EXAFS spectra of BiFeO₃, Bi₂O₃ and Bi-foil. c) XANES spectra of BiFeO₃ samples after 1st sodiation and desodiation compared to Bi₂O₃ and Bi-metal foil as references. d) Corresponding FT EXAFS spectra of 1st sodiation and desodiation.

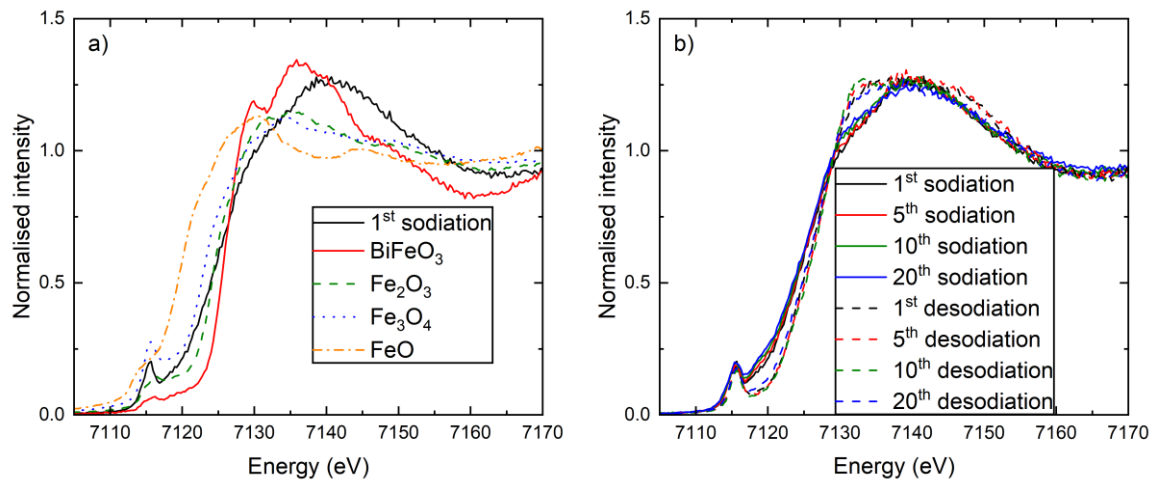


Figure S7: XANES spectra of the Fe K edge. a) Pristine BiFeO₃ and BiFeO₃ after 1st sodiation compared to Fe-oxide references and b) cycled BiFeO₃ samples at different stages of cycling.

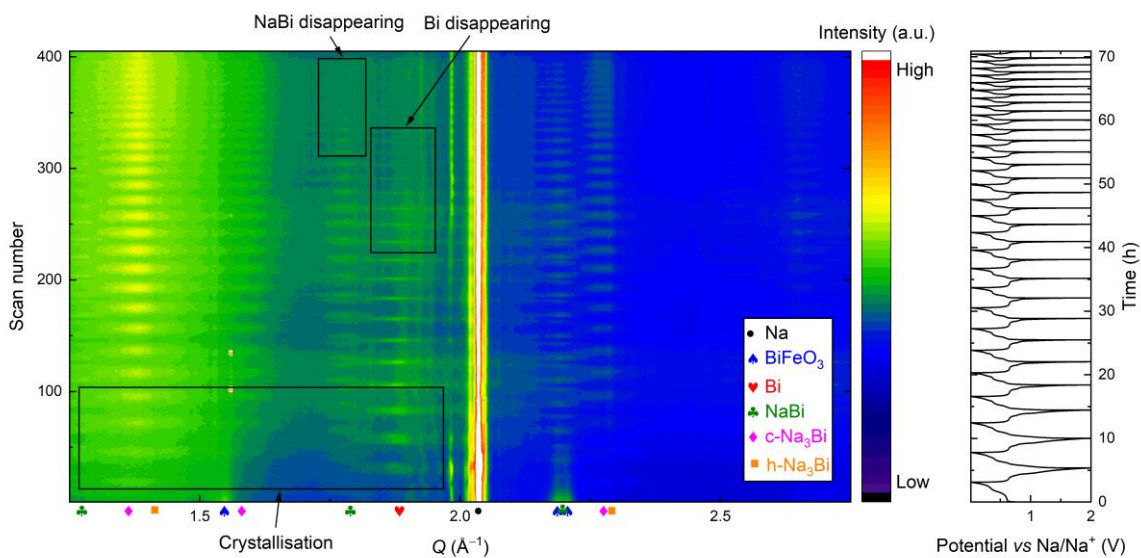


Figure S8: *Operando* XRD visualised as a contour plot (left) with corresponding (de)sodiation curves (right) derived from a measurement of BiFeO₃ over the course of 27 cycles with current density of 0.2 A g⁻¹ and voltage range of 0.01–2.00 V.

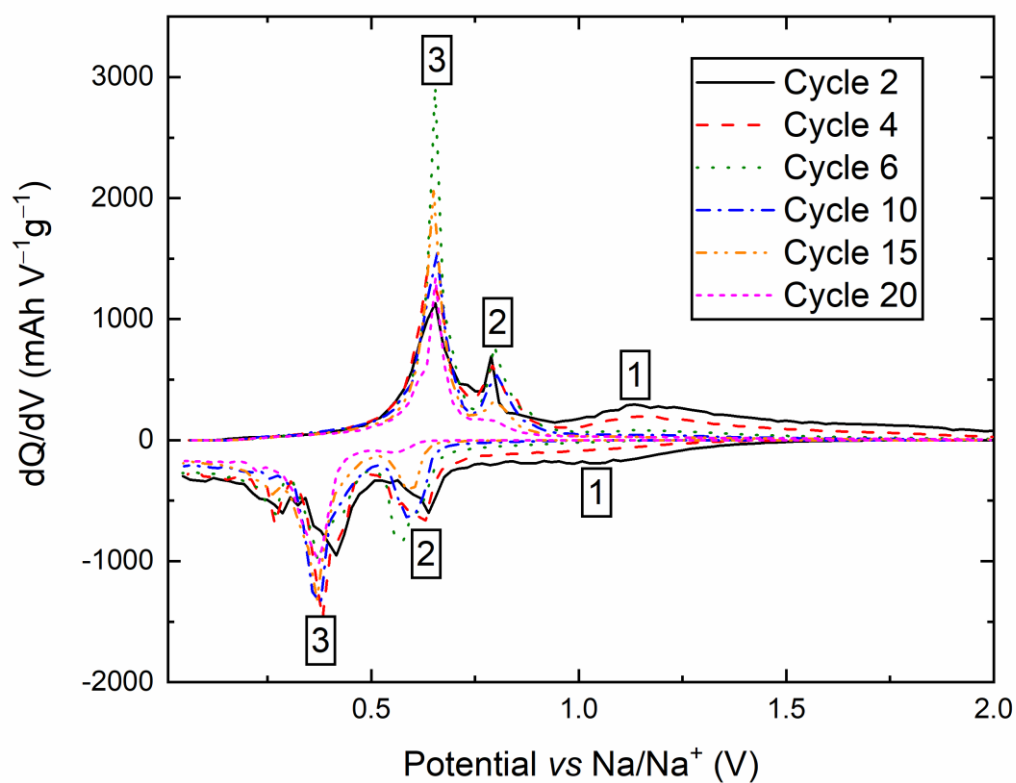


Figure S9: dQ/dV plot derived from (de)sodiation curves presented in Figure 2b in the main article.

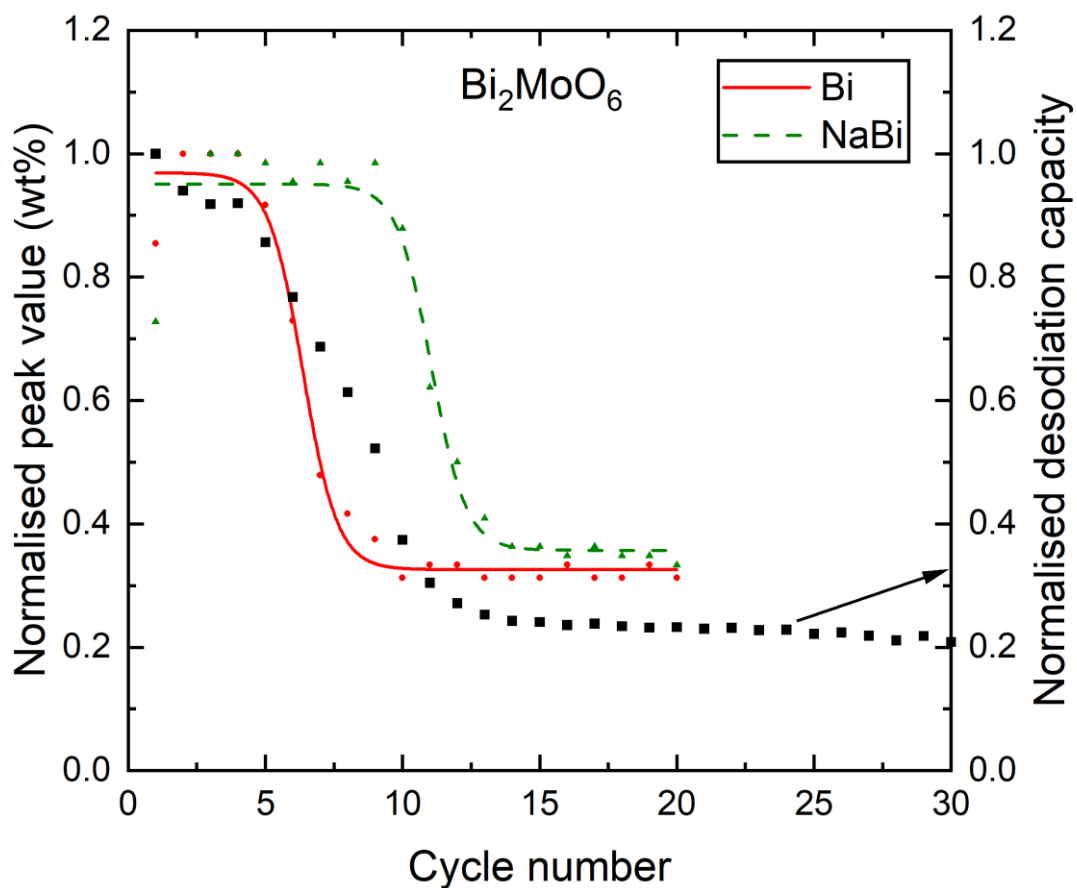


Figure S10: Maximum normalised phase fractions for Bi and NaBi vs cycle number extracted from surface Rietveld refinement on *operando* XRD measurement performed with a specific current of 0.1 A g^{-1} and a voltage range of $0.01\text{--}2.00 \text{ V}$ from our previous study on Bi_2MoO_6 [3].

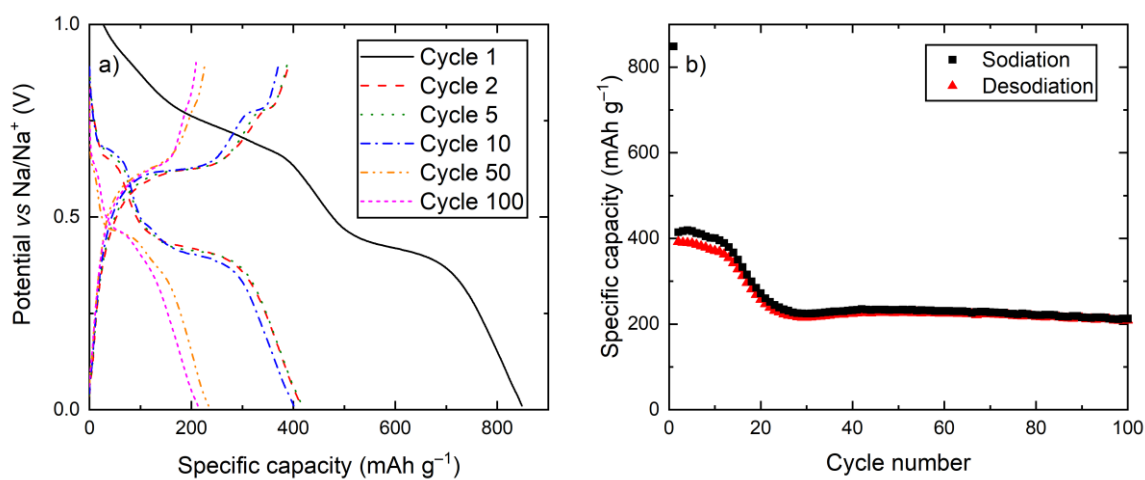


Figure S11: a) (De)sodiation curves and b) capacity per cycle plot from GC measurement on BiFeO_3 cycled between $0.01\text{--}0.90 \text{ V}$ with a current density of 0.1 A g^{-1} .

References

- [1] Sottmann, J.; Herrmann, M.; Vajeeston, P.; Hu, Y.; Ruud, A.; Drathen, C.; Emerich, H.; Fjellvag, H.; Wragg, D. S. How Crystallite Size Controls the Reaction Path in Nonaqueous Metal Ion Batteries: The Example of Sodium Bismuth Alloying. *Chemistry of Materials*, **2016**, *28*(8), 2750-2756.
- [2] Surendran, A.; Enale, H.; Thottungal, A.; Sarapulova, A.; Knapp, M.; Nishanthi, S.; Dixon, D.; Bhaskar, A. Unveiling the Electrochemical Mechanism of High-Capacity Negative Electrode Model-System BiFeO₃ in Sodium-Ion Batteries: An in Operando XAS Investigation. *ACS applied materials & interfaces*, **2022**, *14*(6), 7856-7868.
- [3] Brennhagen, A.; Cavallo, C.; Wragg, D. S.; Vajeeston, P.; Sjøstad, A. O.; Kuposov, A. Y.; Fjellvåg, H. Operando XRD Studies on Bi₂MoO₆ as Anode Material for Na-Ion Batteries. *Nanotechnology*, **2022**, *33*(18), 185402.
- [4] Mei, J.; Liao, T.; Ayoko, G. A.; Sun, Z. Two-Dimensional Bismuth Oxide Heterostructured Nanosheets for Lithium-and Sodium-Ion Storages. *ACS applied materials & interfaces*, **2019**, *11*(31), 28205-28212.
- [5] Kim, M.-K.; Yu, S.-H.; Jin, A.; Kim, J.; Ko, I.-H.; Lee, K.-S.; Mun, J.; Sung, Y.-E. Bismuth Oxide as a High Capacity Anode Material for Sodium-Ion Batteries. *Chemical Communications*, **2016**, *52*(79), 11775-11778.
- [6] Sun, J.; Li, M.; Oh, J. A. S.; Zeng, K.; Lu, L. Recent Advances of Bismuth Based Anode Materials for Sodium-Ion Batteries. *Materials Technology*, **2018**, *33*(8), 563-573.

Paper 5

Combined *operando* PDF and XAS revealing the (de)sodiation mechanism of Bi_2MoO_6

A. Brennhagen, A. Skurtveit, D. S. Wragg, C. Cavallo, A. O. Sjøstad, A. Y. Kuposov, and H. Fjellvåg

Manuscript in preparation

